Charles University in Prague
Faculty of Mathematics and Physics

DOCTORAL THESIS

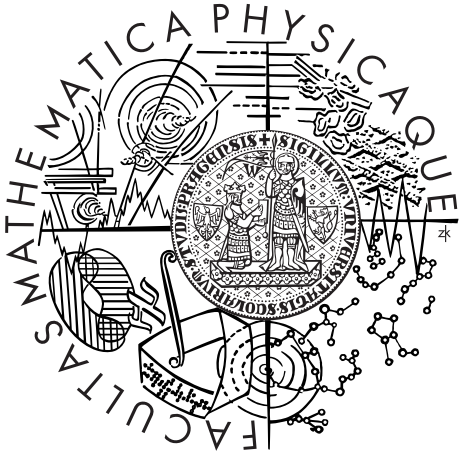

Michal Šindler

Properties of superconductors in the terahertz frequency region

Department of Low Temperature Physics

Supervisor: Professor RNDr. Ladislav Skrbek, DrSc.
Study programme: Physics
Specialization: 4F3 Physics of Condensed Matter and Materials Research

Prague 2012

Acknowledgments

I would like to take this opportunity to thank my friends, family and colleagues who helped me during the work. I learnt a great many things from my university co-students, especially from Jiří Lipovský, Jan Prachař, David Schmoranzer and Pavel Kvasnička. I followed David Schmoranzer, who started his studies one year before me, in his footsteps, so I can say that he was my vanguard, making my life much easier. During my entire doctoral studies I was privileged to have a wonderful roommate in the person of Pavel Paták.

I have to acknowledge all my collegues from far-infrared magneto-optical laboratory. Jan Koláček was kind enough to spend large amounts of time talking about various aspects of superconductivity, in particular about my progress in understanding the topic presented in this thesis. Roman Tesař is commended for his help with practical tasks in the laboratory, especially in creating measurement scripts. Miloš Zíka took care of all supporting technical stuff allowing us to fully concentrate on physical problems.

Outside the laboratory, I would like to acknowledge our coworkers from Terahertz and ultrafast spectroscopy group, namely Petr Kužel, Christelle Kadlec and Filip Kadlec. I believe mutual cooperations between our two groups have been very beneficial for both sides. Further, I would like to acknowledge Petr Kužel for improving parts of this thesis devoted to time-domain terahertz spectroscopy. Štefan Višňovský provided valuable consultations about the propagation of electromagnetic radiation in multilayered media. Ivan Rychetský helped me clarify some aspects of Maxwell-Garnett theory and effective medium approximation.

Most importantly, Ladislav Skrbek guided me through my entire (so-far-short) scientific career, from the very beginning to the present day both as teacher and as supervisor. He dedicated many hours of his time well beyond his duties to my work and provided me with opportunities to work and learn abroad. He was also able to push me to work harder whenever my little lazy nature resisted.

Finally, I would like to acknowledge my parents for their support during all my years at university.

I declare that I carried out this doctoral thesis independently, and only with the cited sources, literature and other professional sources.

I understand that my work relates to the rights and obligations under the Act No. 121/2000 Coll., the Copyright Act, as amended, in particular the fact that the Charles University in Prague has the right to conclude a license agreement on the use of this work as a school work pursuant to Section 60 paragraph 1 of the Copyright Act.

In ..... date ..... Signature

Název práce: Vlastnosti supravodičů v oblasti terahertzových frekvencí

Autor: Michal Šindler

Katedra: Katedra fyziky nízkých teplot

Vedoucí disertační práce: Prof. RNDr. Ladislav Skrbek, DrSc.

Abstrakt: Teplotní závislosti propustnosti tenkých supravodivých vrstev NbN byly měřeny v magnetickém poli ve Faradayově a Voigtově geometrii pro různé polarizace laserového svazku v daleké infračervené oblasti pro frekvence nad a pod disociační energií Cooperova páru. Propustnost v nulovém magnetickém poli je velmi dobře popsána Zimmermannovým rozšířením teorie BCS [Physica C 183, 99-104 (1991)]. Ve vnějším magnetickém poli jsou optické vlastnosti supravodičů kvalitativně i kvantitativně ovlivněny přítomností kvantovaných vírů. Propustnost vícevrstevnatých vzorků - vrstev NbN na různých substrátech - byla analyzována s přihlédnutím k interferenčním jevům, v případě dvojlomné safírové podložky pomocí Yehova formalismu [J. Opt. Soc. Am. 69, 742-756 (1979)]. Ve Voigtově geometrii byl pozorován významný rozdíl pro transmisi elektromagnetického záření s lineární polarizací paralelní s magnetickým polem a pro polarizaci kolmou. Navržený fenomenologický model postihuje pozorované vlastnosti supravodičů pro všechny geometrické konfigurace experimentu.

Klíčová slova: supravodivost, terahertzová spektroskopie, vysokofrekvenční vodivost, kvantované víry

Title: Properties of superconductors in the terahertz frequency region

Author: Michal Šindler

Department: Department of low temperature physics

Supervisor: Prof. RNDr. Ladislav Skrbek, DrSc.

Abstract: Temperature dependence of transmission through thin superconducting NbN films in various magnetic fields applied in both Faraday and Voigt geometries has been measured and analysed for various linear polarisations of laser beam in terahertz range at frequencies both above and below the optical gap. Zero-field data are well explained using the extension of BCS-based model of Zimmermann *et al.* [Physica C 183, 99-104 (1991)]. In external magnetic field, vortex presence substantially influences optical properties of superconductors, both qualitatively and quantitatively. Transmissions through double-layer media - NbN films deposited on various substrates - have been analysed by taking into account interference effects, in case of birefringent sapphire substrate by utilizing Yeh formalism [J. Opt. Soc. Am. 69, 742-756 (1979)]. In Voigt geometry, observed transmissions for linear polarisation of the laser beam parallel with and perpendicular to the applied magnetic field exhibit different features. A developed phenomenological model captures all main experimental observations and accounts for different geometrical configurations.

Keywords: superconductivity, terahertz spectroscopy, high-frequency conductivity, vortices

Contents

Preface

This thesis is devoted to experimental and theoretical investigations of the transmission of thin superconducting NbN films in terahertz frequency range in magnetic field carried out over past four years. Our main aim is to understand high-frequency behavior of classical superconducting thin films in externally applied magnetic field. Although the exact knowledge of physical properties of superconductors is fundamental from the point of view of their future application, to our knowledge there has not yet been systematic study over broad terahertz range for temperature ranging from zero up to the critical temperature in high magnetic fields. Terahertz region currently attracts great attention since a substantial technological progress in generation and detection of terahertz radiation was achieved and advance in hardware technology pushes application to higher frequencies, in future possibly even in terahertz range. Further, controlled vortex motion - fluxonics - might be used in quantum computation. High-frequency vortex dynamics constitutes an essential tool for these aspirations, however, it is not yet properly understood.

The work is a result of collaboration between Department of Low Temperature Physics, Faculty of Mathematics and Physics, Charles University in Prague and Institute of Physics of the Academy of Sciences of the Czech Republic, v. v. i. Experiments have been performed in Far-InfraRed Magneto-optical (FIRM) laboratory in the Institute of Physics in Cukrovarnická 10, Prague. Our small working group includes the author, Roman Tesař, Jan Koláček and Ladislav Skrbek. While Tesař has been in charge of our laboratory equipment, Koláček and Skrbek have provided general overview of our physical research and guidance.

More recently, time-domain terahertz spectroscopy have been employed to study high-frequency conductivity of NbN films in THz range in cooperation with Petr Kužel, Christelle Kadlec and Filip Kadlec from the group of Terahertz and ultrafast spectroscopy, Institute of Physics of the AS of the CR, v.v.i, Na Slovance 2, Prague.

In the presented research, the author actively participated in all described experiments. In particular, he created LabView scripts which automated transmission experiments, analysed the experimental data and spent countless hours 'babysitting' experiments. On the theoretical side, the author studied optical properties of multilayer structures and calculated transmission through superconductor/substrate samples in case of isotropic layers as well as in case of anisotropic layers. The author developed the phenomenological model presented in this thesis.

Besides this thesis, author contributed in writing of four reviewed articles [1, 2, 3, 4] which were published or accepted for publication. Drafts [1, 4] were written entirely by the author and he substantially contributed in numerical calculations in paper [3]. Author contribution to these papers allows him to use selected parts of these articles in this thesis. Additionally, results of ongoing progress in our research have been presented by the author at several international conferences.

1. Introduction

In this chapter theoretical introduction is given. Topics are organised into three sections. First section is devoted to the general dielectric properties of solids and description of propagation of THz radiation. Basic optical variables are introduced so one gets familiar with conventions and notation used in this thesis. Other two sections are devoted to the properties of superconducting materials. First of them describes normal state while the other one, quite extensive, presents selected theoretical aspects of superconductivity.

1.1 General dielectric properties of solids

Electromagnetic radiation can be described by a monochromatic wave

$$\mathcal{E} = \mathcal{E}_0 \mathrm{e}^{i(\tilde{\mathbf{k}}.\mathbf{r}-\omega t)} \tag{1.1}$$

where $\tilde{\mathbf{k}}$ is the wavevector[1], $\mathbf{r}$ is the position vector, the symbol '.' indicates the dot product, ω is the angular frequency ($= 2\pi\nu$), t is the time, $\mathcal{E}$ is the electric intensity and $\mathcal{E}_0$ is the amplitude of electric intensity. This approximation has many advantages: it is easy to work with and it describes laser radiation well [5]. Assuming that the electromagnetic radiation is propagating in the direction of the z-axis, we can rewrite equation 1.1 as

$$\mathcal{E}(z,t) = \mathcal{E}_0 \mathrm{e}^{i(\tilde{k}z-\omega t)}. \tag{1.2}$$

Generally, wavevector $\tilde{\mathbf{k}}$ is a complex quantity

$$\tilde{\mathbf{k}} = \tilde{n}\frac{\omega}{c}\mathbf{s} = (n + i\kappa)\frac{\omega}{c}\mathbf{s}, \tag{1.3}$$

where $\tilde{n}$ is the complex refractive index, c is the speed of light in the vacuum and $\mathbf{s}$ is the unit vector in the direction of propagation. Further, n is the real part of refractive index while the imaginary part κ is called extinction coefficient and it enables to describe absorption. By inserting this expression for complex wavevector into equation 1.2 we obtain

$$\mathcal{E}(z,t) = \mathcal{E}_0 \mathrm{e}^{i(\omega\tilde{n}z/c-\omega t)} = \mathcal{E}_0 \mathrm{e}^{-\kappa\omega z/c} \mathrm{e}^{i(\omega n z/c-\omega t)}. \tag{1.4}$$

This shows that the non-zero extinction coefficient leads to an exponential decay of the wave in the medium. The radiation intensity is given as a magnitude of the time-averaged Poynting vector [6]:

$$I = |<\mathbf{S}>| = \frac{1}{2}|\mathcal{E} \times \mathcal{H}^*| = \frac{1}{2} n c \varepsilon_0 |\mathcal{E}_0|^2. \tag{1.5}$$

Here $\mathcal{H}$ is the magnetic field strength and ε_0 is the permittivity of vacuum. Intensity is proportional to the square of the electric field, $I \propto \mathcal{E}\mathcal{E}^*$, so intensity decays according to Lambert-Beer law as

$$I = I_0 \mathrm{e}^{-\alpha z}, \tag{1.6}$$

[1] Vectors are labeled by bold letters throughout the thesis except for $\mathcal{E}$ and $\mathcal{H}$ which are also vectors.

where the absorption coefficient is

$$\alpha = \frac{2\omega\kappa}{c}. \tag{1.7}$$

So far we described all material properties by refractive index but it is usually preferable to describe optical properties by variables such as relative permittivity ε_r and conductivity σ since they are closely connected with microscopic phenomena. Again, we will introduce a convenient complex form of permittivity

$$\tilde{\varepsilon}(\omega) = \varepsilon_1 + i\varepsilon_2 = \varepsilon_r + i\frac{\sigma}{\varepsilon_0\omega} \tag{1.8}$$

and complex conductivity

$$\tilde{\sigma}(\omega) = \sigma_1 + i\sigma_2 = -i\omega\varepsilon_0\tilde{\varepsilon}. \tag{1.9}$$

These two complex quantities are just two different ways how to fully describe both dielectric and conductive behavior of material. Excellent overview devoted to various optical parameters, such as $\tilde{\varepsilon}$, $\tilde{\sigma}$ and other, and to the relations among them is given by Schwartz [7].

Assuming a non-magnetic material, the refractive index is related to the complex permitivity [8]:

$$\tilde{n} = \sqrt{\tilde{\varepsilon}}. \tag{1.10}$$

The real and imaginary parts of permittivity, the conductivity or the refractive index are not independent. It can be shown [9] that they are related to each other and they obey Kramers - Kronig relations, which enable to determine imaginary part if we know entire frequency dependence of the real part and vice versa. Here we explicitly write Kramers-Kronig relations for conductivity [10]:

$$\sigma_1(\omega) = \frac{2}{\pi}\int_0^\infty \frac{\omega'\sigma_2(\omega')\mathrm{d}\omega'}{\omega'^2 - \omega^2} + \text{constant} \tag{1.11a}$$

$$\sigma_2(\omega) = -\frac{2\omega}{\pi}\int_0^\infty \frac{\sigma_1(\omega')\mathrm{d}\omega'}{\omega'^2 - \omega^2}. \tag{1.11b}$$

We have to point out that in some literature one can find complex refractive index in the form $\tilde{n} = n - i\kappa$. This is because some authors describe monochromatic wave in the form $\mathcal{E} = \mathcal{E}_0 \exp -\mathrm{i}(\tilde{\mathbf{k}}.\mathbf{r} - \omega t)$, so in order to get physically meaningful exponential decay according to Lambert - Beer law (eq. 1.6), sign in front of the imaginary part must be reversed. Differences between these two conventions are summarized in table 1.1.

Table 1.1: Table of conventions

Monochromatic wave	$\mathcal{E}_0 \exp[\mathrm{i}(\mathbf{k}.\mathbf{r} - \omega t)]$	$\mathcal{E}_0 \exp[-\mathrm{i}(\mathbf{k}.\mathbf{r} - \omega t)]$
refractive index	$n + \mathrm{i}\,\kappa$	$n - \mathrm{i}\,\kappa$
permittivity	$\varepsilon_1 + \mathrm{i}\,\varepsilon_2$	$\varepsilon_1 - \mathrm{i}\,\varepsilon_2$
conductivity	$\sigma_1 + \mathrm{i}\,\sigma_2$	$\sigma_1 - \mathrm{i}\,\sigma_2$

When studying interaction of light with solid state material, three basic processes are observed: reflection, propagation and transmission. Propagation is generally accompanied with absorption if some dissipation process takes place. Reflection and transmission occur on interface between the two media with different refractive indices. Following Maxwell equations, the parallel components of the vector fields $\mathcal{E}$, $\mathcal{H}$ are continuous across the interface. The reflection amplitude coefficient r and the transmission amplitude coefficient t are introduced using Fresnel's equations. Let's stress that in the whole thesis we will only deal with the normal incidence. In that case, p-wave and s-wave[2] can not be distinguished, so only one formula for r, respectively t, is needed.

Before we proceed any further, it is necessary to introduce a consistent way of describing the optical variables (r, t, $\mathcal{E}$) in a multilayer medium, which enable to account for all the cases described in this thesis. A multilayer structure consists of N layers numbered in their order as $1, 2 \dots N$. This multilayer is surrounded by environment number 0 from the left and environment number $(N+1)$ from the right. Although it is possible to treat the cases when electromagnetic radiation is incoming from both environments simultaneously, we will consider only the case of radiation propagating from the left to the right. We will use upper indices to associate the variable with that medium for which it applies. We start using this convection by writing the reflection amplitude coefficient for the interface between medium 0 and medium 1 when light propagates from the left to the right

$$r^{(0,1)} = \frac{\mathcal{E}_r^{(0)}}{\mathcal{E}_i^{(0)}} = \frac{\tilde{n}_0 - \tilde{n}_1}{\tilde{n}_0 + \tilde{n}_1} \tag{1.12}$$

and the transmission amplitude coefficient for the same case

$$t^{(0,1)} = \frac{\mathcal{E}_t^{(1)}}{\mathcal{E}_i^{(0)}} = \frac{2\tilde{n}_0}{\tilde{n}_0 + \tilde{n}_1}. \tag{1.13}$$

Lower indices i, t and r stand for incoming, reflected and transmitted waves, respectively. During free propagation the wave acquires a phase

$$\delta = \frac{\tilde{n}\omega}{c} d. \tag{1.14}$$

Capital letters $\mathcal{R}$ and $\mathcal{T}$ describe the reflection intensity coefficient and the transmission intensity coefficient:

$$R = \frac{I_r}{I_i} = |r|^2 ; \tag{1.15a}$$

$$T = \frac{I_t}{I_i} = \frac{(n_{in})}{(n_{out})} |t|^2, \tag{1.15b}$$

where subscript *in* is associated with the medium from which radiation propagates and subscript *out* means the medium where radiation goes out.

[2] s-wave, respectively p-wave, is well-established description of electromagnetic wave with electric component in the plane of the interface, respectively in a perpendicular direction to s-polarized wave above

Now, we can turn our attention to the simplest case of a multilayer structure - a monolayer slab with all media isotropic and homogeneous. This simple case can be described by the method of beams summation. We consider that surrounding media on both sides can in principle be different.

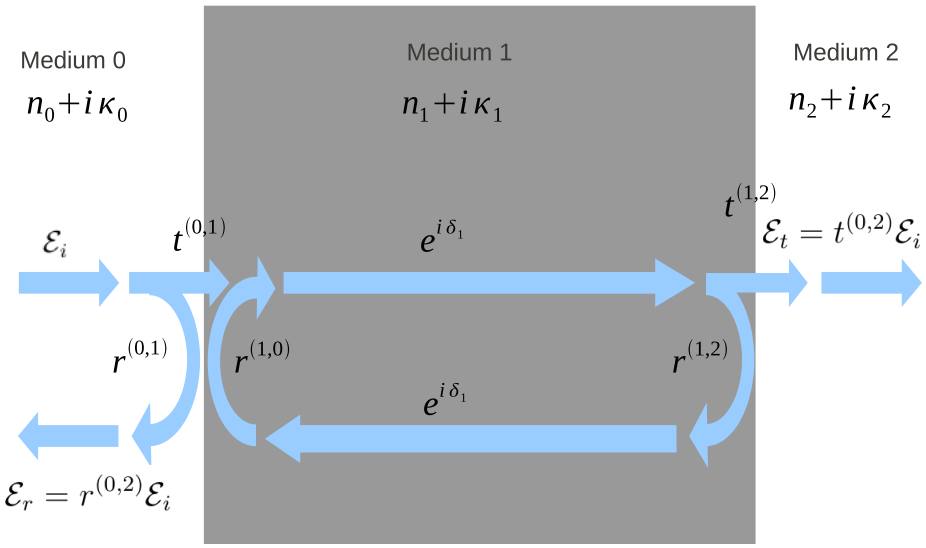

Figure 1.1: Schematic description of Fabry-Perot resonator

Following the beam in figure 1.1, the incoming beam $\mathcal{E}_i$ is both reflected $r^{(0,1)}\mathcal{E}_i$ and transmitted through $t^{(0,1)}\mathcal{E}_i$ at the 01 interface. The transmitted beam is propagating in medium 1 and it reaches the second interface with a phase difference

$$\delta_1 = \frac{\tilde{n}_1\omega}{c}d_1, \tag{1.16}$$

where d_1 is the film thickness. On the interface it is reflected again and transmitted through. According to figure 1.1, a monochromatic wave experiences infinite number of internal reflections and during each "cycle" the wave is partially transmitted through both surrounding environments. The total amount of transmitted radiation is given by sum

$$\frac{\mathcal{E}_t^{(2)}}{\mathcal{E}_i^{(0)}} = t^{(0,1)}e^{i\delta_1}t^{(1,2)} + t^{(0,1)}r^{(1,2)}r^{(1,0)}t^{(1,2)}e^{3i\delta_1} + t^{(0,1)}r^{(1,2)}r^{(1,0)}r^{(1,2)}r^{(1,0)}t^{(1,2)}e^{5i\delta_1} + \cdots . \tag{1.17}$$

In this sum, the first term represents the direct transmission through the layer, the second term considers two internal reflections and acquired phase in the film before it is transmitted to the medium 2, the remaining terms simply consider an even number of internal reflections and acquired phase in an analogical way as the second term. We can rearrange the sum

$$\frac{\mathcal{E}_t^{(2)}}{\mathcal{E}_i^{(0)}} = t^{(0,1)}e^{i\delta_1}t^{(1,2)}(1 + r^{(1,2)}r^{(1,0)}e^{2i\delta_1} + r^{(1,2)}r^{(1,0)}r^{(1,2)}r^{(1,0)}e^{4i\delta_1} + \cdots). \tag{1.18}$$

The term in the brackets represents a geometrical progression with a common ratio $q = r^{(1,2)}r^{(1,0)}e^{i2\delta_1}$, absolute value of which is smaller than unity ($|q| < 1$),

since $|r| < 1$, $|t| < 1$ and $|\exp(i\delta_1)| \leq 1$ (except for very special cases). Therefore we can use a standard formula to sum:

$$S = \frac{1}{1-q} \tag{1.19}$$

and the resulting transmission through a monolayer structure is obtained as

$$t^{(0,2)} = \frac{\mathcal{E}_t^{(2)}}{\mathcal{E}_i^{(0)}} = \frac{t^{(0,1)}t^{(1,2)}e^{i\delta_1}}{1 - r^{(1,2)}r^{(1,0)}e^{i2\delta_1}}. \tag{1.20}$$

By the same method one can obtain the total amplitude reflection coefficient for a monolayer system:

$$r^{(0,2)} = \frac{\mathcal{E}_r^{(0)}}{\mathcal{E}_i^{(0)}} = \frac{r^{(0,1)} + r^{(1,2)}e^{2i\delta_1}}{1 + r^{(0,1)}r^{(1,2)}e^{2i\delta_1}}. \tag{1.21}$$

If we try to deal with a double layer system, we will face a problem: how to sum all internal reflections and transmissions through internal surfaces and it is not clear how to solve this problem. However, for some special cases internal reflections in layer can be neglected ($|r| \ll 1$) and we can use summation of beams analogically as in case of Fabry Perot etalon. One layer is treated as a monolayer structure and internal reflections inside the remaining layers are neglected and only direct transmission is considered.

This can be done for very thin superconducting layers. Let's express transmission as $t = t_{sample}/t_{ref}$, where t_{ref} is the transmission through the bare substrate without a film and t_{sample} is the transmission through the whole double-layer. Further, the thin film approximation ($|\tilde{n}_1(\omega/c)d| \ll 1$) is used to simplify the exponential term: $\exp(i(\omega/c)\tilde{n}_1 d_1) \approx 1 + i(\omega/c)\tilde{n}_1 d_1$ and the refractive index of surrounding enviroment $n_0 = n_3$ is explicitly written as unity. Using all mentioned approximations and formula for refractive index $\tilde{n} = \sqrt{1 + i\tilde{\sigma}/\varepsilon_0\omega}$, the equation for transmission yields

$$t(\omega) = \frac{1 + n_2}{1 + n_2 + Z_0\tilde{\sigma}(\omega)d} \exp[i(\omega/c)\Delta L], \tag{1.22}$$

where Z_0 represents the impedance of free space

$$Z_0 = \mu_0 c_0 = \sqrt{\frac{\mu_0}{\varepsilon_0}} \doteq 377\ \Omega. \tag{1.23}$$

Here μ_0 is vacuum permeability and $\Delta L = d_2 - d_{sub}$ accounts for possibly different thicknesses of bare substrate and substrate in the double-layer.

1.2 Dielectric properties of normal metals

Optical properties of metals are mainly governed by the response of free electrons, although contributions from phonons or from interband transitions have to be taken into account in many cases. The free electron model was proposed by Drude in 1900. It considers the valence electrons to be free. When an electric field is applied, the free electrons accelerate and then undergo collisions with the

characteristic momentum scattering time τ (also known as the relaxation time). The high frequency conductivity is given as

$$\tilde{\sigma}(\omega) = \frac{\sigma_N(0)}{1 - i\omega\tau}, \tag{1.24}$$

where

$$\sigma_N(0) = \frac{Ne^2\tau}{m_0} \tag{1.25}$$

is the DC conductivity, N is a number of electrons per unit volume (for metals, typically in the range $10^{28} - 10^{29}$ m^{-3} [11]), $-e$ is the charge of electron and m_0 is its mass. Drude assumed bare electron mass but nowadays better results are achieved by using effective mass of electron in the medium. Note that, at room temperature, for metals τ is typically 10^{-13} to 10^{-15} s [11, 12].

Let's introduce an important quantity called *plasma frequency* ω_p

$$\omega_p = \left(\frac{Ne^2}{\varepsilon_0 m_0}\right)^{\frac{1}{2}}, \tag{1.26}$$

which in metals is typically in the ultraviolet region.

Using the equation for plasma frequency 1.26 and equation 1.8 one can express the complex permittivity

$$\varepsilon_1 = 1 - \frac{\omega_p^2\tau^2}{1 + \omega^2\tau^2}; \tag{1.27a}$$

$$\varepsilon_2 = \frac{\omega_p^2\tau}{\omega(1 + \omega^2\tau^2)}. \tag{1.27b}$$

High reflectivity of metals can be explained by these equations. For simplicity, let us assume that $\tau \to 0$. The formula for permittivity is then greatly simplified

$$\tilde{\varepsilon} = 1 - \frac{\omega_p^2}{\omega^2}. \tag{1.28}$$

Permittivity is therefore purely real and for $\omega < \omega_p$ it is negative while for $\omega > \omega_p$ it is positive. Negative value of permitivity leads, according equation 1.10, to purely imaginary refractive index. For sufficiently thick medium, the reflectivity $\mathcal{R}$ can be calculated as [8]

$$\mathcal{R} = \left|\frac{\tilde{n} - 1}{\tilde{n} + 1}\right|, \tag{1.29}$$

therefore for $\omega < \omega_p$ reflectivity is unity, and then it decreases for $\omega > \omega_p$, approaching zero at $\omega = \infty$. Therefore metals are shiny for frequencies below ω_p but they are transparent for higher frequencies.

1.3 Properties of superconductors

In this section a brief overview of properties of superconductors, which are important for our experimental efforts, is given.

First, microscopic Bardeen-Cooper-Schrieffer theory explains the origin of superconductivity for classical low-T_c superconductors. Further, it is able to quantitatively describe various properties such as excitation spectrum, ultrasonic attenuation, electromagnetic absorption and many others. We will focus on origin of coherence effects since they are closely related to electromagnetic absorption. Explanation of effects due to the coherence effects is one of the greatest successes of BCS theory since the two-fluid model is unable to explain them even on qualitative level. It might seem that BCS theory is almost almighty but it has also its limits. So far, it has not been able to explain high-T_c superconductivity of cuprates or pnictides. Further, any extension of BCS theory to the cases in which energy gap Δ is not constant in space is very difficult and other approaches are usually utilized.

Second, the energy gap $\Delta(r)$ in the presence of magnetic field is not spatially uniform and Ginzburg-Landau theory is more convenient than BCS theory in this case. We will focus on behavior of second type of superconductors, particularly on effects associated with the presence of vortices.

1.3.1 BCS theory

In 1956 Cooper [13] showed that arbitrarily small attractive interaction between two electrons near the Fermi surface leads to formation of at least one bound pair of electrons with energy smaller than the sum of energies of these individual electrons. Assuming weak interaction that affects only electrons in a thin layer around spherically symmetric Fermi surface, the lowest energy of bound Cooper pair corresponds to the pair of electrons with equal magnitude of momenta but of opposite direction (see fig 1.2). Further, we expect singlet coupling of spins to have lower energy because electrons can be found near each other with greater probability, due to the requirement of total antisymmetry of wavefunction. To summarize, Cooper pairs are formed from electrons with opposite momentum and spin: (k, s) with $(-k, -s)$.

Only a year later, in 1957, Bardeen, Cooper and Schrieffer [14] extended Cooper idea of bound electron pairs and introduced first successful microscopic theory of superconductivity. Schrieffer constructed a coherent state many-particle wavefunction that enables Cooper pairs to exhibit quantum mechanical properties on macroscopic scale including zero DC resistivity. Finally, Bardeen argued that the origin of attractive interaction is due to the electron-phonon interaction as it was first suggested by Fröhlich [15]. In a little oversimplified way, one can imagine that a moving electron with its negative charge attracts positive ions leading to a small lattice distortion. Positive ions overscreen the negative charge of that electron and second electron of the Cooper pair is attracted towards this positively charged area.

A fermionic many particle wavefunction is required to be antisymmetric. This can be utilized by Slater determinant which specifies N-electron antisymmetrized product function. The Slater determinants are conveniently expressed using the language of second quantization. We introduce creation operator $c^*_{k\uparrow}$ which creates electron in state k with spin up and annihilation operator $c_{k\uparrow}$ which empties the corresponding state. Fermion creation and annihilation operators obey the following anticommutation relations:

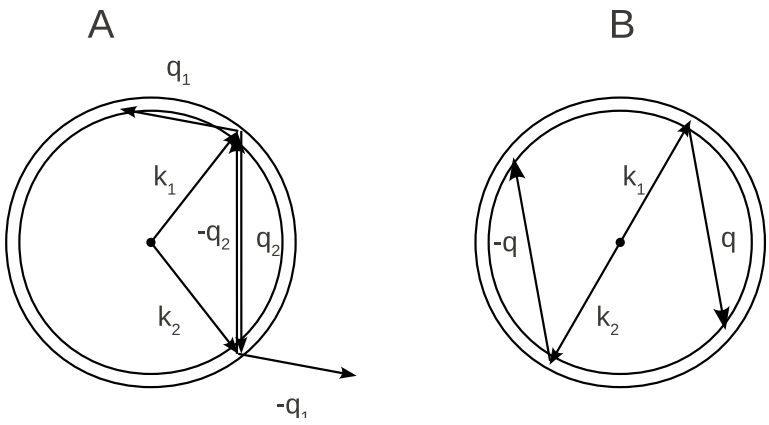

Figure 1.2: Interaction of two electrons near Fermi surface. Total energy and total momentum $\mathbf{K} = \mathbf{k}_1 + \mathbf{k}_2$ of electron pair is conserved during scattering due to the interaction. The momentum of first electron can be changed by interaction from $\mathbf{k_1}$ to $\mathbf{k_1}+\mathbf{q}$ while the momentum of second electron must be simultaneously changed from $\mathbf{k_2}$ to $\mathbf{k_2} - \mathbf{q}$. Magnitude of matrix element is proportional to the number of possible scattering events. In the case A only interaction with $\mathbf{q} = \mathbf{q_2}$ preserves total energy while in the case B number of possible $\mathbf{q}$ is much greater, therefore this case ($\mathbf{K} = 0$ with $\mathbf{k}_1 = -\mathbf{k}_2$) maximizes number of such scattering events and minimizes the energy of the electron pair.

$$\begin{aligned} [c_{ks}, c^*_{k',s'}]_+ &\equiv c_{ks}c^*_{k',s'} + c^*_{k',s'}c_{ks} = \delta_{kk'}\delta_{ss'} \\ [c_{ks}, c_{k',s'}]_+ &= [c^*_{ks}, c^*_{k',s'}]_+ = 0 \end{aligned} \tag{1.30}$$

The particle number operator n_{ks} is defined by

$$n_{ks} = c^*_{ks}c_{ks}. \tag{1.31}$$

In BCS theory the ground state many-particle wavefunction is given as

$$|\psi_G\rangle = \prod_{k=k_1,\ldots,k_M} \left(u_k + v_k c^*_{k\uparrow}c^*_{-k\downarrow}\right)|0\rangle, \tag{1.32}$$

where $|u_k|^2 + |v_k|^2 = 1$ and $|0\rangle$ is vacuum state with no particles present. v_k is generally a complex number and a square of its absolute value, $|v_k|^2$, represents the probability that the pair $(k\uparrow, -k\downarrow)$ is occupied. Analogically, $|u_k|^2$ represents the probability that it is empty.

Bardeen, Cooper and Schrieffer wrote reduced hamiltonian, which contains only terms important for superconductivity

$$H = \sum_{ks} \xi_k c^*_{ks}c_{ks} + \sum_{kl} V_{kl}c^*_{k\uparrow}c^*_{-k\downarrow}c_{-l\downarrow}c_{l\uparrow}. \tag{1.33}$$

Here ξ_k is the single-particle energy relative to the Fermi energy and V_{kl} is the matrix element corresponding to scattering electrons from state $(l\uparrow, -l\downarrow)$ to state $(k\uparrow, -k\downarrow)$ due to the attractive interaction. Hamiltonian can be further simplified assuming a simple form of V_{kl}

$$V_{kl} = \begin{cases} -V & \text{if } |\xi_k| \text{ and } |\xi_l| \leq \hbar\omega_c \\ 0 & \text{otherwise} \end{cases} \tag{1.34}$$

where V is a positive constant and ω_c is maximum phonon frequency corresponding to approximately Debye frequency ω_D [16]. This hamiltonian can be solved by different techniques. Originally, variational method was applied [14]. In this work, the analysis is skipped and only results are shown. A comprehensive step by step solution can be found in some standard superconductivity textbooks such as [10].

The BCS wavefunction (eq. 1.32) minimizes energy with proper choice of coefficients

$$|v_k|^2 = \frac{1}{2}\left(1 - \frac{\xi_k}{E_k}\right); \tag{1.35a}$$

$$|u_k|^2 = \frac{1}{2}\left(1 + \frac{\xi_k}{E_k}\right), \tag{1.35b}$$

where E_k is the excitation energy of a quasiparticle of momentum $\hbar k$. In figure 1.3 we see that distribution of electrons in superconducting state at zero temperature is only slightly different from the Fermi-Dirac distribution function f_k at T_c. The phase transition from normal state to superconducting state is rather due to replacing electron states with random phases by a coherent state with a fixed phase rather than due to changes in occupation of one-electron momentum eigenstates, see figure 1.3.

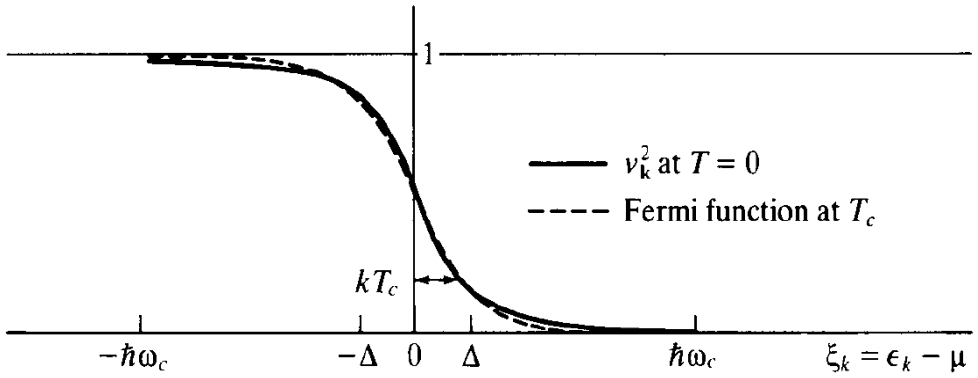

Figure 1.3: Plot of BCS occupation fraction $|v_k|^2$ versus Fermi-Dirac statistics at T_c [10]. Here ϵ_k is the single-particle energy, μ is the chemical potential, in this case Fermi energy, and k is the Boltzmann constant.

Energy E_k is given by

$$E_k = \sqrt{\xi_k^2 + \Delta^2}, \tag{1.36}$$

where Δ corresponds to minimal energy required to add one electron.

Usually, we are interested in excitation of an electron from the ground state rather than adding an extra new electron. In this case, a minimal energy 2Δ is required since it is not possible to excite one electron and leave the other electron from Cooper pair in its original state. In a weak coupling limit $N(0)V \ll 1$ (where $N(0)$ is the density of state on the Fermi surface) the optical gap becomes

$$2\Delta(0) = 3.53\, k_B T_c, \tag{1.37}$$

where k_B is Boltzmann constant, $\Delta(0)$ is the gap at zero temperature and T_c is the critical temperature. Experimental values of $2\Delta(0)$ for different materials and different direction in k space generally fall in the range from $3.0\,k_BT_c$ to $4.5\,k_BT_c$, with most of them clustered near the BCS value [10].

Note that in the case of $\Delta = 0$ and coefficients

$$\begin{aligned} u_k &= 0, \quad v_k = 1, \quad \text{for } k < k_F \\ u_k &= 1, \quad v_k = 0, \quad \text{for } k > k_F \end{aligned} \tag{1.38}$$

the above analyzed description reduces to the description of the normal state. Below T_c the normal state is also a solution of our problem, but with higher energy than the superconducting state. The energy difference between superconducting and normal phase (condensation energy) at zero temperature can be now evaluated as

$$U_s - U_N = -\frac{1}{2}N(0)\Delta^2(0), \tag{1.39}$$

where U is the standard thermodynamic variable for the internal energy density and $N(0)$ denotes the density of states at Fermi surface. In the case of non-zero temperature, we have to introduce the temperature dependent gap $\Delta(T)$ and equation will have the same form. For thermodynamic reasons, the condensation energy can also be expressed as

$$U_s - U_N = -\frac{B_c^2}{2\mu_0}, \tag{1.40}$$

where B_c is the thermodynamic critical field and μ_0 is the permeability of vacuum.

Although variational approach describes the ground state well, it becomes clumsy for treating the excited state. It is possible to diagonalize the BCS hamiltonian 1.33 by suitable change of variables [17]. This Bogoljubov-Valantin approach handles excited quasiparticle from BCS ground state and it is well-suited for description of superconducting state for finite temperatures up to T_c. Futher, we assume real valued u and v. It is necessary to introduce a new set of operators which are linear combinations of the original operators

$$\gamma_{k\uparrow}^* = u_k c_{k\uparrow}^* + v_k c_{-k\downarrow} \tag{1.41a}$$

$$\gamma_{-k\downarrow} = -v_k c_{k\uparrow}^* + u_k c_{-k\downarrow}. \tag{1.41b}$$

In fact, writing $u = \cos\theta$ and $v = \sin\theta$, the new operators are just a 2x2 rotation of the original ones [17]:

$$\begin{pmatrix} \gamma_{k\uparrow}^* \\ \gamma_{-k\downarrow} \end{pmatrix} = \begin{pmatrix} \cos\theta & \sin\theta \\ -\sin\theta & \cos\theta \end{pmatrix} \begin{pmatrix} c_{k\uparrow}^* \\ c_{-k\downarrow} \end{pmatrix}. \tag{1.42}$$

By reverse transformation we can express the old operators in terms of the new ones:

$$c_{k\uparrow}^* = u_k\gamma_{k\uparrow}^* - v_k\gamma_{-k\downarrow} \tag{1.43a}$$

$$c_{-k\downarrow} = +v_k\gamma_{k\uparrow}^* + u_k\gamma_{-k\downarrow}. \tag{1.43b}$$

Hamiltonian in terms of new creation and annihilation operators becomes:

$$\mathcal{H} = E_{0s} + \sum_k E_k(\gamma_{k\uparrow}^*\gamma_{k\uparrow} + \gamma_{-k\downarrow}^*\gamma_{-k\downarrow}), \tag{1.44}$$

where E_{0s} corresponds to energy of superconductor at zero temperature. The sum gives the energy increase due to excitation of quasiparticles since $\gamma_k^*\gamma_k$ is the quasiparticle number operator. These quasiparticles are often called *Bogoliubons* [10] and their wavefunction is a linear combination of normal state one-electron states. Evidently, the energies of these excitations are

$$E_k = (\xi_k^2 + |\Delta_k|^2)^{1/2}. \tag{1.45}$$

Bogoliubons follow the Fermi-Dirac distribution function f_k. BCS theory is thus extended to finite temperatures. Once again, we will not follow calculations since they can be found in standard books on superconductivity [10].

Temperature dependence of the gap $\Delta(T)$ can be obtained from the integral expression numerically

$$\frac{1}{N(0)V} = \int_0^{\hbar\omega_c} \frac{\tanh \frac{1}{2}\beta(\xi^2 + \Delta^2(T))^{1/2}}{(\xi^2 + \Delta^2(T))^{1/2}} \mathrm{d}\xi. \tag{1.46}$$

For weak coupling superconductors, $\Delta(T)/\Delta(0)$ is a universal function of $t = T/T_c$. It is almost constant at low temperatures, then it monotonically decreases to zero at T_c as it is shown in figure 1.4. This temperature dependence can be well-approximated by the following formula [18]:

$$\frac{\Delta(T)}{\Delta(0)} = \sqrt{\cos\left[\frac{\pi}{2}\left(\frac{T}{T_c}\right)^2\right]}. \tag{1.47}$$

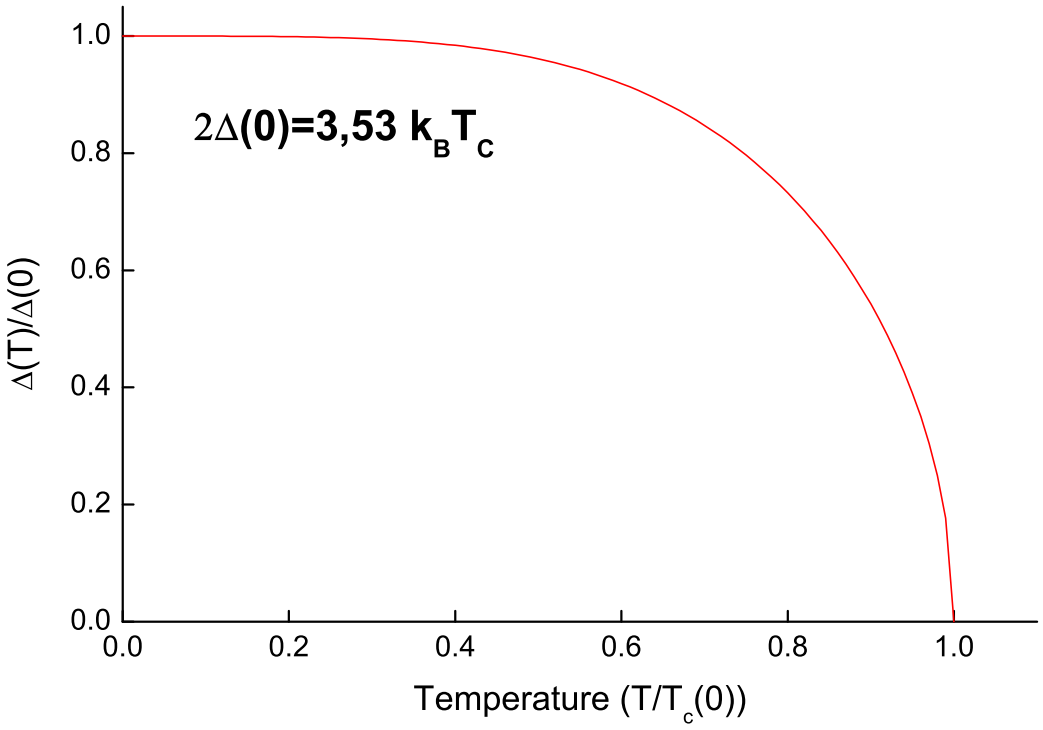

Figure 1.4: Temperature dependence of the gap

Assuming that the density of states is almost constant around Fermi surface in the normal state ($N_n(\xi) = N(0)$), the density of states in superconducting

state becomes

$$\frac{N_s(E)}{N(0)} = \frac{\mathrm{d}\xi}{\mathrm{d}E} = \begin{cases} \frac{E}{\sqrt{(E^2-\Delta^2)}} & (E > \Delta) \\ 0 & (E < \Delta). \end{cases} \tag{1.48}$$

1.3.2 Coherence effects

The interaction hamiltonian describing the effect of an external perturbation on electron can be expressed as

$$H_1 = \sum_{ks,k's'} B_{k's',ks} c^*_{k's'} c_{ks}, \tag{1.49}$$

where the $B_{k's',ks}$ are matrix elements of the perturbing operator between the ordinary one-electron states of the normal metal. In the normal state, each term in this sum is independent and the square of each $B_{k's',ks}$ is proportional to a corresponding transition probability [10]. Superconducting state consists of a phase coherent superposition of one-electron states and interference terms become important. This situation is analogical to interference effects in optics, where in the case of coherent light one has to sum amplitudes while in the case of non-coherent light summing intensities is possible.

In this thesis we assume $s = s'$ since we are interested only in interaction which does not involve spin. Expressing one-electron operators c in terms of quasiparticle operators γ we can see that the terms $c^*_{k's} c_{ks}$ a $c^*_{-k-s} c_{-k'-s}$ connect the same quasiparticle states and they have to be added before squaring. This task is simplified by the fact that matrix elements $B_{k's,ks}$ and $B_{-k-s,-k'-s}$ are expected to differ at most in sign because they both represent processes in which the momentum change of the electron is $k' - k$ [10] and thus the sum of these two terms yields

$$B_{k's',ks}(c^*_{k's'} c_{ks} \pm c^*_{-k-s} c_{-k'-s'}), \tag{1.50}$$

where the sign depends on the type of external perturbation. Positive sign corresponds to *case I*, which is represented, for example, by ultrasonic attenuation. In this case electron interacts with simple scalar deformation potential so it depends only on the magnitude of momentum change, and two matrix elements have the same sign and add coherently. Negative sign corresponds to *case II* with nuclear relaxation and electromagnetic absorption as its typical representatives. On replacing $\mathbf{k}$ by $-\mathbf{k}$ the term describing interaction of the electron with the electromagnetic field $\mathbf{p}.\mathbf{A}$ changes its sign so the negative sign in 1.50 is appropriate. Let's evaluate expression 1.50 in terms of quasiparticle operators

$$B_{k's',ks}[(u_{k'}u_k \mp v_{k'}v_k)(\gamma^*_{k's'}\gamma_{ks} \pm \gamma^*_{-k-s}\gamma_{-k'-s'}) + (v_k u_{k'} \pm u_k v_{k'})(\gamma^*_{k's'}\gamma^*_{-k-s} \pm \gamma_{-k'-s'}\gamma_{ks})]. \tag{1.51}$$

Once again the upper signs correspond to case I, the lower signs to case II. In this equation so called *coherence factors* F are introduced, namely, $(uu' \mp vv')^2$ for the scattering of quasiparticles, and $(vu' \pm uv')^2$ for the creation or annihilation of two quasiparticles. These coherence factors can be evaluated using formulas

1.35 and they become

$$(uu' \mp vv')^2 = \frac{1}{2}\left(1 \mp \frac{\Delta^2}{EE'}\right) \tag{1.52}$$

$$(vu' \pm uv')^2 = \frac{1}{2}\left(1 \pm \frac{\Delta^2}{EE'}\right). \tag{1.53}$$

The physical origin of the coherence factors can be explained fairly simply. We will follow explanation given by Schrieffer [19]. Suppose we are interested in a process in which a quasiparticle is scattered from its initial state, say $k\uparrow$, to a final state, say $k'\uparrow$, by absorbing a boson of momentum $k'-k$. For simplicity we assume no quasiparticles in states $-k\downarrow$,$k'\uparrow$ and $-k'\downarrow$ initially.

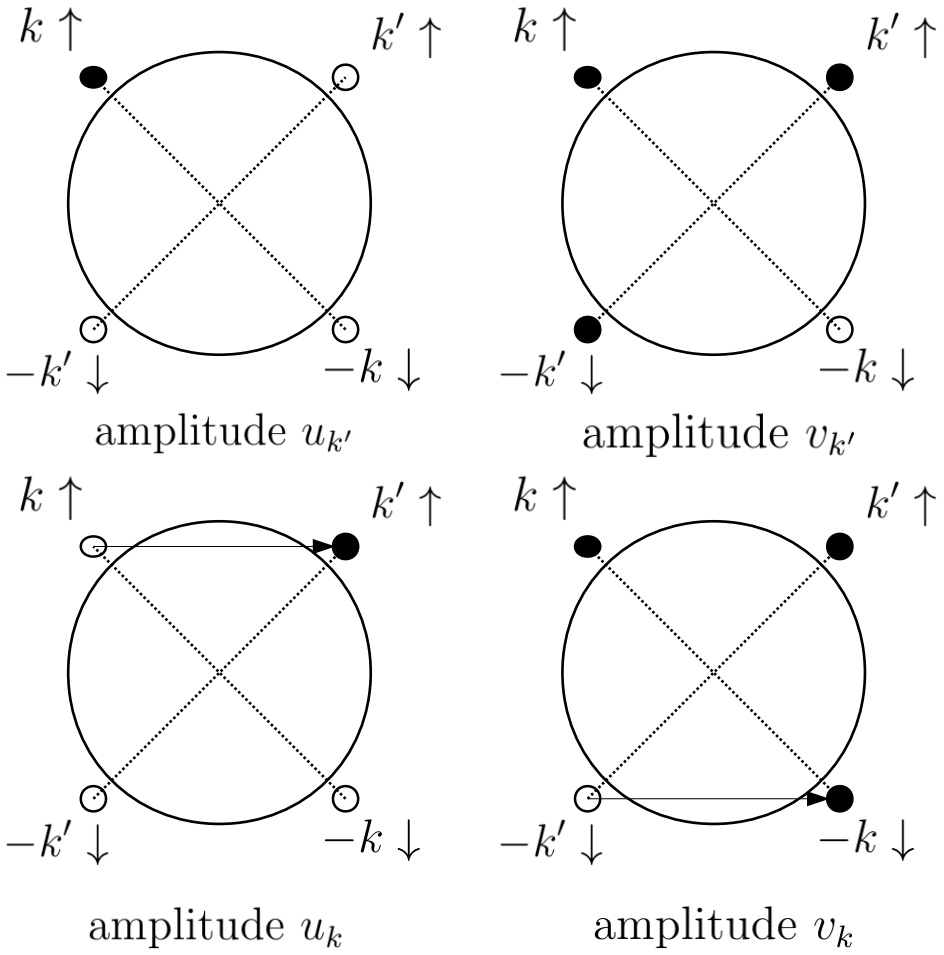

Figure 1.5: Upper panel - initial states for scattering, lower panel - final states [19].

Let's closely observe figure 1.5. A quasiparticle is in $k\uparrow$ state while the pair state ($k'\uparrow$, $-k'\downarrow$) is either empty with a probability amplitude $u_{k'}$ (left upper quadrant in the figure) or occupied with a probability amplitude $v_{k'}$ (right upper quadrant). Since $u_{k'}^2 + v_{k'}^2 = 1$, there is zero amplitude for other possible occupancies of this pair state. By analogy, the final state has $k'\uparrow$ definitely occupied and $-k'\downarrow$ definitely empty, while there is an amplitude u_k such that $k\uparrow$ and $-k\downarrow$ are empty (left lower quadrant), and v_k such that these states are occupied (right lower quadrant).

The interaction hamiltonian 1.49, being a one-body operator, can at most change the state of one electron. Consider the operator $c^*_{k'\uparrow}c_{k\uparrow}$: it transforms the portion of the initial state shown in the left upper quadrant into the final state in the left lower panel. The probability amplitude for this process is clearly $u_k u_{k'}$. In analogy, the operator $c^*_{-k\downarrow}c_{-k'\downarrow}$ affects states displayed on the right and the probability amplitude is $-v_k v_{k'}$. The negative sign arises from ordering operator using anticommutation relations 1.30. The overall amplitude for the quasiparticle scattering is thus $u_k u_{k'} \mp v_k v_{k'}$, in agreement with equation 1.52. Creation and annihilation of quasiparticles can be analyzed in the same way.

It is convenient to use the so-called *semiconductor-model* sign convention, in which each pair of quasiparticles created or destroyed is assigned a negative energy [10]. Both coherence factors thus have the same form

$$F(\Delta, E, E') = \frac{1}{2}\left(1 \mp \frac{\Delta^2}{EE'}\right). \tag{1.54}$$

From now on only electromagnetic absorption (case II) is considered so only the positive sign in equation 1.54 is taken into account. For low frequencies, $\hbar\omega \ll \Delta(T)$, energies E and E' have the same sign and quasiparticles are not excited, so that $F \approx 1$. In case $\hbar\omega \geq \Delta(T)$ quasiparticles are created. Energies E and E' have opposite signs and $F \ll 1$. If both $|E|$ and $|E'|$ are much larger than the gap, there is little difference between properties of the normal and the superconducting state.

Transition rate (probability of transitions per unit time) between electron states with energies E and $E + \hbar\omega$ is expressed as

$$\alpha_s = \int |W|^2 F(\Delta, E, E+\hbar\omega) N_s(E) N_s(E+\hbar\omega) \times [f(E) - f(E+\hbar\omega)] \mathrm{d}E, \tag{1.55}$$

where lower index s indicates that variable with this index describes superconducting state, N_s is the density of states and W is the magnitude of a suitable one-electron matrix element. Using expression 1.54 and equation 1.55, transition rate becomes

$$\alpha_s = |W|^2 N^2(0) \int_{-\infty}^{\infty} \frac{|E(E+\hbar\omega) + \Delta^2|[f(E) - f(E+\hbar\omega)]}{(E^2-\Delta^2)^{1/2}[(E+\hbar\omega)^2 - \Delta^2]^{1/2}} \mathrm{d}E, \tag{1.56}$$

where it is understood that the regions with $|E|$ or $|E+\hbar\omega| < \Delta$ are excluded from the integration [10]. The normal state is characterized by $\Delta = 0$, so transition rate reduces to $\alpha_n = |M|^2 N(0)^2 \hbar\omega$. It is convenient to express the transition rate as a ratio between the superconducting and the normal states

$$\frac{\alpha_s}{\alpha_n} = \frac{1}{\hbar\omega} \int_{-\infty}^{\infty} \frac{|E(E+\hbar\omega) + \Delta^2|[f(E) - f(E+\hbar\omega)]}{(E^2-\Delta^2)^{1/2}[(E+\hbar\omega)^2 - \Delta^2]^{1/2}} \mathrm{d}E. \tag{1.57}$$

1.3.3 Complex conductivity in zero magnetic field

Our discussion of BCS theory has been so far for the case of a pure metal, in which k is a good quantum number, allowing the simple formulation of the BCS

pairing theory. Fortunatelly, extension to the case of impure metals is possible [10]. Purity of sample is characterized by the mean free path l or by momentum scattering time τ. The other important characteristic length is the coherence length ξ. ξ represents the physical size of the Cooper pair bound state in the BCS theory so naturally ξ is also characteristic length for variation of order parameter as will be discussed in the next section devoted to the Ginzburg-Landau theory.

We recognize two important limiting cases. If the mean free path l is much longer than ξ, $l \gg \xi$ the superconductor is said to be in the clean limit and electrodynamic response is non-local, with characteristic length scale given by Pippard coherence length[3] r_0

$$\frac{1}{r_0} = \frac{1}{\xi} + \frac{1}{l}. \tag{1.58}$$

Characteristic representatives of clean limit are very pure metals. In the opposite case, $l \ll \xi$, the superconductor is said to be in the dirty limit and response is well localized. In fact, it is a surprising and very important property of most superconductors that they can remain superconducting even when there are large numbers of impurities making the mean free path l very short. In fact, many alloys are superconducting despite the strongly disordered atomic structure [17].

Absorption of electromagnetic radiation is proportional to $\sigma_1 \mathcal{E}^2$. Absorption is also proportional to the transition rate α, so the ratio σ_{1s}/σ_{1n} is equal to α_s/α_n. Integral 1.57 has to be solved numerically. σ_2 can be calculated using Kramers-Kronig relations.

Historically, Mattis and Bardeen [20] were the first who evaluated complex conductivity from BCS theory. Their work is limited to the case of dirty limit. In this thesis Zimmermann numerical procedure for complex conductivity [21] is utilized. Similar expressions are given by Nam [22, 23], by Leplae [24], by Bickers *et al.* [25] and by other authors. Zimmermann expression applies to isotropic BCS-superconductors with a spherical Fermi surface with arbitrary purity that includes cases of *clean limit* and *dirty limit*. This model became very popular and it has been used by various authors [1, 26, 27, 28].

The typical frequency and temperature dependence of the complex conductivity for a classical BCS-like superconductor (dirty limit) is shown in Fig. 1.6. The upper panel presents the real – dissipative – part of the complex conductivity. At zero temperature, one sees a sharp turning point at the frequency corresponding to the optical gap ($h\nu = 2\Delta(0)$); for higher frequencies dissipation due to the Cooper pair breaking mechanism becomes significant. With increasing temperature the optical gap is reduced and this turning point becomes less pronounced. Quasiparticle population increases with temperature from zero at zero temperature to its normal state value at T_c, consequently, conductivity σ_1 acquires non-zero values even for frequencies below the optical gap; $h\nu < 2\Delta(T)$. Even at somewhat higher temperatures the turning point at the optical gap is still recognizable. At low frequencies, roughly for $h\nu < 0.2 \times 2\Delta(0)$, the temperature dependence exhibits a coherence peak near T_c, which is a manifestation of macroscopic quantum nature of superconductivity. For higher frequencies, σ_1 continuously rises from zero at zero temperature towards its normal-state value, displaying a derivative discontinuity at temperature T^* where $2\Delta(T^*) = h\nu$. This can be thought of as a direct consequence of the Cooper-pair breaking mechanism.

[3] Pippard coherence length is often labeled ξ which we found confusing

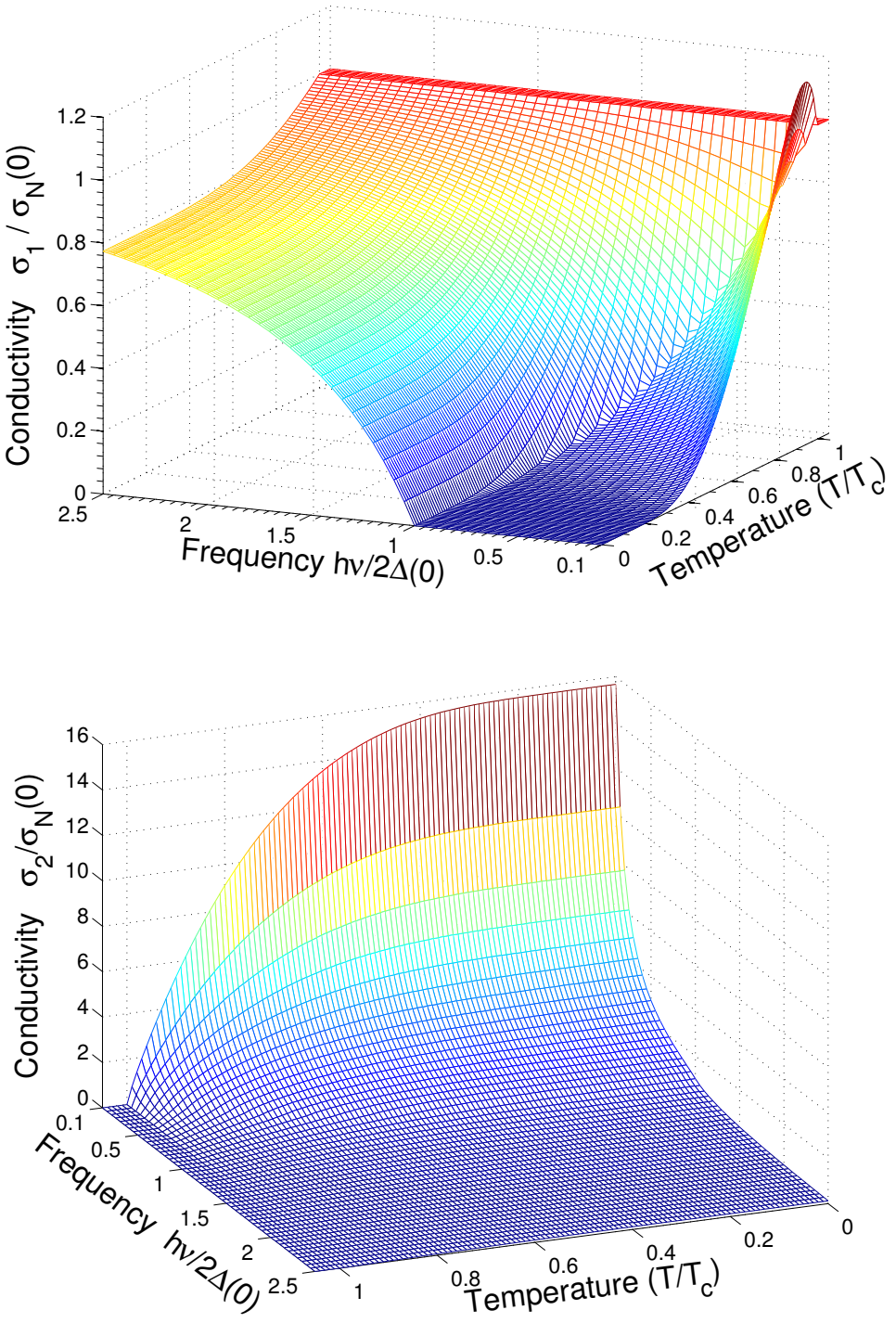

Figure 1.6: Real (upper panel) and imaginary (lower panel) components of complex conductivity normalized to its normal state value of a BCS-like superconductor in dirty limit. Both temperature and frequency scales are in reduced dimensionless units T/T_c and $h\nu/2\Delta(0)$.

For frequencies above the optical gap, σ_1 is finite even at zero temperature and monotonously increases towards its normal state value. The normal state conductivity is well-described by Drude model: $\tilde{\sigma}_N = \sigma_N(0)/\left(1 - i\omega\tau\right)$. If $\omega\tau \ll 1$, then

the real component $\sigma_{1n}(\omega)$ is almost constant, while the imaginary component $\sigma_{2n}(\omega)$ is almost zero.

The imaginary component of conductivity, $\sigma_2(\omega, T)$, is shown in the lower panel of Fig. 1.6. It behaves with frequency as $1/\omega$ and increases towards zero temperature as the condensate fraction grows. This typical $1/\omega$ dependence is a result of Kramers-Kroning relation coming from δ-function in $\sigma_1(\omega)$. Let us note that while the two-fluid model can describe $\sigma_2(\omega, T)$ quite reasonably, it cannot reliably describe $\sigma_1(\omega, T)$ because it does not comprise optical gap and consequently disregards all associated phenomena.

Complex dielectric function of superconducting materials (both in normal and in superconducting state) $\tilde{\varepsilon}(\omega)$ is assumed to be a linear superposition of several contributions. Most important in far-infrared region are those originating from conduction electrons, from phonons and from electronic absorption caused by interband transitions [21]. The contribution from conduction electrons can be expressed in terms of the complex conductivity $\tilde{\sigma}_{el}$ (for $T < T_c$ $\tilde{\sigma}_{el} = \tilde{\sigma}_{BCS}$ and for $T > T_c$ it follows Drude formula). In many cases the phonon and interband absorption terms can be neglected in the THz region, since they are negligible in comparison with the main contribution from conduction electrons. These former terms become more important for higher frequencies (for phonons typically above 10 THz [29]). In the following discussion, we shall neglect them, assuming constant high-frequency part $\varepsilon_\infty = 1$.

The key quantity in optical calculations is the complex refractive index $\tilde{n}$, which can be obtained by straightforward calculation: $\tilde{n} = n + i\kappa = \sqrt{\tilde{\varepsilon}}$. In the normal state the real part of conductivity σ_1 dominates, therefore in the limit of low frequencies the refractive index is given as $\tilde{n} \approx \sqrt{\sigma_1/\varepsilon_0\omega}\,(1+i)/\sqrt{2}$. On the other hand, at low temperature the situation is reversed – the imaginary part of conductivity σ_2 dominates while σ_1 for $h\nu < 2\Delta(0)$ vanishes. Consequently, κ increases towards its zero temperature value, while n decreases, reaching almost zero for frequencies below the optical gap.

1.3.4 Superconductivity in the presence of magnetic field

Ginzburg-Landau theory was born in 1950 [30] as an extension of Landau theory of phase transition to the case of supeconductivity. Superconductivity is characterized by a complex order parameter ψ. $|\psi(r)|^2$ can be identified as the local density of Cooper pairs, $n_s(r)$. In many applications $\psi(r)$ was found to be proportional to the gap parameter $\Delta(r)$. Above the critical temperature in normal state, ψ is equal to zero, i.e. the sample does not exhibit any sign of superconducting behavior.

Near the critical temperature the free-energy density $\mathcal{F}$ can be expanded in a series of the form

$$\mathcal{F} = \mathcal{F}_{n0} + \alpha|\psi|^2 + \frac{\beta}{2}|\psi|^4 + \frac{1}{2m^*}\left|(-i\hbar\nabla - 2e\mathbf{A})\psi\right|^2 + \frac{\mathbf{B}^2}{2\mu_0}. \tag{1.59}$$

Here $\mathcal{F}_{n0}$ is the free-energy density of the normal state in zero magnetic field, α and β are coefficients of Taylor expansion, m^* is effective mass of Cooper pair, $\mathbf{A}$ is magnetic field vector potential and $\mathbf{B}$ is magnetic field. Such expansion is valid only for temperature near the criticial temperature, but some results of Ginzburg-

Landau theory can be extrapolated to lower temperatures. Order parameter ψ is found as a function which minimizes the free-energy, equation 1.59.

In the absence of fields and gradients, free-energy density becomes

$$\mathcal{F}_s = \mathcal{F}_n + \alpha|\psi|^2 + \frac{\beta}{2}|\psi|^4. \tag{1.60}$$

Inspection of 1.60 shows that β must be positive if the theory is to be useful, otherwise the lowest free energgy would occur for arbitrarily large values of $|\psi|^2$, where the expansion is surely inadequate [10]. In order to ψ be zero above T_c and non-zero below T_c coefficient α must be function of temperature so that α is positive above T_c and negative below it. Empiricaly it was found [10] that

$$\alpha \propto \frac{1-t^2}{1+t^2} \tag{1.61}$$

and β can be taken as constant, although it is slightly temperature dependent. Under above described conditions solution below T_c becomes

$$|\psi|^2 = |\psi_\infty|^2 \equiv -\frac{\alpha}{\beta}, \tag{1.62}$$

where the notation ψ_∞ is conventionally used because ψ approaches this value infinitely deep inside the superconductor bulk. When value of ψ_∞ is substituted back into 1.60, condensation energy is found:

$$\mathcal{F}_s - \mathcal{F}_n = -\frac{B_c^2}{2\mu_0} = \frac{-\alpha^2}{2\beta}, \tag{1.63}$$

where B_c is the thermodynamical critical field.

Let's consider a simple case in which magnetic field is not present. ψ is in this case real and it is convient to use its normalized form

$$\psi' = \frac{\psi}{\psi_\infty} \tag{1.64}$$

and formula 1.59 can be expressed as

$$\frac{\hbar^2}{2m^*|\alpha|}\frac{\mathrm{d}^2\psi'}{\mathrm{d}x^2} + \psi' - \psi'^3 = 0. \tag{1.65}$$

From this equation we can see that ψ' can vary on the typical scale of coherence length

$$\xi^2(T) \equiv \frac{\hbar^2}{2m^*|\alpha|}. \tag{1.66}$$

Another characteristic length for superconductors is penetration depth λ which measures how far magnetic field penetrates into the superconducting bulk. Magnetic field parallel with the surface of semi-infinite superconductor ($x > 0$) will exponentially decay inside the superconductor as

$$B(x) = B(0)\exp\left(-\frac{x}{\lambda}\right). \tag{1.67}$$

Let's investigate the case of infinite slab in perpendicular magnetic field. Regions, where superconductivity is fully or partially suppresed, are formed and

magnetic field passes through the slab. Important quantitity is the surface energy of interface between normal and superconducting regions. We can separate two classes of superconductors: *type I* with positive surface energy and *type II* with negative surface energy. Ginzburg-Landau theory introduces important ratio between penetration and coherence length

$$\kappa = \frac{\lambda}{\xi} \tag{1.68}$$

and detailed analysis shows that

$$\begin{array}{ll} 1/\sqrt{2} > \kappa & \text{for type I superconductor} \\ 1/\sqrt{2} < \kappa & \text{for type II superconductor} \end{array} \tag{1.69}$$

The origin of positive surface energy can be explained qualitatively following Tinkham textbook [10]. The surface energy is positive for $\kappa \ll 1$ since there is a region of thickness $\sim (\xi - \lambda)$ from which the magnetic field is held out (contribution to the positive diamagnetic energy) while not enjoying the full condensation energy associated with ψ_∞. The argument is reversed for $\kappa \gg 1$, leading to a negative surface energy. The sign of surface energy has profound effect on behavior of superconductors in magnetic field.

In type I superconductors positive surface energy requires normal state region to minimize surface of interfaces with superconducting regions together with energy associated with magnetic field. Normal state regions with typical dimensions much larger than coherence length ξ are formed. In parallel magnetic field the superconductor expells field from its interior (Meissner-Ochsenfeld effect) up to the critical field $B_c(T)$ where first order transition takes place. Above $B_c(T)$ the material is in normal state. Typical representatives of type I superconductors are elements (Al, Sn, In).

In type II superconductors the surface energy is negative, therefore surface between regions, where superconductivity is suppressed and regions with fully developed superconductivity, are maximized. This leads to the most typical feature of type II superconductors - presence of vortices [31]. Vortex is a topological defect induced by sufficiently large magnetic field which allows magnetic flux $\Phi_0 = h/2e$ to pass through a superconductor. Order parameter ψ is locally supressed around vortex center up to the distance of coherence length $\xi(T)$. In isotropic superconductors ψ is cylindrically symmetric around the vortex center[4] and it can be approximated as

$$\psi \approx \psi_\infty \tanh\left(\frac{\nu r}{\xi}\right), \tag{1.70}$$

where ν is a constant ~ 1, see figure 1.7. The area where ψ is substantially suppresed is called vortex core. Screening currents around the vortex core prevent magnetic field from further penetration inside the superconductor. Magnetic field profile $h(r)$ of a single vortex, assuming $\kappa \gg 1$, can be described as

$$h(r) = \frac{\Phi_0}{2\pi\lambda^2} \mathrm{K}_0\left(\frac{r}{\lambda}\right) \tag{1.71}$$

[4] We assume that there is only one vortex present.

where K_0 is the zeroth-order Hankel function of imaginary argument. For large distance from vortex core magnetic field decreases exponentially as $e^{-r/\lambda}$, as one can expect. Vortices tend to align themselves into a triangular lattice but theoretical energy difference between different alignments are usually small thus allowing different alignments to take place due to the specific material pecularities. With each vortex, there is a positive energy resulting from kinetic energy of screening currents. Therefore first vortices can appear only at sufficiently high magnetic field, so called lower critical field $B_{c1}(T)$. Below B_{c1} the superconductor exhibits full Meissner-Ochsenfeld effect. With increasing magnetic field the density of vortices grows until vortex cores fill almost entire volume and phase transition of second order takes place at upper critical field $B_{c2}(T)$. Typical representatives of type II superconductors are alloys (NbN, Nb_3Sn, Nb_3Ge), cuprates and many other superconductors.

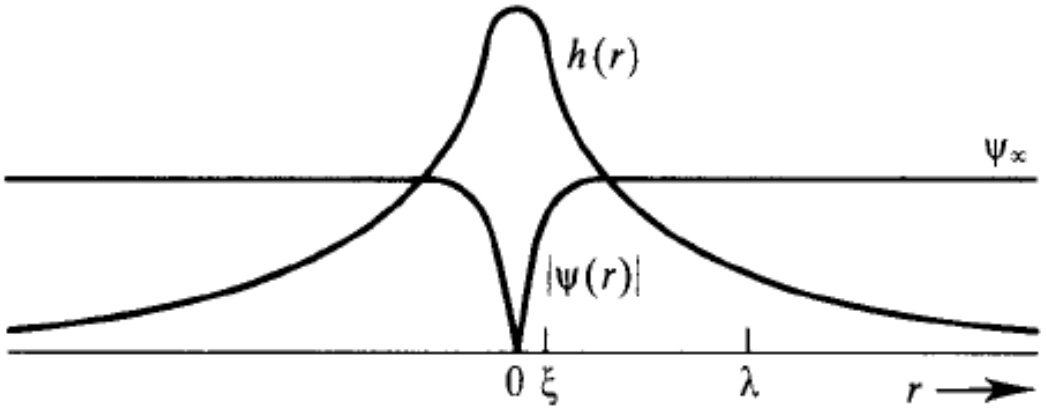

Figure 1.7: Typical structure of isolated vortex [10].

2. Experimental setup

2.1 Laser thermal spectroscopy

Most experimental results shown in this thesis have been obtained by using an experimental method known as *laser thermal spectroscopy*. The basic idea is simple. A monochromatic electromagnetic radiation probes the sample while its temperature (or applied magnetic field) is varied in a controlled way, resulting in obtaining temperature dependence of transmission or reflection. Intensities are usually measured but phase can be measured as well utilizing the Mach-Zender interferometer in the same way as it is implemented in BWO spectroscopy [32, 33]. Phase measurement has its drawback since the detailed measurements of temperature dependence take much more time in comparison with the measurements of transmitted intensity. On the other hand, advantages of laser thermal spectroscopy as a suitable tool to study thin superconducting films were pointed out by several authors [34, 35, 36, 37]. Laser thermal spectroscopy can also be used to study semiconductors with magnetic field dependent gap [38].

Table 2.1: List of available FIR lines. MA=methanol (CH_3OH), FA = formic acid (HCOOH).

Frequency THz	Energy meV	Wavelength μm	Wavenumber cm^{-1}	Intensity	Gas
0.4037	1.670	742.6	13.5	weak	FA
0.5254	2.173	570.6	17.5	medium	MA
0.5617	2.323	533.7	18.7	medium	FA
0.5844	2.417	513.0	19.5	strong	FA
0.6538	2.704	458.5	21.8	weak	FA
0.6929	2.866	432.7	23.1	medium	FA
0.7162	2.962	418.6	23.9	medium	FA
0.9622	3.979	311.6	32.1	weak	FA
1.8213	7.533	164.6	60.8	medium	MA
1.8388	7.605	163.0	61.3	medium	MA
2.5228	10.433	118.8	84.2	very strong	MA
3.1059	12.845	96.5	103.6	very strong	MA
4.2517	17.584	70.5	141.8	very strong	MA
4.8657	20.123	61.6	162.3	very weak	MA

Our experimental setup is described in detail in figure 2.1. As a source of monochromatic far-infrared light the commercially available FIR waveguide laser model 295 is used, pumped by the CO_2 PL4 laser, both made by Edinburgh Instruments Inc. This setup enables generating linearly polarised far-infrared radiation at a series of discrete lines in range from 0.4 to 4.9 THz (13-162 cm^{-1}, 1.7-20 meV, 742-62 μm), see table 2.1 for details. To achieve a successful laser action, several conditions must be fulfilled. First, the waveguide tube of CO_2 laser is filled with mixture of very pure He, N_2 and CO_2 gases, length of its resonator cavity is fine tuned to meet lasing conditions and appropriate excitation energy is

injected into resonator cavity with 130 Hz repetition frequency. The FIR gas laser is tuned in a similar manner. Operating gas can be chosen from many different gases [39] and required power is provided by a CO_2 laser with suitably chosen laser line. In the presented work, all discrete laser lines were produced using only methylalkohol (CH_3OH) and formid acid (HCOOH) gases, see table 2.1. In order to set the laser system correctly, one has to carefully tune all parameters and even then the time stability of laser power can fluctuate at the level of tens percents when laser is operating for several hours.

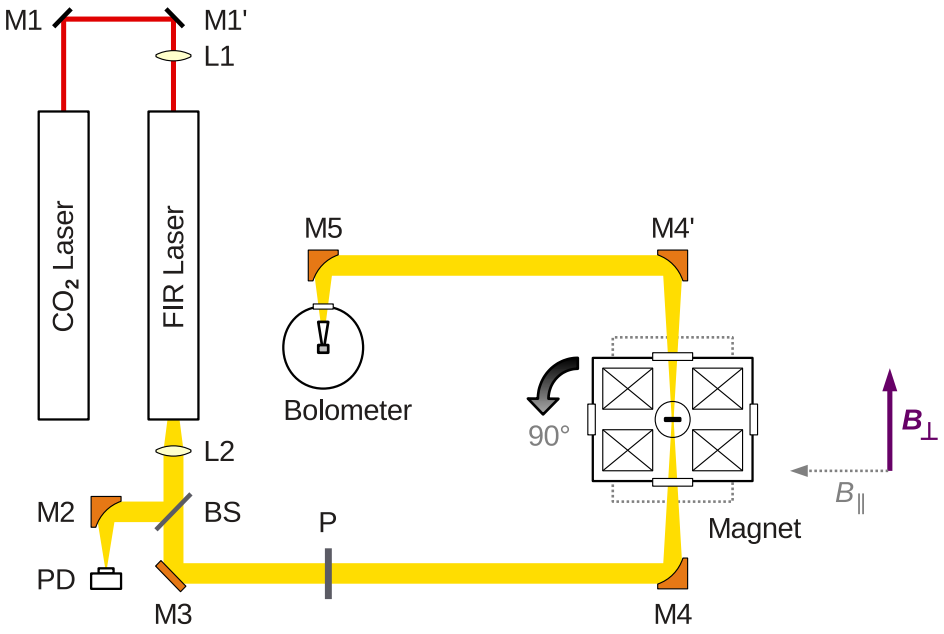

Figure 2.1: Scheme of laser thermal spectroscopy experimental setup in our FIRM laboratory [2]. Optical elements are described by shortcuts: flat mirrors (M_1, M_3), focusing mirrors (M_2, M_4, M_5), lenses (L_1, L_2), mylar beamsplitter (BS), pyrodetector (PD) and wire-grid polariser (P). Further, Faraday ($B_\perp$) and Voigt ($B_\parallel$) configurations are indicated.

Laser beam follows the optical path indicated in figure 2.1. Part of FIR beam is reflected by a mylar beamsplitter (BS) and then focused by a mirror (M2) to a pyroelectric detector (PD), which monitors the laser power. Note that for different wavelengths the ratio between intensity reflected by beamsplitter and intensity transmitted through is different. The beam transmitted through the beamsplitter is concentrated on the sample inside the Spectromag magneto-optical cryostat [40] using a gold coated off-axis parabolic mirror (M4). Wire-grid polariser (P) can be incorporated in the optical path if well specified linear polarisation is required. Intensity transmitted through the sample is collected by mirrors (M4',M5) into the LN-6/C bolometer [41]. The detection element operates at temperature of 4.2 K which is ensured by a small liquid helium dewar. Larger dewar filled with liquid nitrogen further improves thermal stability and

cooling power. The bolometer is equipped with spectrum-sensitive filters allowing only electromagnetic radiation within the range $3 \times 10^{11} - 2 \times 10^{13}$ Hz to pass. The obtained signal is enhanced by a preamplifier with two stages: one is mounted on the cold plate and operates at 60 K and the second stage operates at room temperature. Surrounding effects are effectively eliminated by synchronous detection.

The spectromag cryomagnetic equipment operates in the temperature range from 3 K to 300 K in magnetic fields up 10 T (11 T if helium bath is pumped). The cryostat is placed on non-magnetic pedestal which enables us to rotate the whole system as it is indicated in figure 2.1. In principle, the cryostat can be rotated even when it is operating. Superconducting Helmholtz coils are supplied by a bipolar current source which allows energizing the magnet in both field directions. Persistent mode is conveniently used if constant magnetic field is desirable. Optical access in two perpendicular directions, see figure 2.1, is provided by two pairs of mylar windows and aperture with 0.8 mm diameter on the sample rod, figure 2.2. The sample rod can be rotated about its vertical axis to ensure normal incidence.

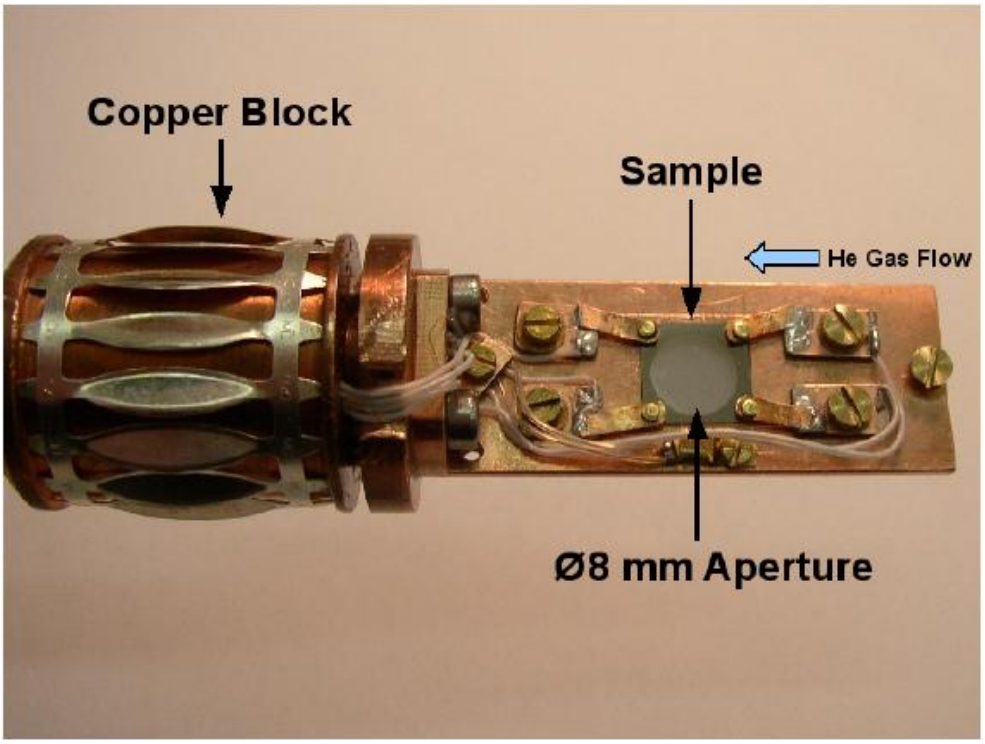

Figure 2.2: Sample holder [2]

The temperature inside the cryostat is controlled by Intelligent Temperature Controller 503S device [42] which regulates a dynamic cooling and a heater. Liquid helium flows from the main bath into the sample space through a needle valve and evaporates in a heat exchanger. A stabilized flow rate is adjusted and the sample surrounded by flowing gas is constantly cooled. A heater is placed in a cooper block near the sample. Temperature of sample is measured by a small Cernox thermometer located nearby, which performs well even in high magnetic field. Error should be less than 3.5% even for the highest attainable fields at low temperatures and smaller otherwise. Temperature gradient between the thermometer

and the sample is a more important issue. To eliminate possible temperature difference, the DC resistivity is monitored by the four-probe method simultaneously with the transmission measurement. In some experiments problems with contact pads occurred but the two-probe method was equally as good in determination of critical temperature. A small current $\sim 10 \quad \mu$A was chosen so it did not heat the sample. Experiment showed that even current ten times larger did not noticeably increase the sample temperature.

Our experimental protocol is to set the magnetic field constant and to cool the sample from T slightly above T_c to the minimum attainable (usually 3 K), then the sample is heated up. For cooling and heating a constant rate of 1 K per minute is used. Slower and faster rates have been tried but it does not affect experimental results. We found that more important is to set conditions properly so that the temperature is swept smoothly with a constant rate. In many experiments we observed that probably the best is to set a constant, reasonably high, gas flow and let the ITC to control only the heater power. It is also possible to set the temperature constant and sweep magnetic field. The transmission is given as a ratio between the signal detected by the bolometer and the signal detected by the pyroelectric detector (PD). This method minimizes effects of any possible time instability in the laser power. Finally, it is convenient to normalize this ratio so that the normal-state transmission is unity.

2.2 Time-domain terahertz spectroscopy (TD TS)

In this section we briefly introduce a complementary far-infrared technique to the laser thermal spectroscopy - *time-domain terahertz spectroscopy*. In particular, we restrict ourselves to the case of steady-state transmission measurements. TD TS measures the electric field of a broadband terahertz pulse (i.e. amplitude and phase) and it is thus capable of determining the optical properties (i.e. $\tilde{n}(\omega)$, $\tilde{\sigma}(\omega)$ or $\tilde{\varepsilon}(\omega)$) of a sample over a broad frequency range at fixed temperature and magnetic field. Our experiments have been performed by the THz group of the Institute of Physics of AS CR. The available spectral range of the spectrometer was 0.1 to 2.5 THz for fields up to 7 Tesla and temperature from room temperatures down to 2 K.

We will explain the principle of the technique using schematic figure 2.3. The basic idea is to use a femtosecond optical pulse to generate THz pulse in a coherent manner; the THz radiation is then transmitted through the sample and the gated detection scheme allows one to measure the THz electric field $\mathcal{E}(t)$ [43, 44]. A femtosecond optical pulse is generated by femtosecond Ti/sapphire oscillator which is pumped by a Nd: vanadate laser. The output pulse is divided into two beams by a beamsplitter: the first one serves for THz pulse generation, the second one is used for the sampling of the transmitted pulse. In the experiment the terahertz pulse is generated by photoconductive switching [45], a femtosecond optical pulse injects electron-hole pairs into ultrafast semiconducting material; a bias field accelerates the free carriers which radiate the THz pulse (i.e. $\mathcal{E}_{THz} = \frac{\partial j(t)}{\partial t}$ where $j(t)$ is the time dependent photocurrent). The THz radiation is detected by a $\langle 110 \rangle$ oriented ZnTe crystal by so called electro-optic sampling technique [46]. The THz pulse induces birefrigence $\Delta n \approx n^3 r_{eff} \mathcal{E}$, which is probed by sampling (gating) the optical pulse. The change of the polarisation state of the

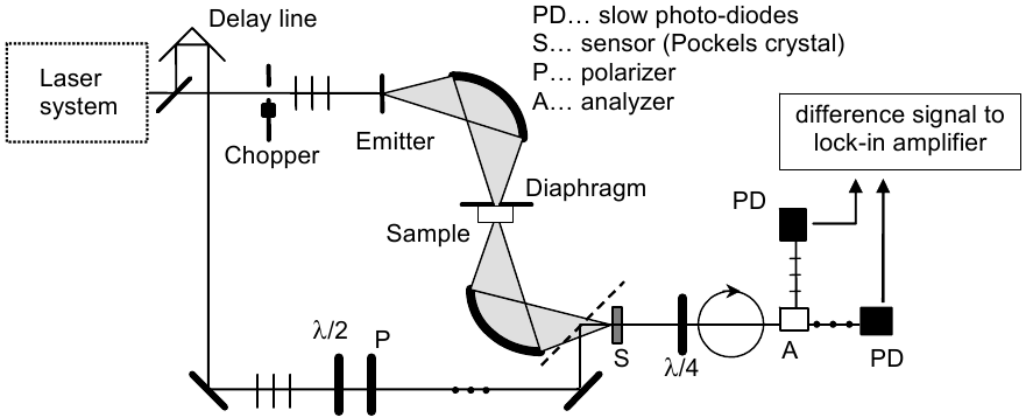

Figure 2.3: Scheme of time-domain terahertz spectroscopy experimental setup. Courtesy of P. Kužel.

sampling pulse is detected by a polarisation-sensitive setup comprising a quater waveplate, a Wollaston prism and a pair of balanced photodiodes (see figure 2.3). The difference of the signals in photodiodes is proportional to the THz field $E(\omega)$ for a given position of the delay line. The optical pulse is much shorter in time domain than the THz pulse. By moving the delay line, one can scan the whole profile $\mathcal{E}(t)$ of the THz pulse.

Having obtained the time dependence of electric field $\mathcal{E}(t)$ it is possible to use Fourier transformation into a frequency domain, see fig.2.4.

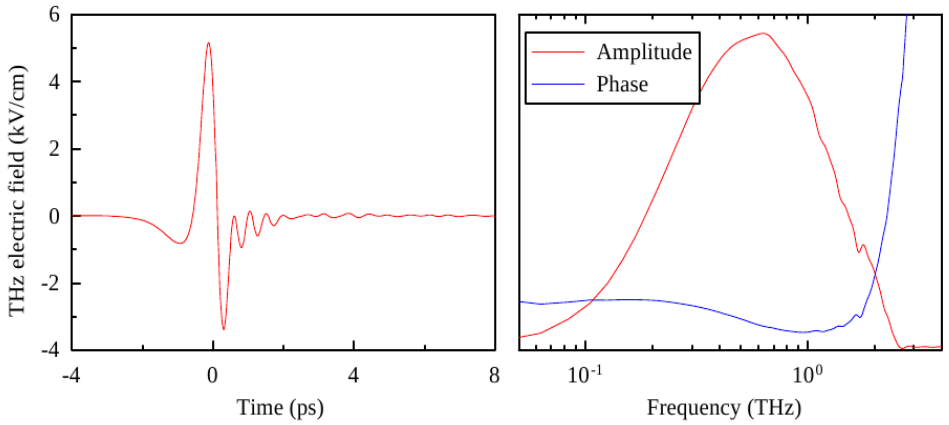

Figure 2.4: Typical THz electric field profile in the time domain (left panel) and in the frequency domain (right panel). Courtesy of P. Kužel.

The measured time profile of the electric field of the THz pulse $\mathcal{E}_{meas}(t)$ is given by convolution of the emitted pulse with instrumental functions describing the propagation before the sample, propagation through the sample, propagation after the sample and the detector response. In order to eliminate all the instrumental function from measurement a reference $\mathcal{E}_{ref}$ must be measured. By calculating ratio of $t(\omega)$ in the Fourier space $t(\omega) = \mathcal{E}_{sample}(\omega)/\mathcal{E}_{ref}(\omega)$ all instrumental functions cancel out and the value of $t(\omega)$ depends only on the properties

of the measured sample. Using Fresnel equations, the complex refractive index or conductive spectra can be numerically determined. In the case of thin metalic film on a thick substrate, multiple internal reflections in the substrate are separated in time, consequently, higher order reflection are removed from the spectra by cutting the waveform in the time domain. The multiple reflections inside the thin film must be all taken into account.

We can assume multiple reflections only in thin metallic layer since the reflections inside optically much thicker substrate are temporally separated. The appropriate equation for transmission, which was derived in chapter 1 (equation 1.22), yields:

$$t(\omega) = \frac{E_{sample}(\omega)}{E_{ref}(\omega)} = \frac{1+\tilde{n}_2}{1+\tilde{n}_2+Z_0\tilde{\sigma}_1(\omega)d_1}\exp(i\Delta\delta), \tag{2.1}$$

where notation from chapter 1 is employed, refractive index of surrounding environment is assumed as unity and $\Delta\delta$ is the difference between phase change due to the sample and the reference. If the same substrate is used as reference, the phase difference yields

$$\Delta\delta = \frac{\omega}{c}\left[(\tilde{n}_1-1)d_1+\tilde{n}_2(d_2-d_2^{ref})\right], \tag{2.2}$$

where the first term is the phase difference due to the different propagation in the film and the second one is the phase difference due to the different thickness of the sample's substrate and the reference substrate.

Let us mention that, due to internal reflections in substrate, another signal $E(t)$, the so called *echo*, is observed $(2n_2d_2/c)$ time shifted after the first. This is conveniently used to determine substrate thickness with high precision.

2.3 Thin films

Typical samples for the experiment are thin superconducting films deposited on suitable transparent dielectric substrate, prepared by various layer growing techniques. It is important that the substrate has similar lattice parameters as the deposited superconducting film. In some cases optimal lattice parameters of the substrate are achieved at the cost of anisotropic properties of the substrate. Substrates substantially influence transmission of such a double layer system, it is therefore important to accurately determine their physical properties.

Critical temperature of a very thin film might appreciably depend on its thickness [47]. Certain films can exhibit higher critical temperatures than bulk materials since they can be prepared with greater purity and with less defects than bulk samples. In our research we mostly use NbN thin films as typical representatives of type II BCS – like superconductors.

As shown by Semenov [48], each individual NbN film has unique properties; this applies in particular to its electric conductivity. In table 2.2, we list properties of all measured NbN films.

The first sample is rectangular in shape, a high-quality 80 nm thick polycrystal NbN layer deposited on a silicon substrate with a very thin ($\approx$ 5 nm) SiO_2 interlayer, prepared by Š. Beňačka in the Institute of Electrical Engineering,

Table 2.2: Parameters of the samples

Film	d_1 [nm]	T_c [K]	$\sigma_N(0)$ $\Omega^{-1}.m^{-1}$	substrate	d_2 [mm]
NbN Beňačka	80	10.8	0.45×10^6	Si	0.25
NbN #383	15	16	0.51×10^6	Al_2O_3	0.33
NbN #544	11.5	12.5	0.46×10^6	Si	0.40

Slovak Academy of Science, Bratislava [49]. From the DC resistance measurement it was found that the sample has finite transition width $\Delta T_c = 0.4$ K.

The second film is high quality 15 nm thick NbN film #383 deposited on R-cut sapphire substrate, prepared by K. Il'in from Institute for Micro- and Nanoelectronic Systems, University of Karlsruhe. The NbN film has been deposited using DC reactive magnetron sputtering of a pure Nb target in Ar/N_2 gas atmosphere with a total pressure of about 5×10^{-3} mbar [48]. The one side polished R-plane sapphire substrate has been placed on a heater kept at a temperature of 750° C during deposition. The main parameters of the deposition process, i.e. the gas pressure, the substrate temperature and the plasma discharge current, were optimized for deposition rate of NbN film of about 0.17 nm/sec. The critical temperature of as deposited film in zero field was found to be $T_c = 16$ K.

The anisotropic sapphire R-cut substrate has the c-axis at angle $\varphi = 57.6°$ with respect to the surface normal. The extraordinary ray axis is oriented diagonally, at the angle 45° with respect to the y – axis. Ordinary and extraordinary refractive indices n_o (orange open circles) and n_e (cyan open circles) can be found in literature [50], see figure 2.5. The extraordinary index $n_e(\varphi = 57.6°)$ (mangenta open circles) associated with R-cut sapphire was calculated using values for n_o and n_e [8]

$$\frac{1}{n_e^2(\varphi)} = \frac{\cos^2(\varphi)}{n_o^2} + \frac{\sin^2(\varphi)}{n_e^2}. \tag{2.3}$$

Sapphire exhibits only a weak dispersion in the THz region, which we take into account by linear fit through data obtained from literature [50]: $n_o = 3.047 + 0.021 \times 10^{-12}\nu$, $n_e = 3.38 + 0.035 \times 10^{-12}\nu$ and $n_e(\varphi = 57.6°) = 3.274 + 0.030 \times 10^{-12}\nu$, see dashed lines in figure 2.5.

Both the ordinary and extraordinary refractive indices were also determined in the supporting time-domain terahertz spectroscopy experiment at room temperature using an identical sapphire substrate. The optical thickness of the substrate, $n_2 d_2$, is to a very good approximation temperature independent [51, 52] which justifies using room temperature values. Real part of both ordinary (pink triangles) and extraordinary (blue triangles) index are in excellent agreement with Palik data, imaginary part is almost frequency independent. Absorption by the substrate is nearly negligible at room temperature and even smaller at low temperatures. Full circles are values of refractive indices obtained by fitting procedure which is described in chapter 4.

The third sample is 11.5 nm thick NbN film #544 deposited on highly resistive Si substrate. It was prepared also by K. Il'in, who also measured its DC resistance and found $T_c = 12.5$ K.

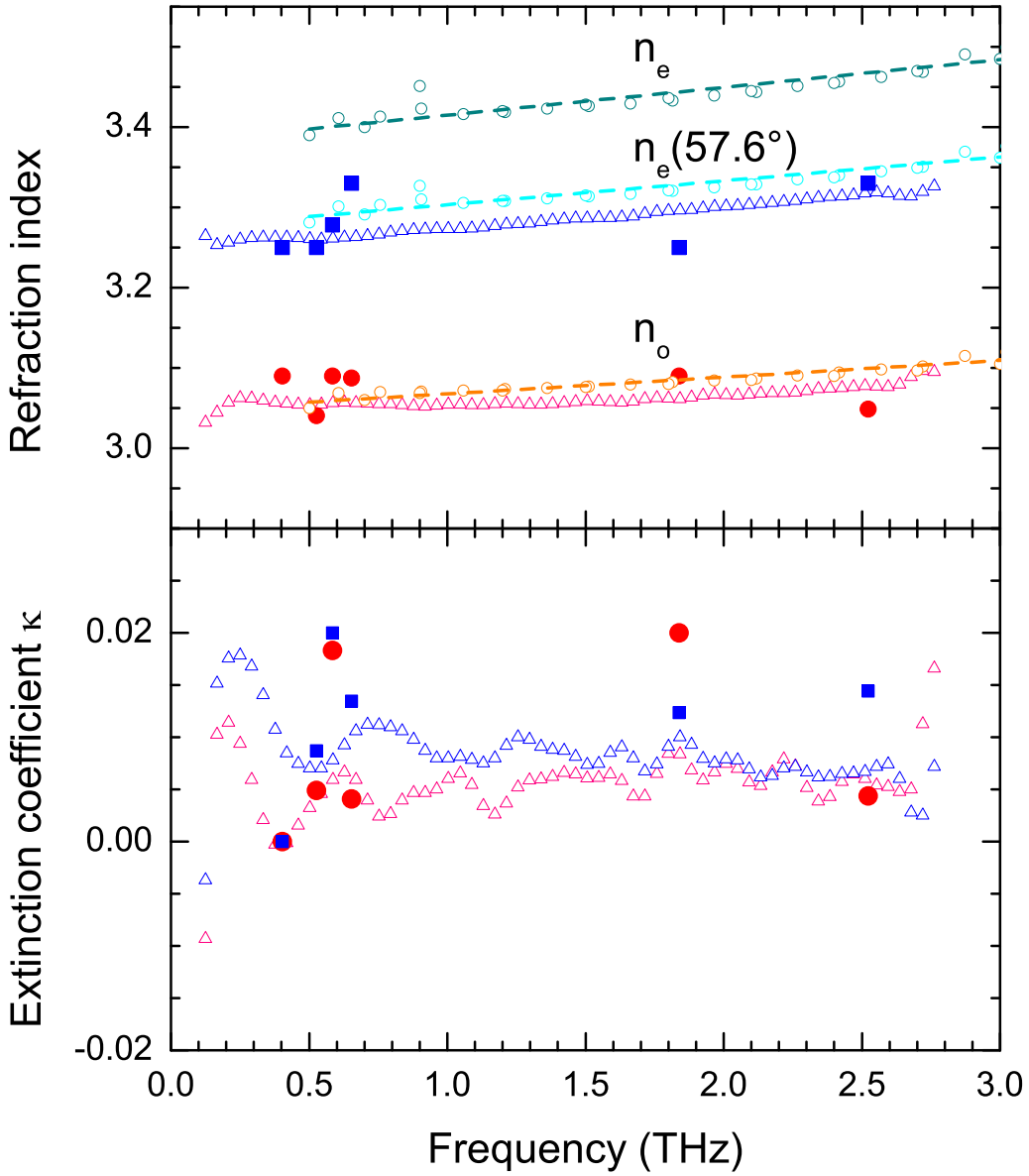

Figure 2.5: Ordinary and extraordinary refractive index of sapphire. Open circles present data from literature [50] and dashed lines linear fit of these data. Open triangles are values obtained by independent measurement and solid symbols values determined by fitting temperature dependent transmission, see chapter 4. For further details see the text.

3. Yeh formalism

3.1 Theoretical overview

A 4 x 4 matrix algebra, which combines and generalizes Abelès 2 x 2 matrix method [53] and Jones 2 x 2 matrix method, is introduced to investigate plane-wave propagation in an arbitrarily anisotropic homogeneous medium [54, 55]. In this method, each layer of finite thickness is represented by a propagation matrix which is diagonal and consists of the phase excursions of the four partial plane waves. Each side of an interface is represented by a dynamical matrix that depends on the direction of the eigenpolarizations in the anisotropic medium.

Assuming we know all optical parameters of involved materials, we can solve the wave equation:

$$\mathbf{k} \times (\mathbf{k} \times \mathcal{E}) + \frac{\omega^2}{c^2} \mu_r \tilde{\varepsilon} \mathcal{E} = 0, \tag{3.1}$$

where μ_r is relative permeability and $\mathbf{k}$ is the wavevector, its x- and y-components are zero since we present special case of normal incidence. Further, we will assume non-magnetic medium, i.e. $\mu_r = 1$. The wavevector is closely connected with the refractive index since $\mathbf{k} = \tilde{n}\frac{2\pi}{\lambda}\mathbf{s}$, where $\mathbf{s}$ is the unit vector in the direction of propagation, λ is the wavelength and $\tilde{n}$ is the complex refractive index.

In order to have nontrivial plane-wave solutions, the determinant of the matrix in eq. 3.1 must vanish:

$$0 = \begin{vmatrix} (\omega^2/c^2)\tilde{\varepsilon}_{xx} - k^2 & (\omega^2/c^2)\tilde{\varepsilon}_{xy} & (\omega^2/c^2)\tilde{\varepsilon}_{xz} \\ (\omega^2/c^2)\tilde{\varepsilon}_{xy} & (\omega^2/c^2)\tilde{\varepsilon}_{yy} - k^2 & (\omega^2/c^2)\tilde{\varepsilon}_{yz} \\ (\omega^2/c^2)\tilde{\varepsilon}_{xz} & (\omega^2/c^2)\tilde{\varepsilon}_{yz} & (\omega^2/c^2)\tilde{\varepsilon}_{zz} \end{vmatrix}. \tag{3.2}$$

This gives a quartic equation in $\mathbf{k}$ which yields four roots $\mathbf{k}_\sigma$, $\sigma = 1, 2, 3, 4$. There is a corresponding eigenpolarization $\mathbf{p}_\sigma$ to each $\mathbf{k}_\sigma$. The electromagnetic radiation can be decomposed into four partial waves

$$\mathcal{E}(z) = \sum_{\sigma=1}^{4} A_\sigma \mathbf{p}_\sigma \exp i(k_\sigma(z - z_n) - \omega t), \tag{3.3}$$

where A_σ is an amplitude. Let's arrange partial waves in following order: $\mathcal{E}_1$ corresponds to the beam traveling in positive z direction with polarisation $\mathbf{p}_1$, $\mathcal{E}_2$ the beam traveling in negative z direction with eigenpolarisation $\mathbf{p}_2 = \mathbf{p}_1$, $\mathcal{E}_3$ is the beam traveling in positive z direction with polarisation $\mathbf{p}_3$ and $\mathcal{E}_4$ is the beam traveling in negative z direction with polarisation $\mathbf{p}_4 = \mathbf{p}_3$. In case of anisotropic medium, $\mathbf{p}_1$ and $\mathbf{p}_3$ are linear polarisations corresponding to the extraordinary and the ordinary beam. In isotropic environment a basis of polarisation vectors can be chosen arbitrarily, in this work we use $\mathbf{p}_1$ parallel with x-axis and $\mathbf{p}_3$ parallel with y-axis. Laboratory coordinate system is defined in figure 3.1.

Magnetic field is obtained using Maxwell equation and it is given by

$$\mathcal{H}(z) = \sum_{\sigma=1}^{4} A_\sigma \mathbf{q}_\sigma \exp i(k_\sigma(z - z_n) - \omega t), \tag{3.4}$$

where

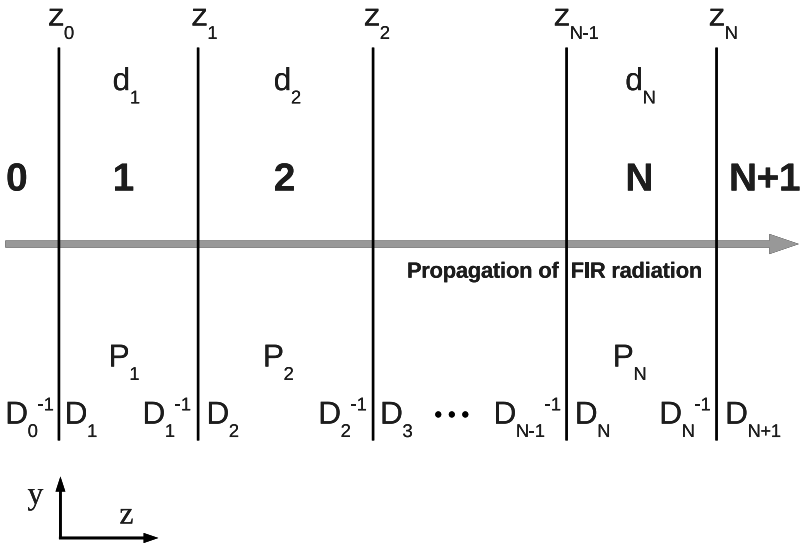

Figure 3.1: Schematics and orientation of a multilayered sample. Individual layers are enumerated $1, 2 \ldots N$ and surrounding environment as 0, $N+1$, respectively. The method of calculating resulting transfer matrix and orientation of the laboratory system are also indicated.

$$\mathbf{q}_\sigma = (c\mathbf{k}_\sigma/\omega\mu) \times \mathbf{p}_\sigma. \tag{3.5}$$

Imposing the continuity of $\mathcal{E}_x$, $\mathcal{E}_y$, $\mathcal{H}_x$ and $\mathcal{H}_y$ at the interface $z = z_n$ leads to

$$\begin{aligned}
\sum_{\sigma=1}^{4} A_\sigma(z_n^-)\mathbf{p}_\sigma(n-1)\cdot\mathbf{x} &= \sum_{\sigma=1}^{4} A_\sigma(z_n^+)\mathbf{p}_\sigma(n)\cdot\mathbf{x} \\
\sum_{\sigma=1}^{4} A_\sigma(z_n^-)\mathbf{p}_\sigma(n-1)\cdot\mathbf{y} &= \sum_{\sigma=1}^{4} A_\sigma(z_n^+)\mathbf{p}_\sigma(n)\cdot\mathbf{y} \\
\sum_{\sigma=1}^{4} A_\sigma(z_n^-)\mathbf{q}_\sigma(n-1)\cdot\mathbf{x} &= \sum_{\sigma=1}^{4} A_\sigma(z_n^+)\mathbf{q}_\sigma(n)\cdot\mathbf{x} \\
\sum_{\sigma=1}^{4} A_\sigma(z_n^-)\mathbf{q}_\sigma(n-1)\cdot\mathbf{y} &= \sum_{\sigma=1}^{4} A_\sigma(z_n^+)\mathbf{q}_\sigma(n)\cdot\mathbf{y},
\end{aligned} \tag{3.6}$$

where z_n^- (z_n^+) correspond to the left (right) side of the interface, see figure 3.1, and expressions on the left hand side of equations are associated with the left side of interface; right hand side of equations are associated with the right side of the interface.

Using these four equations we can associate amplitudes at z_{n-1}^- and z_n^-

$$\begin{pmatrix} A_1(z_{n-1}^-) \\ A_2(z_{n-1}^-) \\ A_3(z_{n-1}^-) \\ A_4(z_{n-1}^-) \end{pmatrix} = D(n-1)^{-1}D(n)P(n) \begin{pmatrix} A_1(z_n^-) \\ A_2(z_n^-) \\ A_3(z_n^-) \\ A_4(z_n^-) \end{pmatrix}, \tag{3.7}$$

where

$$D(n) = \begin{pmatrix} \mathbf{p}_1(n)\cdot\mathbf{x} & \mathbf{p}_2(n)\cdot\mathbf{x} & \mathbf{p}_3(n)\cdot\mathbf{x} & \mathbf{p}_4(n)\cdot\mathbf{x} \\ \mathbf{q}_1(n)\cdot\mathbf{y} & \mathbf{q}_2(n)\cdot\mathbf{y} & \mathbf{q}_3(n)\cdot\mathbf{y} & \mathbf{q}_4(n)\cdot\mathbf{y} \\ \mathbf{p}_1(n)\cdot\mathbf{y} & \mathbf{p}_2(n)\cdot\mathbf{y} & \mathbf{p}_3(n)\cdot\mathbf{y} & \mathbf{p}_4(n)\cdot\mathbf{y} \\ \mathbf{q}_1(n)\cdot\mathbf{x} & \mathbf{q}_2(n)\cdot\mathbf{x} & \mathbf{q}_3(n)\cdot\mathbf{x} & \mathbf{q}_4(n)\cdot\mathbf{x} \end{pmatrix} \tag{3.8}$$

is called the dynamical matrix and

$$P(n) = \begin{pmatrix} \exp(+ik_1(n)d_n) & 0 & 0 & 0 \\ 0 & \exp(+ik_2(n)d_n) & 0 & 0 \\ 0 & 0 & \exp(+ik_3(n)d_n) & 0 \\ 0 & 0 & 0 & \exp(+ik_4(n)d_n) \end{pmatrix} \tag{3.9}$$

is called the propagation matrix, depending only on the phase excursion of these four partial waves.

The transfer matrix can be defined as

$$T(n-1,n) = D(n-1)^{-1}D(n)P(n). \tag{3.10}$$

The matrix equation which relates $A(z_0^-)$ and $A(z_m^-)$ is therefore given by

$$\begin{pmatrix} A_1(z_0^-) \\ A_2(z_0^-) \\ A_3(z_0^-) \\ A_4(z_0^-) \end{pmatrix} = \prod_{i=1}^{(m)} T(i-1,i) \begin{pmatrix} A_1(z_m^-) \\ A_2(z_m^-) \\ A_3(z_m^-) \\ A_4(z_m^-) \end{pmatrix}. \tag{3.11}$$

If m equals to $N+1$, we can define transfer matrix M of entire multilayer system

$$M = \prod_{i=1}^{(N+1)} T(i-1,i) \tag{3.12}$$

and equation 3.11 relates amplitudes of incoming and of outcoming radiation. We can write

$$\begin{pmatrix} A_1(z_0^-) \\ A_2(z_0^-) \\ A_3(z_0^-) \\ A_4(z_0^-) \end{pmatrix} = \begin{pmatrix} M_{11} & M_{12} & M_{13} & M_{14} \\ M_{21} & M_{22} & M_{23} & M_{24} \\ M_{31} & M_{32} & M_{33} & M_{34} \\ M_{41} & M_{42} & M_{43} & M_{44} \end{pmatrix} \begin{pmatrix} A_1(z_n^+) \\ 0 \\ A_3(z_n^+) \\ 0 \end{pmatrix}, \tag{3.13}$$

where we used the fact that radiation does not propagate from the right side of the structure, so that $A_2(z_n^+)$ and $A_4(z_n^+)$ must be to zero. $A_2(z_0^-)$ and $A_4(z_0^-)$ are amplitudes of light reflected from multilayer structure with its eigenpolarisation $\mathbf{p}_2$, $\mathbf{p}_4$, respectively. Similarly, $A_1(z_n^+)$ and $A_3(z_n^+)$ are amplitudes of light transmitted through multilayer structure with its eigenpolarisations $\mathbf{p}_2$, $\mathbf{p}_4$, respectively. This amplitude can be related to incoming light described by amplitudes $A_1(z_0^-)$, $A_3(z_0^-)$ via transmission and reflection coefficients

$$t_{11}^{(0,N+1)} = \left(\frac{A_1(z_N^+)}{A_1(z_0^-)}\right)_{A_3(z_0^-)=0} = \frac{M_{33}}{M_{11}M_{33} - M_{13}M_{31}} \tag{3.14}$$

$$t_{13}^{(0,N+1)} = \left(\frac{A_1(z_N^+)}{A_3(z_0^-)}\right)_{A_1(z_0^-)=0} = \frac{-M_{13}}{M_{11}M_{33} - M_{13}M_{31}} \tag{3.15}$$

$$t_{31}^{(0,N+1)} = \left(\frac{A_3(z_N^+)}{A_1(z_0^-)}\right)_{A_3(z_0^-)=0} = \frac{-M_{31}}{M_{11}M_{33} - M_{13}M_{31}} \tag{3.16}$$

$$t_{33}^{(0,N+1)} = \left(\frac{A_3(z_N^+)}{A_3(z_0^-)}\right)_{A_1(z_0^-)=0} = \frac{M_{11}}{M_{11}M_{33} - M_{13}M_{31}} \tag{3.17}$$

$$r_{21}^{(0,N+1)} = \left(\frac{A_2(z_0^-)}{A_1(z_0^-)}\right)_{A_3(z_0^-)=0} = \frac{M_{21}M_{33} - M_{23}M_{31}}{M_{11}M_{33} - M_{13}M_{31}} \tag{3.18}$$

$$r_{41}^{(0,N+1)} = \left(\frac{A_4(z_0^-)}{A_1(z_0^-)}\right)_{A_3(z_0^-)=0} = \frac{M_{41}M_{33} - M_{43}M_{31}}{M_{11}M_{33} - M_{13}M_{31}} \tag{3.19}$$

$$r_{23}^{(0,N+1)} = \left(\frac{A_2(z_0^-)}{A_3(z_0^-)}\right)_{A_1(z_0^-)=0} = \frac{M_{11}M_{23} - M_{21}M_{13}}{M_{11}M_{33} - M_{13}M_{31}} \tag{3.20}$$

$$r_{43}^{(0,N+1)} = \left(\frac{A_4(z_0^-)}{A_3(z_0^-)}\right)_{A_1(z_0^-)=0} = \frac{M_{11}M_{43} - M_{41}M_{13}}{M_{11}M_{33} - M_{13}M_{31}} \tag{3.21}$$

Using the defined transmission and reflection coefficients, we can simplify the algebra:

$$\begin{pmatrix} A_1(z_N^+) \\ A_3(z_N^+) \end{pmatrix} = \begin{pmatrix} t_{11} & t_{13} \\ t_{31} & t_{33} \end{pmatrix} \begin{pmatrix} A_1(z_0^-) \\ A_3(z_0^-) \end{pmatrix} \tag{3.22}$$

and

$$\begin{pmatrix} A_2(z_0^-) \\ A_4(z_0^-) \end{pmatrix} = \begin{pmatrix} r_{21} & r_{23} \\ r_{32} & r_{43} \end{pmatrix} \begin{pmatrix} A_1(z_0^-) \\ A_3(z_0^-) \end{pmatrix}. \tag{3.23}$$

This way we can obtain electric field $\mathcal{E}(z_0^-)$ or $\mathcal{E}(z_N^+)$ and analyse field inside the m-th layer using the transfer matrices

$$\mathcal{E}(z_m^+) = \left(\prod_{j=m}^{N} T(j, j+1)\right) \mathcal{E}(z_N^+) \tag{3.24}$$

or

$$\mathcal{E}(z_m^-) = \left(\prod_{j=0}^{m-1} T(j, j+1)\right)^{-1} \mathcal{E}(z_0^-). \tag{3.25}$$

Intensity of transmitted wave is given by

$$I = |A_1(z_N^+)|^2 + |A_3(z_N^+)|^2. \tag{3.26}$$

3.2 Application of Yeh formalism

In order to illustrate how Yeh formalism works, we will solve non-trivial case of our NbN/sapphire (R-cut) sample. Helium gas surrounding our sample is isotropic and does not interact with FIR radiation, therefore - $n_0 = n_3 = 1$. In zero magnetic field, NbN is isotropic medium, but by switching magnetic field on

anisotropy is induced (for the moment we assume applied magnetic field in x-axis direction) and in the laboratory system permittivity tensor takes the form:

$$\varepsilon^{sc} = \begin{pmatrix} \varepsilon^{sc}_{xx} & 0 & 0 \\ 0 & \varepsilon^{sc}_{yy} & 0 \\ 0 & 0 & \varepsilon^{sc}_{yy} \end{pmatrix}. \tag{3.27}$$

Sapphire is an important anisotropic uniaxial material with ordinary n_o and extraordinary n_e refractive indices, which are well tabulated. The dielectric tensor in the coordinate system with z-axis parallel with c-crystal axis is given by

$$\varepsilon^{sap} = \begin{pmatrix} \varepsilon_a & 0 & 0 \\ 0 & \varepsilon_a & 0 \\ 0 & 0 & \varepsilon_c \end{pmatrix}. \tag{3.28}$$

The c-axis, in case of R-cut, makes an angle of $\varphi = 57.6°$ with the surface plane. Its projection to surface plane makes an angle of $\vartheta = 45°$ with x-axis. Thus permittivity tensor in our laboratory system yields

$$\begin{pmatrix} \frac{1}{2}(\varepsilon_c - \varepsilon_a)\sin(\varphi)^2 + \varepsilon_a & \frac{1}{4}(\varepsilon_a - \varepsilon_c)\sin(2\varphi) & \frac{1}{2}(\varepsilon_c - \varepsilon_a)\sin(\varphi) \\ \frac{1}{4}(\varepsilon_a - \varepsilon_c)\sin(2\varphi) & \frac{1}{2}\varepsilon_c\cos(\varphi)^2 + \varepsilon_a\left(\sin(\varphi)^2 + \frac{1}{2}\cos(\varphi)^2\right) & \frac{1}{2}(\varepsilon_a - \varepsilon_c)\cos(\varphi) \\ \frac{1}{2}(\varepsilon_c - \varepsilon_a)\sin(\varphi) & \frac{1}{2}(\varepsilon_a - \varepsilon_c)\cos(\varphi) & \frac{1}{2}(\varepsilon_a + \varepsilon_c) \end{pmatrix} \tag{3.29}$$

Using wave equation 3.1, particularly 3.2, we can obtain $\mathbf{k}_\sigma$ and corresponding eigenpolarisation $\mathbf{p}_\sigma$ for all media.

Helium gas

$$\begin{aligned} &\mathbf{p}_1 = \mathbf{p}_2 = (1,0,0) \\ &\mathbf{p}_3 = \mathbf{p}_4 = (0,1,0) \\ &n = 1 \end{aligned} \tag{3.30}$$

NbN

$$\begin{aligned} &\mathbf{p}_1 = \mathbf{p}_2 = (1,0,0) \qquad n_x = \sqrt{\varepsilon_{xx}} \\ &\mathbf{p}_3 = \mathbf{p}_4 = (0,1,0) \qquad n_y = \sqrt{\varepsilon_{yy}} \end{aligned} \tag{3.31}$$

R-cut sapphire

$$\begin{aligned} &\mathbf{p}_1 = \mathbf{p}_2 = (\cos(\vartheta), \sin(\vartheta), 0) \qquad n_o \\ &\mathbf{p}_3 = \mathbf{p}_4 = (\sin(\vartheta), -\cos(\vartheta), -\cos(\varphi)\sin(\varphi)(\varepsilon_c - \varepsilon_{xx})/(\cos(\varphi)^2\varepsilon_c + \sin(\varphi)^2\varepsilon_{xx})) \\ &\tfrac{1}{n_e(\varphi)^2} = \tfrac{\cos^2(\varphi)}{n_o^2} + \tfrac{\sin^2(\varphi)}{n_e^2}. \end{aligned} \tag{3.32}$$

Non-zero z-component of eigenpolarisation corresponding to the extraordinary beam is responsible for the well known fact that Poynting vector and wavevector are not parallel in anisotropic medium [8].

Knowing eigenpolarisation vector we can proceed using equations 3.8 and 3.9. For our case, dynamical matrices of helium gas and superconducting NbN layer have the following structure:

$$D = \begin{pmatrix} 1 & 1 & 0 & 0 \\ \tilde{n}_x & -\tilde{n}_x & 0 & 0 \\ 0 & 0 & 1 & 1 \\ 0 & 0 & -\tilde{n}_y & \tilde{n}_y \end{pmatrix}, \tag{3.33}$$

while dynamical matrix for sapphire is more complicated

$$D_{sap} = \begin{pmatrix} \cos(\vartheta) & \cos(\vartheta) & \sin(\vartheta) & \sin(\vartheta) \\ \tilde{n}_o \cos(\vartheta) & -\tilde{n}_o \cos(\vartheta) & \tilde{n}_e \sin(\vartheta) & -\tilde{n}_e \sin(\vartheta) \\ \sin(\vartheta) & \sin(\vartheta) & -\cos(\vartheta) & -\cos(\vartheta) \\ -\tilde{n}_o \sin(\vartheta) & \tilde{n}_o \sin(\vartheta) & \tilde{n}_e \cos(\vartheta) & -\tilde{n}_e \cos(\vartheta) \end{pmatrix}. \tag{3.34}$$

Propagation through medium is described by propagation matrices $P(n)$ which have the same characteristic structure for all media. For example, for sapphire it is of the form

$$P(n) = \begin{pmatrix} \exp i\frac{2\pi}{\lambda}\tilde{n}_o d_2 & 0 & 0 & 0 \\ 0 & \exp -i\frac{2\pi}{\lambda}\tilde{n}_o d_2 & 0 & 0 \\ 0 & 0 & \exp i\frac{2\pi}{\lambda}\tilde{n}_e(\vartheta) d_2 & 0 \\ 0 & 0 & 0 & \exp -i\frac{2\pi}{\lambda}\tilde{n}_e(\vartheta) d_2 \end{pmatrix}. \tag{3.35}$$

Imaginary part of the refractive index κ in the first and in the third line corresponds to absorption according to Lambert-Beer law. Opposite sign of κ in the second and in the fourth line corresponds to the fact that these modes travel in opposite direction and their intensity decays exponentially from higher values of z to lower values of z.

With explicit expressions for propagation matrices and dynamical matrices, it is easy to calculate optical response of NbN/sapphire double layer using equations for transmission and reflection amplitude coefficients.

Our numerical calculations of transmission were found correct by comparing our data calculated utilizing Yeh formalism with the data calculated for various isotropic cases where analytical formuli are available. Further, Mansuripur [56] found a recursive 2x2 matrix formalism which describes optical properties of multilayer structures equally well as the Yeh formalism. This formalism was used to check that our results of numerical recipes are correct, which was done within limits of numerical errors.

As one can see from the explicit expressions for dynamical and propagation matrices, in the case of isotropic systems both matrices will become block-diagonal

$$\begin{pmatrix} A & 0 \\ 0 & B \end{pmatrix}, \tag{3.36}$$

where A and B are 2x2 matrices and the mode coupling disappears. It is thus possible to investigate each polarisation independently and corresponding formulas are greatly simplified. In non-zero magnetic field the dynamical matrix of NbN film, eq. (3.33), is still block diagonal, thanks to suitably chosen laboratory system, so x- and y-axes correspond to the direction of eigenpolarisations of ordinary and extraordinary beams. By different suitable choice of laboratory system one can make the dynamical matrix of the R-cut sapphire, eq. (3.35), block diagonal, too. However, there is no laboratory system in which these two dynamical matrices would be block diagonal at the same time and Yeh 4×4 matrix formalism is necessary.

If coupling between the modes is absent, we can investigate optical properties individually for each eigenpolarization by 2x2 Abelès formalism [53]. In that case,

formuli for transmission and reflection are greatly simplified. For n-layer system without mode coupling we get recursive formulas for amplitude reflection and transmission coefficients [57]:

$$r^{(0,n)} = \frac{r^{(0,1)} + r^{(1,n)} e^{2i\delta_1}}{1 + r^{(0,1)} r^{(1,n)} e^{2i\delta_1}} \tag{3.37}$$

$$t^{(0,n)} = \frac{t^{(0,1)} t^{(1,n)} e^{i\delta_1}}{1 + r^{(0,1)} r^{(1,n)} e^{2i\delta_1}}. \tag{3.38}$$

4. Transmission in zero magnetic field

Now, we finally move into the experimental part of this thesis. Experimental data are presented and discussed, starting with transmission through three different NbN films in zero magnetic field in this chapter and continue with experiments in non-zero magnetic field in the following chapter.

4.1 Theoretical analysis of transmission of a free film

We begin with theoretical calculation of transmission through a free superconducting film. This starting point will be essential later for understanding of more complicated behavior of multilayered systems. Moreover, theoretical transmission of a free film is also important for other techniques than laser thermal spectroscopy: time-domain terahertz spectroscopy [26, 58] or Backward-Wave Oscillator Spectroscopy [32, 59]. Let us stress, once again, that in this work only the case of normally incident beam is discussed.

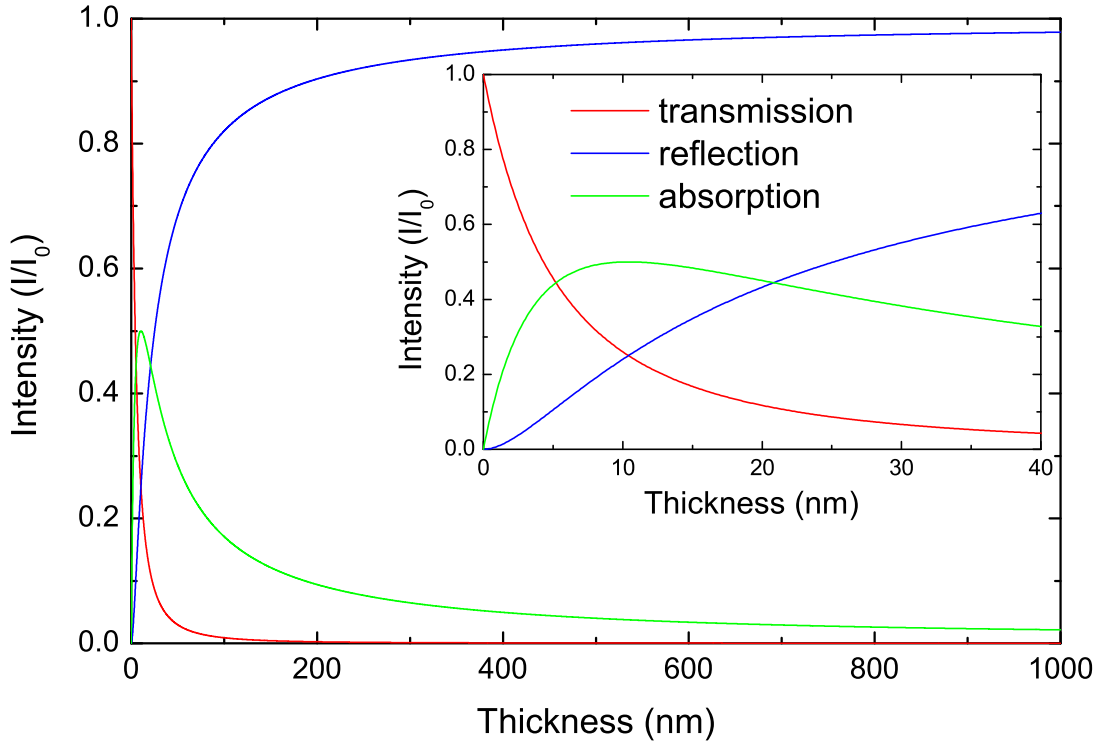

Figure 4.1: Dependence of transmission, reflection and absorption on film thickness for frequency $\nu = 0.4037$ THz . Optical properties of NbN #383 sample in normal state were used in numerical calculations, see table 2.2.

A free film represents a physically ideal system for measuring transmission, which, however, does not depend entirely on optical properties of material –

film thickness is equally as important. In the theoretical limit of zero thickness transmittance $\mathcal{T}$ reaches unity and, consequently, reflectance $\mathcal{R}$ and absorptance $\mathcal{A}$ become zero, see figure 4.1. With increasing thickness (assuming temporarily that film parameters do not depend on thickness) transmission sharply falls while reflection is growing. Absorption is also growing for small thicknesses, however, with thickness increasing further huge reflection leads to a decrease in absorption and, as a consequence, absorption exhibits a maximum for certain film thickness. Note that the described thickness dependence is relevant to a particular wavelength of the incident light.

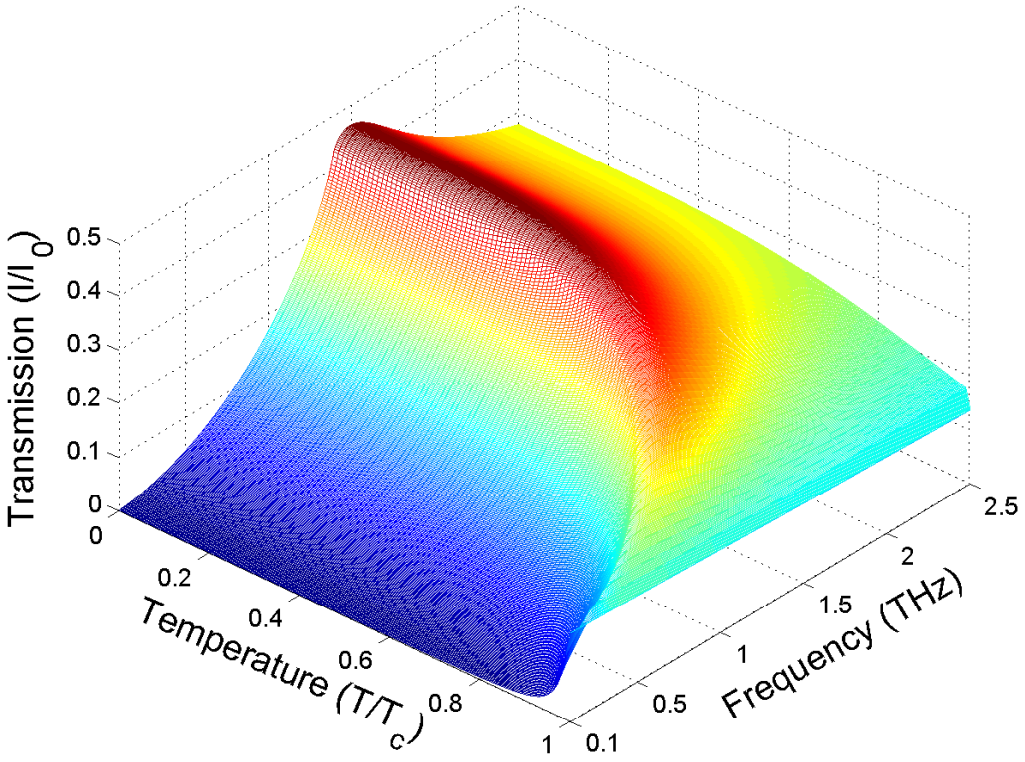

Figure 4.2: Transmission of free NbN film

As an illustrative example, we calculate optical properties of a free NbN film #383 with parameters enlisted in table 2.2. In figures 4.2-4.4 transmission, reflection and absorption are plotted versus normalized dimensionless temperature T/T_c and frequency. The frequency corresponding to the optical gap is $\cong$ 1.39 THz. Similar calculations for different thicknesses of order tens of nanometers show that these quantities – transmission, reflection and absorption – are qualitatively the same.

The behavior of these three interconnected variables can be understood on the basis of $\tilde{\sigma}(T, \nu)$, plotted in figure 1.6. For low temperature and frequency, σ_1 is almost zero and therefore absorption follows this tendency, see figure 4.4. Low resistivity in this region leads to high reflection and, consequently, to a low transmission. By careful observation of transmission in fig. 4.2 one sees a thermal peak in the temperature dependence of transmission for frequencies below

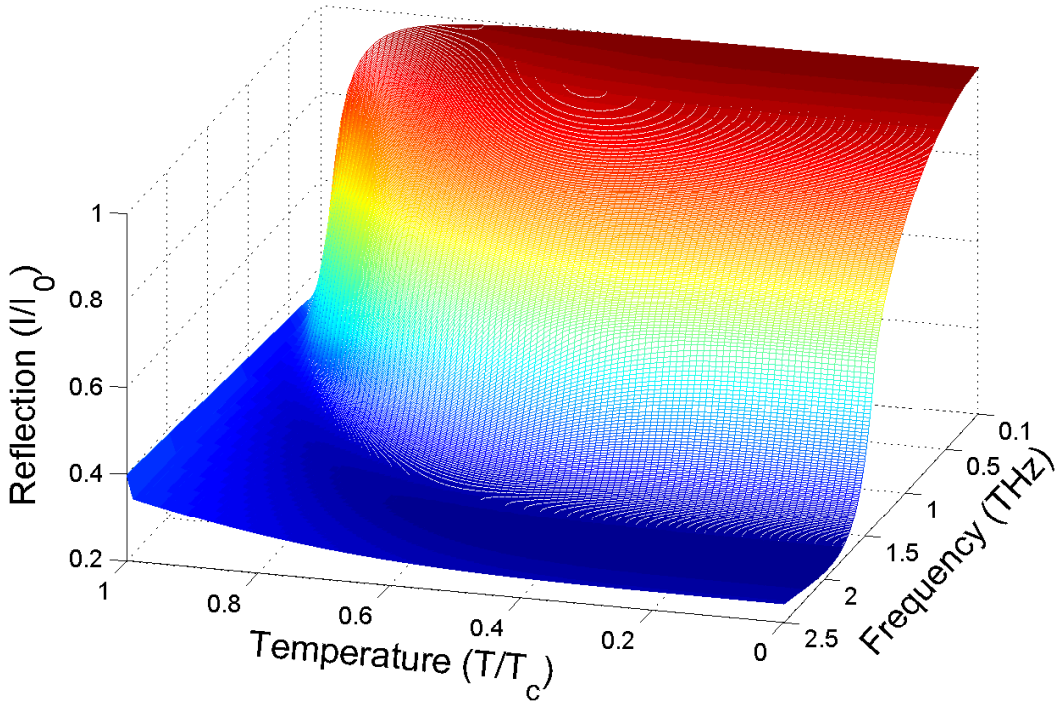

Figure 4.3: Reflection of free NbN film

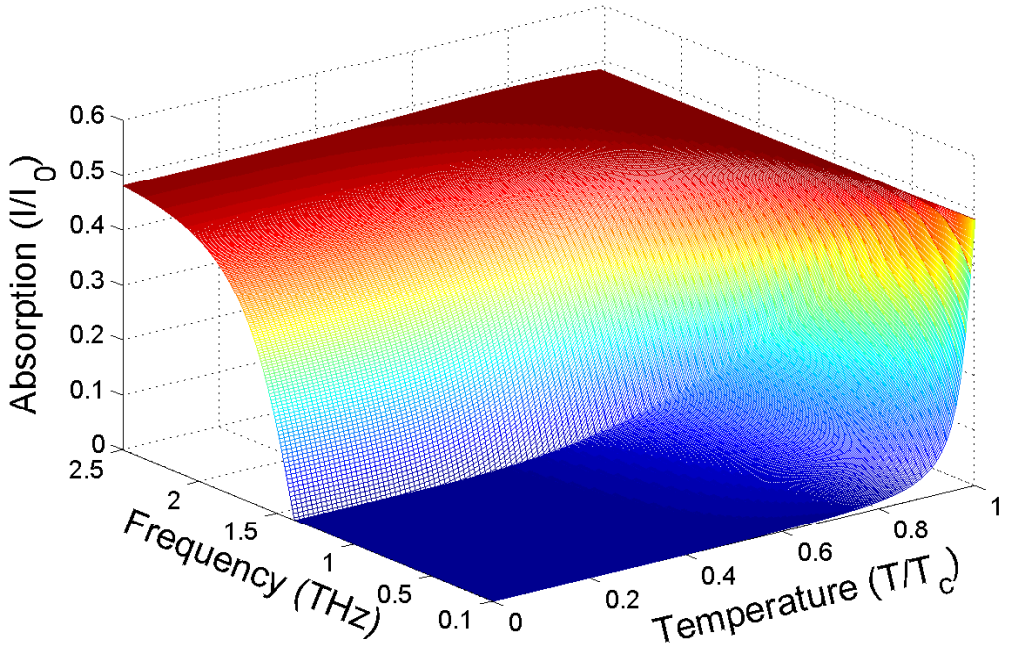

Figure 4.4: Absorption of free NbN film

the optical gap. Numerical analysis explains this peak as a competition between temperature dependencies of $\sigma_1(T)$ and $\sigma_2(T)$, which cause oposite tendencies in resulting transmission. For even lower frequencies, when the coherence peak appears in $\sigma_1(T)$, both the real and imaginary parts of conductivity grow from

T_c towards lower temperature within a small temperature interval and no peak in transmission is present. This excludes any direct connection between the coherence peak and the thermal peak described above. For frequencies around and above the optical gap, $\sigma_2(T)$, the temperature dependence prevails and transmission grows monotonically from T_c towards zero temperature.

4.2 Theoretical analysis of double layer film in zero magnetic field

A thin superconducting film cannot stand alone – an essential part of any thin superconducting sample for optical measurements is its substrate layer, usually much thicker than the superconducting film itself. In order to explain optical response of such a double-layer system, one has to assume all possible interference effects. Moreover, surface roughness and even a very thin oxide layer on superconductor might generally influence transmission.

In order to treat transmission of multilayer systems quantitatively, we utilize Yeh formalism [54, 55]. This powerful tool can be applied even for anisotropic homogeneous layers, as was described in more detail above. If all matrices in Yeh formalism are block diagonal (for example in the case of isotropic film and anisotropic substrate), then ordinary and extraordinary rays are transmitted through double layer separately and transmission can be calculated for each ray in the same way as for isotropic layers. Their intensities should be added at the end [3].

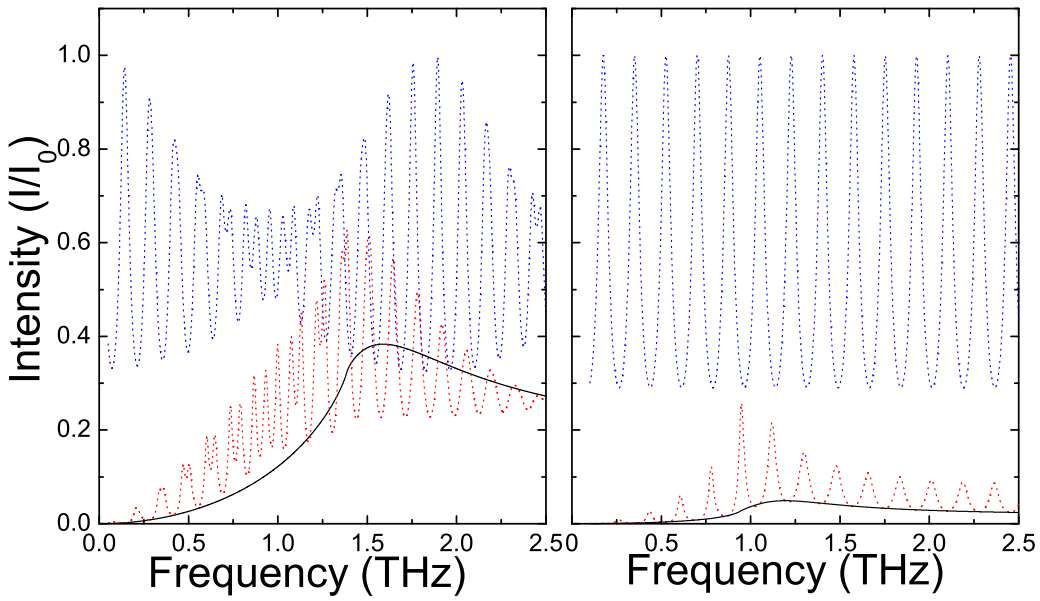

Figure 4.5: Numerical analysis (red dotted line) of transmission of horizontally polarised beam for a NbN #383/sapphire double-layer system (left panel) and NbN(Beňačka)/Si double-layer system (right panel), respectively. Transmissions of free film (black solid line) and of bare substrate (blue dotted line) are also given. Details of numerical calculations are given in the text.

Interference effects due to the substrate are very important since substrates are typically rather thick (d_{sub} is about tenths of millimeter), with optical thickness

$n_{sub}d_{sub}$ (n_{sub} is of orders unity, typically 2-4) comparable with the wavelength (1 THz corresponds to 0.33 mm) of the incident laser beam. The substrate thus behaves as an asymmetric Fabry-Perot resonator. Transmission of such a double-layer system can be greatly enhanced or diminished, see fig. 4.5, where the interference effects are demonstrated by numerical calculation for two particular samples - NbN#383 on sapphire (R-cut) substrate and NbN Beňačka on Si substrate. One sees that the overall transmission of a double layer is given by transmission through the NbN superconducting film, but modulated by the interference effects due to its substrate. One can also compare transmission patterns of NbN film on isotropic substrate (Si) and anisotropic R-cut sapphire substrate. NbN Beňačka film is much thicker than NbN #383 film therefore its transmission is smaller. Note that the transmission in case of NbN on anisotropic R-cut sapphire strongly depends on direction of linear polarisation. In figure 4.5 linear polarisation makes an angle of 45° with polarisation of both ordinary and extraordinary rays. Still, the temperature dependence of transmission of such a double layer system at a fixed frequency preserves all fundamental features of transmission through a free film, but substantially modified. In order to appreciate these changes, we present the temperature dependencies of free film and double layer system for several selected frequencies in fig. 4.6.

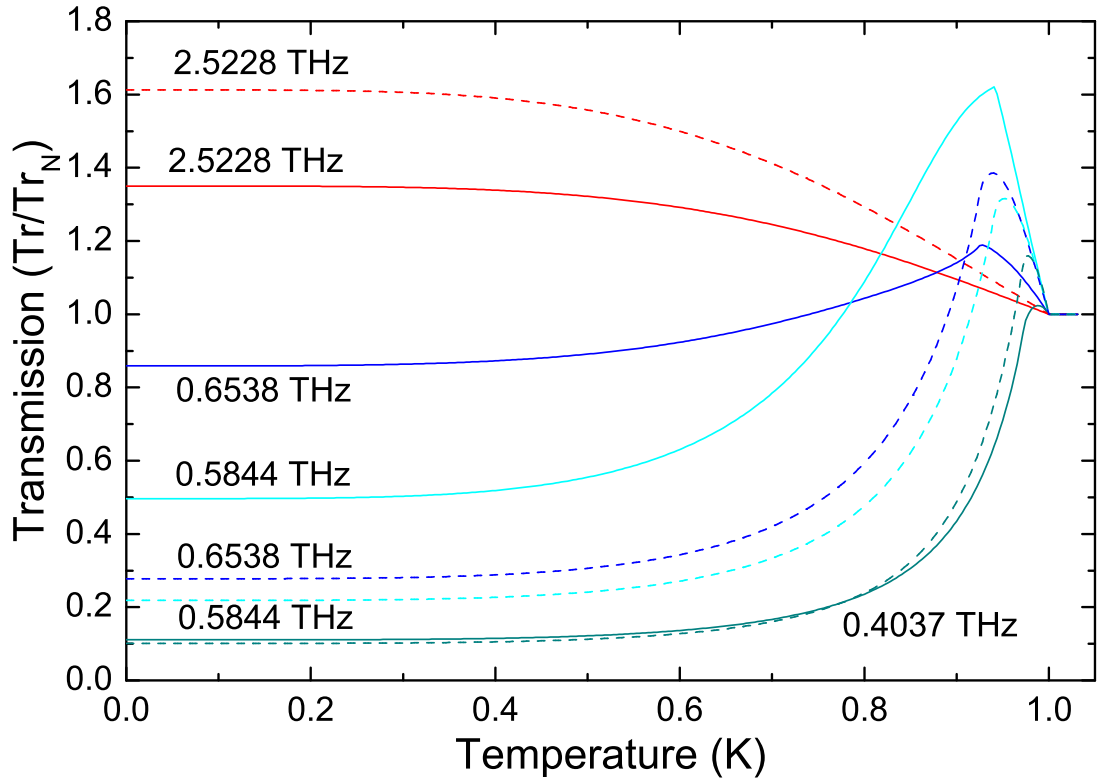

Figure 4.6: Comparison of transmission of free NbN film (solid lines) and NbN thin film on R-cut sapphire substrate (dotted lines) for several experimentally available frequencies as indicated. Transmission is normalized by its normal state value.

In some cases, there is an interlayer between the thin superconducting film and its substrate. If the interlayer is very thin, i.e., phase almost does not change as beam propagates through the interlayer, then its influence on transmission

will be negligible. Following the same argument, oxidized surface of NbN ≈ 1 nm thick [48] will not have any appreciable effect. For optical measurements, ideally, substrate should be a plane-parallel both side polished slab with negligible roughness. Rough surface can be treated by effective medium theory [60] as an effective medium consisting of air or gaseous helium and the substrate's material – if the roughness is small enough, diffraction effects can be neglected. In that case, slightly rough surface can be thought of as another interlayer and can be neglected. Let us stress that the superconducting film itself cannot be neglected since it has enormously high values of refractive index in comparison with the interlayer material.

Note that any anisotropy of superconducting film (some superconductors are anisotropic by nature or anisotropy can be induced by external magnetic field) in general requires the full power of Yeh formalism.

4.3 Experimental observation of transmission

In the last two sections numerical calculations of temperature dependence of transmission through our sample were described in detail. Now, when we might be confident to understand all features of transmission in laser thermal spectroscopy, the numerically calculated transmission curves must be compared with the experimentally acquired data.

In this section experiments performed on two different samples (NbN/Si and NbN/sapphire) are presented. Since each sample has its peculiarities, they are treated separately.

First, let's concentrate on NbN sample prepared by Beňačka. Basic sample parameters are enlisted in table 2.2. NbN film is connected to the Si substrate by a very thin SiO_2 interlayer (≈ 5 nm thick). Such an interlayer hardly influences transmission, so the sample can be treated as an effective double-layer system. Indeed, exact calculations of three-layer system were made and no difference was found. We estimated value of momentum scattering time as 5 fs with reasonable agreement with other experiments [26, 48]. Numerical calculation shows that transmission is not very sensitive to the exact value of τ since its value in order of few femtosecond makes $\tilde{\sigma}_N$ almost constant in THz region and $\tilde{\sigma}_S$ is well described by the dirty limit ($\tau \to 0$). The optical gap was estimated as $2\Delta(0) = 4.16\, k_B T_c$ in excellent agreement with Semenov [48], so that its magnitude is 3.87 meV (0.94 THz) for $T_c = 10.8$ K. Ikebe [26] and Pambianchi [61] reported $2\Delta(0) = (4.1 \pm 0.1)\, k_B T_c$ while other authors found both lower and higher values [62, 63]. In experiment two different lines are used: 0.4037 THz line is well below the optical gap ($h\nu/2\Delta(0) = 0.43$) while 2.523 THz line is well above the optical gap ($h\nu/2\Delta(0) = 2.7$). Experimental data are shown in fig 4.7 together with theoretical curves which will be discussed later.

An explicit formula for amplitude transmission coefficient for isotropic homogeneous NbN/Si sample using equation 3.37 for double-layer system yields

$$t^{(0,3)} = \frac{t^{(0,1)} t^{(1,2)} t^{(2,3)} e^{i(\delta_1+\delta_2)}}{1 + r^{(1,2)} r^{(2,3)} e^{i2\delta_2}} \left(1 + r^{(0,1)} \frac{r^{(1,2)} + r^{(2,3)} e^{2i\delta_2}}{1 + r^{(1,2)} r^{(2,3)} e^{2i\delta_2}} e^{i2\delta_1} \right)^{-1}, \qquad (4.1)$$

and the transmitted intensity becomes $\mathcal{T} = |t^{(0,3)}|^2$. This formula can be easily

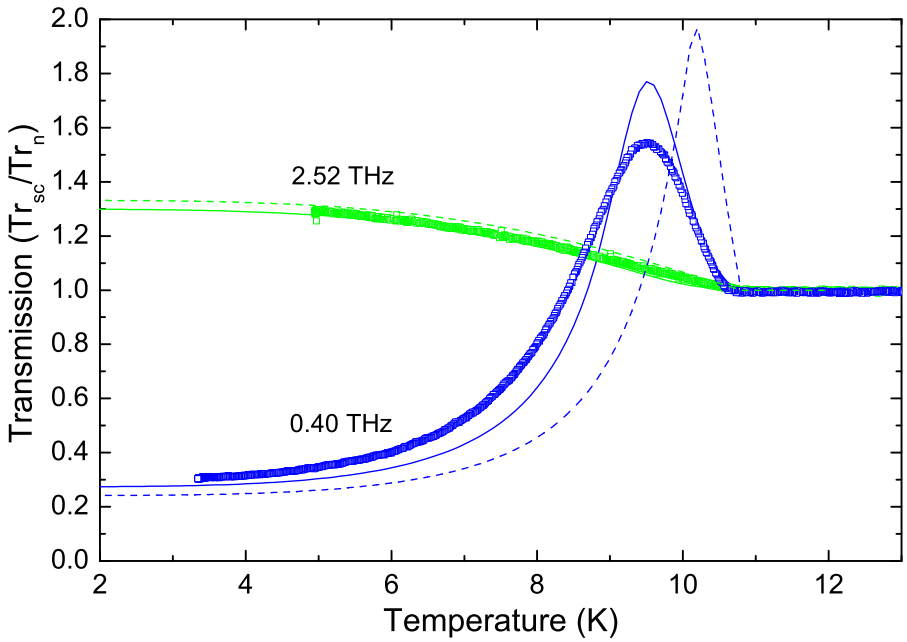

Figure 4.7: The observed zero field transmissions for two frequencies are plotted versus temperature. Symbols represent experimental data, dashed lines are calculated curves for BCS superconductor with the sharp transition and solid lines are calculated using modified conductivity as described in the text.

modified to account for non-zero angle of incidence [57]. We compared transmissions for low angles of incidence and found that even if the sample is a bit tilted (up to $\approx 6°$), one can still consider this as normal incidence. In the experiment, the surface of the sample is adjusted with much better precision.

In figure 4.7 the numerical calculations following the recipe from previous sections are given by dashed lines. Although it qualitatively describes the character of the data, quantitative agreement is rather poor. Any misalignment of sample surface or reasonably high deviations of sample parameters cannot account for this quantitative disagreement.

Better agreement can be achieved by treating our real sample not as a homogeneous superconductor with sharp transition but as a mixture of superconductors with different T_c and corresponding optical gaps $2\Delta(0) = 4.16\, k_B T_c$. This view is supported by the dc electric resistance measurement showing transition width $\Delta T_c \simeq 0.4$ K. Spread of T_c in the mixture will be even larger than the spread of T_c suggested by resistivity measurements because zero dc resistance does not exclude presence of non-superconducting regions. Since there is no reason, known to us, to assume any specific distribution function of T_c in such a mixture, we assume that all T_c within suitably chosen temperature interval are represented with equal probability. For convenience, we approximate our NbN sample as a mixture of ten ideal superconducting materials with 9.8 K $\leq T_c \leq$ 10.8 K. Conductivity computed this way (solid lines in figure 4.7) agrees notably better with the experimental data. Note that there are other ways how to account for imper-

fections of real sample, i.e. $\Delta T_c \neq 0$. For example, the film can be though of as a series of much thinner superconducting films with slightly different properties. Careful studies of transition from normal state to superconductivity and microscopic structure would improve our treatment of superconducting film as a real imperfect sample but instead of performing such experiments we decided to focus our experimental efforts to study better quality samples with sharp transition and we conclude that by taking into account imperfections of the real sample better agreement with theoretical data is achieved.

Second, NbN sample deposited on R-cut sapphire substrate is studied. Transition to the superconducting state is sharper so we can assume that behavior of the sample is well described by perfectly sharp transition in contrast to the previously described sample. The major issue is the anisotropy of substrate, see figure 2.5.

Transmission is measured for horizontal and vertical linear polarisation. In our special case, angle between the electric vector of the incident beam and the extraordinary ray axis of the sapphire substrate is 45°, therefore the relative transmissions of the horizontally and vertically polarized radiations should be equal. Note that intensities of horizontal and vertical polarisation are different, which might affect the accuracy of transmission measurements but not the resulting dependence. Transmission was measured in both polarisations and the observed difference was less than 5%, which can most likely be attributed to a slight misalignment of the sample. Even for the 0.4037 THz line, for which the transmission in the zero-temperature limit is very weak, the relative difference is still within 10%.

The extraordinary and ordinary rays are perpendicular to each other, therefore they do not interfere and we can treat each ray in the same way as before and sum their intensities with proper weights

$$\mathcal{T} = |t_e^{(0,3)}|^2 \cos^2(\alpha) + |t_o^{(0,3)}|^2 \sin^2(\alpha), \tag{4.2}$$

where $t_e^{(0,3)}$, respectively $t_o^{(0,3)}$, are transmission amplitude coefficients according equation 4.1 assuming extraordinary, respectively ordinary, refractive index. Here α is the angle between direction of linear polarisation corresponding to the extraordinary ray and polarisation used in experiment. The calculations for both vertical and horizontal polarisations were made assuming the following values: $\alpha = 45°$, $\tau = 3.86$ fs [48] and $2\Delta(0) = 4.15\, k_B T_c$. While variations of the film parameters within their experimental errors affect the calculated transmission only slightly, the results are much more sensitive to the exact values of ordinary and extraordinary indices of the substrate. This is understandable, since the interference effects greatly influence transmission.

To achieve the best agreement between calculated and experimental transmission values, optical properties of the substrate were slightly refined within their experimental errors, see figure 2.5. Resulting calculated curves (solid lines in figure 4.8) agree with experimental data remarkably well for all measured frequencies. Determined values of $n_{2e}(\varphi)$ (full blue circles), n_{2o} (full red circles) respectively, slightly deviate from independently measured values. Values of refractive indices determined in such a way can account for slight deviation from normal incidence or slight inaccuracy in determination of thickness, thus achieving better agreement with experimental data than expected since this agreement

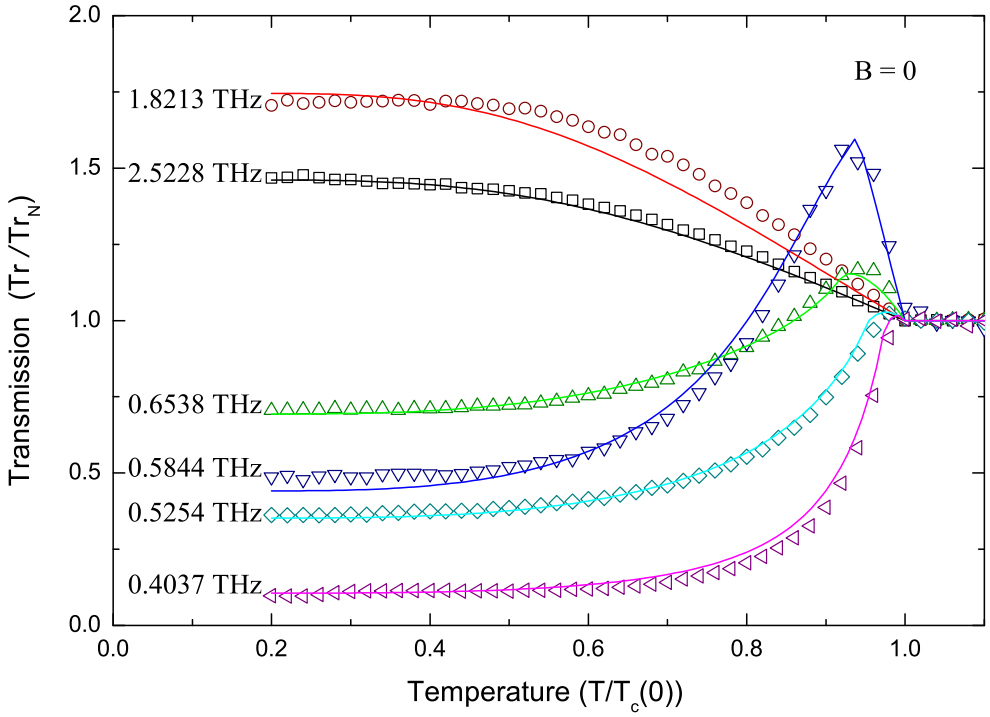

Figure 4.8: Normalized transmission as measured (individual data points) and calculated (solid lines) as described in the text for six different frequencies as indicated, plotted versus reduced temperature T/T_c.

seems to be better than agreement between individual measurements.

Now, we will focus on the set of experimental data obtained without implementing the wire-grid polariser. FIR laser provides linearly polarised beam. Since excellent agreement of calculated and measured data was achieved (fig 4.8), it seems reasonable to assume that α which minimizes the difference between the experiment and calculated data according to equation 4.2 corresponds to the polarisation used in the experiment. Additional determination of direction of linear polarisation is in principle possible, but not fully faithful, as it is not possible to adjust the laser system to exactly the same state as it was during the measurement. Moreover, in measurements without polariser the intensity of incoming radiation is not reduced by the polariser.

In figures 4.9-4.13, the temperature dependencies of transmission are given for five different lines. Three different calculated curves are given for each measured dependence. Transmission of far-infrared radiation with eigenpolarisation corresponding to ordinary (black lines) and extraordinary rays (green lines) in R-cut sapphire limits transmission of radiation with linear polarisation described by angle α (blue lines) defined by equation 4.2. In most cases values of α are clustered around 45°, which is in good agreement with estimated directions of laser polarisation given in the laser manual [39]. Laser lines relevant to this experiment are parallel with the polarisation of CO_2 pump radiation. Brewster window ensures that the polarisation is partially polarised in vertical direction. In the case of 0.4037 THz line, it seems almost impossible to distinguish between transmission of ordinary and extraordinary ray except for a narrow temperature region just below T_c, which is strongly influenced by the finite width of transition. The angle

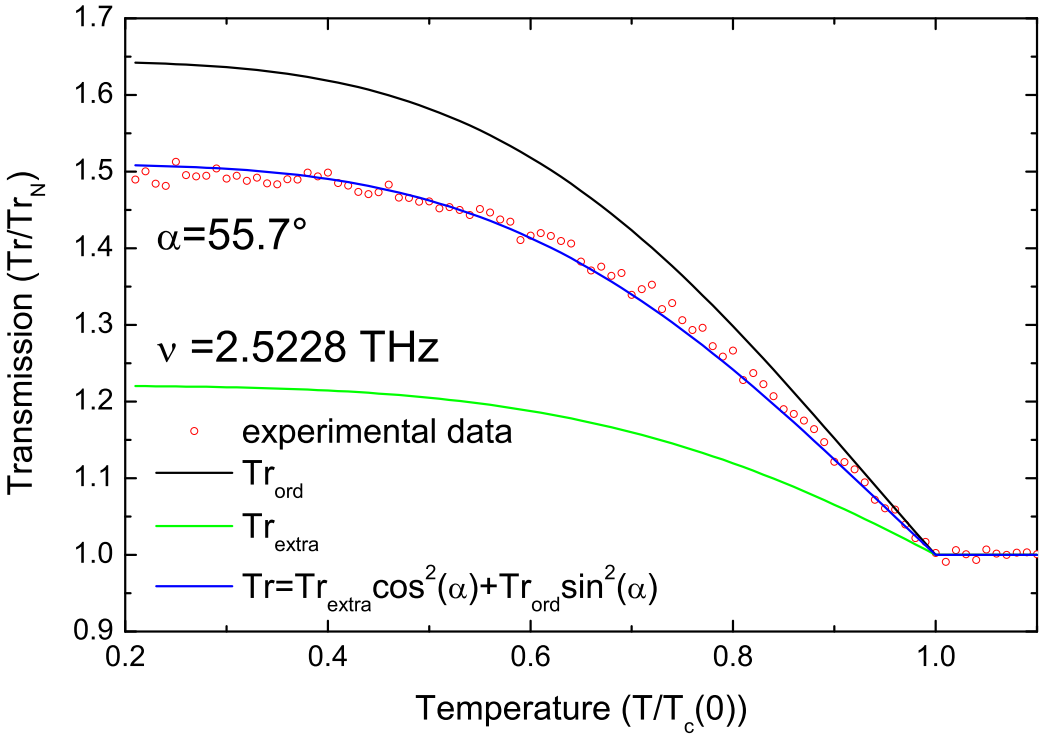

Figure 4.9: Transmission through NbN/R-cut sapphire sample as measured without wire-grid polariser for 2.52 THz line (red circles). Lines present numerical calculations described in detail in the text.

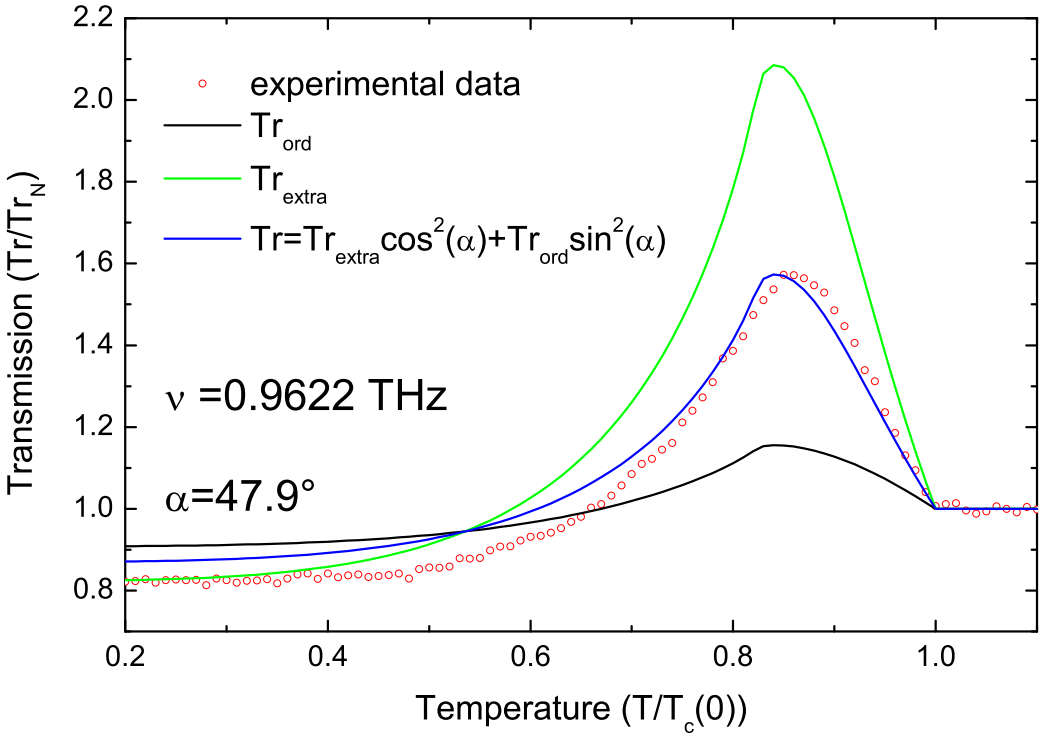

Figure 4.10: Transmission through NbN/R-cut sapphire sample as measured without wire-grid polariser for 0.96 THz line (red circles). Lines present numerical calculations described in detail in the text.

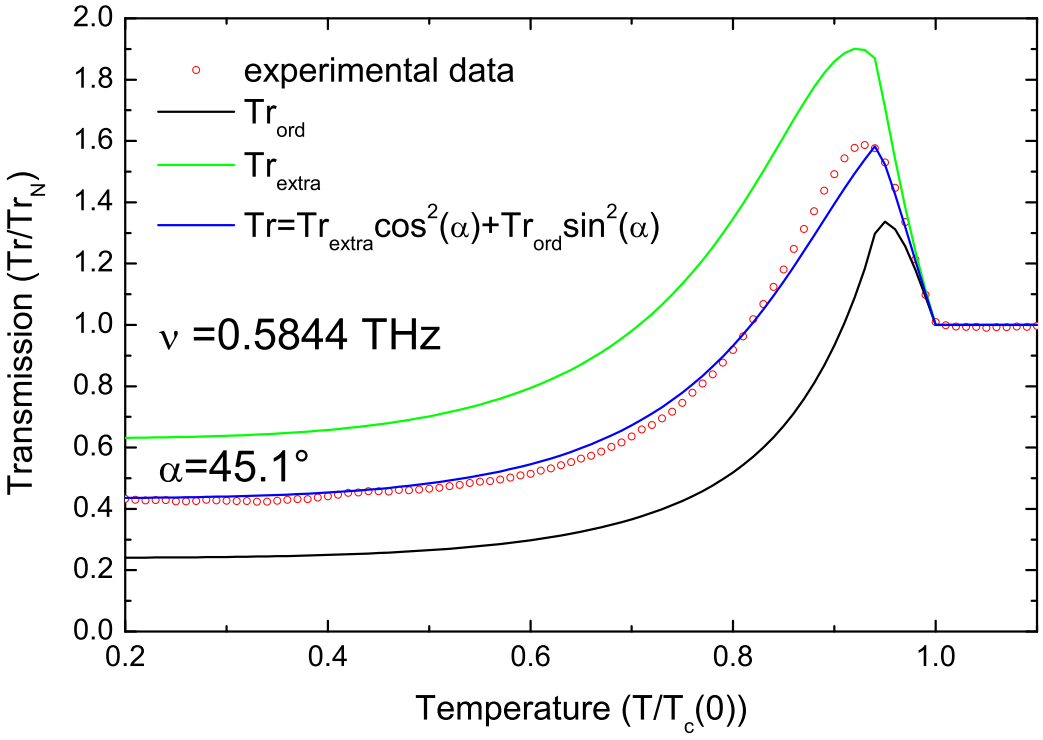

Figure 4.11: Transmission through NbN/R-cut sapphire sample as measured without wire-grid polariser for 0.58 THz line (red circles). Lines present numerical calculations described in detail in the text.

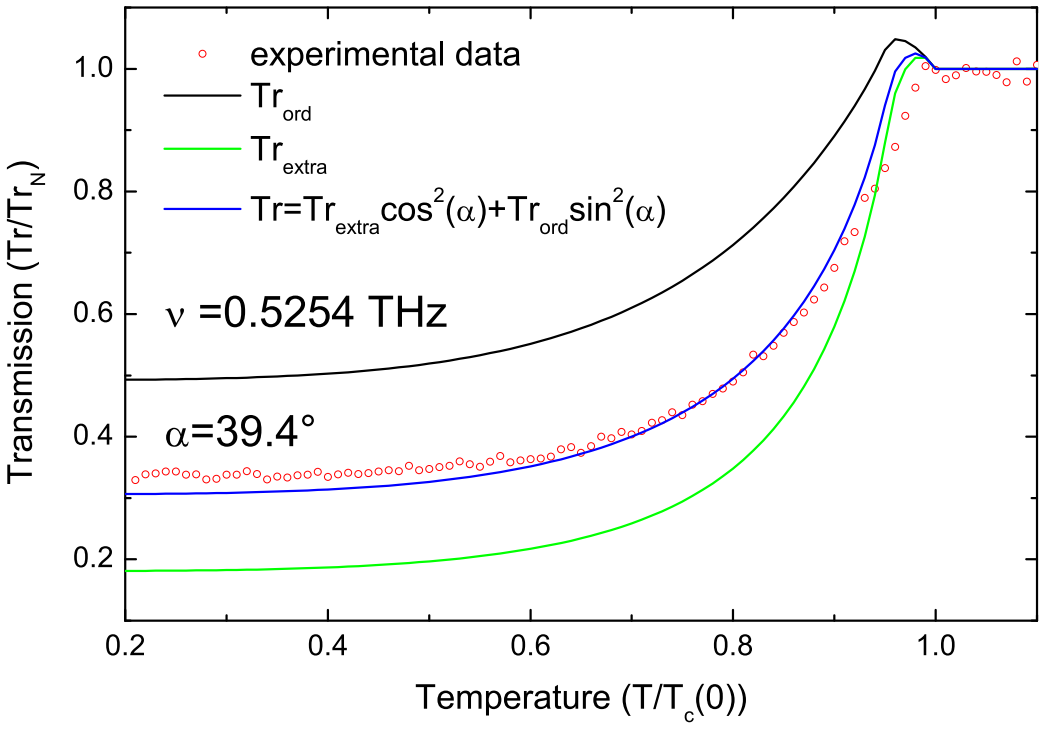

Figure 4.12: Transmission through NbN/R-cut sapphire sample as measured without wire-grid polariser for 0.53 THz line (red circles). Lines present numerical calculations described in detail in the text.

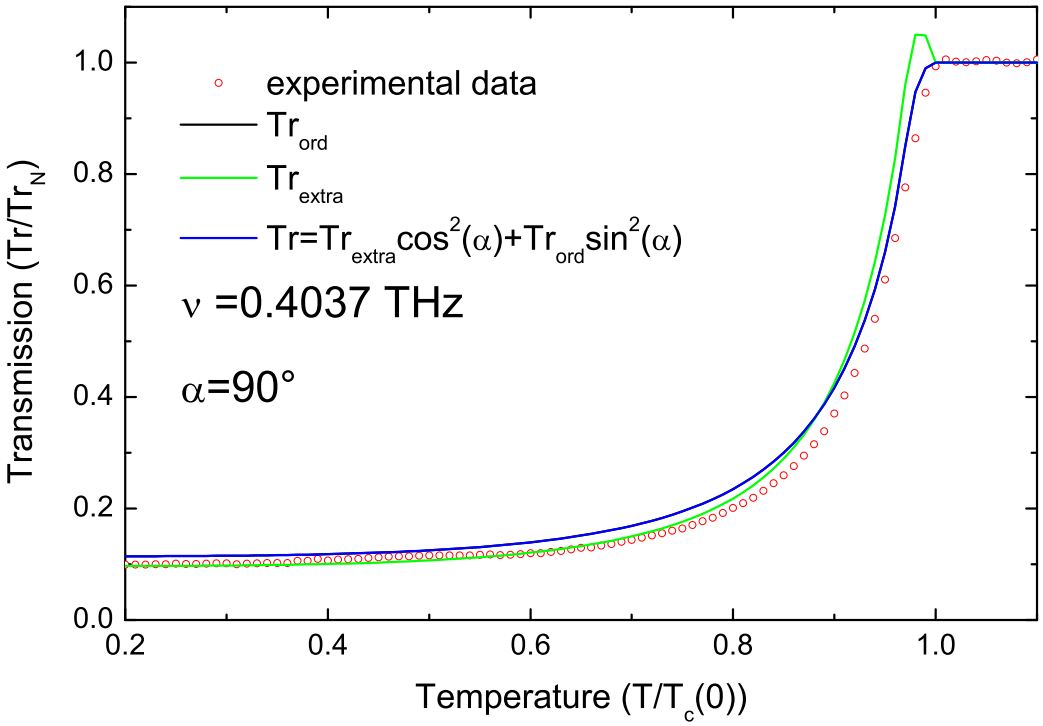

Figure 4.13: Transmission through NbN/R-cut sapphire sample as measured without wire-grid polariser for 0.40 THz line (red circles). Lines present numerical calculations described in detail in the text.

α is thus probably not determined well in this particular case. The main point of this part dedicated to measurements without wire-grid polariser is to determine the α angle, important for interpretation of measurements performed in magnetic field which will be discussed later.

4.4 Complex conductivity observed by Time Domain THz Spectroscopy

In this section, complementary measurements to the laser thermal spectroscopy experiments are presented. The complex conductivity $\tilde{\sigma}(\omega)$ is determined in a broad frequency range (0.25 - 2.25 THz) by time-domain THz spectroscopy (TD TS) for fixed temperatures.

In these experiments, it is essential to measure the reference precisely since any inaccuracy will affect all experimental results. Transmission through the 0.404 mm thick Si substrate was measured as a reference. Then the transmission through our NbN#544 film on Si substrate was measured above T_c which determined important sample parameters - normal-state DC conductivity $\sigma_N(0)$, momentum scattering time τ and the thickness of substrate d_2. Values of $\sigma_N(0)$ and τ are obtained by fitting the Drude formula to the measured data, see figure 4.14. τ is very small for metals (several femtoseconds) and it can not be determined with high precision. We see that $\tilde{\sigma}_N(\omega)$ is nearly purely real and almost constant in the THz range. For reasonably high temperatures above T_c the properties of NbN in the normal state are expected to be temperature independent as

we observed that transmission of NbN samples measured by laser thermal spectroscopy was constant above T_c. $\sigma_N(0)$ was determined as $0.462 \times 10^6\ \Omega^{-1}\, m^{-1}$ and momentum scattering time as 21 fs. It was important to take into account experimental errors, see figure 4.15. Let's note neglecting these instrumental errors in fitting procedures leads to slightly different values of normal-state parameters: $\sigma_N(0) = 0.472 \times 10^6\ \Omega^{-1}\, m^{-1}$ and $\tau = 19$ fs. The thickness of highly resistive Si is determined using the second signal, so called *echo*, and is found to be 405 nm.

Complex conductivity of NbN thin film was measured at several different temperatures below $T_c = 12.5$ K. Representative ensemble is presented in figure 4.14. σ_2 exhibits typical $1/\omega$ dependencies while typical sharp edge feature due to existence of the optical gap is observed in $\sigma_1(\omega)$. Unfortunately, the temperature sensor was not placed in direct contact with the sample so we discovered that an offset of up to 5.5 K existed between the measured temperature and the temperature of the sample. As we have already shown, both experimentally and theoretically, optical properties of NbN films are strongly temperature dependent except in the low temperature region. High-complex conductivity of superconducting film thus can be measured and NbN film can be, in principle, used as a thermometer. We used Zimmermann model [21] to fit the experimental data having temperature of the sample to be the only variable parameter of the fit. The remaining parameters were either specified prior to the experiment, see table 2.2, or reasonably estimated, $2\Delta(0) = 4.15\, k_B T_c$. Any variations in these remaining parameters do not improve the fit we obtained. Experimental errors are essentially due to the uncertainty of the thickness of the reference substrate (with respect to the thickness of the substrate with the film), see figure 4.15. They are not constant throughout the measured frequency range. These errors were used to weight the least square sum in the fitting procedure. $\Delta\sigma_2$ grows almost linearly with frequency while frequency dependence of $\Delta\sigma_1$ is more complicated. $\sigma_1(\omega)$ is determined less accurately in low frequency region. Careful observation of σ_1 (black points in figure 4.14) reveals an unexpected dip around 0.5 THz. This dip is most likely an experimental artifact and direct consequence of low experimental accuracy in the low frequency region.

To summarize this section, by minimizing the sum of least squares fitting the Zimmerman's model [21] with temperature as only one free parameter to the measured data, the actual temperature of the sample is determined and theoretical curves are compared with the experimental data, see solid lines in figure 4.14. Theoretical values of σ_2 are in excellent agreement with the measured data. In the case of σ_1, the calculated dependence qualitatively describes measured data but theoretical curves seem to shift the sharp edge due to the optical gap $2\Delta(T)$ in comparison with the experiment. It is probably due to a rather high inaccuracy of σ_1 in this frequency region. Further, σ_2 is determined quite accurately in this frequency region so that the fitting procedure prefers to optimize $\sigma_2(\omega)$ rather than $\sigma_1(\omega)$. Similar far-infrared studies on NbN film [26, 62] do not indicate any failures of the Zimmermann model.

To summarize this chapter, transmission through different NbN films was measured by laser thermal spectroscopy technique and time-domain terahertz spectroscopy. All samples are quite similar and in all cases the Zimmerman model was able to describe their THz properties both qualitatively and quantitatively.

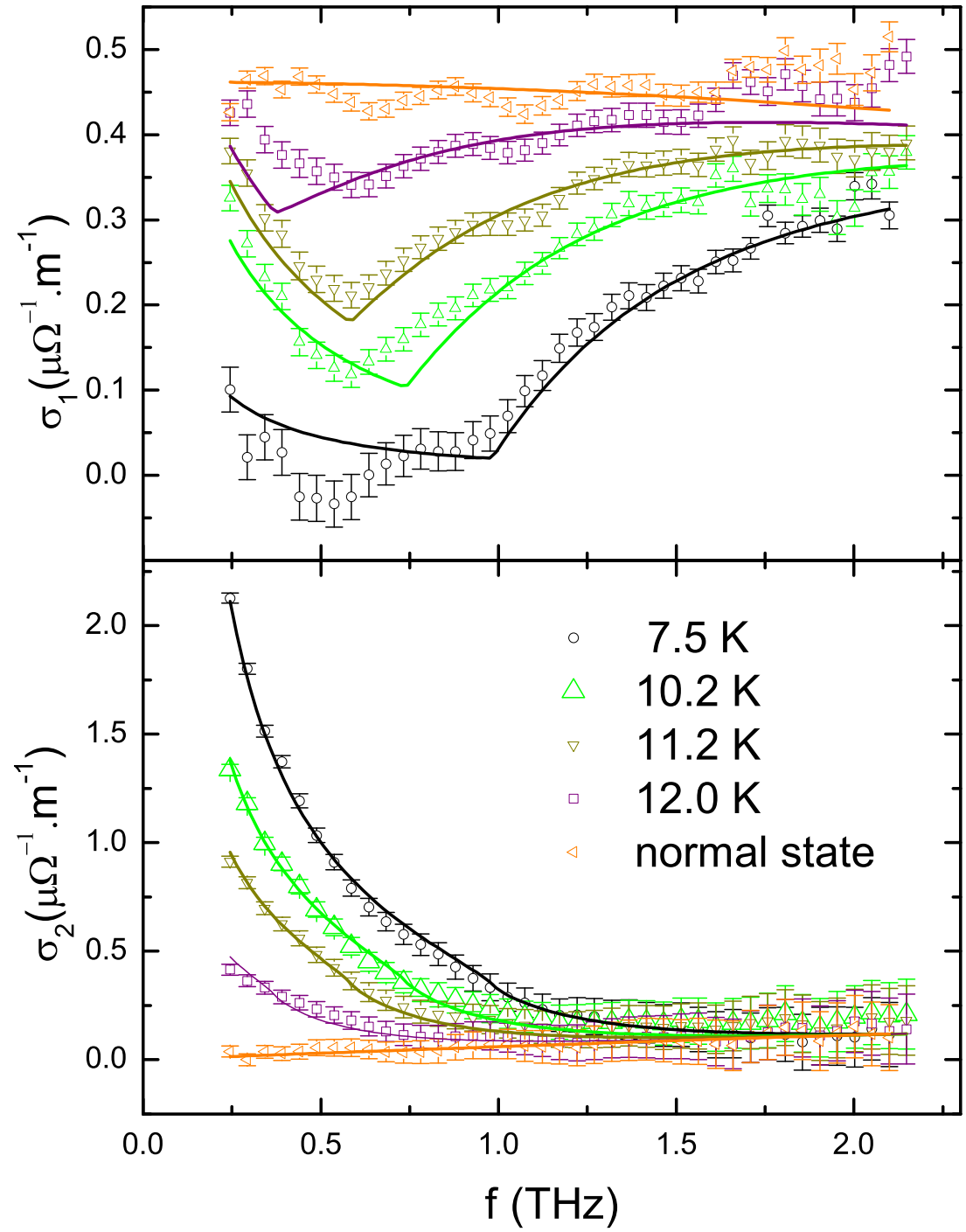

Figure 4.14: Real (top panel) and imaginary (bottom panel) part of high-frequency conductivity of NbN film #544. Individual points are the experimental data, numerical calculations are represented by solid lines. Normal state conductivity is described by Drude model (orange line) while the remaining theoretical curves follows the Zimmermann model [21]

.

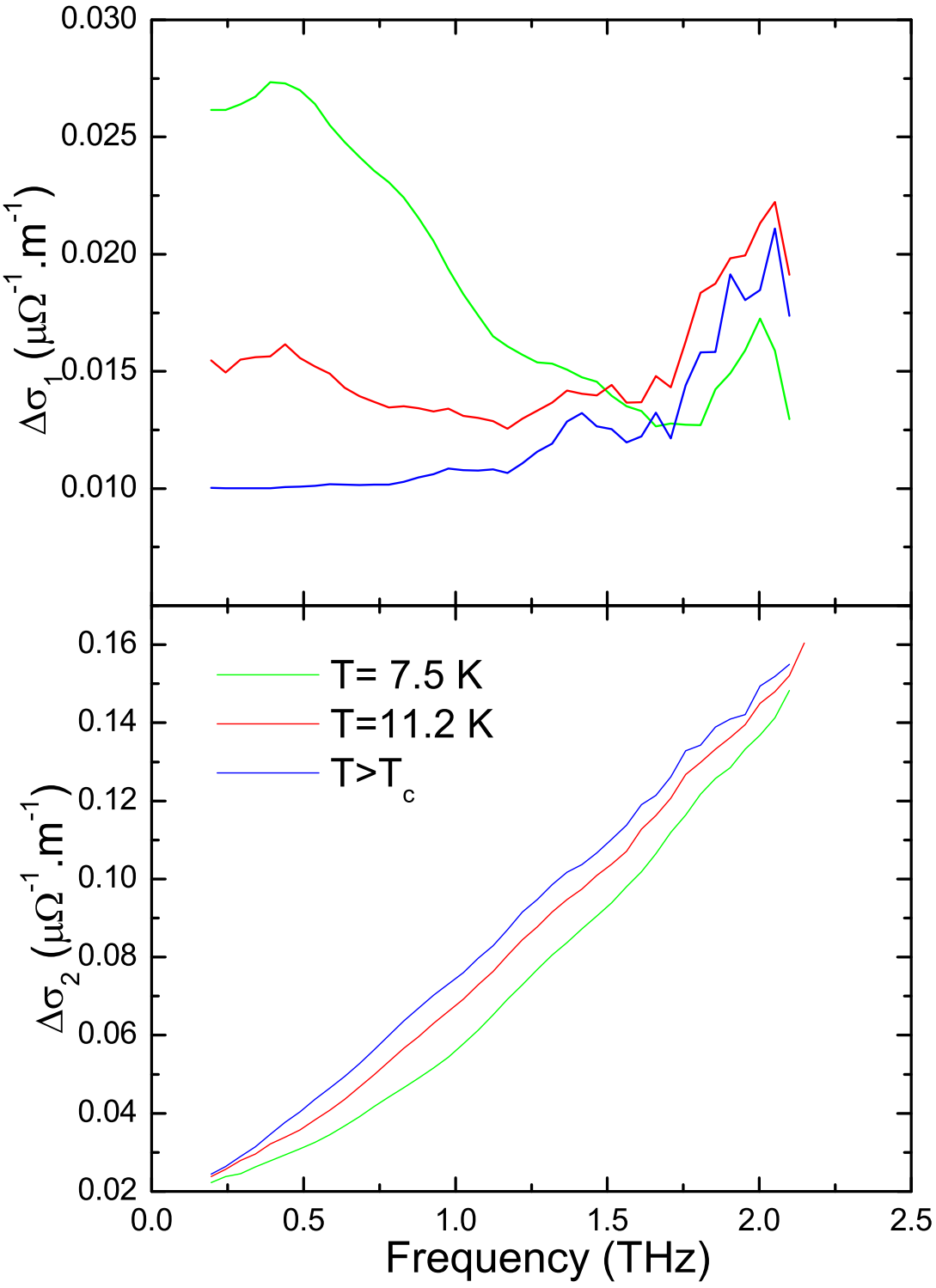

Figure 4.15: Analysis of errors in experiment. In the top (bottom) panel typical error bars for the real part of conductivity σ_1 (imaginary part of conductivity σ_2) are given.

5. Non-zero magnetic field

As it was already discussed, magnetic field substantialy changes properties of superconductors, especially in case of thin films geometry becomes an important issue. In our experiment we recognize three fundamental geometrical configurations in regard of applied magnetic field, sample position and linear polarisation with respect to each other. In *Faraday configuration*, see figure 5.1, external magnetic field is applied perpendicularly to the plane of the film and optical properties of a NbN film do not depend on the direction of linear polarisation. In *Voigt configuration*, magnetic field is applied parallel with the sample surface. Optical properties depend on the direction of linear polarisation in this case. Different properties are expected when THz electric field is applied along with the vortex axis and perpendicularly to it.

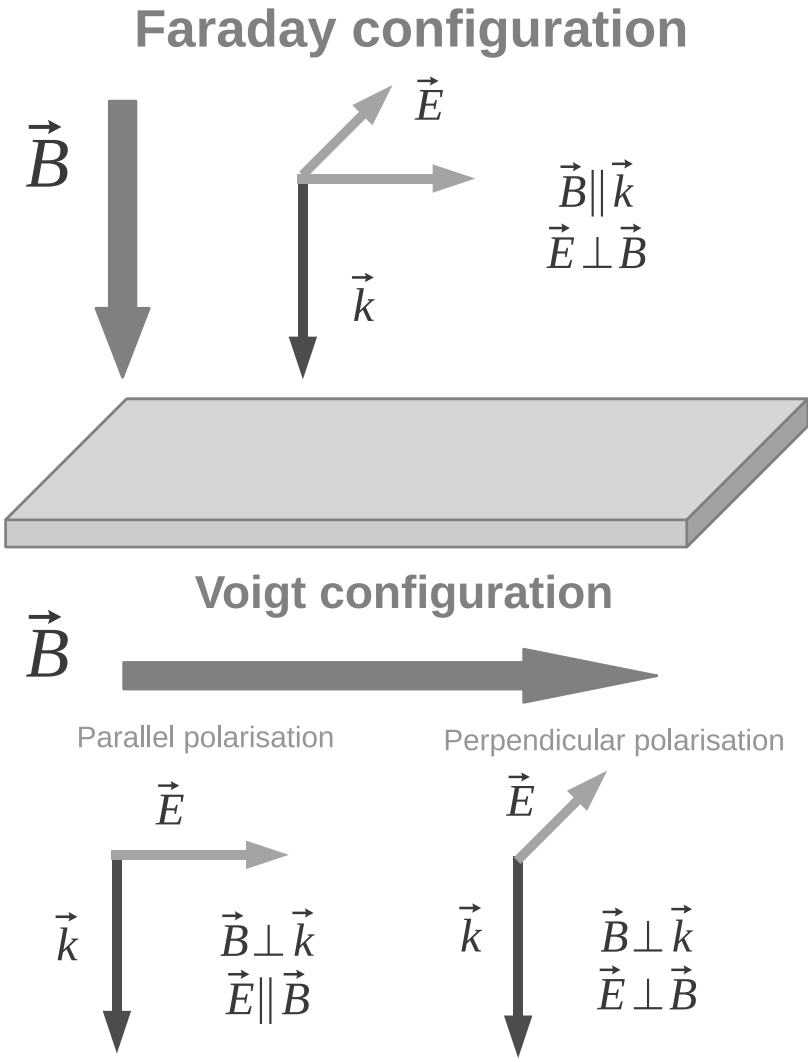

Figure 5.1: Magneto-optical configurations relevant to the experiment. $\vec{E}$ is electric component of electromagnetic radiation, $\vec{B}$ is applied magnetic field and $\vec{k}$ is wavevector.

First, we will discuss features common to both configurations, then each configuration will be treated separately - presenting experimental results and phenomenological theoretical description.

5.1 Features common for Faraday and Voigt geometry

In both Faraday and Voigt configurations vortices will appear in the interior of the superconducting sample in sufficiently high magnetic field ($B_{c1} < B < B_{c2}$). Two similar models are introduced to account for their presence. Further, the extension of these models is given to include effects of vortex motion. In this chapter, when we refer to the critical temperature or other parameters, we have in mind that these variables can have different values, even different functional dependencies, for Faraday or Voigt configuration.

Although vortices have been observed by a number of different techniques utilizing measurements of local magnetic flux or registering suppression of superconductivity, a satisfactory microscopic theoretical description is still missing. Clem [64] proposed a very simple treatment of vortices that works surprisingly well. He assumed that normal state properties inside vortex cores are locally restored and the system can be thought of as a superconducting material with cylindrical inclusions of normal state material. The situation becomes more complicated as individual vortices interact with each other and might move. Moreover, physical properties of the superconducting matrix are modified by magnetic field.

To the best of our knowledge, there is as yet no fundamental theoretical model that would consider all physical phenomena associated with the presence of quantized vortices in type II superconductors. We will therefore limit our theoretical considerations to phenomenological level.

In order to understand magneto-optical measurements in THz region, we propose a simple phenomenological model, which neglects vortex motion and treats the superconducting thin film as a system consisting of a superconducting matrix and cylindrical inclusions of normal state material that represent vortex cores. Coherence length ξ is of order of a few nm (Ikebe [26] estimates the coherence length $\xi \cong 5$ nm for NbN at zero temperature) and the intervortex distance is usually of the same order – so the typical wavelengths in far-infrared range are much larger. We can therefore use the long wavelength limit – electromagnetic radiation does not sense individual vortices and the system can be thought of as a homogeneous one, possessing an effective complex conductivity $\tilde{\sigma}_{eff}$, which in turn can be described by suitable effective medium theories.

Effective medium theories include the effects due to the local field and define the effective dielectric function of the inhomogeneous medium in terms of volume-averaged fields, $\langle \mathcal{E} \rangle$ and $\langle \mathcal{H} \rangle$, and responses $\langle \mathbf{D} \rangle$ and $\langle \mathbf{B} \rangle$ [60, 65]. Different approximations are made to tackle this problem. Here *Maxwell-Garnett theory* (MGT) and *effective medium aproximation* (EMA) are presented. We should keep in mind that in both theories a random distribution of inclusions is assumed which is in disagreement with actual more realistic periodic distribution of vortices. Let's assume a two component composite only. The volume fraction of vortex cores is $f_n = V_n/V$ while the superconducting fraction f_s must be equal to $1 - f_n$.

The vortex core fraction f_n can be approximated by [26, 28]

$$f_n = B/B_{c2}(T). \tag{5.1}$$

For relatively high temperatures, $B_{c2}(T)$ can be obtained by interpolation of the measured values and f_n is described correctly. For low temperatures, $B_{c2}(T)$ is extrapolated using suitable theoretical description. This procedure, however, might lead to incorrect values of f_n at low temperatures. As we will see, different theoretical models describing measured values equally well, will give different values of $B_{c2}(0)$ and, consequently, different values of f_n. On the other hand, direct measurement of B_{c2} for some of our samples at low temperatures would require very high magnetic field above 10 tesla which represents the maximum attainable field in our experimental setup.

The normal state conductivity of NbN, $\tilde{\sigma}_n$, is considered to be independent on magnetic field. This was confirmed by our transmission measurements when magnetic field was increased up to 10 tesla and no appreciable change was observed. Although we are aware that magnetic field generally modifies the superconducting state conductivity $\tilde{\sigma}_s$, we limit ourselves to a rather crude approximation, assuming that Zimmerman *et al.* expressions are valid even if T_c is replaced by its field value $T_c(B)$. A somewhat more rigorous treatment of superconducting fraction is also possible in some cases, e.g., by utilizing the pair-breaking theory of Abrikosov and Gorkov [66]. Experimentally it is possible to measure $\tilde{\sigma}_s$ in very thin films, i.e. $d < \xi$, applying magnetic field along the film surface in which case a macroscopic wavefunction must be uniform in the entire sample and no vortices appear. Xi [67] reports such a measurement on a 10-nm-thick $Nb_{0.5}Ti_{0.5}N$ film with coherence length $\xi = 20$ nm at low temperature. Both real and imaginary parts of conductivity $\tilde{\sigma}(\omega)$ are only slightly quantitavely modified, thus justifying our crude approximation.

Maxwell-Garnett formulated his theory for dilute systems assuming that the inclusions feel the external field that coincides with the local field for the filler, see fig 5.2. In our case vortices are considered as inclusions and superconducting environment surrounding the vortices is the filler. Mutual interaction between inclusions is thus neglected. More generally, it was found that MGT formulas can hold even for higher concentrations of inclusions as long as the filler is percolated [68].

Considering the special case of cylindrical inclusions, MGT gives the formula

$$\tilde{\sigma}_{MGT} = \frac{2f_n\tilde{\sigma}_s(\tilde{\sigma}_n - \tilde{\sigma}_s)}{(1-f_n)(\tilde{\sigma}_n - \tilde{\sigma}_s) + 2\tilde{\sigma}_s} + \tilde{\sigma}_s \tag{5.2}$$

if electric field is perpendicular to the vortex axis and

$$\tilde{\sigma}_{MGT} = f_n\tilde{\sigma}_n + (1-f_n)\tilde{\sigma}_s \tag{5.3}$$

if electric field is parallel with the vortex axis. The latter formula can be qualitatively understood as that charges move independently along the vortex cores and in the superconducting matrix.

In contrast to the MGT, the EMA considers mutual interation between the inclusions. Both superconducting and vortex core components are considered to be surrounded by an effective medium with effective permittivity ε_{eff}, see

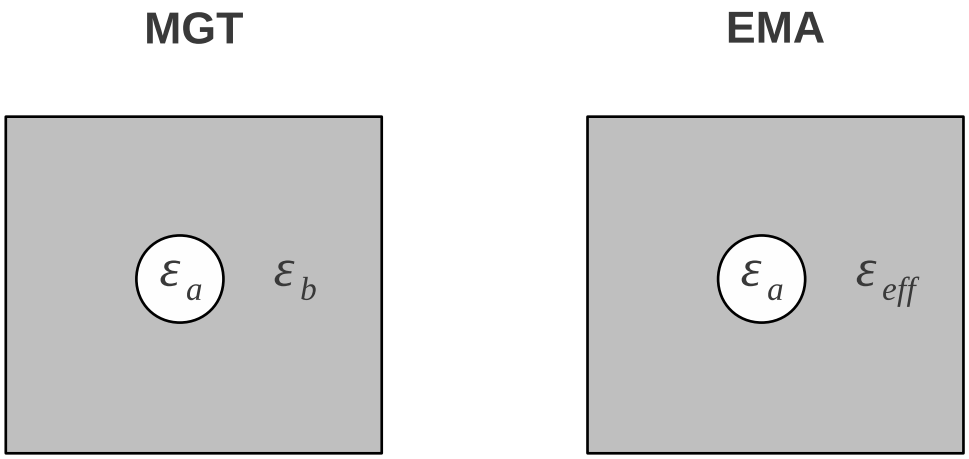

Figure 5.2: Schematically pictured difference between the Maxwell-Garnett theory and effective medium approximation. MGT considers each individual inclusion to be surroundend by a filler without any other inclusion, while EMA treats each component as it is surrounded by an effective medium possessing an effective permittivity.

figure 5.2. Local field and effective conductivity values are found in the self-consistent way, for details see [65]. The EMA, in contrast with the MGT, predicts a percolation threshold. In case of cylindrical inclusions, the EMA assumes that if the concentration of superconducting filler becomes smaller than 1/2 it stops being perfectly percolated. This is not in agreement with the common view of vortex behavior in superconductor. However, f_s is less than one half except for a narrow temperature range just below T_c and very high magnetic fields.

Considering now our case of cylindrical vortex cores, the EMA gives the following expression for linear polarisation perpendicular to the vortex axis [65]:

$$\tilde{\sigma}_{EMA} = \frac{1}{2}\left(\beta \pm \sqrt{\beta^2 + 4\tilde{\sigma}_n\tilde{\sigma}_{sc}}\right). \tag{5.4}$$

Here $\beta = (1 - 2f_n)(\tilde{\sigma}_n - \tilde{\sigma}_{sc})$ and the sign is chosen so that $\sigma_{1EMA} \geq 0$, i.e., we choose physically relevant solution of quadratic equation. In case of linear polarisation aligned parallel with the vortex axis EMA naturally gives the same expression 5.3 as MGT.

To summarize, MGT better describes the picture in which vortex cores are considered as cylindrical normal state inclusions completely surrounded by the superconducting filler. On the other hand, EMA seems to better describe local field thanks to its self-consistent way of treating local fields.

Although the expression for the two mentioned magneto-optical configurations, when electric component of electromagnetic radiation is applied perpendicularly to the vortex axis, is formally the same, these two cases are not identical. The reason is that $T_c(B)$ acquires different values for magnetic field parallel with the thin film and perpendicular to it. Additionally, the vortex lattices will be very different for $\mathbf{B}^{\perp}$ and $\mathbf{B}^{\parallel}$. In perpendicular field (assuming no crystal defects) vortices will arrange themselves into a triangular lattice [10]. In parallel field this is

not possible, because the film thickness is of the same order as ξ or intervortex distance. Vortices will align themselves into rows [69]. Generally, THz radiation can cause vortices to move. In the special case when electric field points in the same direction as the vortex axis $\mathbf{E} \parallel \mathbf{B}$ vortices do not move and dissipation term due to the vortex dynamics is zero.

Coffey and Clem [70] solved self-consistently the modified London equation in the presence of vortices and expressed their result in terms of complex penetration depth $\tilde{\lambda}$. The results can be conveniently expressed in terms of complex conductivity

$$\tilde{\sigma}^{cc} = \frac{(1-f_n)\tilde{\sigma}_s + f_n\tilde{\sigma}_n}{1+(1-f_n)\tilde{\sigma}_s/\tilde{\sigma}_{vd}}, \tag{5.5}$$

where the conductivity induced by the vortex dynamics σ_{vd} can be expressed following Bardeen and Stephen [71] as $\tilde{\sigma}_n/f_n$. Vortices are assumed to be located in a potential well so that they oscillate only around their equilibrium position. As it was discussed in earlier chapter, two-fluid model is inferior in comparison with the BCS theory which must be used if substantial number of quasiparticles is present. Therefore this model is justified only for low temperatures and frequencies below the optical gap. Modern approach by Time-Dependent Ginzburg-Landau (TDGL) theory [72] suffers the same limitations so it was able to explain low-temperature measurements of complex conductivity in THz region performed by Ikebe [26] only in a limited frequency range.

An explicit formula considering local field effects treated by MGT and vortex dynamics following Coffey-Clem model was derived in Ikebe's paper [26]:

$$\tilde{\sigma}^{cc}_{MGT} = \frac{\tilde{\sigma}_{MGT}}{1+\frac{f_n\tilde{\sigma}_s}{\tilde{\sigma}_n\left(1+\frac{f_n}{1-f_n}\frac{2\tilde{\sigma}_s}{\tilde{\sigma}_n+\tilde{\sigma}_s}\right)}}. \tag{5.6}$$

In EMA, a similar explicit formula can be obtained following the same procedure:

$$\sigma^{cc}_{EMA} = \frac{\tilde{\sigma}_{EMA}}{1+f_n(1-f_n)\frac{2\tilde{\sigma}_{EMA}}{\tilde{\sigma}_s+\tilde{\sigma}_{EMA}}\frac{\tilde{\sigma}_s}{\tilde{\sigma}_n}}. \tag{5.7}$$

5.2 Faraday configuration

Now, we can finally fully concentrate on obtained experimental data. In Faraday configuration, measurements performed on two different films are considered - NbN (Beňačka) and NbN#383 (Il'in).

Let's start with experiments performed on Beňačka sample. Temperature dependence of transmission was measured for magnetic fields up to 9 tesla with 1 tesla step for frequency well below the optical gap (0.4037 THz), see figure 5.3. Transmission in small magnetic field exhibits qualitatively similar behavior as in zero magnetic field. With increasing magnetic field the transmission peak decreases and shifts to lower temperatures while low-temperature transmission slowly approaches its normal-state value. For highest attainable fields transmission becomes nearly the same as in the normal state over entire temperature interval.

Starting from temperature above T_c, transmission is constant until a sharp increase occurs at T_c. This allowed us to determine T_c with reasonable accuracy,

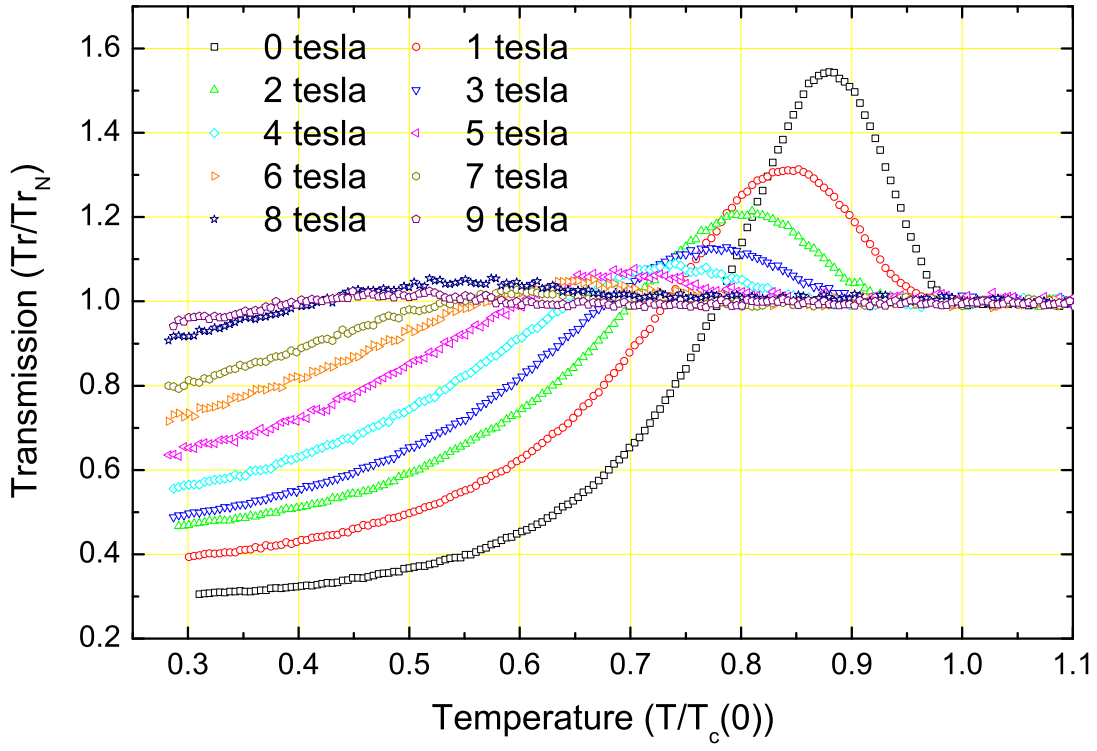

Figure 5.3: Experimental data of transmission of 0.4037 THz line through NbN (Beňačka) in Faraday orientation.

see figure 5.4. Transmission data measured in magnetic field above 5 tesla do not exhibit sharp increase any more and T_c is hard to determine and thus it is determined less accurately than in the case of the low-field data, see error bars in figure 5.4.

We fit these experimental data with three different functions. Note that dependencies of $B_{c2}(T)$ and $T_c(B)$ express the same physics - a line in $T-B$ phase diagram below which the material is superconducting. Beňačka measured T_c in zero magnetic field more precisely so we fix $T_c(0)$ to its value of 10.8 K in all following fits. Following Tinkham [10] and Ikebe [26] recommendation, the upper critical field is given as

$$B_{c2} = B_{c2}(0)\frac{1-t^2}{1+t^2}, \tag{5.8}$$

where t is the reduced temperature $(T/T_c(B=0))$. This formula predicts linear decrease of T_c with magnetic field almost up to $B_{c2}(0)$ where it deviates from linear dependence and takes almost parabolic form. Although it seems to describe experimental data up to 7 tesla well, for higher magnetic field the experimental data seem to deviate and the extrapolated value of upper critical field $B_{c2}(0) = 27.6$ tesla seems too high. In our previous work [73] we used

$$B_{c2} = B_{c2}(0)\sqrt{1-t^2}. \tag{5.9}$$

Although the fitting gives reasonably high value of upper critical field $B_{c2}(0) = 10.9$ tesla, overall agreement with experimental data is not fully satisfactory. Following the Ginzburg-Landau expression of B_{c2} in terms of coherence length as $B_{c2} = \Phi_0/(2\pi\xi^2(T))$ and assuming the two-fluid temperature dependence of $\xi(T)$

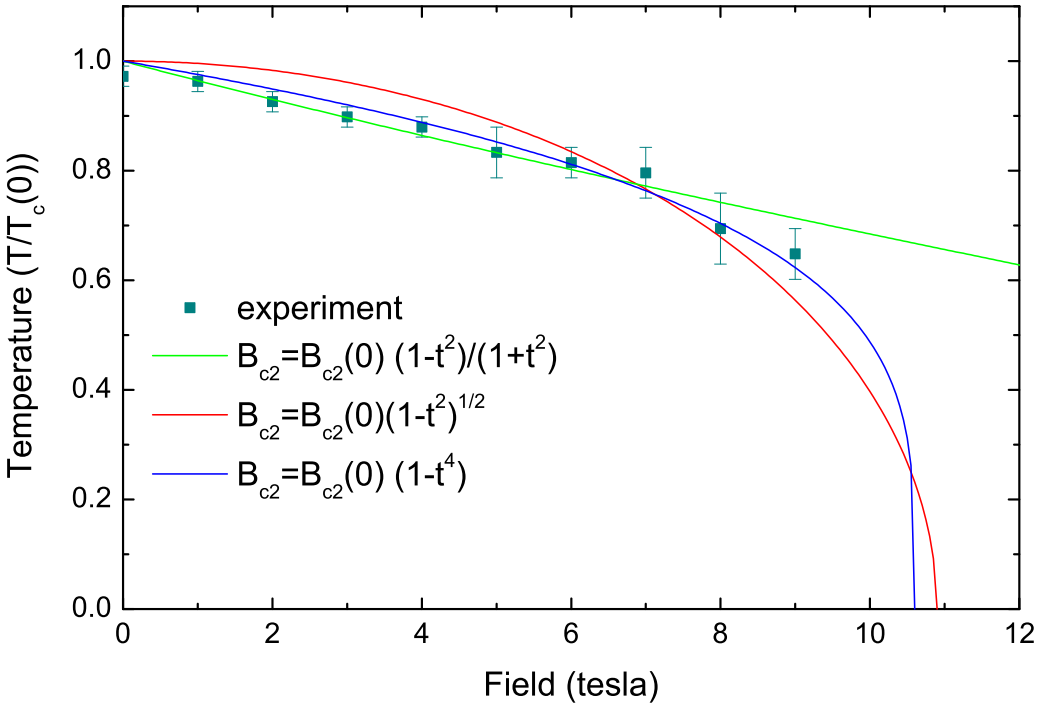

Figure 5.4: Critical temperature T_c of Beňačka sample as determined from the transmission data (points). For higher magnetic fields T_c was determined less precisely, which is reflected by larger error bars.

we get expression

$$B_{c2} = B_{c2}(0)(1 - t^4) \tag{5.10}$$

that seems to best describe our experimental data and it estimates a reasonable value of $B_{c2}(0) = 10.6$ tesla.

So in the following, vortex core volume fraction f_n is evaluated using this dependence of $B_{c2}(T)$ (eq. 5.10). This approach is a little different from the one published in our previous article [1]. However, the difference is almost negligible. Note that all parameters needed for calculation of transmission are determined so no parameter is optimized by fitting its value. Following previous chapter, transmission is calculated utilizing the Maxwell-Garnett theory (figure 5.5) and the effective medium approximation (figure 5.6). Contribution from the vortex dynamics (eq. 5.6, 5.7 respectively) is presented by dotted lines at low temperatures only. We found that effective medium approximation describes the experimental data (figure 5.3) better than Maxwell-Garnett theory and further improvement is obtained by including vortex motion following the Coffey-Clem model.

Let's now discuss transmission through NbN/R-cut sapphire sample in Faraday geometry. In previous chapter, experiments performed without wire-grid polariser were discussed and the angle of linear polarisation α was determined for zero-magnetic field measurement. Now we describe the temperature dependence of transmission was measured in perpendicular field up to 10 tesla with the remaining settings unchanged, see figures 5.7 -5.10. Systematic difference between transmissions obtained during cooling and heating was not observed. This can be thought of as a proof that the temperature of the sample was measured correctly, with no appreciable temperature difference between the sample and the

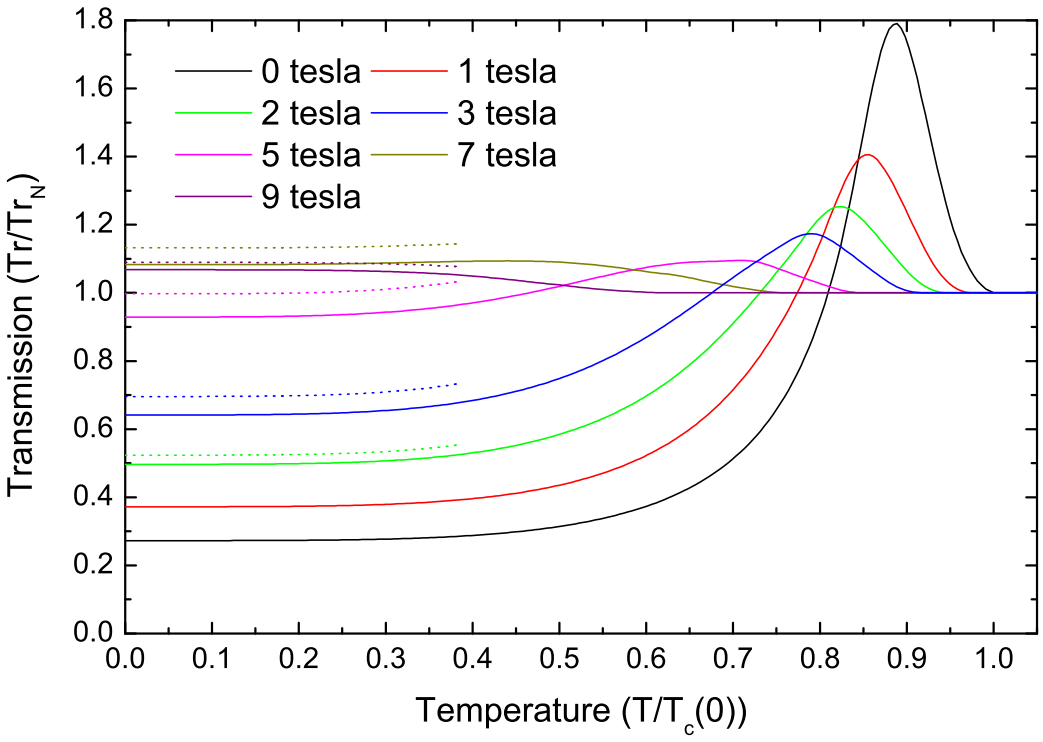

Figure 5.5: Numerical calculation of transmission using Maxwell-Garnett theory without vortex motion (solid lines) and with Coffey-Clem contribution (dotted lines at low temperatures).

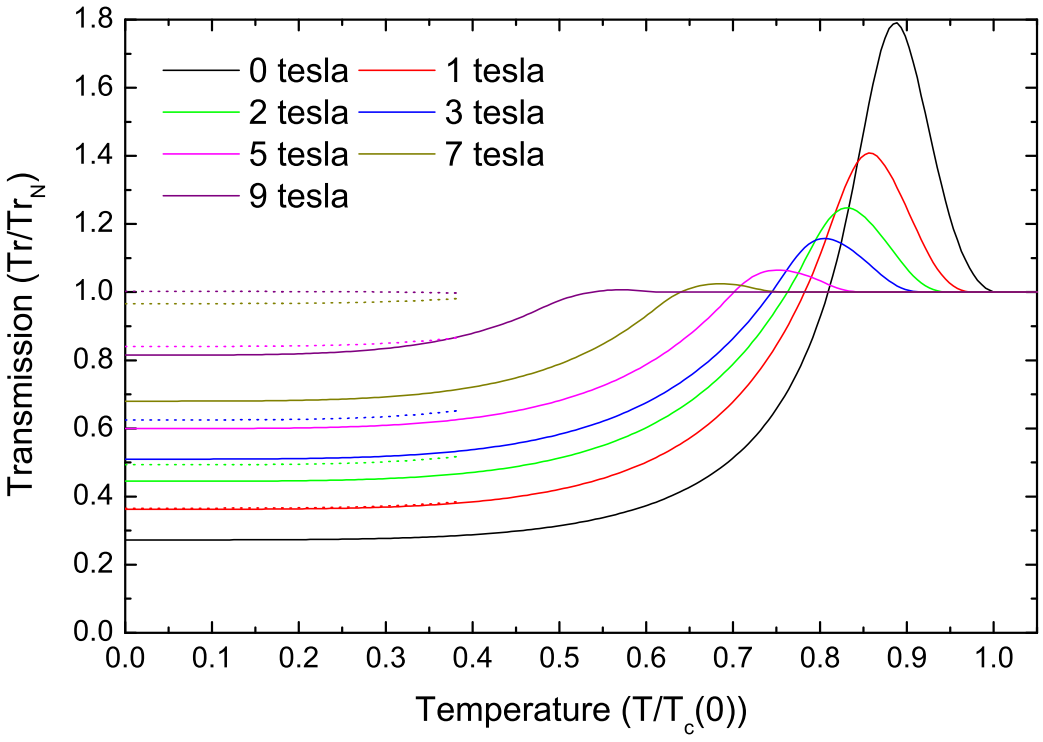

Figure 5.6: Numerical calculation of transmission using effective medium approximation without vortex motion (solid lines) and with Coffey-Clem contribution (dotted lines at low temperatures).

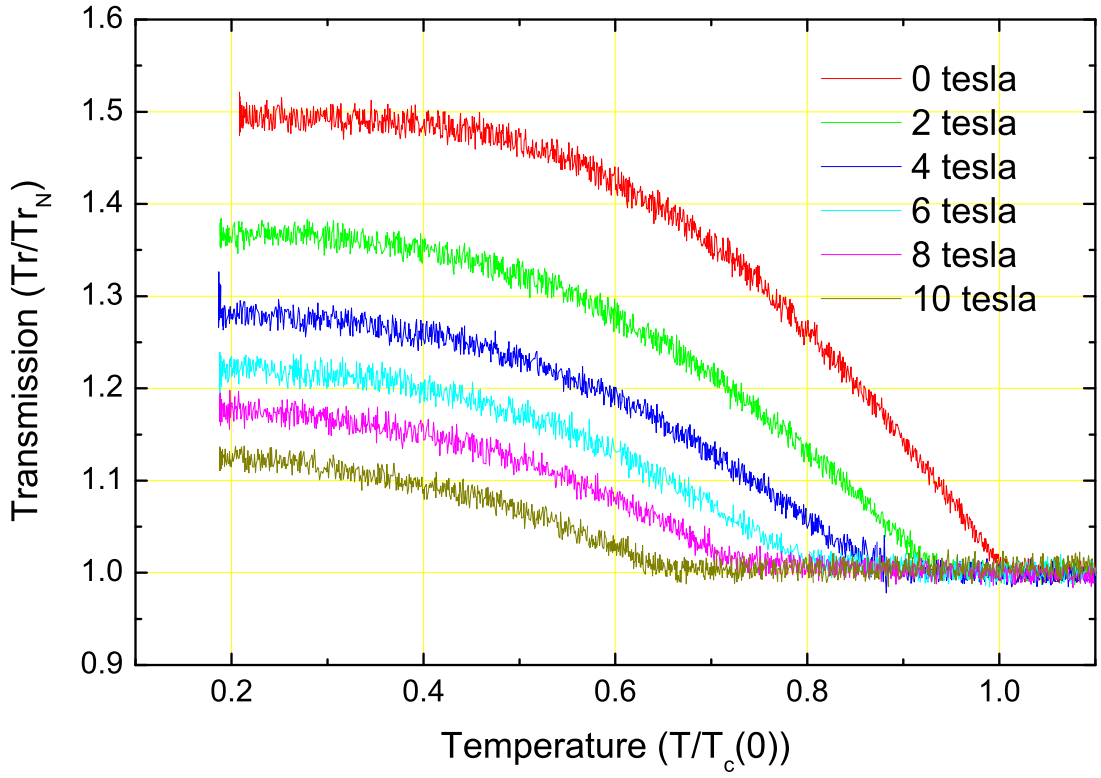

Figure 5.7: Transmission through NbN/sapphire sample, $\nu = 2.5228$ THz

temperature sensor. Frequencies used in experiment were not selected randomly but having in mind three qualitatively different physical situations - laser line 2.5228 THz has energy greater than the optical gap[1], line 0.962 THz is close to the optical gap and the remaining frequencies are well below $2\Delta(0)$. In all cases the transmission has a tendency to approach the normal-state transmission with increasing magnetic field.

In contrast with experiments on Beňačka sample, the sample resistance was measured simultaneously with the transmission, see typical example in figure 5.11, and T_c is determined with higher precision. Data obtained during cooling and heating are in excellent agreement without any hysteresis. Transition to the superconducting state occurs within small temperature region ΔT_c. In literature, there is no general agreement how to define superconducting transition temperature [74]. Various authors consider it in term of the onset, 5%, 10%, midpoint, 90%, 95% and zero resistance points. In this thesis T_c is determined as a midpoint. The onset of superconductivity suggests that superconducting regions are being formed. The sharpness of the drop to zero resistance is a measure of the quality or purity of the sample [74]. Impure samples have broader transition, on the other hand, they can exhibit higher T_c. With increasing magnetic field ΔT_c becomes broader. Note that the experimentally obtained $T_c(B)$ in figure 5.12 are linearly dependent on magnetic field up to maximum attainable magnetic field (10 T). A reasonably looking fit was obtained using formula 5.8, but extrapolation to the low-temperature region is not perfectly justified. Extrapolated values of $B_{c2}(T)$ at low temperatures are very sensitive to any error in our measured data.

[1] $2\Delta(0)$ was determined as 5.7 meV, i.e. 1.38 THz, for the discussed NbN #383 sample

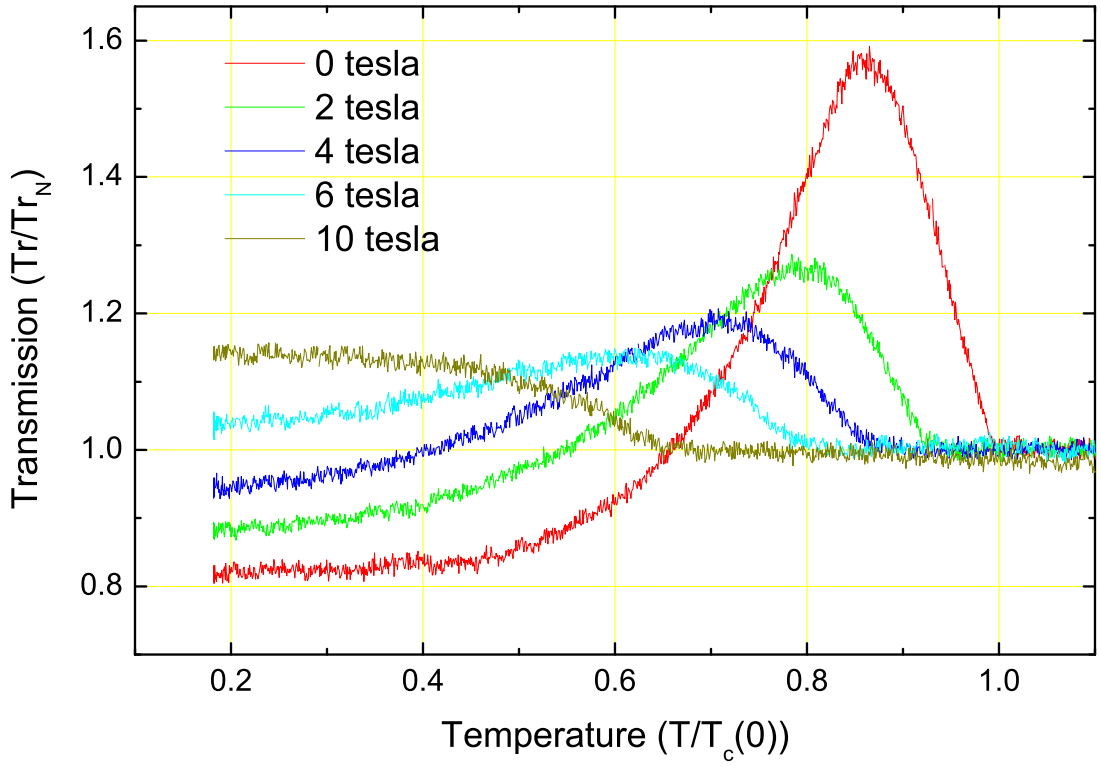

Figure 5.8: Transmission through NbN/sapphire sample, $\nu = 0.962$ THz

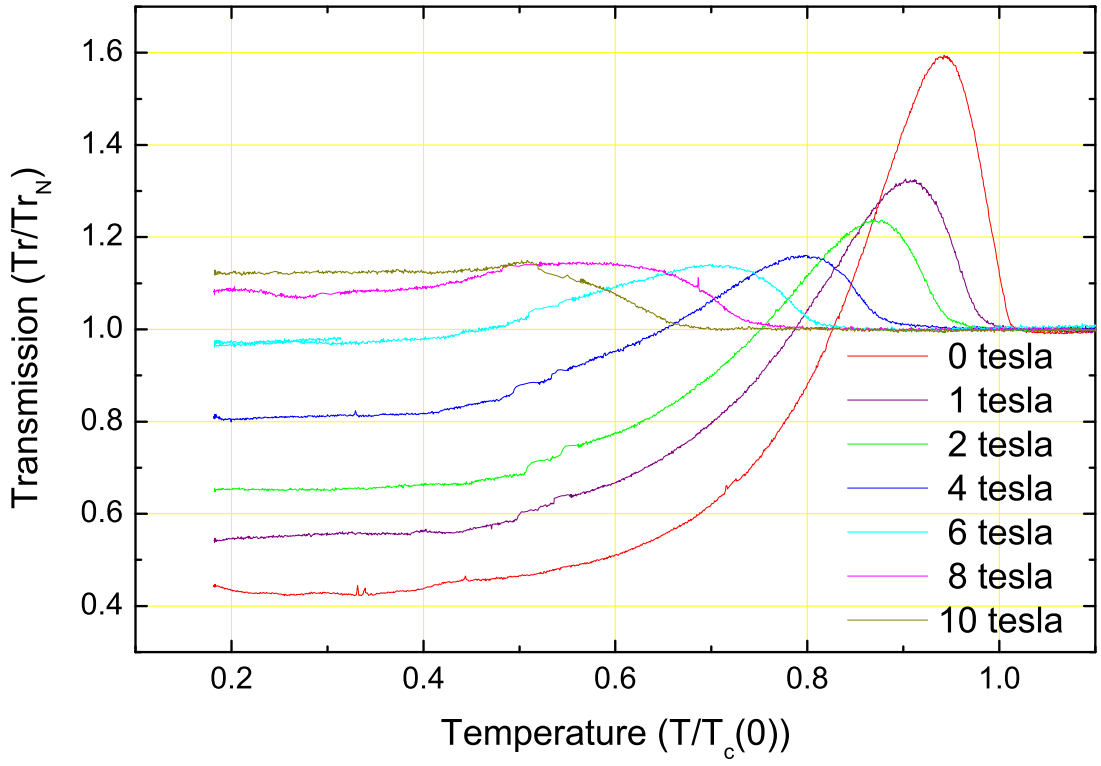

Figure 5.9: Transmission through NbN/sapphire sample, $\nu = 0.5844$ THz

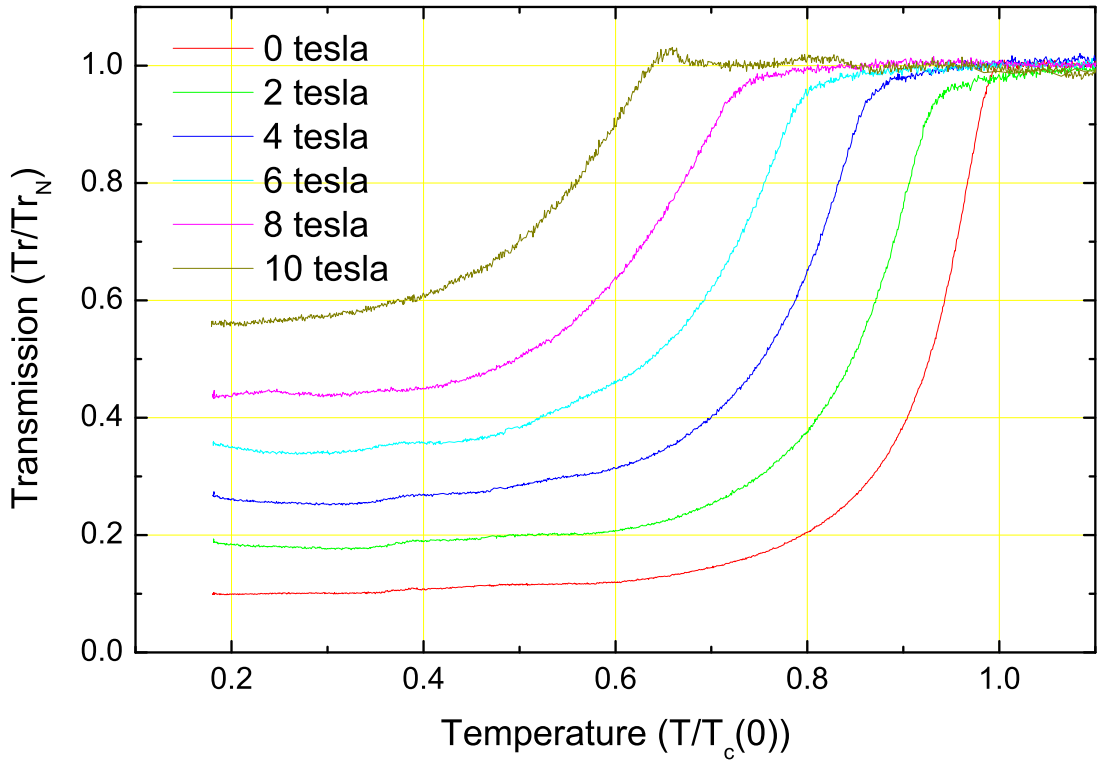

Figure 5.10: Transmission through NbN/sapphire sample, $\nu = 0.4037$ THz

Further, in case of NbN/Si sample this formula seems to fail for low temperatures. The apparently succesfull formula 5.10 is unable to describe the sharp drop of T_c with magnetic field.

The conclusion of this analysis is that we can not reliably determine $f_n(T) = B/B_{c2}(T)$, one of the key parameters of our numerical analysis. Estimated values of $B_{c2}(T)$ at low temperatures are too high to be determined directly with available experimental equipment. Possible solution is to measure $\tilde{\sigma}(\omega)$ by TD TS in high magnetic field starting from low temperature towards T_c. Values of f_n can be determined in this case by fitting measured spectra by our model with f_n as a only one free parameter[2].

In spite of the fact that we can not reliably determine $f_n(T)$, we briefly present our numerical calculations utilizing the effective medium approximation approach, see figures 5.13 and 5.14 showing that the model captures all essential features of the measured data. Thermal peaks are diminished with increased magnetic field and transmission at low temperatures changes with magnetic field in the same manner as the experimental data do, but only on the qualitative level. Analysis of low-temperature transmission for different values of magnetic field suggests that values of $B_{c2}(0)$ around (15 ± 2) tesla might satisfactory explain low temperature transmission. Maxwell-Garnett theory gives similar results but, once again, the effective medium approximation seems to be more successful.

[2]This experiments have not been performed since experimental equipment was not fully installed at the time.

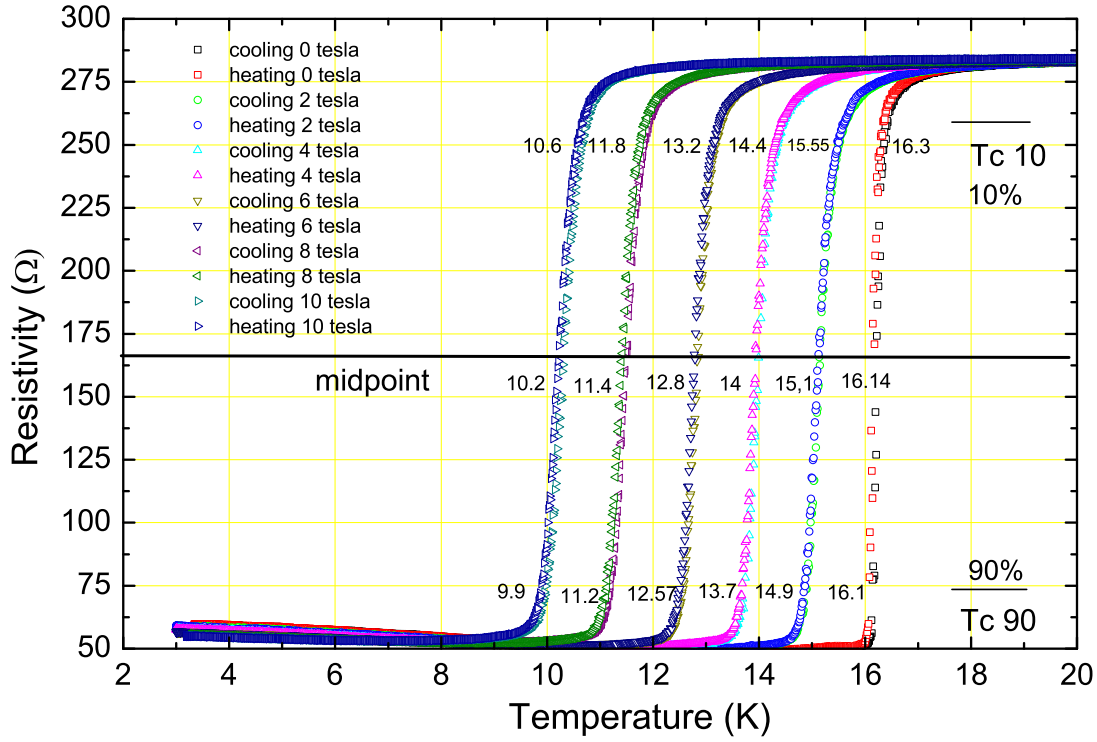

Figure 5.11: Typical example of determination of T_c from resistivity measurements.

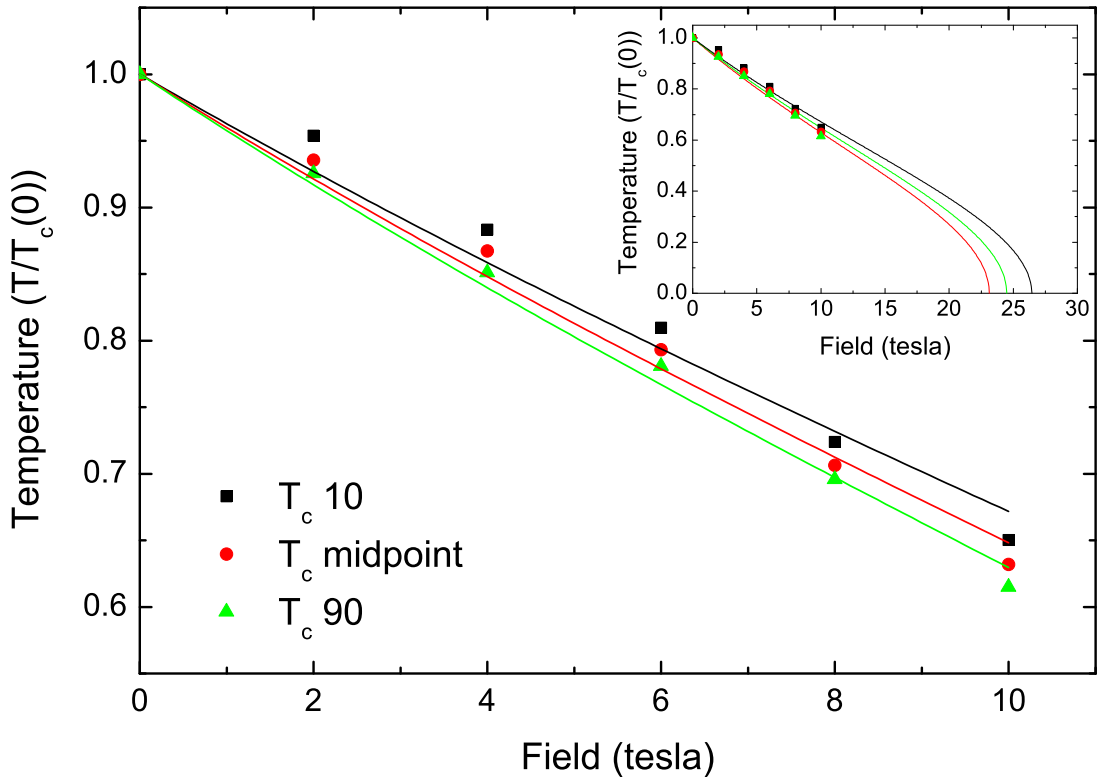

Figure 5.12: Upper critical magnetic field B_{c2} determined from resistivity measurements.

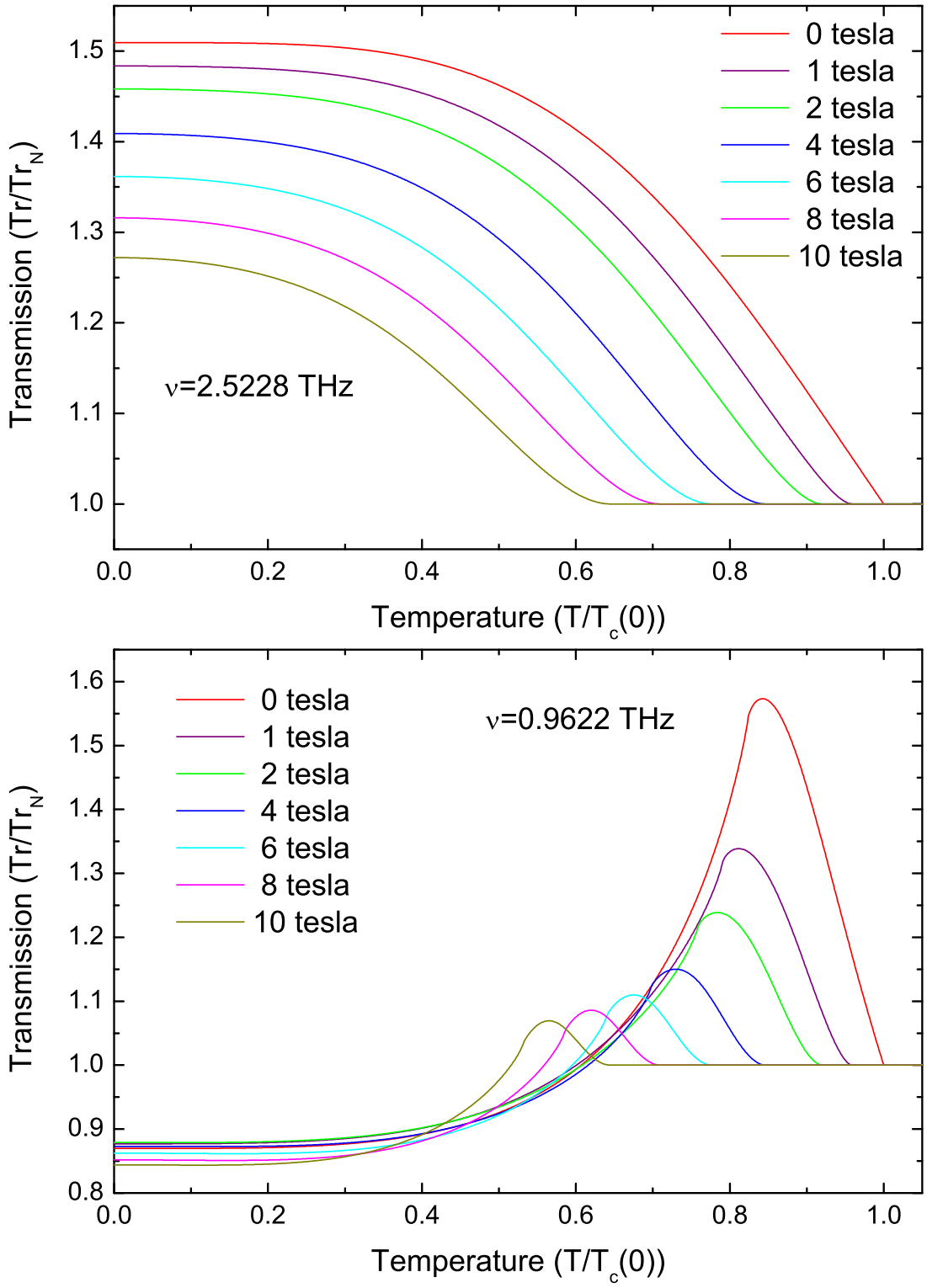

Figure 5.13: Numerical calculation of transmission using effective medium approximation. $B_{c2}(0) = 24.26$ tesla is assumed in our calculations, see figure 5.12.

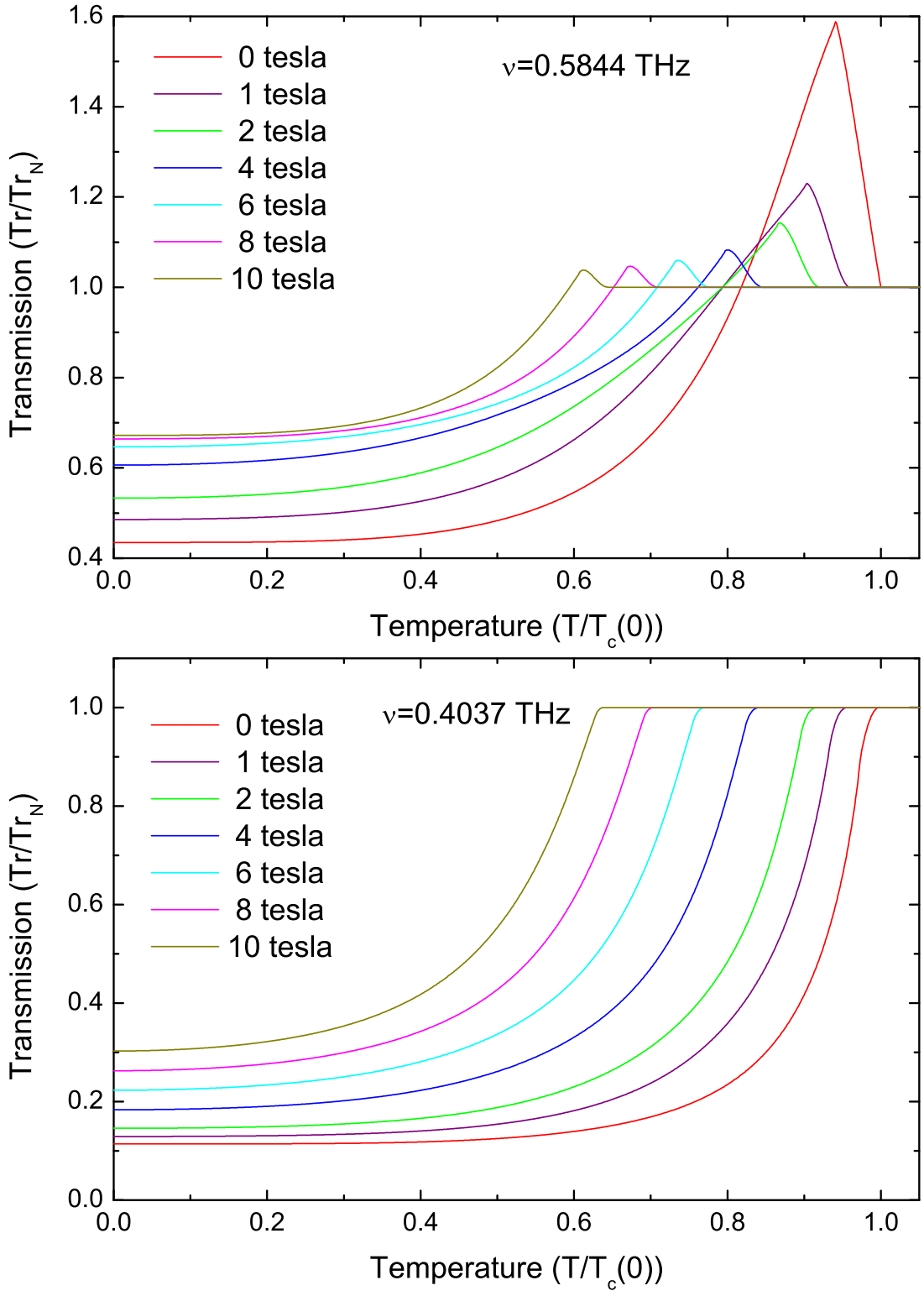

Figure 5.14: Numerical calculation of transmission using effective medium approximation. $B_{c2}(0) = 24.26$ tesla is assumed in our calculations, see figure 5.12.

5.3 Voigt configuration

Transmission of far-infrared radiation through NbN/sapphire sample was also measured in Voigt orientation utilizing two fundamental directions of linear polarisation, the THz electric field pointing parallel with the vortex axis and perpendicular to it. Boundary conditions force vortices to exit the sample perpendicularly with respect to the sample surface. Therefore vortices prefer to stay parallel with the surface even if the sample surface and applied magnetic field are not exactly parallel. In our experiment, this misalignment does not exceed 1°. Further, in case of very thin films such as ours ($d_{film} = 15$ nm), the applied magnetic field is not fully expelled from the interior of the sample, as the penetration depth is much larger than the sample thickness. Positive diamagnetic contribution to the free energy is diminished and thin superconducting films can remain superconducting in much larger fields than bulk samples. Abrikosov used Ginzburg-Landau theory and estimated the value of lower critical field B_{c1} [75] when first vortices appear. For very thin films his non-analytic expression of B_{c1} can be roughly approximated as $(\lambda/d_{film})B_{c1}^{bulk}$. Thus B_{c1} can be greatly enhanced in very thin films up to magnetic fields of few tesla. For even thinner films ($\xi > d_{film}$) phase transition of second order occurs at B_{c1} and vortex phase does not occur. We have experimentally measured susceptibility of our sample and it was determined that B_{c1} is roughly (0.3 ± 0.1) T. So, B_{c1} is indeed greatly enhanced in comparison with its bulk value $B_{c1}^{bulk} = 9.3$ mT [76]. In magnetic fields just above B_{c1} vortices will arrange themselves in a row with vortices positioned in the middle of the film [69]. With increasing field more vortices are added in this row and, as a consequence, the distance between vortices decreases. At higher magnetic field $B_{c1}^{(2)}$ structural transition from one to two vortex rows occurs and for even higher magnetic fields more vortex rows appear if the geometry of the film allows that. Our film is very thin ($d_{film} \approx 3\xi$)[3], so only one row can be placed inside.

In non-zero magnetic field, both NbN film and R-cut sapphire are anisotropic, which leads to new features. Matrices in Yeh formalism are no longer block diagonal and it is no longer possible to decompose the beam into two different parts with their own eigenpolarisations - mode coupling occurs. This prevents us to treat transmission of linearly polarised beam parallel to and perpendicular with applied magnetic field independently.

Let us consider our experimental results, see figures 5.15-5.19. One can appreciate a nice agreement between transmission obtained while cooling and heating our sample in almost all cases. In the case of 0.58 THz transmission measurement beam with perpendicular polarisation had only small intensity and experimental data are very noisy. Original data were smoothed by adjacent averaging, see the top panel in figure 5.17. Transmission in low magnetic fields (2 tesla) deviates from its zero field values only slightly in all observed cases, ussually within experimental error, so it can not be reliably distinguished from the zero-field transmission. With increasing field transmission becomes more sensitive to the magnetic field and the direction of linear polarisation. Only transmission of 0.4037 THz

[3] ξ can be estimated from formula for upper critical field in Faraday configuration as $\xi(0) = \sqrt{\Phi_0/(2\pi B_{c2}(0))}$. Assuming value of $B_{c2}(0)$ roughly as 20 T coherence length becomes ≈ 4 nm.

laser line is insensitive to the direction of linear polarisation, see figure 5.19. On the other hand, huge differences in transmission for different polarisations have been observed, especially in the case of 0.58 and 0.65 THz line (figures 5.16 and 5.17) for the largest magnetic fields.

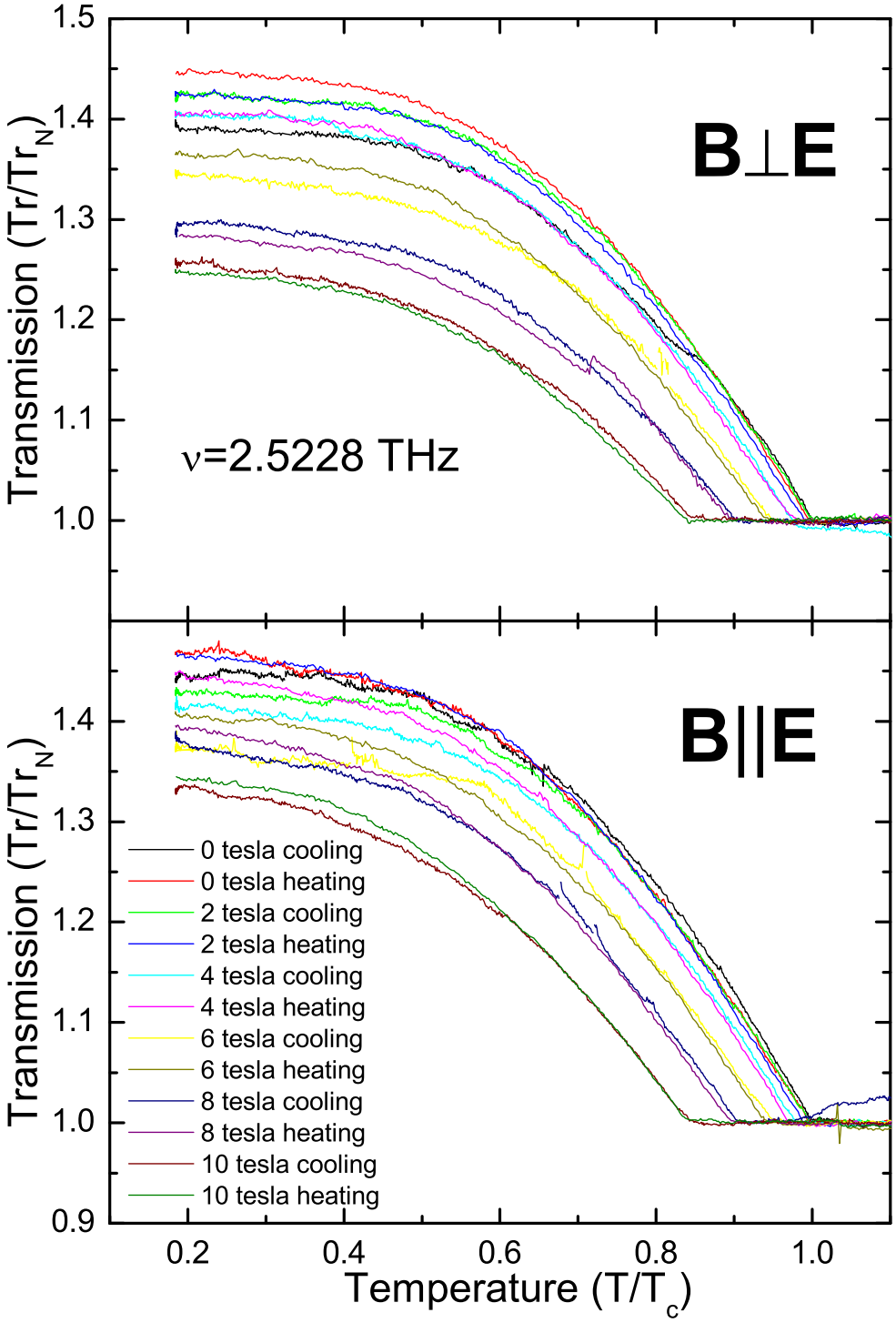

Figure 5.15: Transmission through NbN/sapphire sample in Voigt orientation for perpendicular to the applied magnetic field (top panel) and linear polarisation parallel with magnetic field (bottom panel), $\nu = 2.5228$ THz

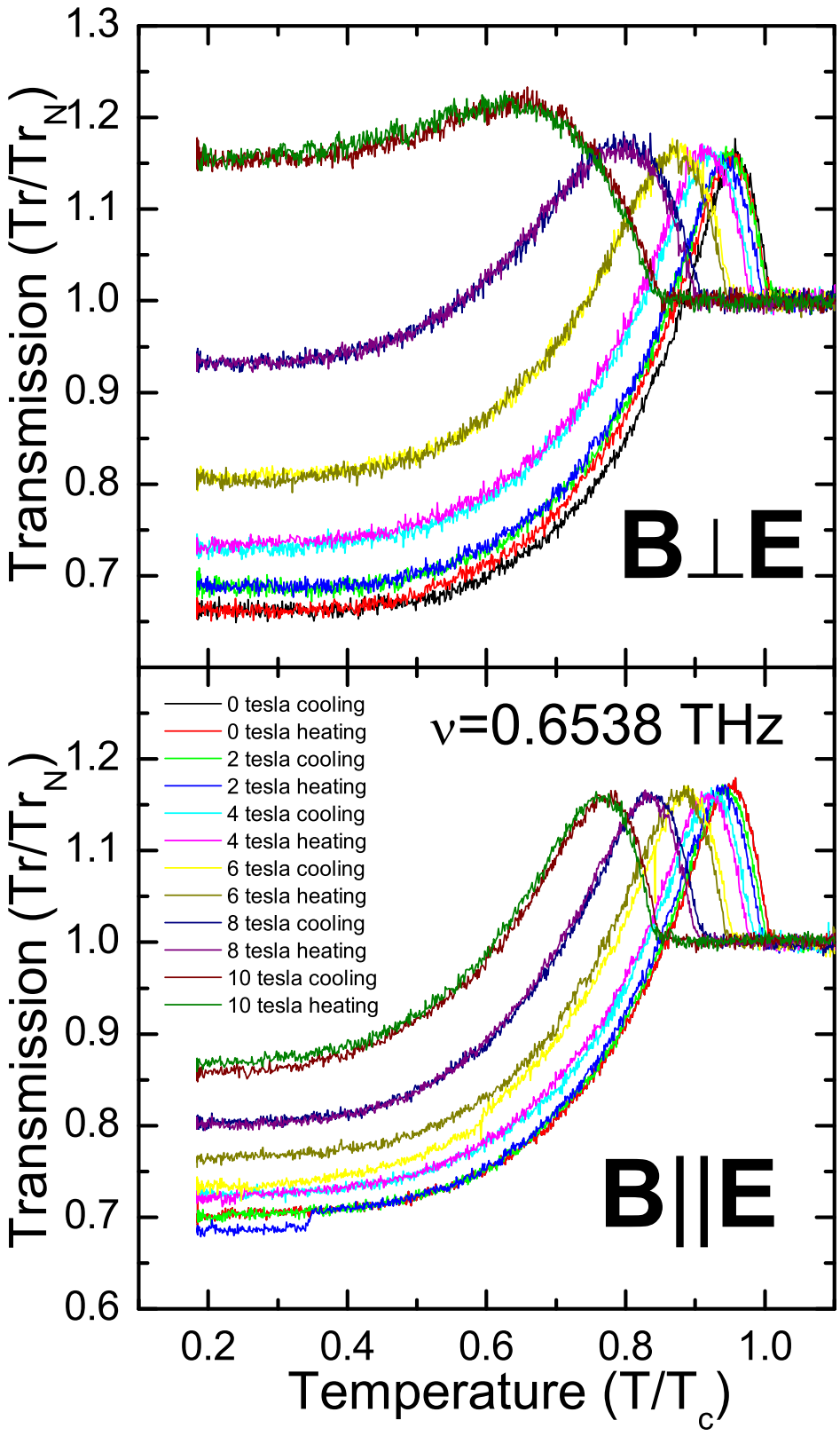

Figure 5.16: Transmission through NbN/sapphire sample in Voigt orientation for perpendicular to the applied magnetic field (top panel) and linear polarisation parallel with magnetic field (bottom panel), $\nu = 0.6538$ THz

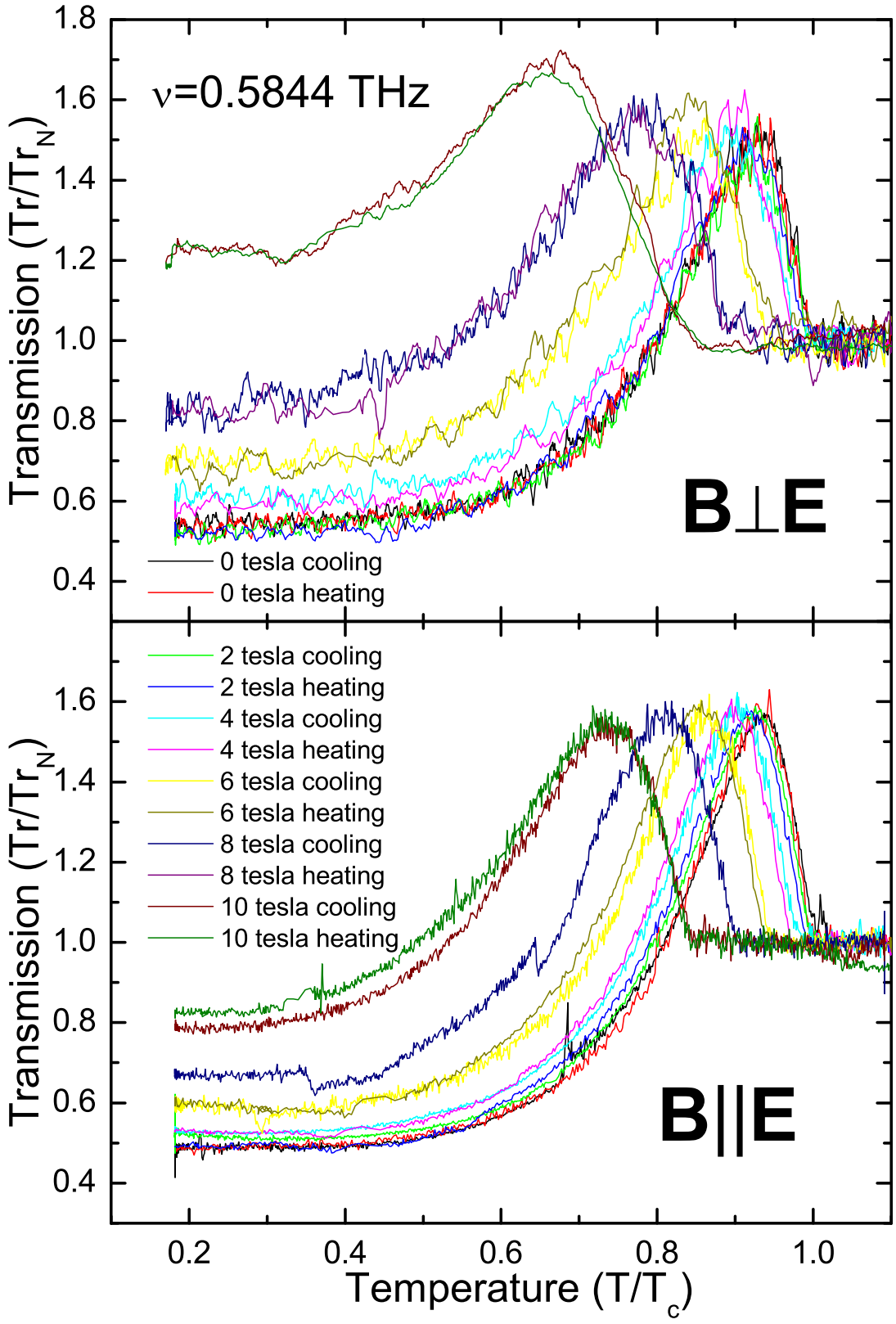

Figure 5.17: Transmission through NbN/sapphire sample in Voigt orientation for perpendicular to the applied magnetic field (top panel) and linear polarisation parallel with magnetic field (bottom panel), $\nu = 0.5844$ THz

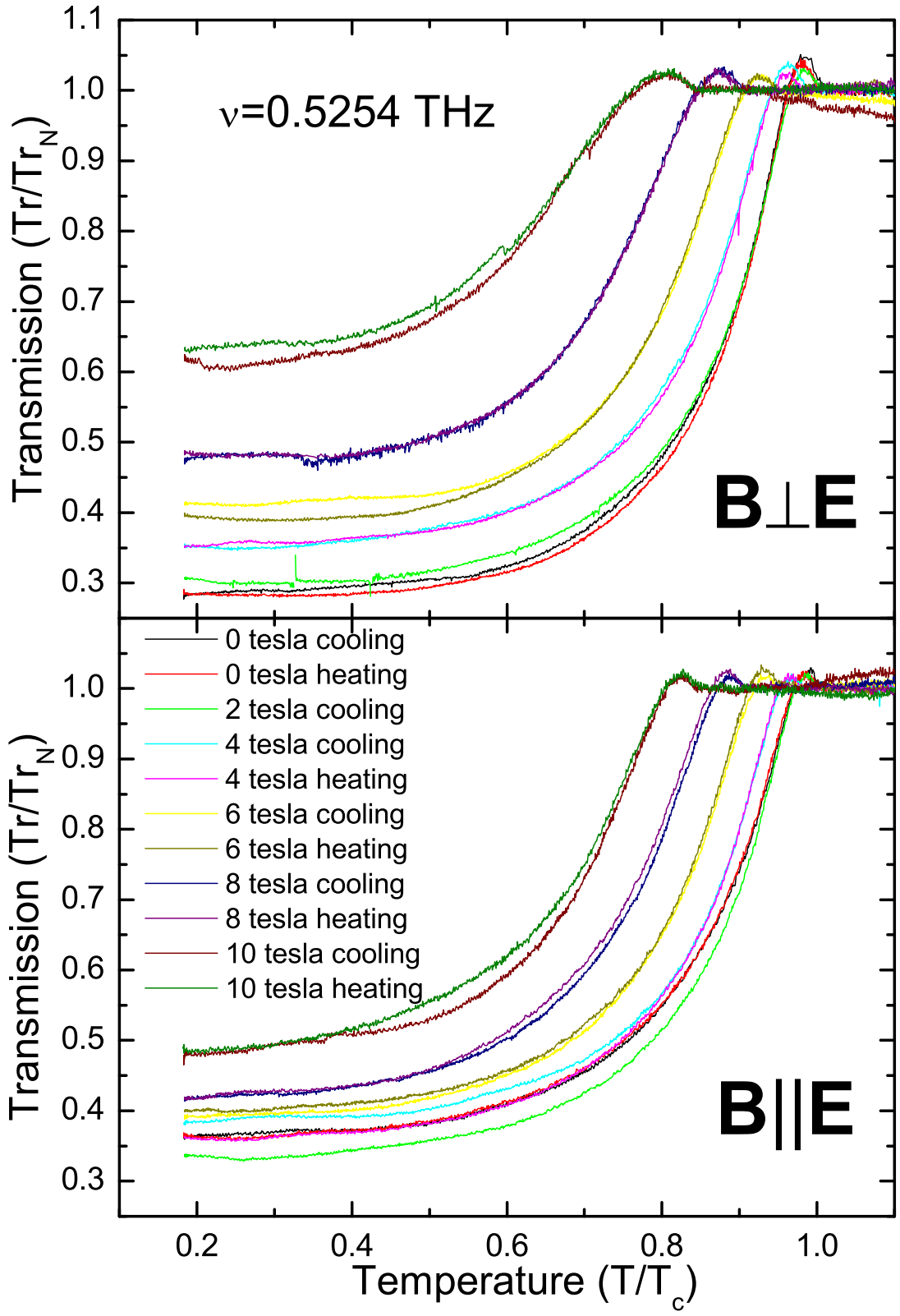

Figure 5.18: Transmission through NbN/sapphire sample in Voigt orientation for perpendicular to the applied magnetic field (top panel) and linear polarisation parallel with magnetic field (bottom panel), $\nu = 0.5254$ THz

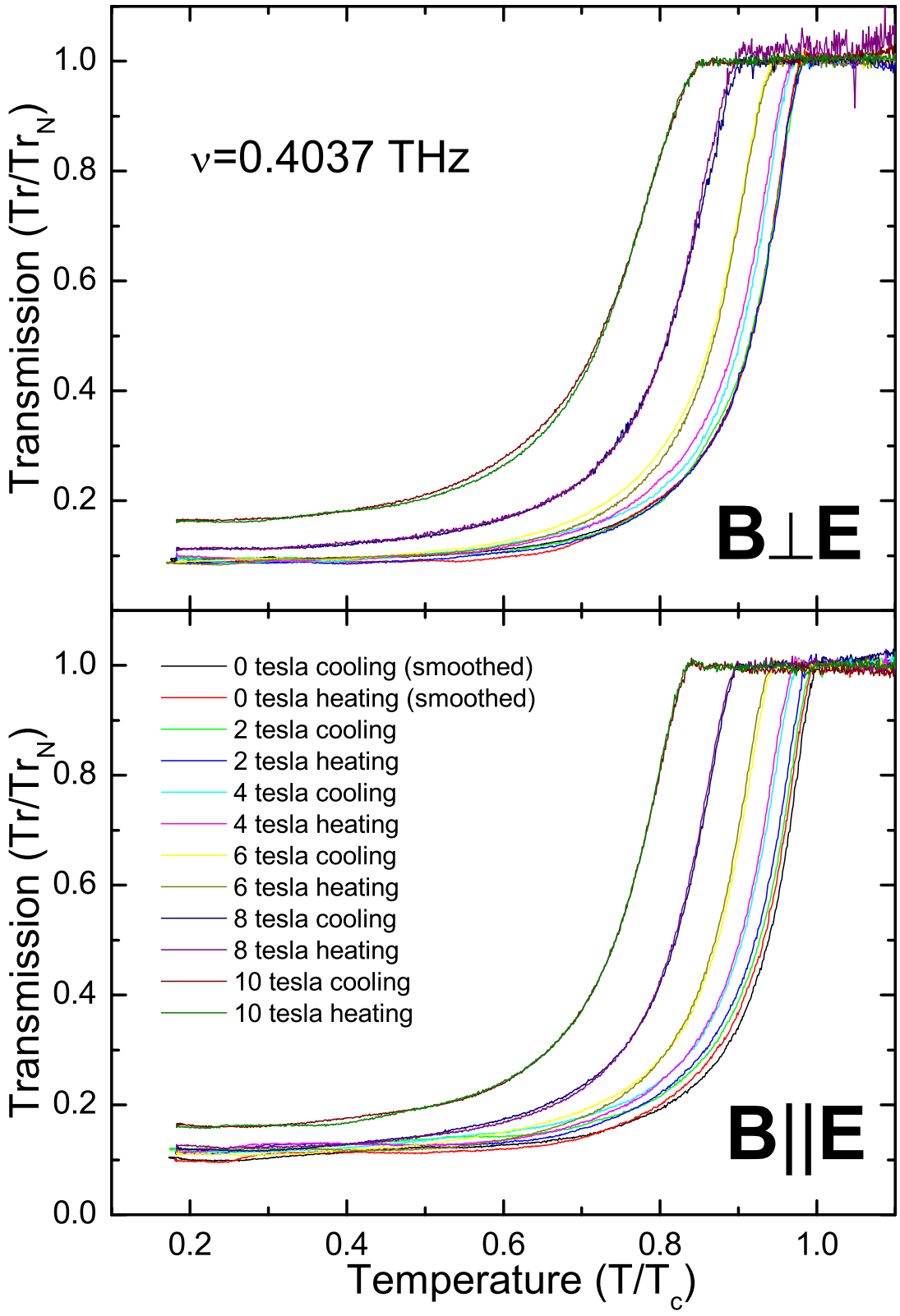

Figure 5.19: Transmission through NbN/sapphire sample in Voigt orientation for perpendicular to the applied magnetic field (top panel) and linear polarisation parallel with magnetic field (bottom panel), $\nu = 0.4037$ THz

The key variable in our model is $f_n(T)$. Once again, its temperature depen-

dence is obtained by extrapolation of our experimentally determined values of $T_c(B)$, see figure 5.20. Time dependent Ginzburg Landau theory predicts upper critical field in the thin film limit in parallel field [77] as:

$$B_{c2} = B_{c2}(0)\sqrt{1 - \frac{T}{T_c}}. \tag{5.11}$$

Our results are also well-described by this formula with $B_{c2}(0) = 25.1$ tesla. In the same paper [77], it was found that this formula well describes experimental data but upper critical field was not measured for temperatures below $T/T_c < 0.3$. Our experimental data can be equally well described by the equation 5.9, which can be used to extrapolate the value of the upper critical field at zero temperature: $B_{c2}(0) = 18.4$ tesla. Once again, it is clear that extrapolation of $B_{c2}(T)$ is an important issue.

Even though that there are some doubts concerning values of $f_n(T)$ in the low temperature region we can compare our phenomenological model using EMA model and Drew formula 5.11 with our experimental data. Numerical calculations for transmission of the beam with the parallel polarisation are presented in figure 5.21. These theoretical curves capture all esential features of the experimental data - with the applied magnetic field the thermal peaks become diminished and, almost constant transmission at the low temperatures shifts in agreement with the experiment. Note that vortex dynamics influence transmission even in this case due to the mode coupling which is indicated by dashed lines. However, all these remarks are valid only on the qualitative level and quantitative agreement is rather poor. The situation for perpendicular polarisation is even less encouraging, see figure 5.22. Here the effective medium approximation fails to describe experimentally observed transmission even on qualitative level.

However, dotted lines indicate large contribution due to the vortex motion according Coffey-Clem model. It improves the agreement of the theoretical model with the experiment for 2.52 THz, 0.65 THz and 0.58 THz laser lines while the contribution for 0.54 THz and 0.40 THz laser line leads to much higher transmission than that observed in experiments. Using the MGT model or different dependence of $B_{c2}(T)$ (eq. 5.9) - with or without vortex contribution - does not provide better description of experimental data. Note that in case of 2.52 THz Coffey-Clem model was not applied since the limit of its applicability is $h\nu > 2\Delta(0)$ and quasiparticles are excited even at zero temperature.

To conclude this section, transmission in Voigt configuration was systematically measured for 5 different frequencies up to 10 tesla for two fundamental linear polarisations - parallel with and perpendicular to the direction of applied magnetic field. Substantial difference between transmission for these two polarisations is observed. In the case of parallel polarisation experimental data are partially explained by our phenomenological model while in the case of perpendicular polarisation phenomenological model fails to describe experimental data without assuming contribution from vortex motion. Although Coffey-Clem contribution modifies the transmission substantialy and improves the agreement with some of our experimental data, overall quantitative agreement was not reached. In future experiments, film deposited on anisotropic substrate should be avoided so the transmission of parallel and perpendicular polarisation can be treated independently. Let's stress that majority of superconducting film parameters, such as

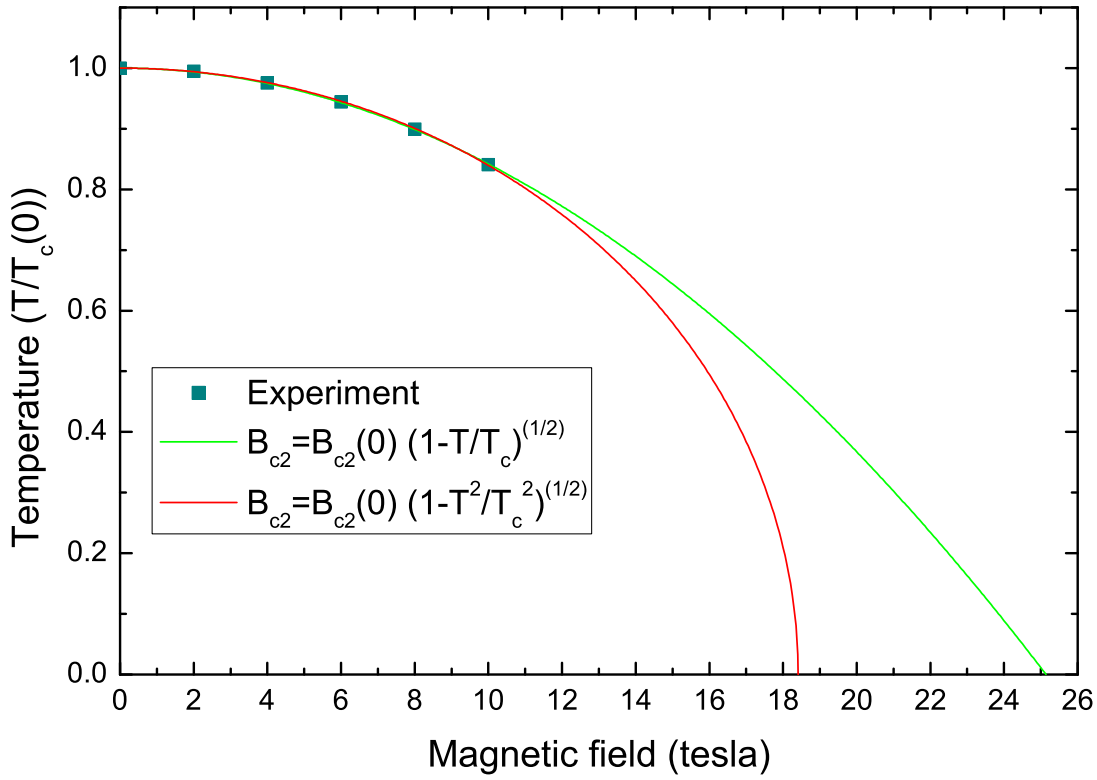

Figure 5.20: Critical temperature of NbN #383 sample versus applied magnetic field

T_c or B_{c2}, are the same for both polarisation. The idea is to obtain full, both qualitative and quantitative, agreement with the experimental data for parallel polarisation before investigating more complex case of the transmission of perpendicularly polarised beam. Effects due to the vortex motion are well pronounced in that case so vortex dynamics can be studied.

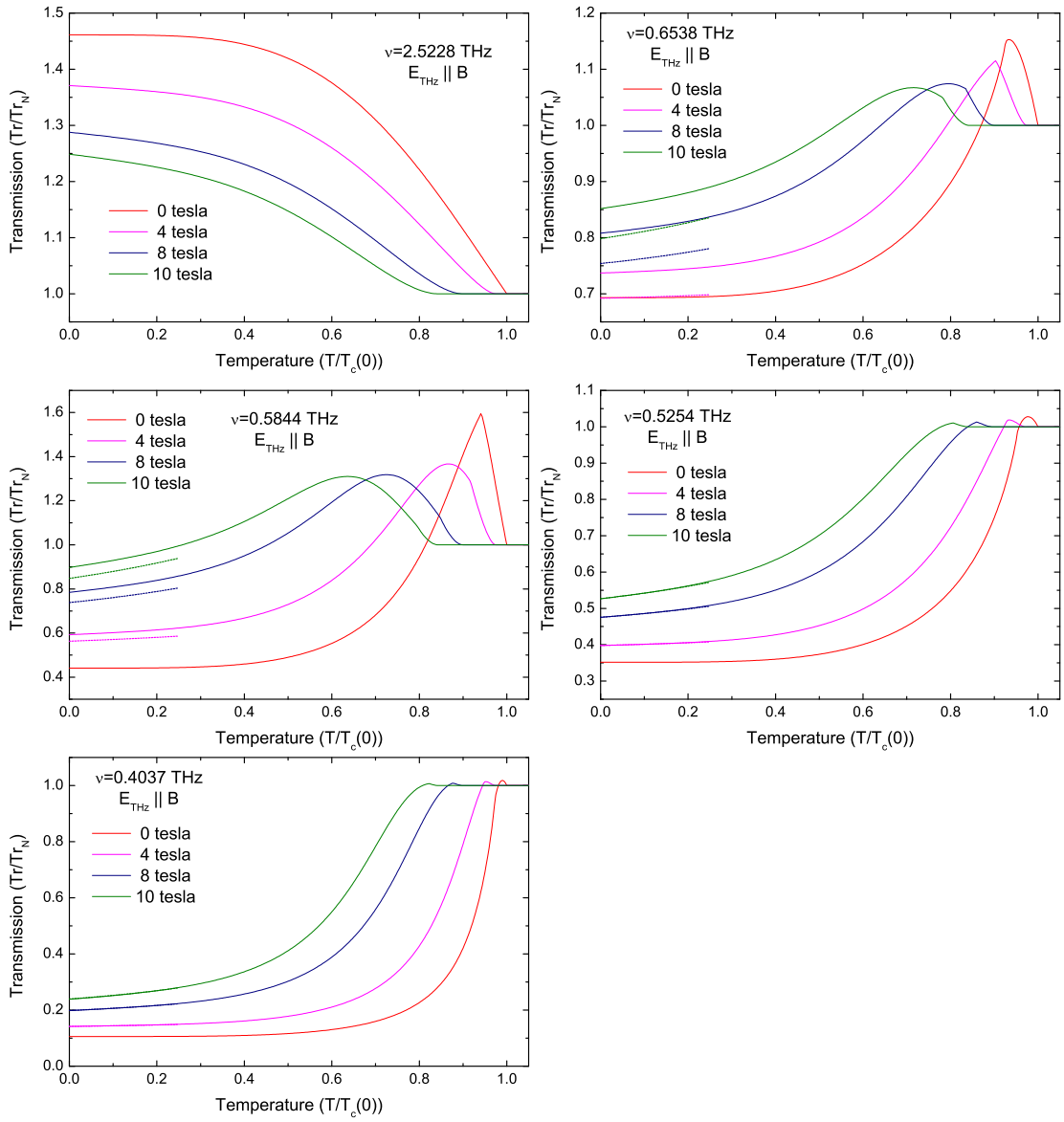

Figure 5.21: Numerical calculation of transmission through NbN/sapphire sample without vortex motion (solid lines) and with Coffey-Clem contribution (dashed lines at low temperatures) in Voigt orientation for linear polarisation parallel with applied magnetic field.

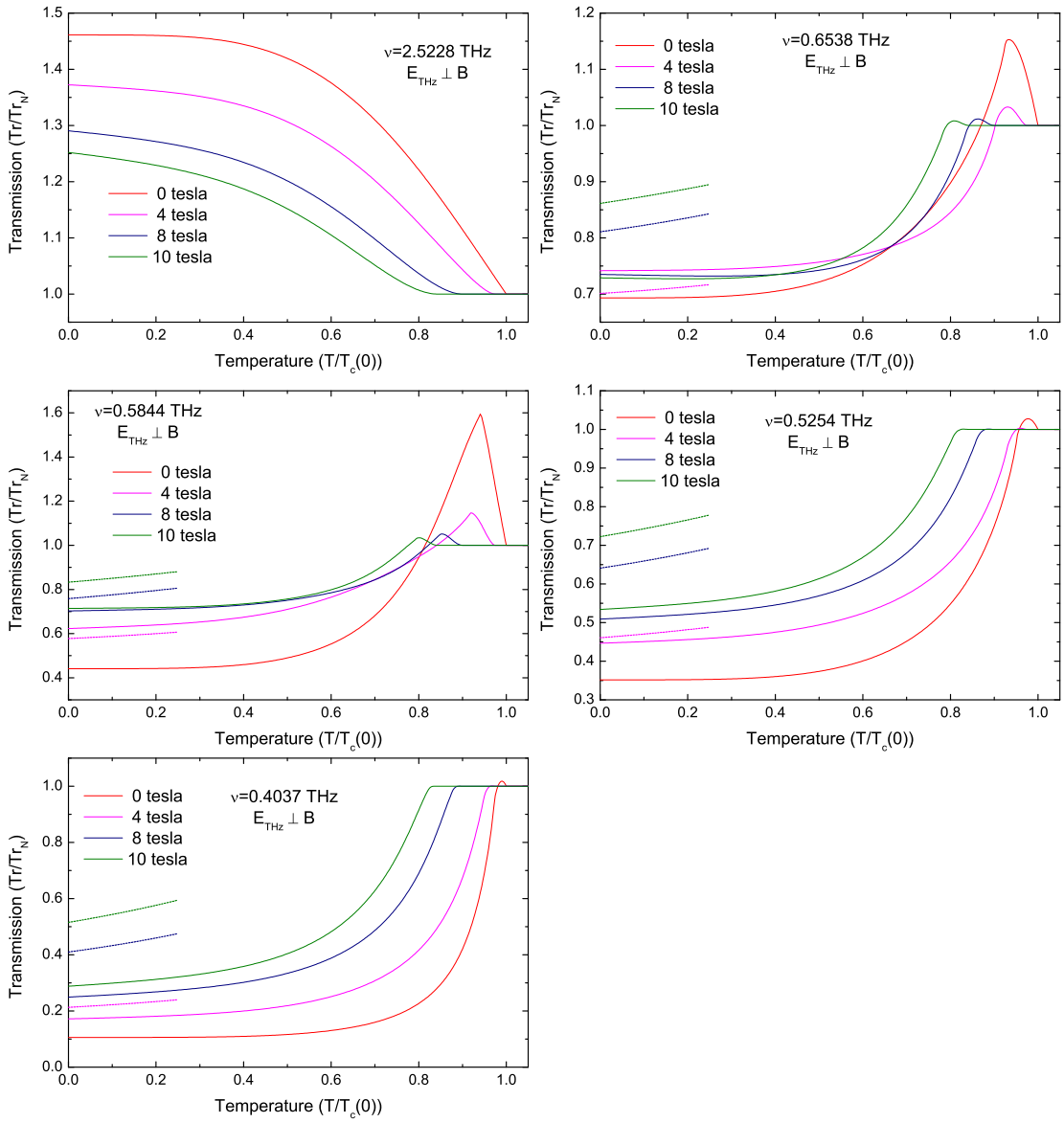

Figure 5.22: Numerical calculation of transmission through NbN/sapphire sample without vortex motion (solid lines) and with Coffey-Clem contribution (dashed lines at low temperatures) in Voigt orientation for linear polarisation perpendicular to applied magnetic field.

6. Conclusions

We have systematically measured magneto-optical properties of thin superconducting NbN films in THz range in various magnetic fields (Faraday and Voigt geometry) up to 10 tesla by means of laser thermal spectroscopy. Our experimental setup enables us to conveniently measure temperature dependent transmission at fixed frequencies. In case of Voigt geometry, wire-grid polariser is conveniently used to study optical response in two fundamental configurations - with polarisation parallel with and perpendicular to the vortex axes.

Optical properties of NbN films in zero magnetic field are well-described by Zimmerman's model [21]. The optical gap was found to be $4.16\,k_BT_c$ for all measured NbN samples which suggests applicability of strong-coupling approximation.

In order to obtain quantitative agreement with experimental data for the Beňačka sample we described the real sample as a mixture of superconductors with different critical temperatures T_c and corresponding optical gaps. This view is supported by the dc electric resistance measurement showing broad transition from normal to superconducting state.

In the case of NbN/sapphire sample, full quantitative agreement of theoretical curves with experimental data was achieved assuming a sharp superconducting transition. Numerical calculations are in case of anisotropic substrate very sensitive to values of ordinary and extraordinary refractive indices. To achieve the best agreement between calculated and experimental transmission data, the values of both ordinary and extraordinary refractive indices of substrate were slightly refined within experimental errors of their independent determinations.

Complex conductivity of NbN thin film deposited on highly resistive Si was measured by time-domain terahertz spectroscopy. While the former experiments tackle indirectly temperature dependence of complex conductivity, Time domain THz spectroscopy determines complex conductivity over THz region from 0.25 THz to 2.1 THz at fixed temperature. In these experiments temperature was not reliably determined but numerical calculations with temperature as the only free parameter showed reasonably good agreement with this experiment.

In applied magnetic field, vortices greatly influence properties of superconductors including their THz conductivity. We utilized simple Clem model in which the rather complex structure of vortex is approximated as a cylinder of normal state material with radius proportional to the coherence length ξ surrounded by fully superconducting environment. ξ is of order of few nanometers, thus much smaller than any wavelength exploited in experiments. Under these conditions the long-wavelength limit is justified and the superconducting film, inhomogenous at microscopic scale, can be thought of as homogeneous with an effective conductivity. Two models - Maxwell-Garnett theory (MGT) and effective medium approximation (EMA) - consider effects of local electric field and we used them to describe optical properties of superconductor in mixed phase. In all cases, EMA seems to work slightly better than MGT.

Although the theory of effective medium is capable of capturing essential features of the measured data, further improvement can be achieved by taking into account vortex motion in the frame of Coffey-Clem model. This model is limited

to low temperatures and frequencies below the optical gap. The key quantity for any effective medium theory is volume fraction of inclusions, in our case magnetic field and temperature dependent vortex core fraction, $f_n \simeq B/B_{c2}(T)$. Our NbN samples exhibit high upper critical magnetic field $B_{c2}(0)$, far above the maximum magnetic field accessible in our experiment and, as a consequence, its low temperature values had to be extrapolated.

In Faraday orientation, upper critical magnetic field of the Beňačka sample is reasonably well described by $B_{c2} = B_{c2}(0)(1-T^4/T_c^4(0))$ with $B_{c2}(0) = 10.6$ tesla and both EMA and MGT describe transmission of 0.4037 THz line through the Beňačka sample well. By utilizing EMA with Coffey-Clem correction for vortex dynamics, excellent agreement with experimental data is reached. Transmission through the NbN #383 sample is substantially influenced by anisotropic behavior of its birefringent sapphire substrate. Linear polarisation of the beam was not specified by polariser but we were able to determine polarisation from zero field transmission measurement. Numerical calculations describe transmission experiments performed at several discrete frequencies well but on the qualitative level only, since we were unable to reliably extrapolate B_{c2}. Previous case of the Beňačka sample and its numerical analysis lead us to believe that quantitative agreement might be possible if $B_{c2}(T)$ is better determined over the entire temperature interval from T_c to zero.

In Voigt orientation, the most interesting experimental data have been obtained. Transmissions for linear polarisation parallel with and perpendicular to the vortex axes exhibit very different behavior with increasing magnetic field. Due to anisotropic nature of substrate these two cases cannot be treated separately due to the mode coupling. Again, extrapolation of $B_{c2}(T)$ to low temperatures is tricky and limits our analysis. Nevertheless, we were able to obtain fairly good semi-quantitative description of transmission of the parallel polarised beam. EMA fails to describe transmission of perpendicularly polarised beam even on the qualitative level. Our analysis suggests that Coffey-Clem contribution due to vortex motion is large and some of our experimental data are reasonably described by it while for other data this correction fails.

In the near future, we plan to systematically measure transmission of NbN films deposited on MgO isotropic substrate utilizing laser thermal spectroscopy and time-domain terahertz spectroscopy for both Faraday and Voigt geometries. Utilizing both experimental techniques should solve various problems mentioned in the text, especially determination of f_n, and it will enable comparison of results of these methods by measuring the same sample. Hopefully, phase sensitive setup utilizing Mach-Zender interferometer [32] will be available in FIRM laboratory.

List of tables

List of symbols used in thesis

Although all variables are introduced in text, alphabetically ordered list of variables is given for clarity. In thesis we tried to label variables uniquely but in some cases we could not avoid using the same letter for various variables. In our opinion introducing unconventional notation would be even more confusing. We believe that reader will not have difficulties in understanding our notation.

A_σ ..... magnitude of corresponding partial wave

α ..... absorption coefficient

α ..... transition rate

α, β ..... coefficients of Taylor expansion in Ginzburg-Landau theory

α ..... the angle between direction of linear polarisation corresponding to the extraordinary ray and polarisation used in experiment

B ..... magnetic field

B_c ..... thermodynamical critical magnetic field

B_{c1} ..... lower critical magnetic field

B_{c2} ..... upper critical magnetic field

c ..... speed of light in vacuum

c_{ks}, c_{ks}^* ..... annihilation, respectively creation, operator

D ..... dynamical matrix

δ ..... phase

Δ ..... the energy gap

e ..... elementary charge (positive)

E ..... energy

$\mathcal{E}$ ..... electric component of electromagnetic wave

ξ ..... single-particle energy relative to the Fermi energy

ξ ..... coherence length

ε_0 ..... permittivity of vacuum

$\tilde{\varepsilon}$ ..... complex permittivity (relative)

$\tilde{\varepsilon}_1$ ..... real part of $\tilde{\varepsilon}$

$\tilde{\varepsilon}_2$ ..... imaginary part of $\tilde{\varepsilon}$

F ..... coherence factor

f_k ..... Fermi-Dirac distribution function

f_n ..... vortex cores volume fraction

$\mathcal{F}$ ..... free-energy density

Φ_0 ..... quantum of magnetic flux

φ ..... angle between c-axis of sapphire and the surface normal, $\varphi = 57.6°$

$\gamma^*_{k\uparrow}, \gamma_{k\uparrow}$ ..... Bogoljubov-Valantin creation, respectively annihilation, operator

$\mathcal{H}$ ..... magnetic field strength

H ..... hamiltonian

h ..... microscopic magnetic field

h ..... Planck constant

$\hbar$ ..... Planck constant $(h/2\pi)$

i ..... complex unit

I ..... intensity

k_B ..... Boltzmann constant

k ..... quasi-momentum

$\mathbf{k}$ ..... wavevector

$\mathbf{k_F}$ ..... Fermi wavevector

κ ..... imaginary part of refractive index $\tilde{n}$

κ ..... ratio between the penetration depth and the coherence length $\kappa = \lambda/\xi$

l ..... mean free path

λ ..... penetration depth

λ ..... wavelength

m_0 ..... mass of electron

μ_0 ..... permeability of vacuum

M ..... transfer matrix of entire multilayer system

$\tilde{n}$ ..... complex refractive index

N ..... number of electrons per unit volume

$N(0)$ ..... density of states at Fermi surface

n ..... describes the n-th layer

n ..... real part of $\tilde{n}$

ν ..... frequency

ψ ..... order parameter

ψ' ..... normalized order parameter $\psi' = \psi/\psi_\infty$

P ..... propagation matrix

$\mathbf{p}$ ..... eigenpolarisation vector

$\mathbf{r}$ ..... position vector

r_0 ..... Pippard coherence length

$r^{(0,1)}$ ..... reflection amplitude coefficient for interface between medium 0 and medium 1

$\mathcal{R}$ ..... reflection intensity coefficient

$\mathbf{s}$ ..... unit vector in the direction of propagation

s ..... spin variable

$\mathbf{S}$ ..... Poynting vector

σ ..... conductivity

σ ..... (subscript) summation index

$\tilde{\sigma}$ ..... complex conductivity

σ_1 ..... real part of $\tilde{\sigma}$

σ_2 ..... imaginary part of $\tilde{\sigma}$

$\tilde{\sigma}_{EMA}$ ..... complex conductivity following effective medium approximation

$\tilde{\sigma}_{MGT}$ ..... complex conductivity following Maxwell-Garnett theory

$\tilde{\sigma}^{vd}$ complex conductivity including vortex dynamics according to Coffey-Clem model

$\tilde{\sigma}_{vd}$ ..... complex conductivity Bardeen Stephen

t ..... time

$t^{(0,1)}$ ... transmission amplitude coefficient for interface between medium 0 and medium 1

$\mathcal{T}$ ..... transmission intensity coefficient

$T(n-1,n)$ ..... transfer matrix

T ..... temperature

T_c ..... critical temperature

t ..... reduced temperature $t = T/T_c$

τ ..... momentum scattering time

ϑ angle of projection sapphire c-axis into the surface plane with x-axis, $\vartheta = 45°$

U ..... internal energy density

u_k, v_k ..... coefficients of BCS wavefunction

W ..... one-electron matrix element

ω ..... angular frequency

ω_p ..... plasma frequency

ω_c ..... maximum phonon frequency

x, y, z ..... Cartesian coordinates

Z_0 ..... impedance of free space

Bibliography

[1] M. Šindler, R. Tesař, J. Koláček, L. Skrbek, and Z. Šimša, *Far-infrared transmission of a superconducting NbN film*, Phys. Rev. B **81**, 184529 (2010).

[2] R. Tesař, J. Koláček, Z. Šimša, M. Šindler, L. Skrbek, K. Il'in, and M. Siegel, *Terahertz transmission of NbN superconductor thin film*, Physica C **470**, 932-934 (2010).

[3] R. Tesař, M. Šindler, K. Il'in, J. Koláček, M. Siegel, and L. Skrbek, *Terahertz thermal spectroscopy of a NbN superconductor*, Phys. Rev. B **84**, 132506 (2011).

[4] M. Šindler, R. Tesař, J. Koláčcek, and L. Skrbek, *Interpretation of transmission through type II superconducting thin film on dielectric substrate as observed by laser thermal spectroscopy*, Physica C (accepted to publication).

[5] B. A. Saleh, M. C. Teich, *Základy fotoniky*, Matfyzpress, Praha, 1994.

[6] P. Malý, *Optika*, Karolinum, Praha, 2008.

[7] A. Schwartz, M. Dressel, A. Blank, T. Csiba, G. Grüner, A. A. Volkov, B. P. Gorshunov, and G. V. Kozlov, *Resonant techniques for studying the complex electrodynamic response of conducting solids in the millimeter and submillimeter wave spectral range*, Rev. Sci. Instrum. **66**, 2943-2953 (1995).

[8] M. Born, E. Wolf, *Principles of Optics*, Pergamon, Oxford, 1975.

[9] Ch. Kittel, *Úvod do fyziky pevných látek*, Academia, Praha, 1985.

[10] M. Tinkham, *Introduction to Superconductivity*, Dover Publications, New York, 2004.

[11] M. Fox, *Optical Properties of Solids*, New York: Oxford University Press, 2001.

[12] N. W. Ashcroft, N. D. Mermin, *Solid State Physics*, Saunders College Publishing, Philadelphia, 1976.

[13] L. N. Cooper, *Bound Electron Pairs in a Degenerate Fermi Gas*, Phys. Rev. **104**, 1189-1190 (1956).

[14] J. Bardeen, L. N. Cooper, and J. R. Schrieffer, *Theory of superconductivity*, Phys. Rev. **108**, 1175-1204 (1957).

[15] H. Frohlich, *Theory of the Superconducting State. I. The Ground State at the Absolute Zero of Temperature*, Phys. Rev. **79**, 845-856 (1950).

[16] J. Celý, *Kvazičástice v pevných látkách*, VUTIUM, Brno, 2004.

[17] J. F. Annett, *Superconductivity, Superfluids and Condensates*, New York: Oxford University Press, 2004.

[18] T. P. Sheahen, *Rules for the Energy Gap and Critical Field of Superconductors*, Phys. Rev. **149**, 368-370 (1966).

[19] J. R. Schrieffer, *Theory of Superconductivity*, New York : W. A. Benjamin, 1967.

[20] D. C. Mattis, and J. Bardeen, *Theory of the Anomalous Skin Effect in Normal and Superconducting Metals*, Phys. Rev. **111**, 412-417 (1958).

[21] W. Zimmermann, E.H. Brandt, M. Bauer, E. Seider, and L. Genzel, *Optical conductivity of BCS superconductors with arbitrary purity*, Physica C **183**, 99-104 (1991).

[22] S. B. Nam, *Theory of Electromagnetic Properties of Superconducting and Normal Systems. I*, Phys. Rev. B **156**, 470-486 (1967).

[23] S. B. Nam, *Theory of Electromagnetic Properties of of Strong-Coupling and Impure Superconductors. II*, Phys. Rev. B **156**, 487-493 (1967).

[24] L. Leplae, *Derivation of an expression for the conductivity of superconductors in terms of the normal-state conductivity*, Phys. Rev. B **27**, 1911-1912 (1983).

[25] N. E. Bickers, D. J. Scalapino, R. T. Collins, and Z. Schlesinger, *Infrared conductivity in superconductors with a finite mean free path*, Phys. Rev. B **42**, 67-75 (1990).

[26] Y. Ikebe, R. Shimano, M. Ikeda, T. Fukumura, and M. Kawasaki, *Vortex dynamics in a NbN film studied by terahertz spectroscopy*, Phys. Rev. B **79**, 174525 (2009).

[27] K. Steinberg, M. Scheffler, and M. Dressel, *Quasiparticle response of superconducting aluminum to electromagnetic radiation*, Phys. Rev. B **77**, 214517 (2008).

[28] H. J. Lee, J. H. Jung, K. W. Kim, M. W. Kim, T. W. Noh, Y. J. Wang, W. N. Kang, Eun-Mi Choi, and Hyeong-Jin Kim, *Complicated nature of the gap in MgB_2: Magnetic-field-dependent optical studies*, Phys. Rev. B **65**, 224519 (2002).

[29] Yun-Shik Lee, *Principles of Terahertz Science and Technology*, Springer, New York, 2009.

[30] V. L. Ginzburg and L. D. Landau, *On the Theory of Superconductivity*, Zh. Eksperimen. i. Teor. Fiz. **20**, 1064 (1950).

[31] A. A. Abrikosov, *On the magnetic properties of superconductors of the second group*, Zh. Eksperimen. i. Teor. Fiz. **32**, 1442-1452 (1957).

[32] B. Gorshunov, A. Volkov, I. Spektor, A. Prokhorov, A. Mukhin, M. Dressel, S. Uchida, and A. Loidl, *Terahertz BWO-Spectroscopy*, International Journal of Infrared and Millimeter Waves **26**, 1217-1240 (2005).

[33] A. A. Volkov, Y. G. G, Goncharov. V. Kozlov, S. P. Lebedev, and A. M. Prokhorov, *Dielectric measurements in the submillimeter wavelength region*, Infrared Phys. **25**, 369-373 (1985).

[34] H. Shibata, S. Kimura, S. Kashiwaya, S. Ueno,M. Koyanagi, T. Masao, N. Terada, E. Kawate, and Y. Tanaka, *Far-Infrared Reflectance and Transmittance Studies of YBa2Cu3O7-x Single-Crystal Thin Films*, Jap. J. of Appl. Phys. **40**, 3163-3170 (2001).

[35] G. D. Holah, and S. Perkowitz, *Far infrared laser thermal spectroscopy of superconductors*, International Journal of Infrared and Millimeter Waves **2**, 581-586 (1981).

[36] S. W. McKnight, B. L. Bean, and S. Perkowitz, *Far-infrared laser spectroscopy of V_3Si*, Phys. Rev. B **19**, 1437-1442 (1979).

[37] D. E. Oates, A. C. Anderson, C. C. Chin, J. S. Derov, G. Dresselhaus and M. S. Dresselhaus, *Surface-impedance measurements of superconducting NbN films*, Phys. Rev. B **43**, 7655-7663 (1991).

[38] R. Grimes, *Far Infrared Studies of III-V and II-VI 2 and 3 Dimensional Semiconductors*, Doctoral thesis, University of Nottingham, 1990.

[39] Far-infrared laser, model 295, Edinburgh Instruments.

[40] Superconducting Magnetic System, Operator's Handbook, Oxford Instruments, 2006.

[41] Silicon bolometer IFS 66V/S, Infrared Laboratories, 2001.

[42] ITC503 Temperature controller, Operator's Handbook, Oxford Instruments, 2005.

[43] P. U. Jepsen, D. G. Cooke, and M. Koch, *Terahertz spectroscopy and imaging - Modern techniques and applications*, Laser Photon. Rev. **5**, 124-166 (2011).

[44] R. D. Averitt and A. J. Taylor, *Ultrafast optical and far-infrared quasiparticle dynamics in correlated electron materials*, J. Phys.: Condens. Matter **14**, 1357 - 1390 (2002).

[45] A. Dreyhaupt, S. Winnerl, T. Dekorsy, and M. Helm, *High-intensity terahertz radiation from a microstructured large-area photoconductor*, Appl. Phys. Lett. **86**, 121114 (2005).

[46] A. Nahata, A. S. Welling, and T. F. Heinz, *A wideband coherent terahertz spectroscopy system using optical rectification and electro-optic sampling*, Appl. Phys. Lett. **69**, 2321 (1996).

[47] L. Kang, B. B. Jin, X. Y. Liu, X. Q. Ji J. Chen, Z. M. Ji, W. W. Xu, P. H. Wu, S. B. Mi, A. Pimenov, Y. J. Wu, and B. G. Wang, *Suppression of superconductivity in epitaxial NbN ultrathin films*, J. of Appl. Physics **109**, 033908 (2011).

[48] A. Semenov,B. Günther, U. Böttger, H.-W. Hübers,H. Bartolf, A. Engel, A. Schilling, K. Il'in, M. Siegel,R. Schneider, D. Gerthsen, and N. A. Gippius, *Optical and transport properties of ultrathin NbN films and nanostructures*, Phys. Rev. B **80**, 054510 (2009).

[49] R. Tesař, J. Koláček, E. Kawate, Š. Beňačka, Š. Gaži, and Z. Šimša, Far-infrared thermal spectroscopy of low-T_c and high-T_c superconductor films, Supercond. Sci. Technol. **16**, 916-921 (2003).

[50] E. D. Palik, *Handbook of Optical Constants of Solids*, Academic Press, New York, 1985.

[51] E. V. Loewenstein, D. R. Smith, and R. L. Morgan, *Optical Constants of Far Infrared Materials.2:Crystalline Solids*, Appl. Opt. **12**, 398-406 (1973).

[52] W. B. Cook and S. Perkowitz, *Temperature dependence of the far-infrared ordinary-ray optical constants of sapphire*, Appl. Opt. **24**, 1773-1775 (1985).

[53] F. Abelès, *Recherche sur la propagation des ondes electromagnétiques sinusoidales dans les milieux stratifiés. Applications aux couches minces*, Ann. Physique (Paris) **5**, 596-640, 706-782 (1950).

[54] P. Yeh, *Electromagnetic propagation in birefrigent layered media*, J. Opt. Soc. Am. **69**, 742-756 (1979).

[55] P. Yeh, *Optics of anisotropic layered media: A new* 4×4 *matrix algebra*, Surface Science **96**, 41-53 (1980).

[56] M. Mansuripur, *Analysis of multilayer thin-film structures containing magneto-optic and anisotropic media at oblique incidence using 2 X 2 matrices*, J. App. Phys. **67**, 6466-6475 (1990).

[57] O. S. Heavens, *Optical Properties of Thin Solid Films*, Dover, New York, 1991.

[58] S. D. Brorson, R. Buhleier, I. E. Trofimov, J. O. White, Ch. Ludwig, F. F. Balakirev,H.-U. Habermeier, and J. Kuhl, *Electrodynamics of high-temperature superconductors investigated with coherent terahertz pulse spectroscopy*, J. Opt. Soc. Am. B **13**, 1979-1993 (1996).

[59] A. V. Pronin,M. Dressel, A. Pimenov, A. Loidl,I. V. Roshchin, and L. H. Greene, *Direct observation of the superconducting energy gap developing in the conductivity spectra of niobium*, Phys. Rev. B **57**, 14416 (1998).

[60] T. C. Choy, *Effective Medium Theory Principles and Applications*, Oxford University Press, New York,1999.

[61] M. S. Pambianchi, S. M. Anlage, E. S. Hellman, E. H. Hartford Jr., M. Bruns, and S. Y. Lee, *Penetration depth, microwave surface resistance, and gap ratio in NbN and* $Ba_{1-x}K_xBi03$ *thin films*, Appl. Phys. Lett. **64**, 244-246 (1994).

[62] M. Beck, M. Klammer, S. Lang, P. Leiderer, V. V. Kabanov, G. N. Goltsman, and J. Demsar, *Energy-Gap Dynamics of Superconducting NbN Thin Films Studied by Time-Resolved Terahertz Spectroscopy*, Phys. Rev. Lett. **107**, 177007 (2011).

[63] D. Karecki, R. E. Peña, and S. Perkowitz, *Far-infrared transmission of superconducting homogeneous NbN films: Scattering time effects*, Phys. Rev. B **25**, 1565-1571 (1982).

[64] J. R. Clem, *Simple Model for the Vortex Core in a Type II Superconductor*, Journal of Low Temperature Physics **18**, 427-434 (1975).

[65] G. L. Carr, S. Perkowitz, D. B. Tanner, *Far infrared properties of inhomogeneous material*, Infrared and millimeter waves, Vol. 13, pp. 171-263, Orlando, FL, Academic Press, Inc. (1985).

[66] S. Skalski, O. Betbeder-Matibet, and P. R.Weiss, *Properties of Superconducting Alloys Containing Paramagnetic Impurities*, Phys. Rev. **136**, 1500-1518 (1964).

[67] X. Xi, J. Hwang, C. Martin, D. B. Tanner, and G. L. Carr, *Far-Infrared Conductivity Measurements of Pair Breaking in Superconducting* $Nb_{0.5}Ti_{0.5}N$ *Thin Films Induced by an External Magnetic Field*, Phys. Rev. Lett. **105**, 257006 (2010).

[68] I. Rychetský, and J. Petzelt, *Dielectric Spectra of Grainy High-Permittivity Materials*, Ferroelectrics **303**, 137 - 140 (2004).

[69] D. A. Luzhbin, *Structure of the Abrikosov Vortex Lattice in a Thin Superconducting Film in a Parallel Magnetic Field*, Physics of the Solid State **43**, 1823-1826 (2001).

[70] M. W. Coffey, and J. R. Clem, *Unified theory of effects of vortex pinning and flux creep upon the rf surface impedance of type-II superconductors*, Phys. Rev. Lett. **67**, 386-389 (1991).

[71] J. Bardeen and M. J. Stephen, *Viscosity of Type-II Superconductors*, Phys. Rev. **140**, 1197-1207 (1965).

[72] Pei-Jen Lin, and P. Lipavský, *Time-dependent Ginzburg-Landau theory with floating nucleation kernel: Far-infrared conductivity in the Abrikosov vortex lattice state of a type-II superconductor*, Phys. Rev. B **80**, 212506 (2009).

[73] M. Šindler, *Vortex dynamics in superconductors*, Diploma thesis, Charles University in Prague, 2008.

[74] Ch. P. Poole Jr., H. A. Farach, R. J. Creswick, *Superconductivity*, Academic Press, London, 1995.

[75] A. A. Abrikosov, *On the lower critical field of thin layers of superconductors of the second group*, h. Eksperimen. i. Teor. Fiz. **46**, 1464-1469 (1964).

[76] M. P. Mathur, D. W. Deis, J. R. Gavaler, *Lower Critical Field Measurements in NbN Bulk and Thin Films*, J. Appl. Phys. **43**, 3158-3161 (1972).

[77] A. J. Drew, M. W. Wisemayer, D. O. G. Heron, S. Lister, S. L. Lee, A. Potenza, C. H. Marrows, R. M. Dalgliesh, T. R. Charlton, and S. Langridge, *Using spin-polarized neutron reflectivity to probe mesoscopic vortex states in a Pb thin film superconductor*, Phys. Rev. B **80**, 134510 (2009).

Selected Publications

Physica C 470 (2010) 932–934

Contents lists available at ScienceDirect

Physica C

journal homepage: www.elsevier.com/locate/physc

Terahertz transmission of NbN superconductor thin film

R. Tesař [a,b,*], J. Koláček [a], Z. Šimša [a], M. Šindler [a,b], L. Skrbek [b], K. Il'in [c], M. Siegel [c]

[a] Institute of Physics ASCR, v. v. i., Cukrovarnická 10, CZ-162 53 Praha 6, Czech Republic
[b] Faculty of Mathematics and Physics, Charles University, Ke Karlovu 3, CZ-121 16 Praha, Czech Republic
[c] Institute for Micro- and Nanoelectronic Systems, University of Karlsruhe, Hertzstr. 16, 76187 Karlsruhe, Germany

ARTICLE INFO

Article history:
Available online 21 February 2010

Keywords:
Far-infrared transmission
NbN
Superconducting film
Magnetic vortices
Terahertz waves

ABSTRACT

Transmission of terahertz waves through a thin layer of the NbN superconductor deposited on a sapphire substrate was studied as a function of temperature in zero field as well as in magnetic field perpendicular to the sample. For photon energies lower than optical gap, detailed temperature measurements in zero field provide BCS-like curves with a pronounced peak below the critical temperature. In accordance with the BCS model, the temperature peak disappears as the energy of incident radiation is increased above the gap. In non-zero field, the temperature behavior of transmission is modified because the gap is suppressed and vanishes at upper critical field. In addition, the presence of quantized vortices in the superconducting film substantially changes shape of the temperature curves.

1. Introduction

Vortex dynamics in superconductors is experimentally most effectively studied in the terahertz frequency region. A number of experiments have already been performed, nevertheless, some questions still remain open. Recently Ikebe et al. [1] used terahertz time-domain spectroscopy to study vortex dynamics in the NbN thin film at 3 K. They used the Maxwell Garnett theory [2] and the modified Coffey–Clem self-consistent theory [3] to reveal how vortices contribute to ac conductivity in the THz frequency range. In this paper, we describe our experimental setup, report first observed temperature and magnetic field dependences of terahertz wave transmission through a NbN thin film sample deposited on a sapphire substrate and compare these results with available theories.

2. Experimental setup

Our experimental setup is schematically shown in Fig. 1. Its essential parts are the CO_2 laser pumping the far-infrared (FIR) laser source [4], the SM4000 Spectromag cryomagnetic system [5] and the helium cooled bolometer [6].

The FIR laser generates a coherent, linearly polarized, monochromatic radiation at discrete wavelengths in the range from 40 μm to 1 mm. From a number of the available far-infrared lines only few sufficiently intense lines have so far been exploited in our experiment, as listed in Table 1. To achieve a successful laser action, several conditions must be satisfied. First, the waveguide tube of the FIR laser is filled with the operating gas at a low pressure. Appropriate excitation energy emitted from the strong infrared CO_2 laser is injected into the resonator cavity with 130 Hz repetition frequency. The length of the FIR resonator is fine tuned to meet the lasing condition. Part of the FIR output beam reflected by a mylar beamsplitter (BS) is focused by a mirror (M2) to a pyroelectric detector (PD) which is used for monitoring the laser power. The beam transmitted through the beamsplitter is concentrated on the sample using a gold coated off-axis parabolic mirror (M4). Radiation transmitted through the sample is collected by mirrors (M4′, M5) to the bolometer detector. Transmission of the sample is proportional to the ratio of signals from bolometer and pyrodetector. This method effectively eliminates any possible time instability in the laser power.

The Spectromag cryomagnetic equipment enables to measure optical transmission at temperatures ranging from 3 K to 300 K in magnetic fields up to 11 T. The system stands on a simple non-magnetic rotation stage designed for an easy change of the field configuration as indicated by the curved arrow in Fig. 1. The horizontal split pair of superconducting coils provides optical access in two perpendicular directions through four pairs of mylar windows. The sample rod can be rotated manually about vertical axis to adjust position of the sample perpendicular or parallel with the magnetic field. The magnet coils are supplied by a bipolar current source which allows energizing the magnet in both field directions.

The temperature of the sample can be controlled automatically by a dynamic cooling and heating. Liquid helium flows from the main bath into the sample space through a needle valve and evaporates in a heat exchanger. A stabilized flow rate is adjusted

* Corresponding author. Address: Institute of Physics ASCR, v. v. i., Cukrovarnická 10, CZ-162 53 Praha 6, Czech Republic.
E-mail address: tesar@fzu.cz (R. Tesař).

0921-4534/$ - see front matter © 2010 Elsevier B.V. All rights reserved.
doi:10.1016/j.physc.2010.02.077

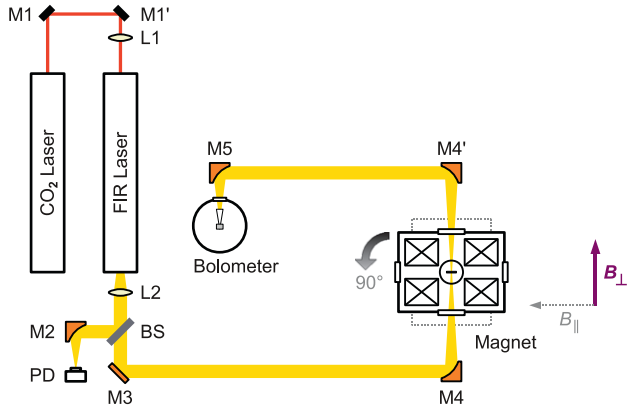

Fig. 1. Schematic drawing of the experimental setup showing two different orientations of magnetic field ($B_\perp$, $B_\parallel$), flat mirrors (M1, M3), focusing mirrors (M2, M4, M5), lenses (L1, L2), beamsplitter (BS) and pyrodetector (PD).

Table 1
Far-infrared laser lines frequently used in the experiment. MA, methyl alcohol (CH_3OH); FA, formic acid (HCOOH).

Wavelength (μm)	Frequency (THz)	Intensity	Pump line	Gas
70.5120	4.25165	Very strong	9P34	MA
96.5224	3.10594	Very strong	9R10	MA
118.8341	2.52278	Very strong	9P36	MA
164.7832	1.81931	Strong	9R10	MA
311.5540	0.96225	Week	10R22	FA
405.5848	0.73916	Medium	9R18	FA
458.5229	0.65382	Week	9R38	FA
513.0157	0.58437	Strong	9R28	FA
570.5687	0.52543	Medium	9P16	MA
742.5720	0.40372	Week	9R40	FA

and the sample surrounded by flowing gas is constantly cooled. A heater placed in a copper block near the sample enables varying the sample temperature. Calibrated field independent Cernox sensor is used for an accurate temperature measurement. Four contacts in corners of the superconducting film allow for a simultaneous monitoring of the dc resistance as shown on the photo of the sample holder in Fig. 2.

FIR radiation transmitted through the sample is focused to the bolometer which is mounted in the center of a small liquid helium dewar. The light passes through a wedged white polyethylene vacuum window, a far-infrared cut-on filter and a Winston cone collector to the composite silicon bolometer element. The detector operates at a temperature of 4.2 K, which is ensured by a thermal bond to liquid helium bath. The first stage of the preamplifier is mounted on the cold plate and operates at temperature of 60 K, the second stage is mounted outside the dewar at room temperature.

The sample is a 15 nm thick NbN superconducting film on the sapphire substrate with dimensions $10 \times 10 \times 0.33\ mm^3$. The NbN film has been deposited using DC reactive magnetron sputtering of a pure Nb target in Ar/N_2 gas atmosphere with a total pressure of about 5×10^{-3} mbar. The one side polished R-plane sapphire substrate has been placed on a heater kept at a temperature of 750 °C during deposition. The main parameters of the deposition process, i.e. the gas pressure, the substrate temperature and the plasma discharge current, were optimized for deposition rate of NbN film of about 0.17 nm/s. The critical temperature of as deposited film in zero field was found to be $T_c \approx 16$ K. For more details on the preparation and properties of such NbN films on sapphire see [7].

3. Experimental results

We have measured optical properties of the thin NbN film in its normal and superconducting state as functions of temperature and magnetic field. It is convenient to analyze the temperature dependences of the far-infrared transmission $\mathcal{T}$ normalized to that in the normal state $\mathcal{T}_N$, taken slightly above the critical temperature.

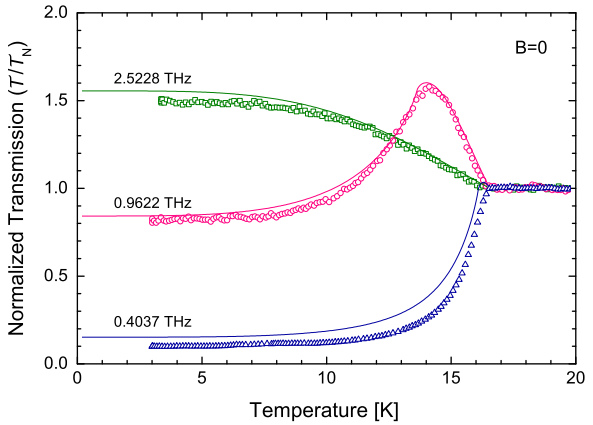

Fig. 3. Normalized transmission of the NbN thin film (relative to values above T_c) in zero magnetic field for three representative frequencies. Full lines are theoretical curves following from the BCS model as described in Section 4.

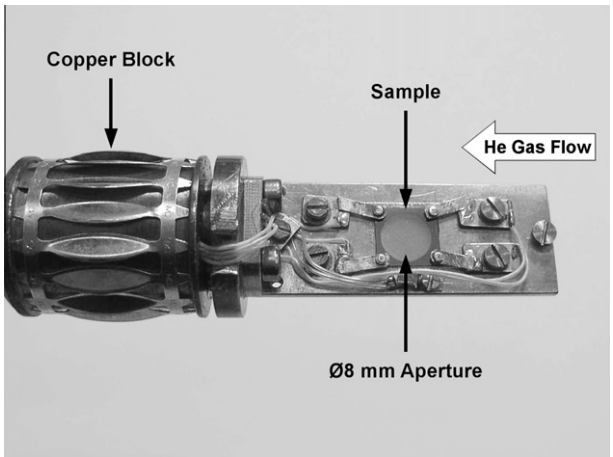

Fig. 2. Sample holder.

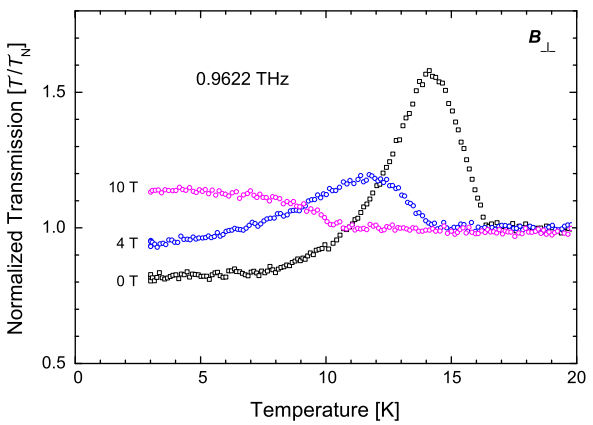

Fig. 4. Temperature dependences of normalized transmission in field perpendicular to the sample.

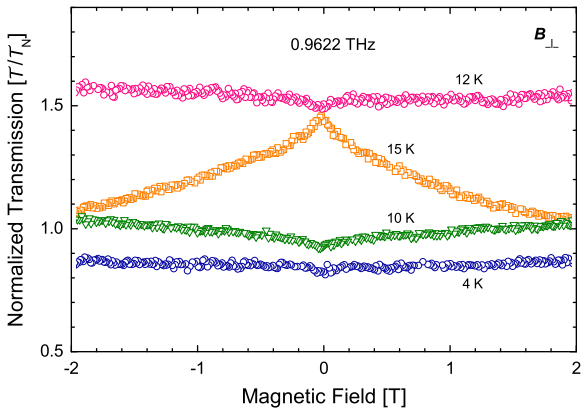

Fig. 5. Normalized transmission in field perpendicular to the sample at several temperatures.

Typical examples of our zero field measurements are shown in Fig. 3. For frequencies low enough compared with the optical gap, $\hbar\omega \ll 2\Delta_0$, we observe a monotonous transition from normal to superconducting state. At frequencies near the gap, $\hbar\omega \lesssim 2\Delta_0$, a pronounced peak is formed below the critical temperature that disappears at very high frequencies, $\hbar\omega > 2\Delta_0$.

Fig. 4 presents transmission measured at a laser line with photon energy near the optical gap for several magnetic fields perpendicular to the sample. It is obvious that the onset of the peak shifts to lower temperatures as the T_c is depressed by increasing magnetic field. The peak is gradually reduced in height and disappears completely when the applied field diminishes the optical gap below the laser photon energy, $2\Delta_0(H) < \hbar\omega$. The shape of the curve is then similar to that measured at high frequency in zero field, only the critical temperature is shifted accordingly.

Fig. 5 shows transmission measured as a function of magnetic field at selected temperatures. The transmission is nearly field independent at 4 K. For temperatures on the left and right hand sides of the peak (cf. Fig. 3), the transmission at zero field has minimum and maximum, respectively.

4. Discussion

In order to understand the observed behavior of transmission through the sample, we have to consider interference effects resulting from multiple reflections of the incoming laser light in the film as well as in the substrate. These can be computed using standard formulas [8,9], assuming that all optical interfaces are ideal. As the wavelengths of all our FIR lines exceed the optical thickness of the NbN film, interference effects within the superconducting film itself are negligible.

The NbN is supposed to be a homogenous isotropic BCS type-II superconductor. Since the coherence length is much smaller then both the magnetic penetration depth and the wavelength of the incident light, the local limit is appropriate.

4.1. Zero field results

We describe the NbN superconductor using the complex optical conductivity $\sigma(\omega, T)$ given by an explicit integral expression in [10]. Temperature dependence of the BCS gap is approximated by an analytical function [11]

$$\Delta(T) = \Delta_0 \sqrt{\cos\frac{\pi}{2}\left(\frac{T}{T_c}\right)^2}. \quad (1)$$

The optical properties are calculated from the index of refraction n

$$n^2 = \varepsilon_r(\omega, T) = \varepsilon_r(\infty) + \frac{i\sigma(\omega, T)}{\omega\varepsilon_0}, \quad (2)$$

where at high frequencies the relative permittivity can be approximated with unity $\varepsilon_r(\infty) \approx 1$. By use of (2) and formulas in [10] we can calculate the temperature dependence of the relative transmission in zero magnetic field. As seen in Fig. 3 the experimental data are in good agreement with the theoretical curves obtained from the BCS model.

4.2. Non-zero field results

As NbN represents a superconductor of the second kind, in magnetic fields exceeding $H_{c1} \approx 10$ mT vortices penetrate into the sample and modify its optical properties substantially, as seen in Figs. 4 and 5. To describe experimental observations, the above suggested model for zero field must be modified by taking into account the presence of vortices and their dynamics in applied magnetic field.

Systematic measurements of the transmission over a temperature range (3–20) K in magnetic fields up to 11 T (both in parallel and perpendicular configuration with respect to the sample) are under progress. The detailed analysis of the data as well as a developed theoretical model that takes into account magnetic vortices and more realistic optical properties of the substrate will be given in a later paper.

5. Conclusions

We have built an experimental setup capable of investigating far-infrared optical properties of thin films over a wide temperature range in magnetic fields of various configurations up to 11 T. Our zero-field transmission data on NbN thin film sample deposited on a sapphire substrate are well understood in frame of the BCS based model [10]. More detailed experimental and theoretical description of optical properties in magnetic fields exceeding H_{c1} will be published elsewhere.

Acknowledgments

This work was supported by GAČR under Contract #202/08/0326, the European program NES is also acknowledged.

References

[1] Y. Ikebe, R. Shimano, M. Ikeda, T. Fukumura, M. Kawasaki, Phys. Rev. B 79 (2009) 174525.
[2] J.C. Maxwell Garnett, Philos. Trans. R. Soc. Lond. A (1904) 385–420.
[3] M.W. Coffey, J.R. Clem, Phys. Rev. Lett. 67 (1991) 386.
[4] Far-infrared laser, model 295, Edinburgh Instruments.
[5] Spectromag, model SM4000-11, Oxford Instruments.
[6] Silicon bolometer, Infrared Laboratories.
[7] A. Semenov, B. Günther, U. Böttger, H.W. Hübers, H. Bartolf, A. Engel, A. Schilling, K. Ilin, M. Siegel, R. Schneider, D. Gerthsen, N.A. Gippius, Phys. Rev. B 80 (2009) 054510.
[8] O.S. Heavens, Optical Properties of Thin Solid Films, Butterworth, London, 1955.
[9] M. Born, E. Wolf, Principles of Optics, Pergamon, Oxford, 1975.
[10] W. Zimmermann, E.H. Brandt, M. Bauer, E. Seider, L. Genzel, Physica C 183 (1991) 99–104.
[11] T.P. Sheahen, Phys. Rev. 149 (1966) 368–370.

Far-infrared transmission of a superconducting NbN film

M. Šindler,[1] R. Tesař,[2] J. Koláček,[2] L. Skrbek,[1] and Z. Šimša[2]
[1]*Faculty of Mathematics and Physics, Charles University, Ke Karlovu 3, 12116 Prague 2, Czech Republic*
[2]*Institute of Physics, Academy of Sciences, Cukrovarnická 10, 16253 Prague 6, Czech Republic*
(Received 7 April 2010; published 26 May 2010)

We report far-infrared optical properties of a thin NbN superconductor in magnetic field, B, up to 10 T. Transmission, $Tr(T,B)$, of monochromatic linearly polarized laser beam with frequency below and above an optical gap is measured both below and above T_c. $Tr(T,B=0)$ is well described by the BCS-based model that approximates the sample as a mixture of superconductors with different T_c. $Tr(T,B\neq 0)$ appears qualitatively different for Voigt and Faraday geometry. To calculate optical properties, we use Bruggeman's approach and present a phenomenological model accounting for both field orientations. The model captures all observed features of the $Tr(T,B)$ data.

DOI: 10.1103/PhysRevB.81.184529 PACS number(s): 74.78.−w, 74.25.Gz, 74.25.Ha, 74.25.N−

I. INTRODUCTION

Far-infrared spectroscopy serves as a sensitive tool for investigating physical properties of superconductors, as their optical gap $2\Delta(0)$ is comparable with the energy of radiation quanta. Photons with energy higher than the gap can break Cooper pairs, which strongly influences high-frequency conductivity. Measurements of optical properties of superconductors thus enable deduction of important physical phenomena. Most authors present infrared transmission spectra measured at fixed temperatures using a continuous source of radiation[1,2] or a set of many monochromatic laser lines[3] while we report a complementary method using monochromatic source of radiation while sweeping the temperature.[4,5] In gigahertz frequency region, Oates *et al.*[6] reported both approaches.

Superconductors of the second type in magnetic field larger than the lower critical field $B>B_{c1}$ are in Abrikosov state. Superconductivity in the vortex core region is suppressed and its conductivity approaches normal-state value. Electric currents flowing through the material interact with the vortices, cause their motion, and the nondissipative regime is lost. Motion of the vortex lattice thus also influences conductivity. Controlled vortex motion—*fluxonics*—currently represents a hot topic of investigation. High-frequency vortex dynamics constitutes an essential tool for these aspirations, however, it is not yet properly understood. One of the most successful theoretical models is that by Coffey and Clem.[7] At present, there is aspiration to understand vortex dynamics by means of the time-dependent Ginzburg-Landau theory.[8] This paper represents our experimental contribution to this effort.

II. EXPERIMENT

We report far-infrared transmission of a thin superconducting (sc) NbN film deposited on silicon substrate in magnetic field B up to 10 T for both Faraday ($\boldsymbol{B}^{\perp}s$) and Voigt ($\boldsymbol{B}^{\parallel}s$) orientations with respect to the sample surface s. Our far-infrared gas laser can be tuned to various frequencies including 0.4037 THz (3.3 meV) and 2.5228 THz (10.4 meV) reported in our previous paper.[5] By using a beam splitter, the laser output is monitored by a pyroelectric detector and the transmitted intensity is measured by a helium-cooled bolometer. Transmission is measured at normal incidence in a constant magnetic field while temperature is swept continuously from above T_c to minimum attainable and back. The temperature of the sample monitored by a Cernox thermometer (error in T due to magnetic field less than 3.2%) is controlled by adjusting He-gas flow rate and by a resistive heater. To keep measurement times reasonable, sweep rate of 1K/min was chosen [sweep rates (0.5–2) K/min as well as cool-down and heat-up data series showed no appreciable differences]. Our experimental method was described in more detail in previous papers.[4,5]

The investigated high-quality polycrystalline NbN sample on Si substrate with a very thin SiO_2 interlayer[9] was prepared by Benačka, who measured its basic properties listed in Table I. It is important to characterize each NbN sample individually, since various NbN films[10] can display different T_c.

A. Zero magnetic field data

The T-dependent transmission, shown in Fig. 1, is in good quantitative agreement with our previous experiments.[4] Transmission in the normal state $Tr_n(T_c<T)$ is constant and serves as a suitable reference for transmission of the sc state Tr_{sc}; all measured transmission dependencies are expressed in a normalized dimensionless form as $Tr=Tr_{sc}/Tr_n$. There are two important cases: (i) $\hbar\omega>2\Delta(0)$, represented by 2.5228 THz line with the photon energy safely above the optical gap and (ii) $\hbar\omega<2\Delta(0)$ for 0.4037 THz line, which is more complicated. The quantity $2\Delta(T)$ is almost constant at low temperature, approximately equal to the $T\rightarrow 0$ value, but with increasing temperature it falls toward zero at T_c. For each frequency there is a temperature where the energy of radiation exceeds $2\Delta(T)$ and Cooper pairs can absorb photons. In case (i) Tr monotonously decreases with temperature until it reaches its normal-state value and remains constant up to 16 K and in case (ii) a well-pronounced peak is observed. The T_c onset can easily be determined from $Tr(T)$ data.

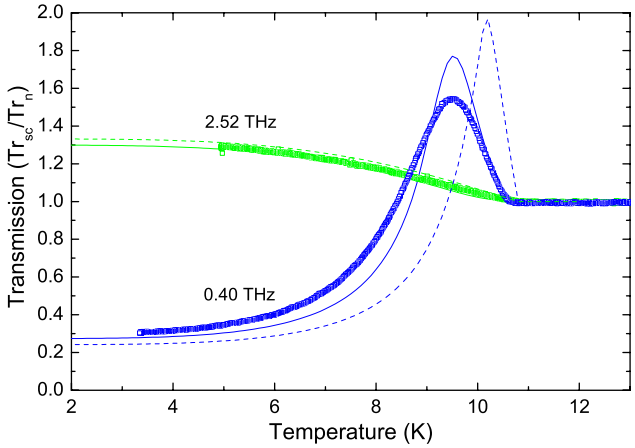

FIG. 1. (Color online) The observed zero-field transmissions for two frequencies are plotted versus temperature. Symbols represent experimental data, dashed lines are calculated curves for BCS superconductor with the sharp transition and solid lines are calculated using modified conductivity as described in the text.

B. Finite magnetic field data

In $B>0$ the optical response of material depends on mutual orientation of $\boldsymbol{B}$ and electric component of light $\boldsymbol{E}$. $\boldsymbol{B}$ determines orientation of the vortex lattice, therefore it is useful to measure in both ($\boldsymbol{B}^{\perp}$) and ($\boldsymbol{B}^{\parallel}$) geometries. In both cases, $T_c(B)$ is easily determined since transmission of sc state deviates from constant normal-state value at T_c.

In Faraday orientation (Fig. 2), Tr in small B exhibits qualitatively similar behavior as in $B=0$. With increasing B the transmission peak decreases and shifts to lower temperatures while low-T transmission slowly approaches its normal-state level. For highest attainable fields Tr becomes nearly the same as in the normal state over entire T interval.

III. PHENOMENOLOGICAL MODEL

Let us attempt to interpret the family of measured Tr curves phenomenologically. If our model is successful, it ought to shed light on optical properties of second type sc in the terahertz range. In order to interpret these data one has to calculate relevant material properties of superconductor and only then to evaluate Tr and compare it with the experimental data sets.

In order to evaluate transmission of our double-layer system, the refractive index and the thickness of each layer have to be known. Refractive index of NbN is given as $\tilde{n}_1=\sqrt{\tilde{\varepsilon}}$. As a first step, we evaluate the complex permittivity of our NbN superconductor

$$\tilde{\varepsilon}=1+i\tilde{\sigma}(\omega)/(\varepsilon_0\omega)+\chi_0, \tag{1}$$

where the contribution from conductive electrons is described by complex conductivity ($\tilde{\sigma}=\sigma_1+i\sigma_2$) and the contribution from all other effects via χ_0. This last term can be neglected, since contribution from conductive electrons in our frequency range dominates. Complex conductivity calculation will be described later.

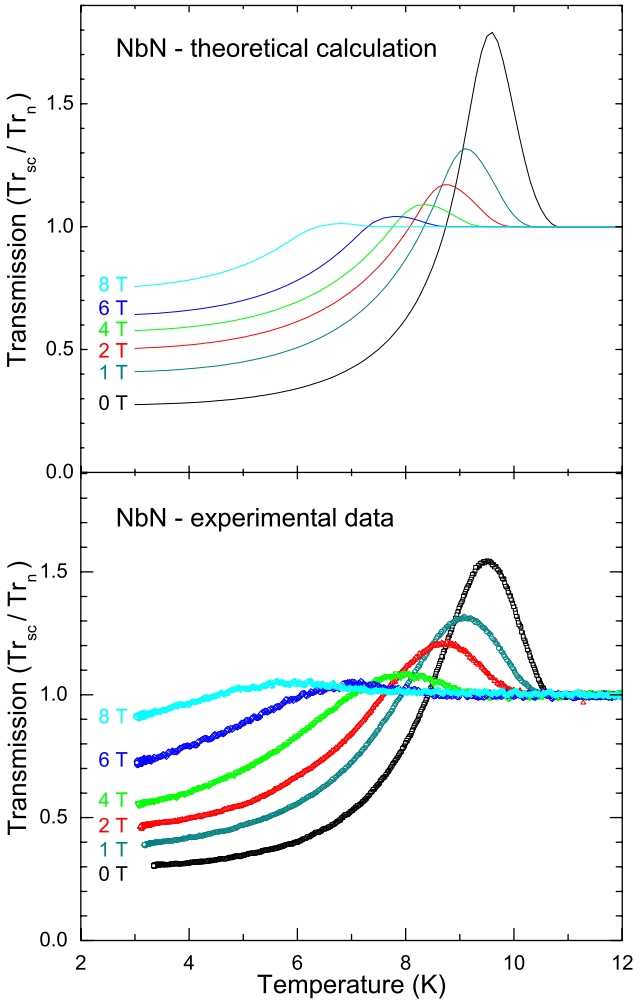

FIG. 2. (Color online) Temperature-dependent transmission in Faraday orientation ($B^{\perp}$). Experimental data are points and theoretical calculations are lines.

We take into account interference effects. Assuming ideally parallel and flat surfaces, relevant quantities describing transmission through interface are transmission and refractive amplitude coefficients

$$t_{ij}=\frac{\tilde{n}_i-\tilde{n}_j}{\tilde{n}_i+\tilde{n}_j};\quad r_{ij}=\frac{2\tilde{n}_i}{\tilde{n}_i+\tilde{n}_j}. \tag{2}$$

Propagation through material is proportional to $e^{i\delta_i}$, where

TABLE I. Parameters of the sample.

Layer	d_1 (nm)	T_c (K)	ΔT_c (K)	$\sigma_N(0)$ (Ω^{-1} m^{-1})	Substrate	d_2 (mm)	n_2
NbN	80	10.8	0.4	0.45×10^6	Si/SiO_2	0.25	3.5

$$\delta_i = \frac{n_i \omega}{c} d_i. \tag{3}$$

Indices i and j relate to material layers and c is the speed of light. Indices 0 and 3 describe surrounding medium (gaseous helium in this case, $n_0 = n_3 = 1$), index 1 relates to the superconducting layer and index 2 to the substrate. Finally, for the whole multilayer structure the transmission coefficient can be explicitly written as[11]

$$t = \frac{t_{01} t_{12} t_{23} e^{i(\delta_1 + \delta_2)}}{1 + r_{12} r_{23} e^{i2\delta_2}} \left(1 + r_{01} \frac{r_{12} + r_{23} e^{2i\delta_2}}{1 + r_{12} r_{23} e^{2i\delta_2}} e^{i2\delta_1} \right)^{-1}, \tag{4}$$

and the transmitted intensity Tr becomes

$$Tr = \frac{n_0}{n_3} |t|^2. \tag{5}$$

In our case it reduces to $Tr = |t|^2$.

Surface roughness might influence transmission, especially when surface imperfections are comparable with, or bigger than, the wavelength λ. In our case of submillimeter waves, however, this should not lead to significant difficulties. Our calculations show that slight deviations (less than 7°) from the normal incidence can be neglected; our experiment is performed at more precise orientation of the sample.

A. Zero magnetic field

Permittivity in the terahertz region is almost entirely governed by the response of conductive electrons that justifies neglecting other contributions. We used BCS-theory-based formula for calculating complex conductivity following Zimmermann *et al.*[12] The essential input parameter is normal-state high-frequency conductivity, which is well described by Drude model: $\tilde{\sigma}(\omega) = \sigma_N(0)/(1 - i\omega\tau)$. Reasonable estimation for momentum scattering time[1,10] is $\tau \approx 5$ fs. The crucial parameter is the optical gap. BCS theory predicts its value $2\Delta(0) = 3.53 k_B T_c$, but many materials, including NbN, exhibit deviations from this formula.[13] For our sample we estimate[1,10] $2\Delta(0) = 4.16 k_B T_c$ (3.87 meV). Temperature dependence of the gap is well approximated by[14]

$$\frac{\Delta(T)}{\Delta(0)} = \sqrt{\cos\left[\frac{\pi}{2} \left(\frac{T}{T_c} \right)^2 \right]}. \tag{6}$$

Together with other sample parameters given in Table I, the calculation gives the dashed line in Fig. 1. Although it qualitatively describes the character of the data, quantitative agreement is rather poor.

Better agreement can be achieved by treating our real sample not as a homogeneous sc with sharp transition but as a mixture of superconductors with different T_c and corresponding optical gaps $2\Delta(0) = 4.16 k_B T_c$. This view is supported by the dc electric-resistance measurement showing $\Delta T_c = 0.4$ K. Spread of T_c in the mixture will be even larger than the spread of T_c suggested by resistivity measurements because zero dc resistance does not exclude presence of nonsuperconducting regions. Since there is no reason to assume any specific distribution function of T_c in such a mixture, we assume that all T_c within suitably chosen T interval are represented with the same probability. For convenience, we approximate our NbN sample as a mixture of ten ideal sc materials with $9.8 \le T_c \le 10.8$ K. Conductivity computed this way (solid lines in Fig. 1) agrees notably better with the experimental data.

On a qualitative level, transmission in case of $\hbar\omega > 2\Delta(0)$ is influenced by the absorption caused by breaking of Cooper pairs and by presence of thermally activated quasiparticles. Absorption would be higher at lower temperatures, since Cooper pair density is higher. It leads to a decrease in reflection and, consequently, to an increase in transmission.

In case of $\hbar\omega < 2\Delta(T)$ energy of photons is not high enough for breaking Cooper pairs and the absorption occurs due to thermally excited quasiparticles only. With increasing T the optical gap gradually decreases until at some T optical gap reaches energy of incident photons. For higher T the Cooper pair-breaking mechanism is set on contributing thus to absorption. As a result absorption exhibits a peak. Although it may seem confusing, the highest transmission occurs at the highest absorption. It is because the increase in absorption leads to a decrease in reflection, which governs optical properties.

B. Finite magnetic field

We assume that conductivity of normal state does not depend on magnetic field. This assumption is supported experimentally, as at 16 K in magnetic field up to 10 T transmission within experimental accuracy remains constant.

In a sufficiently high magnetic field the superconductor is in Abrikosov state, inhomogeneous at nanoscale level. Each vortex has a complex structure, consisting of cylindrical core area with diameter equal to coherence length ξ in which the order parameter is suppressed. In this paper, we do not aim to describe all complexity of the vortex lattice. Following Clem,[15] we assume fully normal vortex cores surrounded by fully superconducting bulk material. Normal-state volume $f_n = V_N/V$ is proportional to both the core area $\pi\xi(T)^2$ and the vortex density. Temperature dependence of f_n is given by temperature dependence of coherence length $\xi(T)^2 = \xi_0^2 \{1 - [T/T_c(0)]^4\}^{-1}$ and must reach unity at experimentally determined $T_c(B)$. It is satisfied by the following formula:

$$f_n = \frac{1 - T_c(B)^4/T_{c0}^4}{1 - T^4/T_{c0}^4}. \tag{7}$$

Superconducting phase $f_{sc} = 1 - f_n$ is assumed to behave in a similar way as a superconductor without magnetic field. Thus our sample is treated as an effective mixture of ideal BCS superconductors with sharp transitions, with critical temperatures equally distributed over temperature range $(T_c - 1\ \mathrm{K}, T_c)$. Additionally, we assume that $2\Delta(0)$ has zero field value and for its temperature dependence in Eq. (6) we use $T_c(B)$ instead of $T_c(B=0)$.

For NbN, ξ is few nanometers (Ikebe[1] estimated 5 nm), several orders of magnitude smaller than the wavelength inside the sample, so we can use the long-wavelength limit, i.e., consider the material as a composite system with some effective high-frequency permittivity $\tilde{\varepsilon}_{eff}$. Optical properties

of such composite systems can be described by various effective medium theories. We have to consider a theory that will distinguish between Faraday ($B^{\perp}$) and Voigt ($B^{\parallel}$) sample orientations. Generalized Bruggeman's theory for ellipsoidal inclusions[16] describes two-composite system for any fraction ratios and respects the geometry by considering polarization effects due to local fields when it calculates the effective permittivity of the composite system.

In ($B^{\parallel}$) case we use linear polarization having electric field component parallel with axes of vortex cores. Therefore local charges inside the sample are not induced and Bruggeman's theory gives a simple result for permittivity

$$\tilde{\varepsilon}_{eff} = f_n \tilde{\varepsilon}_n + (1 - f_n)\tilde{\varepsilon}_{\mathrm{sc}}, \tag{8}$$

where $\tilde{\varepsilon}_n$ and $\tilde{\varepsilon}_{\mathrm{sc}}$ are permittivities of normal and superconducting phases, respectively.

In ($B^{\perp}$) case, electric field of the laser beam acts in the direction perpendicular to the vortex core axis and creates local field that is different from the applied field. It can be shown that the following formula applies:[16]

$$\tilde{\varepsilon}_{eff} = \frac{1}{2}(\beta + \sqrt{\beta^2 + 4\tilde{\varepsilon}_n \tilde{\varepsilon}_{\mathrm{sc}}}), \tag{9}$$

where $\beta = (2f_n - 1)\tilde{\varepsilon}_{\mathrm{sc}} + (1 - 2f_n)\tilde{\varepsilon}_n$. The theoretical lines shown in Figs. 2 and 3 were calculated using this approach. Despite the simplicity of the model, the experimental data sets are described surprisingly well, including the qualitative difference between Faraday and Voigt sample orientations.

We emphasize that our model does not take into account any vortex motion. In principle, the laser beam interacts with vortices also via the Magnus force; this effect is neglected in our analysis. Good agreement between calculated and observed temperature-dependent transmission suggests that this term is either small or the vortex lattice in our NbN sample is strongly pinned.

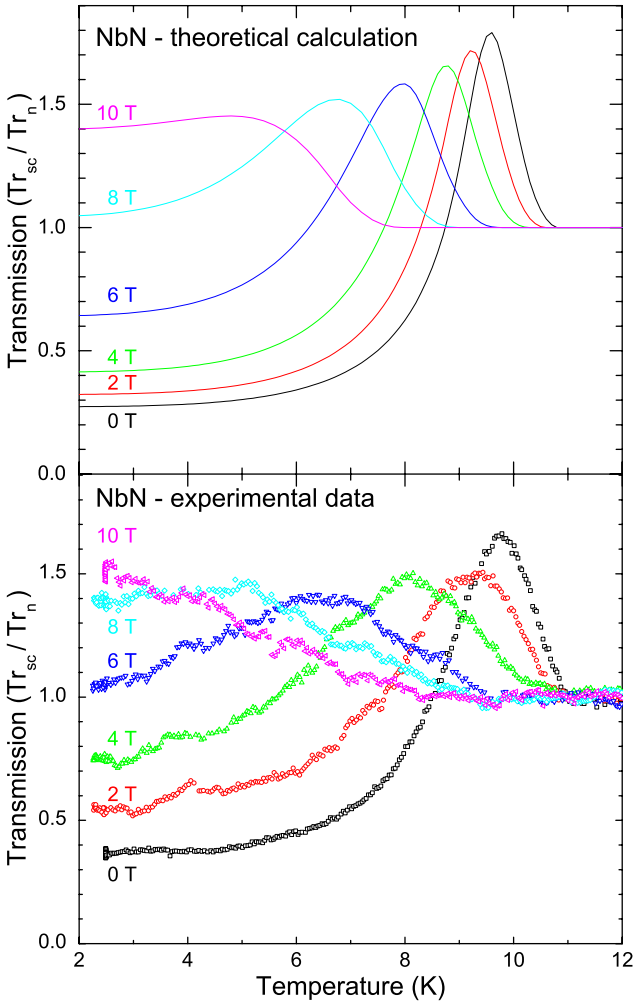

FIG. 3. (Color online) Temperature-dependent transmission in Voigt orientation ($B^{\parallel}$). Experimental data are points and theoretical calculations are lines.

IV. CONCLUSIONS

We have investigated far-infrared magneto-optical properties of the thin-film NbN sample (B up to 10 T) deposited on a Si substrate using our new experimental apparatus. As for T-dependent transmission in $B=0$, presented measurements agree with previous data obtained with the same sample using the old experimental equipment.[4] Two cases are probed by laser beams of two different frequencies—(i) energy above the optical gap and (ii) energy below the optical gap (its zero-temperature value), displaying qualitatively different behavior. The above-mentioned model describes a behavior of transmission for both cases qualitatively well, but better quantitative agreement is achieved by modeling our imperfect real sample as a mixture of superconductors with different T_c and corresponding optical gaps $2\Delta = 4.16 k_B T_c$.

We have probed the Abrikosov state of our sample using 0.4037 THz laser beam by measuring $Tr(T, B_{c1} < B \leq 10$ T) curves in both ($B^{\perp}$) and ($B^{\parallel}$) geometries, giving qualitatively different results. For clarity, in this work we present only the $B \neq 0$ data obtained with one sample using one particular laser line as a representative data set, although data obtained with several laser lines on this sample as well as on additional NbN samples are available. Further detailed investigations are under progress and will be reported elsewhere.

We are not aware of any relevant microscopic theory that would describe transmission in magnetic field. We have therefore developed a phenomenological theoretical model, based on the following assumptions. Vortex lattice was simplified according to Clem model with entirely normal-state vortex cores and a fully superconducting surrounding bulk—a mixture of ideal superconductors with different T_c spread over about 1 K. The corresponding $Tr(T,B)$ curves have been calculated by means of Bruggeman's approach, allowing to take into account various mutual orientations of $\boldsymbol{B}$ and electric component $\boldsymbol{E}$ of the polarized terahertz radiation, leading to different induced local fields. Good semiquantitative agreement with the observed data suggests that our phenomenological model is capable of capturing essential physics and can be used for further investigations aiming at determining the role of vortex motion that would lead to better understanding and eventually to practical use of superconductors in fluxonics.

ACKNOWLEDGMENTS

We are grateful to Š. Beňačka for preparing and characterizing the NbN sample and P. Kužel and I. Rychetský for stimulating discussions. This work is supported by GACR under Grant No. 202/08/0326 and ESF project NES.

[1] Y. Ikebe, R. Shimano, M. Ikeda, T. Fukumura, and M. Kawasaki, Phys. Rev. B **79**, 174525 (2009).
[2] H. J. Lee, J. H. Jung, K. W. Kim, M. W. Kim, T. W. Noh, Y. J. Wang, W. N. Kang, E. M. Choi, H. J. Kim, and S. I. Lee, Phys. Rev. B **65**, 224519 (2002).
[3] D. Karecki, R. E. Peña, and S. Perkowitz, Phys. Rev. B **25**, 1565 (1982).
[4] R. Tesař, J. Koláček, E. Kawate, Š. Beňačka, Š. Gaži, and Z. Šimša, Supercond. Sci. Technol. **16**, 916 (2003).
[5] R. Tesař, J. Koláček, Z. Šimša, M. Šindler, L. Skrbek, K. Il'in, and M. Siegel, Physica C (to be published).
[6] D. E. Oates, A. C. Anderson, C. C. Chin, J. S. Derov, G. Dresselhaus, and M. S. Dresselhaus, Phys. Rev. B **43**, 7655 (1991).
[7] M. W. Coffey and J. R. Clem, Phys. Rev. Lett. **67**, 386 (1991).
[8] P.-J. Lin and P. Lipavsky, Phys. Rev. B **80**, 212506 (2009).
[9] The SiO_2 interlayer between the film and the substrate is very thin (≈5 nm according to Š. Benačka), therefore it hardly influences far-infrared optical properties of our sample. This enables treating it as an effective double-layer system.
[10] A. Semenov, B. Günther, U. Böttger, H.-W. Hübers, H. Bartolf, A. Engel, A. Schilling, K. Ilin, M. Siegel, R. Schneider, D. Gerthsen, and N. A. Gippius, Phys. Rev. B **80**, 054510 (2009).
[11] R. M. A. Azzam and N. M. Bashara, *Ellipsometry and Polarized Light* (Elsevier, Amsterdam, 1987).
[12] W. Zimmermann, E. H. Brandt, M. Bauer, E. Seider, and L. Genzel, Physica C **183**, 99 (1991).
[13] M. Tinkham, *Introduction to Superconductivity* (Dover, New York, 2004).
[14] T. P. Sheahen, Phys. Rev. **149**, 368 (1966).
[15] J. R. Clem, J. Low Temp. Phys. **18**, 427 (1975).
[16] T. C. Choy, *Effective Medium Theory Principles and Applications* (Oxford University Press, New York, 1999).

Terahertz thermal spectroscopy of a NbN superconductor

R. Tesař,[1] M. Šindler,[1,2] K. Il'in,[3] J. Koláček,[1] M. Siegel,[3] and L. Skrbek[2]
[1]*Institute of Physics, Academy of Sciences of the Czech Republic, Cukrovarnická 10, CZ-16200 Praha, Czech Republic*
[2]*Faculty of Mathematics and Physics, Charles University, Ke Karlovu 3, CZ-12116 Praha, Czech Republic*
[3]*Institute for Micro- and Nanoelectronic Systems, Karlsruhe Institute of Technology, Hertzstraße 16, D-76187 Karlsruhe, Germany*
(Received 22 June 2011; published 25 October 2011)

We report far-infrared optical properties of a NbN superconductor. Transmission through a high-quality NbN film grown on a birefringent sapphire substrate above and below its superconducting transition down to the zero-temperature limit is measured at six different frequencies from 0.4 to 2.5 THz both above and below its optical gap. The experimental results agree with theoretical calculations developed based on utilization and extension of the BCS model of Zimmermann *et al.* [Physica C **183**, 99 (1991)] applied for the NbN film. Full quantitative agreement over the entire ranges of temperature and frequencies is found based solely on the physical properties of this NbN film sample and on the parameters of an identical sapphire substrate as measured in time-domain spectroscopy experiments, without use of any additional fitting parameters.

DOI: 10.1103/PhysRevB.84.132506 PACS number(s): 74.25.N−, 74.25.Gz, 74.78.−w

I. INTRODUCTION

The exact knowledge of physical properties of conventional superconductors such as NbN is fundamental from the point of view of their future application. At first glance it might seem that all of them are indeed well known and understood. A closer look shows, however, that some of them are still understood rather poorly. The high-frequency conductivity serves as an example—in principle, the Mattis-Bardeen theory[1] can be used to calculate it, but some terahertz frequency experiments still lack a satisfactory explanation. This Brief Report represents our effort to improve this situation.

Time-domain terahertz spectroscopy provides data in a broad frequency region and enables one to determine the complex conductivity; see, e.g., Ikebe *et al.*[2] On the other hand, laser thermal spectroscopy is advantageous in that the transmission measurements are performed quasistatically. It enables precise measurement of transmission at fixed laser frequencies as a function of temperature in the vicinity of the superconducting transition, where a peculiar behavior was observed, and has proved to be a very useful experimental method.[3,4]

Earlier we performed experiments in the terahertz frequency range,[4,5] but a satisfactory theoretical explanation has not been found. Our previous experiments suffered from the fact that the NbN sample we used displayed a rather broad superconducting transition.[5] In order to get better agreement between the experiment and the BCS theory we had to artificially treat it as a mixture of superconductors with different T_c's.

In this Brief Report we present experimental data on a much higher-quality NbN film obtained using our setup,[4] as well as additional supporting experiments.[6] Further, we discuss a full analysis of the thermal and frequency behavior of the NbN superconductor in terms of a developed BCS-based model that takes into account optical properties of the birefringent sapphire substrate. Without using any additional fitting parameters, we demonstrate full quantitative agreement between theory and experiment over entire ranges of temperature and frequency.

II. EXPERIMENT

We have measured far-infrared (FIR) transmission of a superconducting NbN film of nominal thickness $d_1 = 15$ nm grown epitaxially on a sapphire substrate. We estimate the thickness uncertainty of ± 1 nm to be due to the partially oxidized NbN surface layer.[7]

The quality of our NbN sample is very high, as is apparent from the temperature dependence of its dc resistivity displayed in Fig. 1, showing that the resistance drops to zero within an interval of 0.5 K. Measurements of the dc electrical conductivity have been performed using a $0.7 \times 10\ \mathrm{mm}^2$ strip cut for this purpose from our actual sample and measured by the four-probe method, as sketched in the upper inset of Fig. 1. The critical temperature has been determined as $T_c \approx 16$ K. The normal-state dc resistivity has been estimated as $\rho_0 = (2.0 \pm 0.2) \times 10^{-6}\ \Omega\,\mathrm{m}$, with the accuracy limited mainly by the uncertainty of the film cross section and the size and separation of the potential contacts. The lower inset in Fig. 1 shows that the normal-state resistivity is nearly temperature independent over the entire temperature range up to room temperature with a residual resistivity ratio of 0.97.

FIR transmission is strongly influenced by optical interference of multiple internal reflections, especially in a relatively thick substrate. Thus for accurate numerical analysis of transmission it is important to have a well-determined optical thickness of the substrate. Our NbN sample is grown on a birefringent *R*-cut sapphire with dimensions $10 \times 10\ \mathrm{mm}^2$ and thickness $d_2 = 0.333$ mm. Sapphire is an important anisotropic uniaxial material with ordinary, n_o, and extraordinary, n_e, refractive indices that are tabulated.[8] The structure and orientation of our sample in the experiment are shown in Fig. 2. The extraordinary ray axis is oriented diagonally (at an angle $\alpha = 45^\circ$ with respect to the y axis), while $\vartheta = 57.6^\circ$ is the angle between the c axis of the sapphire crystal and the z axis oriented normally to the substrate.

Both the ordinary and extraordinary refractive indices were determined in the supporting independent time-domain terahertz spectroscopy experiment[6] at room temperature, using an identical sapphire substrate, as shown in Fig. 3. While the

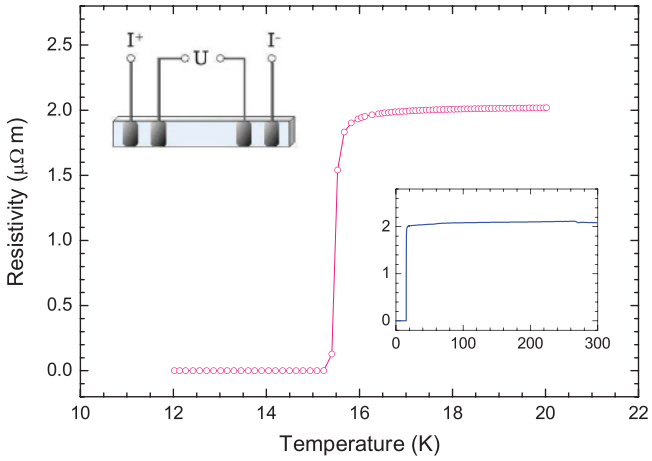

FIG. 1. (Color online) Temperature dependence of the electrical resistivity of the NbN sample in the vicinity of its critical temperature T_c (red). The lower inset shows the extension of the temperature range up to room temperature (blue); the upper inset is a sketch of the sample strip and the four-probe method used in this measurement.

real part of the refractive index increases slightly, approximately linearly with frequency ν, the imaginary part is almost frequency independent. The optical thickness of the substrate, $n_2 d_2$, is to a good approximation temperature independent.[9,10] Absorption by the substrate is nearly negligible at room temperature and is even smaller at low temperature. The values of refractive indices deduced from the time-domain spectroscopy experiment are given in Table I together with those tabulated by Palik:[8] the agreement is excellent. Additionally, these measurements allowed us to determine that the polarization of the ordinary ray is parallel with the diagonal direction of the square sapphire substrate.

Our experimental setup has been described in detail in our previous report.[4] In short, the FIR gas laser can be tuned to various terahertz frequencies. A wire grid polarizer was inserted in the optical path to ensure a horizontal or vertical orientation of the FIR laser beam polarization. The sample is placed in the cryomagnetic system and its temperature tuned and controlled by means of a heater and by flowing He gas.

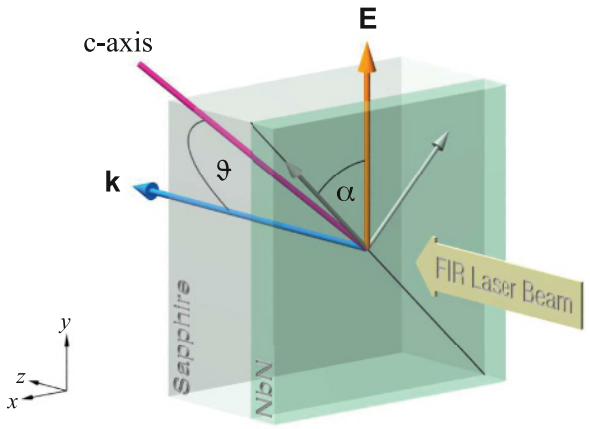

FIG. 2. (Color online) Schematic representation of the double-layer structure of the NbN sample on the sapphire substrate. For notation details, see the text.

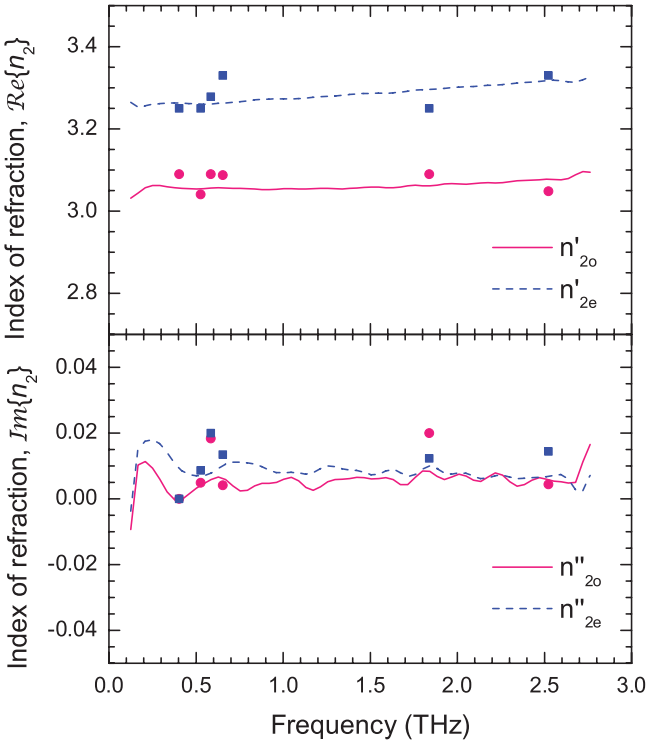

FIG. 3. (Color online) Real and imaginary parts of the refractive indices of the *R*-cut sapphire substrate. Lines, data from terahertz time-domain spectroscopy; single points, obtained from the best fit of the FIR transmission. The full (red) and dashed (blue) lines represent the ordinary and the extraordinary ray, respectively.

To eliminate a possible temperature difference between the sensor and the true temperature of the sample, the dc resistivity is monitored by the four-probe method simultaneously with the transmission measurement. This allows, in particular, determination of the superconducting transition temperature T_c with sufficient precision.

Since NbN is an isotropic superconductor, the only anisotropy introduced in the system is due to the birefringent sapphire substrate. In the special case of a 45° angle between the electric vector of the incident beam and the extraordinary ray axis of the sapphire substrate (and only in this case), the relative transmission of the horizontally and vertically polarized radiation should be equal. Transmission was measured in both polarizations and the observed difference was less than 5%, which can most likely be attributed to a slight misalignment of the sample. Even for the 0.4037 THz line, for which the

TABLE I. Parameters of the sapphire substrate.

			Palik, Ref. 8		Ref. 17
ν (THz)	n_{2o}	$n_{2e}(\vartheta)$	n_o	n_e	$n_e(\vartheta)$
0.4037	3.06	3.26	3.06	3.39	3.29
0.5254	3.05	3.26	3.06	3.40	3.29
0.5843	3.06	3.26	3.06	3.40	3.29
0.6538	3.06	3.26	3.06	3.40	3.29
1.8191	3.06	3.30	3.08	3.44	3.33
2.5228	3.08	3.32	3.10	3.47	3.35

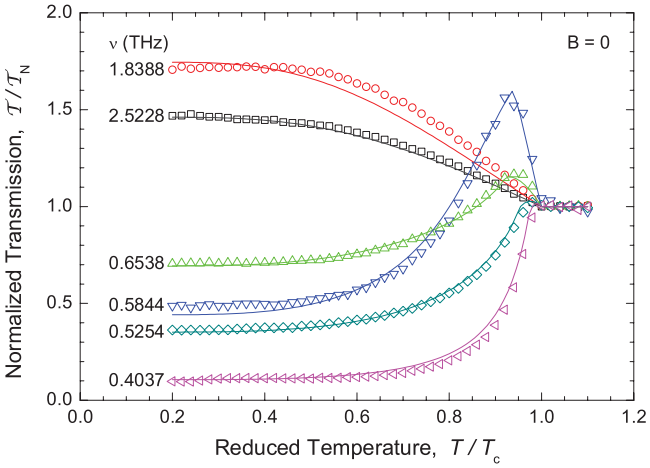

FIG. 4. (Color online) Normalized transmission as measured (individual data points) and calculated (solid lines) as described in the text for six different frequencies as indicated, plotted versus relative temperature T/T_c.

transmission in the zero-temperature limit is very weak, the relative difference is still within 10%.

Our experimental data for the horizontally polarized beam are displayed in Fig. 4 as individual data points. The sample temperature was swept up and down at a low rate of about 1 K/min, without observable temperature hysteresis. The far-infrared transmission, $\mathcal{T}$, is related to that in the normal state, $\mathcal{T}_N$, taken slightly above T_c.

The transmission of photons with energies far below the optical gap displays a monotonic increase toward the critical temperature. As the frequency approaches the optical gap, the characteristic BCS thermal peak starts to appear close below T_c. As the frequency increases further, the peak becomes wider and its center shifts toward a lower temperature. Above the optical gap, the transmission displays a monotonic decrease and in the high-frequency limit approaches the normal-state transmission.

III. THEORETICAL MODEL

The theoretical calculation and subsequent numerical evaluation of transmission requires precise values of the refractive indices of both the NbN film and the sapphire substrate. Additionally, precise knowledge of the relative permittivity of the superconductor film for angular frequency ω is also needed, which is given by[11]

$$\varepsilon(\omega,T) = \varepsilon_\infty + \frac{i\sigma(\omega,T)}{\omega\varepsilon_0}, \tag{1}$$

where $\varepsilon_\infty \approx 1$ is the core permittivity, ε_0 denotes the permittivity of vacuum, and $\sigma(\omega,T)$ is the optical complex conductivity. Other contributions, such as that from phonons, are negligible in our spectral range, as proved by Ikebe *et al.*[2] and Semenov *et al.*[7] The refractive index of the superconducting film $n_1 = \sqrt{\varepsilon(\omega,T)}$, and the indices of the substrate n_{2o}, n_{2e} enter the recurrence relations[12] for the transmission coefficients t_{03} of the extraordinary and ordinary rays. The electric vector of a monochromatic wave incident normally on the double-layered system shown in Fig. 2 can be decomposed in the directions parallel and perpendicular to the plane containing the **k** wave vector and the c axis of the sapphire crystal. The extraordinary and ordinary rays do not interfere with each other and travel through the system independently, resulting in summation of their intensities at the output. Due to the geometry of the system, the transmissivities are the same for both horizontally and vertically polarized beams:

$$\mathcal{T} = |t_{03}(n_{2e})|^2 \cos^2\alpha + |t_{03}(n_{2o})|^2 \sin^2\alpha\,. \tag{2}$$

The transmission in the normal state, $\mathcal{T}_N$, can be calculated in the same way, replacing the BCS conductivity by the Drude formula for a normal metal:

$$\sigma_N(\omega) = \frac{\sigma_0}{1 - i\omega\tau}, \tag{3}$$

where σ_0 and τ are the dc conductivity and the relaxation rate of the NbN film, respectively.

The optical conductivity $\sigma(\omega,T)$ of a BCS superconductor is well described by the theoretical approach of Zimmermann *et al.*[13] We utilize their approach, but instead of their simple approximation for the gap temperature dependence we use values obtained by numerically solving the BCS gap equation.[14,15] The model parameters T_c and σ_0 are sufficiently well established and their variations within experimental errors do not appreciably influence the calculated transmission. The values of the optical gap $2\Delta_0 = 4.15 k_B T_c$ and the relaxation rate τ as low as 3.86 fs have been taken from the literature.[7] In our frequency range, however, $\omega\tau < 0.1$, and the dirty limit $\tau \to 0$ seems appropriate.

The parameters for sapphire—the ordinary and extraordinary refractive indices n_{2o} and n_{2e} and the substrate thickness $d_2 = 0.333$ mm—have been determined from our time domain spectroscopy experimental data. As the optical system is anisotropic, calculation of the transmission is rather complicated. While variations of the film parameters (within their experimental errors) hardly affect the calculated transmission, we found that the results are much more sensitive to the ordinary and extraordinary indices of the substrate. This is understandable, since the optical thickness of the substrate is responsible for interference effects.

To achieve the best agreement between calculated and experimental transmission values, we have modified the substrate parameters slightly, within their experimental errors. This procedure yields optimum indices of refraction that are displayed in Fig. 3 as individual data points. Their scatter can most likely be attributed to small experimental errors in transmission measurements, which in turn could be caused by standing waves in the optical path and/or by small misalignment of the sample with respect to the polarization vector. The optimal calculated values of transmission of light for six different frequencies from 0.4 up to 2.5 THz plotted versus temperature as solid lines, together with the experimental data points, are displayed in Fig. 4.

IV. DISCUSSION AND CONCLUSIONS

The temperature dependencies of FIR transmissions at six frequencies $h\nu$ close to $2\Delta_0$ have been measured on a high-quality NbN epitaxial film deposited on a birefringent sapphire substrate. Linearly polarized laser lines with photon energies

in the vicinity of the optical gap revealed typical BCS behavior. The transmission of photons with energies far below/above the optical gap showed monotonic decrease/increase toward the zero-temperature limit. The transmissions for photon energies close to the optical gap follow a complex behavior with a characteristic BCS thermal peak. Let us stress that our approach, unlike that of Ikebe *et al.*,[2] enables the study of quasistatic FIR transmission over a full range of temperature.

The experimental results are found to agree with theoretical calculations developed based on utilization of the BCS model of Zimmermann *et al.*[13] applied for a NbN film with the numerical solution of the gap equation[14] replacing the original simple approximation for the temperature dependence of the gap. Full quantitative agreement within error bars over the entire range of temperature and frequency is found based solely on physical properties of this NbN film sample and an identical sapphire substrate as measured in additional experiments. This important quantitative step was not possible to achieve with our previously investigated NbN samples, where a more or less satisfactory agreement was possible only when the superconducting transition temperature was artificially smeared out over a temperature interval of order of 1 K. In addition, we have found that transmission is notably affected by interference effects in the substrate, which acts as a Fabry-Pérot étalon possessing temperature-dependent surface reflectivity.

In conclusion, the reported results represent a textbook example of thermal spectroscopy of a conventional BCS superconductor: a full quantitative agreement between the experimental data spanning broad ranges of temperature and frequency and the fundamental BCS-based microscopic theory with no free parameters. They constitute therefore a valuable basis for a further important extension: a detailed quantitative investigation of the terahertz properties of superconducting thin films in a magnetic field and in a nonequilibrium regime.

ACKNOWLEDGMENTS

The authors are grateful to P. Kužel and C. Kadlec for measurement of the refractive indices of the substrate and to J. Šebek, J. Prokleška, and M. Žáček for the dc conductivity measurements. This work was supported by GAČR under Contract No. P204/11/0015, by MSMT Grant No. MSM0021620834, and in part by the Karlsruhe DFG Center for Functional Nanostructures under Subproject No. A4.3. The ESF program NES is also acknowledged.

[1] D. C. Mattis and J. Bardeen, Phys. Rev. **111**, 412 (1958).
[2] Y. Ikebe, R. Shimano, M. Ikeda, T. Fukumura, and M. Kawasaki, Phys. Rev. B **79**, 174525 (2009).
[3] S. Perkowitz, Phys. Rev. B **25**, 3420 (1982).
[4] R. Tesař, J. Koláček, Z. Šimša, M. Šindler, L. Skrbek, K. Il'in, and M. Siegel, Physica C **470**, 932 (2010).
[5] M. Šindler, R. Tesař, J. Koláček, L. Skrbek, and Z. Šimša, Phys. Rev. B **81**, 184529 (2010).
[6] P. Kužel, H. Němec, F. Kadlec, and C. Kadlec, Opt. Express **18**, 15338 (2010).
[7] A. Semenov *et al.*, Phys. Rev. B **80**, 054510 (2009).
[8] E. D. Palik, *Handbook of Optical Constants of Solids* (Academic Press, New York, 1985).
[9] E. V. Loewenstein, D. R. Smith, and R. L. Morgan, Appl. Opt. **12**, 398 (1973).
[10] W. B. Cook and S. Perkowitz, Appl. Opt. **24**, 1773 (1985).
[11] The convention $E(t) = E_0 \exp(-i\omega t)$ leads to notation for the complex conductivity: $\sigma = \sigma' + i\sigma''$, the complex permitivity: $\varepsilon = \varepsilon' + i\varepsilon''$, and the complex index of refraction: $n = n' + in''$.
[12] O. S. Heavens, *Optical Properties of Thin Solid Films* (Dover, New York, 1991).
[13] W. Zimmermann, E. H. Brandt, M. Bauer, E. Seider, and L. Genzel, Physica C **183**, 99 (1991).
[14] M. Tinkham, *Introduction to Superconductivity* (Dover, New York, 2004).
[15] B. Muehlschlegel, Z. Phys. **155**, 313 (1959).
[16] M. Born and E. Wolf, *Principles of Optics* (Pergamon, Oxford, 1975).
[17] For *R*-cut sapphire the magnitude of the extraordinary index $n_e(\vartheta)$ has to be recalculated as (see also Ref. 16)

$$\frac{1}{n_e(\vartheta)^2} = \frac{\cos^2\vartheta}{n_o^2} + \frac{\sin^2\vartheta}{n_e^2}.$$

Interpretation of transmission through type II superconducting thin film on dielectric substrate as observed by laser thermal spectroscopy

M. Šindler[a,b], R. Tesař[a], J. Koláček[a], L. Skrbek[b]

[a] *Institute of Physics ASCR, v. v. i., Cukrovarnická 10, CZ-162 53 Praha 6, Czech Republic*
[b] *Faculty of Mathematics and Physics, Charles University, Ke Karlovu 3, CZ-121 16 Praha, Czech Republic*

Abstract

We provide a thorough analysis of THz properties of BCS-like superconducting thin films. Temperature and frequency dependence of complex conductivity in zero magnetic field is discussed by utilizing the Zimmerman *et al.* explicit BCS based formula [Physica C 183 (1991) 99]. We extend this approach by employing the effective medium theory and develop a phenomenological model capable of accounting for the influence of external magnetic field. Using Yeh powerful formalism [Surface Sci. 96 (1980) 41] we calculate optical transmission of linearly polarised laser beam normally incident to a multilayered sample consisting of a thin NbN film grown on birefringent sapphire substrate, entirely covering ranges of interest in temperature and frequency. A proposal to exploit linear polarisation of the incident beam parallel with principal axes of conductivity tensor is explained and theoretical predictions for a realistic NbN sample are computed and discussed.

Keywords: Far-infrared transmission, NbN, superconducting film, vortices, terahertz waves
PACS: 74.25.Gz, 74.25.Ha, 74.25.nj, 74.78.-w

1. Introduction

Far-infrared techniques have played crucial role in experimental validation of Bardeen-Cooper-Schrieffer (BCS) theory thanks to their ability of studying physical behavior of quasiparticles and Cooper pairs, in particular in determining the optical gap 2Δ. BCS theory is universally recognized as a microscopic theory explaining various physical features of many superconducting materials, especially metals, alloys and diatomic compounds. An important limitation of BCS theory is that it generally does not describe behavior of superconductors in externally applied magnetic field, except in some special cases [1]. Indeed, in external magnetic field superconductors of type II exhibit very complex properties due to inhomogeneity of the energy gap associated with quantization of magnetic flux and, consequently, with the existence of quantized vortices. They in turn sense an applied electric field so it is our belief that experimental efforts in far-infrared region provide a very convenient way to study vortex motion. Further, in external magnetic field quantized vortices in the interior of type II superconductors appreciably influence their high-frequency complex conductivity and these studies could play a crucial role in stimulating further advances in superconductivity theory.

In this paper, we provide a thorough analysis of THz properties of classical BCS-like superconducting thin films. This theoretical attempt is closely related to our experimental efforts [2, 3, 4] based on laser thermal spectroscopy technique [5]. Temperature and frequency dependence of complex conductivity following the Zimmerman *et al.* [6] explicit formula based on BCS theory is discussed and utilized together with effective medium theory to account for the influence of external magnetic field. Transmission through a realistic thin superconducting film sample is discussed based on analysis of a free standing film and a bare substrate. Better quality superconducting films are in some cases obtained by growing them on anisotropic substrates. In order to describe complex multiple reflections of normally incident beam inside the multilayered superconducting film/substrate sample, Yeh formalism [7, 8] is employed (see Appendix). We show that in applied magnetic field in the general case of anisotropic substrate this powerful tool becomes essential. Our goal is to describe transmission in broad frequency and temperature ranges both

Email address: sindler@fzu.cz (M. Šindler)

in zero-field and under influence of externally applied magnetic field, where we pay close attention to geometry.

A crucial test of the presented model will be experimental verification of its predictive power, especially in testing predicted differences in transmission that ought to be observed in measurements in magnetic field parallel with the sample surface using normally incident linearly polarised beam but in different mutual orientation with respect to the magnetic field direction. Verification of this prediction will have to await until further detailed experimental studies on available high quality NbN film samples grown on birefringent sapphire substrate are completed and carefully analyzed.

2. Basic theoretical considerations

2.1. Zero magnetic field

Complex conductivity of superconductors in zero magnetic field is well described by the Mattis-Bardeen extension of BCS theory [9]. Following Zimmerman *et al.* [6], an explicit expression for the complex optical conductivity $\tilde{\sigma}_{BCS}$ of a homogeneous BCS superconductor with arbitrary electron mean free path can usefully be utilized, covering whole range of BCS superconductors from clean to dirty limit. Although the Zimmerman *et al.* formula does not include the strong-coupling case, it still works well for a number of superconductors possessing somewhat larger (or smaller) gaps than the theoretical BCS prediction $2\Delta(0) \cong 3.53\, k_B T_c$ [10], such as NbN with the optical gap $(4 - 4.2) \times k_B T_c$ [11, 12]. For high-temperature superconductors complex conductivity does not follow the model of Zimmerman *et al.* and more robust two-fluid model is often used [13] for describing it.

The typical frequency and temperature dependence of the complex conductivity for a classical BCS-like superconductor (dirty limit) is shown in Fig. 1. The upper panel presents the real – dissipative – part of the complex conductivity. At zero temperature, one sees a sharp turning point at the frequency corresponding to the optical gap ($h\nu = 2\Delta(0)$); for higher frequencies dissipation due to the Cooper pair breaking mechanism becomes significant. With increasing temperature the optical gap is reduced and this turning point becomes less pronounced. Quasiparticle population increases with temperature from zero at zero temperature to its normal state value at T_c, consequently, conductivity σ_1 acquires non-zero values even for frequencies below the optical gap; $h\nu < 2\Delta(T)$. Even at somewhat higher temperatures the turning point at the optical gap

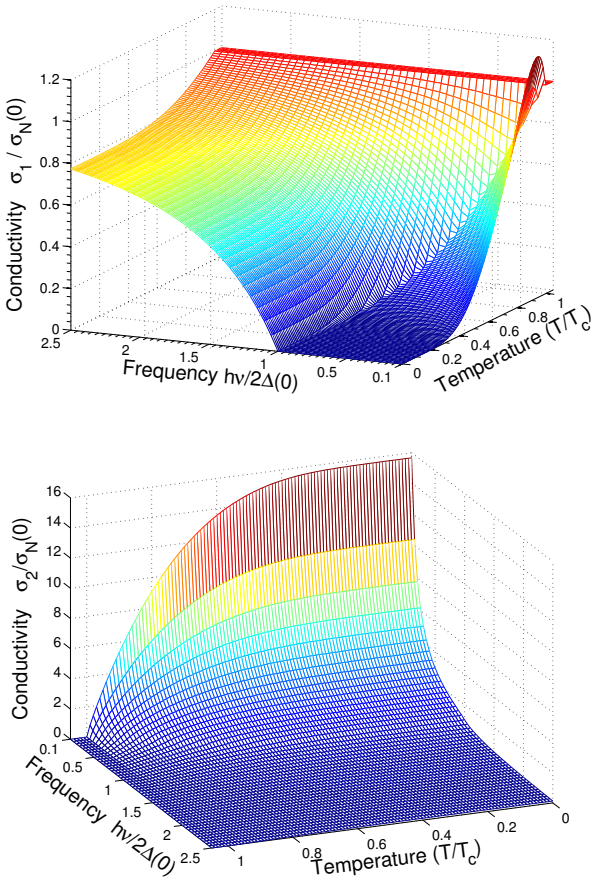

Figure 1: (Color online) Real (upper panel) and imaginary (lower panel) components of complex conductivity normalized to its normal state value of a BCS-like superconductor in dirty limit. Both temperature and frequency scales are in reduced dimensionless units T/T_c and $h\nu/2\Delta(0)$.

is still recognizable. At low frequencies, roughly for $h\nu < 0.2 \times 2\Delta(0)$, the temperature dependence exhibits a coherence peak near T_c, which serves as a manifestation of macroscopic quantum nature of superconductivity. For higher frequencies, σ_1 continuously rises from zero at zero temperature towards its normal-state value, displaying a derivative discontinuity at temperature T^* where $2\Delta(T^*) = h\nu$. This can be thought of as a direct consequence of the Cooper-pair breaking mechanism. For frequencies above the optical gap, σ_1 is finite even at zero temperature and monotonously increases towards its normal state value. The normal state conductivity is well-described by Drude model: $\tilde{\sigma}_N = \sigma_N(0)/(1 - i\omega\tau)$, where τ is the collision time. If $\omega\tau \ll 1$, then the real component $\sigma_{1n}(\omega)$ is almost constant, while the imaginary component $\sigma_{2n}(\omega)$ is al-

most zero.

The imaginary component of conductivity, $\sigma_2(\omega, T)$, is shown in the lower panel of Fig. 1. It behaves with frequency as $1/\omega$ and increases towards zero temperature as the condensate fraction grows. This typical $1/\omega$ dependence is a result of Kramers-Kroning relation coming from δ-function in $\sigma_1(\omega)$. Let us note that while the two-fluid model can describe $\sigma_2(\omega, T)$ quite reasonably, it cannot reliably describe $\sigma_1(\omega, T)$ because it does not comprise optical gap and consequently disregards all associated phenomena.

Complex dielectric function of superconducting materials (both in normal and in superconducting state) $\tilde{\varepsilon}(\omega)$ is assumed to be a linear superposition of several contributions. Most important in far-infrared region are those originating from conduction electrons, from phonons and from electronic absorption caused by interband transitions [6]. The contribution from conduction electrons can be expressed in terms of the complex conductivity $\tilde{\sigma}_{el}$ (for $T < T_c$ $\tilde{\sigma}_{el} = \tilde{\sigma}_{BCS}$ and for $T > T_c$ it follows Drude formula). In many cases the phonon and interband absorption terms can be neglected in the THz region, since they are negligible in comparison with the main contribution from conduction electrons. These former terms become more important for higher frequencies (for phonons typically above 10 THz [14]). In the following discussion, we shall neglect them, assuming $\varepsilon_\infty = 1$.

The key quantity in optical calculations is complex refractive index $\tilde{n}$, which can be obtained by straightforward calculation: $\tilde{n} = n + i\kappa = \sqrt{\tilde{\varepsilon}}$. In the normal state the real part of conductivity σ_1 dominates, therefore in the limit of low frequencies the refractive index is given as $\tilde{n} \approx \sqrt{\sigma_1/\varepsilon_0\omega}\ (1 + i)\,/\,\sqrt{2}$. On the other hand, at low temperature the situation is reversed – the imaginary part of conductivity σ_2 dominates while σ_1 for $h\nu < 2\Delta(0)$ vanishes. Consequently, κ increases towards its zero temperature value, while n decreases, reaching almost zero for frequencies below the optical gap.

2.2. Finite magnetic field

In this subsection we discuss behavior of thin films of type II superconductors in magnetic field. Clearly, externally applied magnetic field strongly affects physical properties of superconductors. Critical temperature T_c becomes reduced until it vanishes at the upper critical magnetic field B_{c2}. In sufficiently large magnetic field ($B > B_{c1}$) vortex matter is introduced into a superconducting layer. Quantized magnetic vortex represents a topological defect inside the superconductor. Energy gap is suppressed in a cylindrical volume with typical radius of the coherence length ξ and magnetic flux penetrates superconductor through a cylindrical volume with typical radius of the penetration depth. If, however, a superconducting layer has relevant typical dimension comparable with or smaller than the coherence length ξ, the superconductor is in the so called non-vortex regime. This is only possible for extremely thin films in parallel magnetic field, as discussed by Xi *et al.* [1].

Although vortices have been observed by a number of different techniques utilizing measurements of local magnetic flux or registering suppression of superconductivity, a satisfactory microscopic theoretical description is still missing. Clem [15] proposed a very simple treatment of vortices that works surprisingly well. He assumed that normal properties inside vortex cores are locally restored and the system can be thought of as a superconducting material with cylindrical inclusions of normal state material. The situation becomes more complicated as individual vortices interact with each other and might move. Moreover, physical properties of the superconducting matrix are modified by magnetic field.

To the best of our knowledge, there is as yet no fundamental theoretical model that would consider all physical phenomena associated with the presence of quantized vortices in type II superconductors.

In order to interpret magneto-optical measurements in THz region, we propose a simple phenomenological model, which neglects vortex motion and treats the superconducting thin film as a system consisting of a superconducting matrix and cylindrical inclusions of normal state material that represent the vortex lattice. Coherence length ξ is of order of a few nm (Ikebe [11] estimates the coherence length $\xi \cong 5$ nm for NbN at zero temperature) and the intervortex distance is usually of the same order – so the typical far infrared wavelengths are much larger. We can therefore use the long wavelength limit – electromagnetic radiation does not sense individual vortices and the system can be thought of as a homogeneous one, possessing an effective permittivity $\tilde{\varepsilon}_{eff}$, which in turn can be described by suitable effective medium theories.

Our model utilizes generalized Bruggeman theory for cylindrical inclusions [16], which can describe two composite systems for any volume fraction of vortex cores ($f_n = V_n/V$) and respects the geometry by considering polarisation effects via local electric fields. On the other hand, Lee [17] treated a similar case by Maxwell-Garnett theory (MGT).

The normal state volume fraction f_n is proportional to the area occupied by vortex cores, i.e. $\pi\xi(T)^2$,

and to vortex density. Upon increasing the temperature of a type II superconductor in external magnetic field, the fraction of its normal state will monotonously grow until superconductor becomes fully normal at T_c . Thus the superconducting to normal state transition can be thought of as continuous grow of the normal state area until f_n reaches unity at T_c. Using the temperature dependence of coherence length $\xi(T) = \xi(0)[1 - (T/T_c)^4]^{-1/2}$ we can describe the normal state fraction as

$$f_n = \frac{1 - \left(\frac{T_c(B)}{T_c(0)}\right)^4}{1 - \left(\frac{T}{T_c(0)}\right)^4} , \qquad (1)$$

where one ought to carefully distinguish between critical temperature in zero field $T_c(0)$ and critical temperature in non-zero field $T_c(B)$. The superconducting matrix fraction is given by $f_s = 1 - f_n$.

Let us mention here that different approximations for the temperature dependence of normal state fraction are possible. For example, Ikebe [11] expressed f_n via magnetic field and obtained somewhat different temperature dependence. As both these approaches have the same physical basis, it is hardly surprising that resulting temperature dependencies are qualitatively the same.

Although we are aware that magnetic field generally modifies $\tilde{\sigma}_{SC}$, we limit ourselves to a rather crude approximation, assuming that Zimmerman *et al.* expressions are valid even if T_c is replaced by its field value $T_c(B)$. A somewhat more rigorous treatment of superconducting fraction is also possible in some cases, e.g., by utilizing the pair-breaking theory of Abrikosov and Gorkov [18].

There are three principal mutual orientations of the thin film sample, external magnetic field and linear polarisation of the normally incident laser beam. In the case of Faraday orientation, magnetic field is perpendicular to the sample and any changes of its physical properties induced by magnetic field are isotropic in the plane of the sample. It follows that optical properties are the same for any direction of linear polarization and in the experiment it can be chosen arbitrarily. Note in passing that some experiments [20] suggest that utilization of circularly polarised radiation might also be useful. In Voigt orientation, when magnetic field is parallel with the surface of the thin film sample, two principal geometries are available - linear polarisation with electric field component parallel ($\mathbf{E} \parallel \mathbf{B}$) or perpendicular ($\mathbf{E} \perp \mathbf{B}$) to the magnetic field direction and anisotropic behavior is expected [19].

The simplest case to treat is the Voigt configuration - the case of $\mathbf{E} \parallel \mathbf{B}$. The local field is identical with the applied field and Brugemann expression for effective permittivity [16] reads

$$\tilde{\varepsilon}_{eff} = f_n\tilde{\varepsilon}_n + f_s\tilde{\varepsilon}_{SC} . \qquad (2)$$

Permittivity, resp. conductivity, is just the weighted average of normal state conductivity ($\tilde{\sigma}_N \approx \sigma_N(0) + 0i$). As f_n increases, the frequency and temperature dependence of σ_1 is shifted towards its normal state value. Similarly, σ_2 is pushed towards zero.

For the remaining two cases – Faraday configuration and the case of $\mathbf{E} \perp \mathbf{B}$ in Voigt configuration - the local field due to the charge induced on the interface between vortex inclusion and superconducting matrix leads to the same expression [16]

$$\tilde{\varepsilon}_{eff} = \frac{1}{2}\left(\beta \pm \sqrt{\beta^2 + 4\tilde{\varepsilon}_n\tilde{\varepsilon}_{sc}}\right) , \qquad (3)$$

where $\beta = (1 - 2f_n)(\tilde{\varepsilon}_n - \tilde{\varepsilon}_{sc})$ and the sign of the square root is chosen so that $Im(\varepsilon_{eff}) > 0$. Although the expression for the two mentioned magneto-optical configurations is formally the same, these two cases are not identical. The reason is that $T_c(B)$ acquires different values for magnetic field parallel with the thin film and perpendicular to it. Additionally, the vortex lattices will be very different for $\mathbf{B}^{\perp}$ and $\mathbf{B}^{\parallel}$. In perpendicular field (assuming no crystal defects) vortices will arrange themselves into a triangular lattice [10]. In parallel field this is not possible, because the film thickness is of the same order as ξ or intervortex distance. Generally, THz radiation can cause vortices to move. However, not in the special case when electric field points in the same direction as the vortex axis $\mathbf{E} \parallel \mathbf{B}$, when dissipation from vortex dynamics ought to be switched off.

3. Brief description of a complementary experiment

In a typical experimental run, we set the frequency of incoming laser beam (between 0.40 THz and 2.52 THz) and transmission of linearly polarised beam normally incident to a sample is measured while the temperature of the sample and/or applied magnetic field is slowly (avoiding any hysteresis) swept. Absolute value of transmission is difficult to determine, therefore transmission - the quantity of interest - is displayed normalized, so that its normal state value (with good accuracy constant above the critical temperature) is unity. Further details can be found in our previous publications [2, 3, 4].

Typical samples for the experiment are thin superconducting films deposited on suitable transparent dielectric substrate, prepared by various layer growing tech-

niques. It is important that the substrate has similar lattice parameters as the deposited superconducting film. In some cases optimal lattice parameters of the substrate are achieved at the cost of anisotropic properties of the substrate. Substrates substantially influence transmission of such a double layer system, it is therefore important to accurately determine their physical properties.

Critical temperature of a very thin film might appreciably depend on its thickness [21]. Certain films can exhibit higher critical temperatures than bulk materials since they can be prepared with greater purity and with less defects than bulk samples. In our research we mostly use NbN thin films as typical representatives of type II BCS – like superconductors.

As shown by Semenov [12], each individual NbN film has unique properties; this applies in particular to its electric conductivity. In table 1, we list properties of one particular NbN film, which will serve as our model example for subsequent numerical analysis. This film was grown on an anisotropic sapphire R-cut substrate – the c-axis at angle $\varphi = 57.6°$ with respect to the surface normal. The extraordinary ray axis is oriented diagonally, at the angle $\alpha = 45°$ with respect to the y – axis. Ordinary and extraordinary refractive indices n_o and n_e can be found in literature [22]. Extraordinary index $n_e(\varphi = 57.6°)$ associated with R-cut sapphire can be calculated using values for n_o and n_e [23]

$$\frac{1}{n_e(\varphi)^2} = \frac{\cos^2(\varphi)}{n_o^2} + \frac{\sin^2(\varphi)}{n_e^2} \tag{4}$$

Sapphire exhibits only a weak dispersion in the THz region, which we take into account by linear fit through data obtained from literature [22]: $n_o = 3.047 + 0.021 \times 10^{-12}\nu$ and $n_e(\varphi = 57.6°) = 3.274 + 0.030 \times 10^{-12}\nu$. Further, we assume that the optical gap at zero temperature is given as $2\Delta(0) = 4.16\ k_B T_c$.

Table 1: Parameters of the sample

Film	d_1 [nm]	T_c [K]	$\sigma_N(0)$ $\Omega^{-1}.m^{-1}$	substrate	d_2 [mm]
NbN	15	16	0.51×10^6	Al_2O_3	0.33

4. Transmission calculation

4.1. Free film in zero magnetic field

We begin with theoretical calculation of transmission through a free superconducting film. This starting point will be essential later for understanding of more complicated behavior of multilayered systems. Moreover, theoretical transmission of free film is also important for other techniques than laser thermal spectroscopy: Time Domain Terahertz Spectroscopy [11, 13] or Backward-Wave Oscillator Spectroscopy [24]. Let us stress, however, that in this article only the case of normally incident beam is discussed.

A free film is physically ideal system for measuring transmission, which, however, does not depend entirely on its superconducting properties – its thickness is equally as important. In the theoretical limit of zero thickness transmittance $\mathcal{T}$ reaches unity and, consequently, reflectance $\mathcal{R}$ and absorptance $\mathcal{A}$ become zero. With increasing thickness (assuming temporarily that film parameters do not depend on thickness) transmission sharply falls while reflection is growing. Absorption is also growing for small thicknesses, however, with thickness increasing further huge reflection leads to a decrease in absorption and, as a consequence, absorption exhibits a maximum for certain film thickness. Note that the described thickness dependence depends significantly on wavelength of the incident light.

As an illustrative example, we calculate optical properties of a free NbN film with parameters listed in table 1. In Fig. 2 transmission, reflection and absorption are plotted versus normalized dimensionless temperature T/T_c and frequency. Similar calculations for different thicknesses of order tens of nanometers show that these quantities – transmission, reflection and absorption – are qualitatively the same.

The behavior of these three interconnected variables can be understood on the basis of $\tilde{\sigma}(T, \nu)$, as plotted in Fig. 1. For low temperature and frequency, σ_1 is almost zero and therefore absorption follows this tendency, see lower panel of Fig. 2. Low resistivity in this region leads to high reflection and consequently to a low transmission. By careful observation of transmission in upper panel of Fig. 2 one sees a thermal peak in the temperature dependence of transmission for frequencies below the optical gap. Numerical analysis explains this peak as a competition between temperature dependencies of $\sigma_1(T)$ and $\sigma_2(T)$, which cause opposite tendencies on resulting transmission. For even lower frequencies, when the coherence peak appears in $\sigma_1(T)$, both the real and imaginary parts of conductivity grow from T_c towards lower temperature within a small temperature interval and no peak in transmission is present. This excludes any direct connection between the coherence peak and the thermal peak described above. For frequencies around and above the optical gap, $\sigma_2(T)$, the temperature dependence prevails and transmission grows monotonically from T_c towards zero temperature.

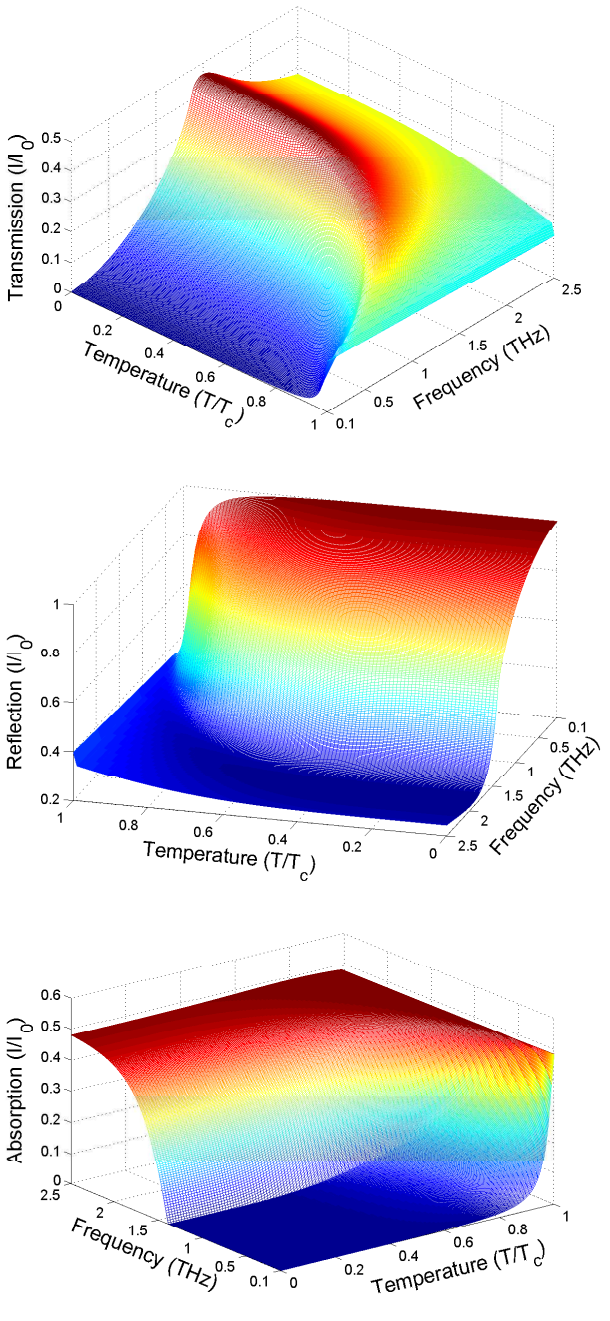

Figure 2: (Color online) Transmission (upper panel), reflection (middle panel) and absorption (lower panel) of free NbN film with parameters from table 1. These quantities are expressed in dimensionless form, as a ratio between the transmitted (reflected, absorbed) intensities and the incoming intensity I_0. The frequency corresponding to the optical gap is ≅ 1.39 THz.

4.2. Double layer film in zero magnetic field

A thin superconducting film cannot stand alone – an essential part of any thin superconducting sample for optical measurements is its substrate layer, usually much thicker than the superconducting film itself. In order to explain optical response of such a double-layer system, one has to assume all possible interference effects. Moreover, surface roughness and even a very thin oxide layer on superconductor might generally influence transmission.

In order to treat transmission of multilayer systems quantitatively, we utilize Yeh formalism [7, 8]. This powerful tool can be applied even for anisotropic homogeneous layers, as described in more detail in Appendix. If all matrices in Yeh formalism are block diagonal (for example in the case of isotropic film and anisotropic substrate), then ordinary and extraordinary rays are transmitted through double layer separately and transmission can be calculated for each ray in the same way as for isotropic layers and their intensities should be added at the end [4].

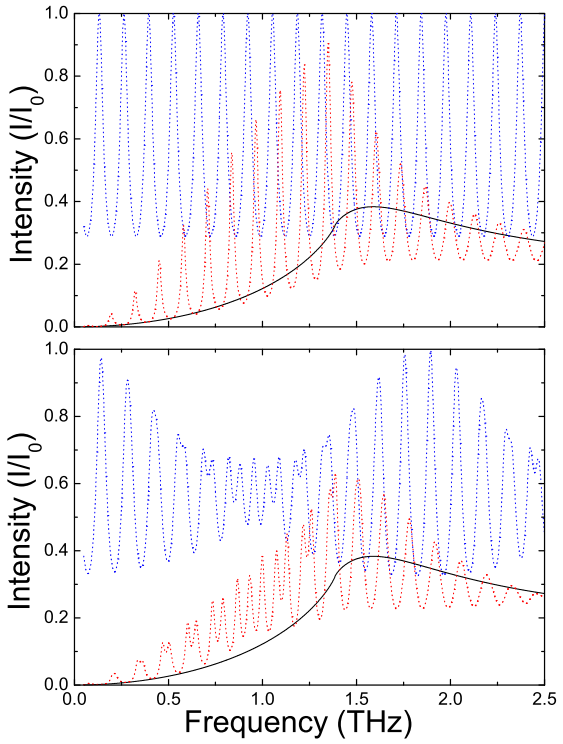

Figure 3: (Color online) Numerical analysis (red dotted line) of interference effects for a NbN/sapphire double-layer system. Transmission of free film (black solid line) and of bare substrate (blue dotted line) is also given. In upper figure we assumed that NbN film mentioned in the text is deposited on 0.333 mm thick isotropic Si substrate with refractive index n_{Si} = 3.4175 constant with variation less than 0.0001 in whole range of interest [14]. Bottom figure displays the case of NbN on R-cut sapphire.

Interference effects due to the substrate are very im-

portant since substrates are typically rather thick (d_{sub} is about tenths of millimeter), with optical thickness $n_{sub}d_{sub}$ (n_{sub} is of orders unity, typically 2-4) comparable with the wavelength (1 THz corresponds to 0.33 mm) of the incident laser beam. The substrate thus behaves as an asymmetric Fabry-Perot resonator. Transmission of such a double-layer system can be greatly enhanced or diminished, see Fig 3, where the interference effects are demonstrated by numerical calculation for two particular examples of NbN on Si and sapphire (R-cut) substrates. One sees that the overall transmission of a double layer is given by transmission through the NbN superconducting film, but modulated by the interference effects due to its substrate. One can also compare transmission of NbN film on isotropic substrate (Si) and anisotropic R-cut sapphire substrate. Still, the temperature dependence of transmission of such a double layer system at a fixed frequency preserves all fundamental features of transmission through a free film, but substantially modified. In order to appreciate these changes, we present the temperature dependence of free film and double layer system for several selected frequencies in Fig. 4.

In some cases, there is an interlayer between the thin superconducting film and its substrate. If the interlayer is very thin, i.e., phase almost does not change as beam propagates through the interlayer, then its influence on transmission will be negligible. Following the same argument, oxidized surface of NbN $\approx$ 1 nm thick [12] will not have any appreciable effect. For optical measurements, ideally, substrate should be a plane-parallel both side polished slab with negligible roughness. Rough surface can be treated by Bruggeman theory as an effective medium consisting of air or gaseous helium and the substrate's material – if the roughness is small enough, diffraction effects can be neglected. In that case, slightly rough surface can be thought of as another interlayer and can be neglected. Let us stress that the superconducting film itself cannot be neglected since it has enormously high values of refractive index in comparison with the interlayer material.

Note that any anisotropy of superconducting film (some superconductors are anisotropic by nature or anisotropy can be induced by external magnetic field) in general requires the full power of Yeh formalism.

4.3. Double layer film in non-zero magnetic field

Description of transmission through a superconducting thin film in non-zero magnetic field becomes much more complicated. In the case of Voigt orientation one can measure anisotropic optical properties. Matrices in Yeh formalism are no longer block diagonal and it is

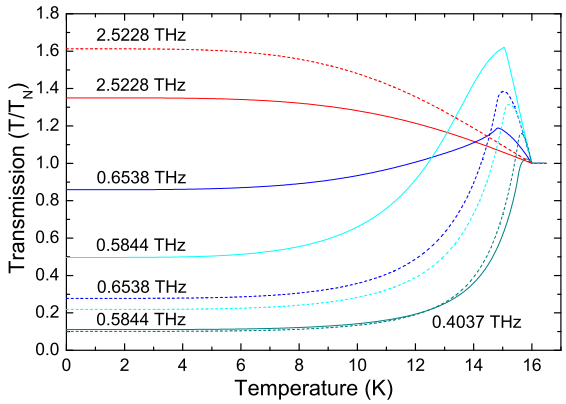

Figure 4: (Color online) Comparison of transmission of free NbN film (solid lines) and NbN thin film on R-cut sapphire substrate (dotted lines) for several experimentally available frequencies as indicated. Transmission is normalized by its normal state value.

no longer possible to decompose the beam into two different parts with their own eigenpolarisations – mode coupling occurs. Fortunately, in the case of our model sample – NbN thin layer on sapphire – this anisotropic non-linear system behaves quite reasonably and exhibits properties similar to those in zero magnetic field.

Returning to the transmission of a free film (Fig. 2), changes occurring in magnetic field can be explained relatively easily. First of all, the critical temperature decreases with increasing magnetic field. Further, magnetic field spoils superconducting properties, which results in decreasing reflectivity for lower frequencies and temperatures and, as a consequence, the low transmission plateau is shifted up. At the same time the maximum in transmission is shifted towards lower frequencies and temperatures. Not surprisingly, transmission of superconducting state has a tendency to change towards its normal state value. Although this crude qualitative description holds for both vertical and horizontal polarisations, there are important quantitative differences. Let us stress that the presence of the birefringent sapphire substrate makes these tendencies less straightforward.

Our main aim in this section is to give theoretical prediction of typical temperature dependencies of transmission for several frequencies available in our experiment. Theoretical calculations of transmission in parallel magnetic field (computed for 0,2,4,6,8 and 10 T) for two typical linear polarisations of electric field – vertical ($\mathbf{E} \perp \mathbf{B}$) and horizontal ($\mathbf{E} \parallel \mathbf{B}$) – for frequencies demonstrating typical cases for our NbN double-layer are given in Fig. 5. Experimentally determined critical temperatures $T_c(B)$ were used – their values can easily be seen in Fig. 5 as a transmission onset at $T_c(B)$.

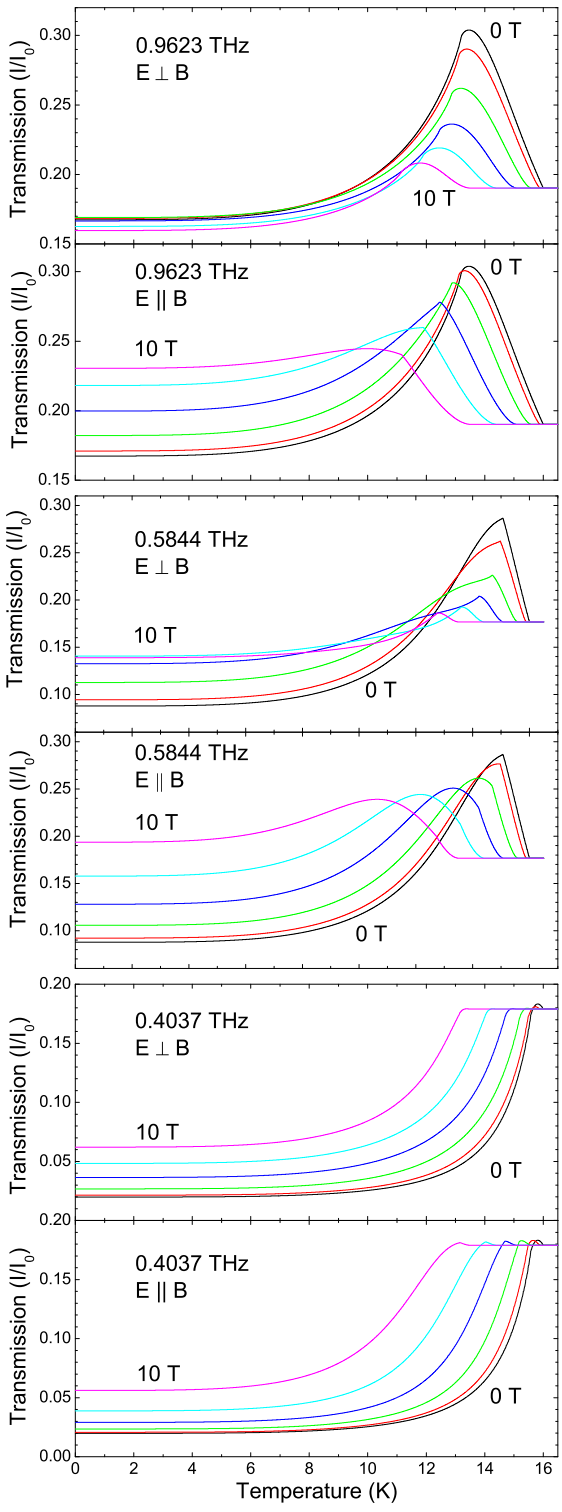

Figure 5: (Color online) Temperature dependencies of transmission of thin NbN film in (horizontal) magnetic field (0, 2, 4, 6, 8 and 10 T) for three selected frequencies as indicated, for both horizontal and vertical beam polarisations.

Note that results for Faraday configuration will be qualitatively the same as for the case of vertical polarisation since both these cases follows the same formula (3) and the only difference in the frame of our model is the different $T_c(B)$ dependence.

The predicted temperature dependence of transmission for low frequencies (Fig. 5 - lower panel) as well as for those above the optical gap are very similar for vertical and horizontal polarisation. Especially for frequencies above the optical gap, properties of superconducting and normal state are almost the same and this is why any difference between polarisations due to presence of vortices is hardly expected. A crucial test of our theory is in the intermediate frequency interval – at frequencies slightly lower than the gap frequency. One can see in upper and middle panel of Fig. 5 that substantial differences in transmission for vertical and horizontal polarisation are indeed expected.

Experimental efforts should therefore concentrate on this critical interval of frequencies, where this predicted anisotropy in transmission ought to be easily observable. Moreover, comparison of theoretical predictions with experiments might shed light on possible importance of vortex dynamics. Indeed, for polarisation parallel with vortex axis one may expect better agreement with theoretical prediction since in this case transmission is hardly influenced by possible vortex motion. Additionally, optical measurements in Voigt orientation for horizontal and vertical polarisation might serve as a useful tool in proving the existence and investigating physical properties of the non-vortex regime [1], starting from film thicknesses much smaller than the coherence length and increasing the thickness up to films thick enough to undoubtedly display vortex dynamics.

Any quantitative prediction how vortex dynamics might affect transmission seems extremely tricky, as vortex motion will not only increase dissipation (σ_1) but at the same time a decrease in the imaginary part of conductivity can be expected. We are not aware of any model capable of accounting for vortex motion over the whole temperature and frequency ranges. Thus we did not include vortex motion in our transmission calculation. However, in the linear regime for low frequencies and low temperatures such that $2\Delta(T) \gg h\nu$ the response due to the vortex motion can be described by Coffey-Clem model [25, 19] or time-dependent Ginzburg-Landau theory [26]. Together with influence of thick substrate prone to interference effects, any quantitatively accurate prediction of transmission changes are not feasible without further improvements of the theoretical model which will have to explicitly include other ingredients, such as BCS response, local

charge effects and vortex dynamics.

Let us comment on one substantial disadvantage of our experimental method. Measured transmission alone cannot provide complete information on THz properties of a superconductor, in that it is not possible to obtain complex conductivity. On the other hand, we already demonstrated that transmission serves as a convenient quantity for testing various models and provides useful physical insights. In fact, one can also measure reflection and knowing both transmission and reflection, the complex conductivity can in principle be deduced [27], however, non-linear nature of equations describing interference effects does not make such an analysis straightforward. Corresponding values of reflection and transmission do not have to correspond to unique values of σ_1 and σ_2, which makes correct analysis together with further complications due to noise and other sources of experimental errors extremely tricky. A simple test, starting from σ_1 and σ_2 to calculate transmission and reflection and adding realistic noise and then subsequent use of Newton method to obtain complex conductivity, revealed that the input values do not always coincide with the output values. Simultaneous measurement of transmission and phase is experimentally more demanding, however, in this case the non-linear system of equations should be numerically more stable. It is therefore more advantageous to simultaneously measure transmission and phase rather than transmission and reflection [28].

5. Conclusions

To conclude, we attempted to discuss THz properties of classical superconducting films using the explicit Zimmerman *et al.* formula for conductivity. We did not consider the strong coupling case, however, our BCS theory based approach works well also for superconductors with $2\Delta(0)/k_BT_c$ ratio larger than the theoretical BCS value of 3.53. As an illustrative example, transmission of NbN thin layer on anisotropic substrate is computed and presented, and has been found in good quantitative agreement with our previous experiments [4] performed in zero magnetic field.

When magnetic field is introduced into superconductors, BCS theory is no longer capable of exact treatment of their optical properties, as quantized magnetic vortices significantly alter their superconducting properties. We incorporated Clem description of a single vortex into effective medium theory and predicted different behavior for various mutual orientations of applied magnetic field and linear polarisation of incoming radiation with respect to the film surface. Since our proposed model is based on zero field BCS conductivity, it becomes less precise for higher magnetic field. Its predicting power is further limited by the fact that it neglects vortex dynamics. On the other hand, in our earlier study [3] we have found that it is capable of explaining experimental data rather well, at least at qualitative level and partly also at quantitative level. To the best of our knowledge, there is no other model capable of quantitative description of complex conductivity in various magnetic fields over sufficiently broad temperature and frequency range.

Our model calculations lead to a very interesting option for observing the influence of vortex presence and vortex dynamics, by measuring optical properties using linear polarisation parallel with and perpendicular to vortex axes. In case of horizontal polarisation, radiation does not cause vortices to move and vortex dynamics will not contribute. In experimentally almost identical situation but with vertical polarisation, electric field forces vortices to move. It may be very instructive to compare these two measurements in order to determine possible influence of vortex motion. Further, measurements with horizontal and vertical polarisation on superconducting films of variable thickness (from thicknesses smaller than the coherence length to thick films displaying essentially bulk superconducting features) ought to indicate an onset of vortex regime. Our experimental efforts directly related to the outlined problems are under progress and a full account will be reported elsewhere.

Acknowledgments

One of us (MŠ) is very grateful to Š. Višňovský for valuable advices regarding numerical calculation of transmission, especially in frame of Yeh formalism. This work was supported by GAČR under contract P204/11/0015. Grant ME 10069 and the European program NES are also acknowledged. The work of MŠ was supported by SVV-2012-265303 program of Charles University in Prague.

APPENDIX: Yeh formalism

The aim of this appendix is to describe calculation of transmission through a multilayer system using Yeh formalism in detail. Multilayer system of interest is introduced in Fig. .6. Explicit formulae for numerical calculations are also given.

Yeh formalism, a 4 x 4 matrix algebra, which combines and generalizes Abelès 2 x 2 matrix method and

Jones 2 x 2 matrix method, is introduced to investigate plane-wave propagation in an arbitrarily anisotropic homogeneous medium [7, 8]. In this method, each layer of finite thickness is represented by a propagation matrix which is diagonal and consists of the phase excursions of the four partial plane waves. Each side of an interface is represented by a dynamical matrix that depends on the direction of the eigenpolarisations in the anisotropic medium.

A wave equation has to be solved in each layer, with condition for non-trivial plane-wave solution leading to a quartic equation for the wavevector $\mathbf{k}$. The four solutions correspond to beams with two different eigenpolarisations $\mathbf{p}$, traveling in positive and in negative directions. Although eigenpolarisation does not have to be normalized, here we do so for convenience. We assume that electromagnetic radiation propagates along the z-axis normally to the sample surface, see figure .6. Thus, electromagnetic radiation is decomposed into four partial waves

$$\mathbf{E}(z) = \sum_{\sigma=1}^{4} A_\sigma \mathbf{p}_\sigma \exp i(k_\sigma(z - z_n) - \omega t) \ , \qquad (.1)$$

where A_σ denotes the amplitude and $\mathbf{p}_\sigma$ is the eigenpolarisation vector. Amplitude A_σ and eigenpolarisation $\mathbf{p}_\sigma$ depend on the z-coordinate which takes into account the corresponding layer. Partial waves are ordered, so $\mathbf{E}_1$ corresponds to the beam with $\mathbf{p}_1$ polarisation traveling in positive z - direction, $\mathbf{E}_2$ beam traveling in negative z - direction with the same polarisation $\mathbf{p}_1$, $\mathbf{E}_3$ beam with $\mathbf{p}_3$ polarisation traveling in positive z - direction and $\mathbf{E}_4$ beam traveling in negative z - direction with the same polarisation $\mathbf{p}_3$. In the case of anisotropic environment the partial waves correspond to ordinary and extraordinary rays. For isotropic material, polarisation can be chosen arbitrarily. For convenience, we assume linear polarisation. Magnetic field is obtained from Maxwell equation and is given by

$$\mathbf{H}(z) = \sum_{\sigma=1}^{4} A_\sigma \mathbf{q}_\sigma \exp i(k_\sigma(z - z_n) - \omega t) \ , \qquad (.2)$$

where

$$\mathbf{q}_\sigma = (c\mathbf{k}_\sigma/\omega\mu) \times \mathbf{p}_\sigma \ . \qquad (.3)$$

Imposing the continuity of E_x, E_y, H_x and H_y at the interface $z = z_n$ leads to

$$\begin{aligned}
\sum_{\sigma=1}^{4} A_\sigma(z_n^-)\mathbf{p}_\sigma(n-1)\cdot\mathbf{x} &= \sum_{\sigma=1}^{4} A_\sigma(z_n^+)\mathbf{p}_\sigma(n)\cdot\mathbf{x} \\
\sum_{\sigma=1}^{4} A_\sigma(z_n^-)\mathbf{p}_\sigma(n-1)\cdot\mathbf{y} &= \sum_{\sigma=1}^{4} A_\sigma(z_n^+)\mathbf{p}_\sigma(n)\cdot\mathbf{y} \\
\sum_{\sigma=1}^{4} A_\sigma(z_n^-)\mathbf{q}_\sigma(n-1)\cdot\mathbf{x} &= \sum_{\sigma=1}^{4} A_\sigma(z_n^+)\mathbf{q}_\sigma(n)\cdot\mathbf{x} \\
\sum_{\sigma=1}^{4} A_\sigma(z_n^-)\mathbf{q}_\sigma(n-1)\cdot\mathbf{y} &= \sum_{\sigma=1}^{4} A_\sigma(z_n^+)\mathbf{q}_\sigma(n)\cdot\mathbf{y}, \qquad (.4)
\end{aligned}$$

where z_n^- (z_n^+) correspond to the left (right) side of the interface and expressions on the left hand side of equations are associated with the left side of interface; right hand side of equations are associated with the right side of the interface.

Using these four equations we can associate amplitudes at z_{n-1}^- and z_n^-

$$\begin{pmatrix} A_1(z_{n-1}^-) \\ A_2(z_{n-1}^-) \\ A_3(z_{n-1}^-) \\ A_4(z_{n-1}^-) \end{pmatrix} = D(n-1)^{-1}D(n)P(n) \begin{pmatrix} A_1(z_n^-) \\ A_2(z_n^-) \\ A_3(z_n^-) \\ A_4(z_n^-) \end{pmatrix}, \qquad (.5)$$

where $D(n)$ is the dynamical matrix

$$D(n) = \begin{pmatrix} \mathbf{p}_1(n)\cdot\mathbf{x} & \mathbf{p}_2(n)\cdot\mathbf{x} & \mathbf{p}_3(n)\cdot\mathbf{x} & \mathbf{p}_4(n)\cdot\mathbf{x} \\ \mathbf{q}_1(n)\cdot\mathbf{y} & \mathbf{q}_2(n)\cdot\mathbf{y} & \mathbf{q}_3(n)\cdot\mathbf{y} & \mathbf{q}_4(n)\cdot\mathbf{y} \\ \mathbf{p}_1(n)\cdot\mathbf{y} & \mathbf{p}_2(n)\cdot\mathbf{y} & \mathbf{p}_3(n)\cdot\mathbf{y} & \mathbf{p}_4(n)\cdot\mathbf{y} \\ \mathbf{q}_1(n)\cdot\mathbf{x} & \mathbf{q}_2(n)\cdot\mathbf{x} & \mathbf{q}_3(n)\cdot\mathbf{x} & \mathbf{q}_4(n)\cdot\mathbf{x} \end{pmatrix}. \qquad (.6)$$

and $P(n)$ is the propagation matrix, which describes free propagation in the layer and depends only on the phase excursion of these four partial waves

$$P = \begin{pmatrix} e^{(+ik_1 d)} & 0 & 0 & 0 \\ 0 & e^{(+ik_2 d)} & 0 & 0 \\ 0 & 0 & e^{(+ik_3 d)} & 0 \\ 0 & 0 & 0 & e^{(+ik_4 d)} \end{pmatrix}. \qquad (.7)$$

There are no off-diagonal terms since we are working in eigenpolarisation basis.

The transfer matrix can be defined as

$$T(n-1, n) = D(n-1)^{-1}D(n)P(n). \qquad (.8)$$

The matrix equation which relates amplitudes $A(z_0^-)$ and $A(z_m^+)$ is therefore given by

$$\begin{pmatrix} A_1(z_0^-) \\ A_2(z_0^-) \\ A_3(z_0^-) \\ A_4(z_0^-) \end{pmatrix} = \prod_{i=1}^{(m)} T(i-1, i) \begin{pmatrix} A_1(z_m^+) \\ A_2(z_m^+) \\ A_3(z_m^+) \\ A_4(z_m^+) \end{pmatrix} \qquad (.9)$$

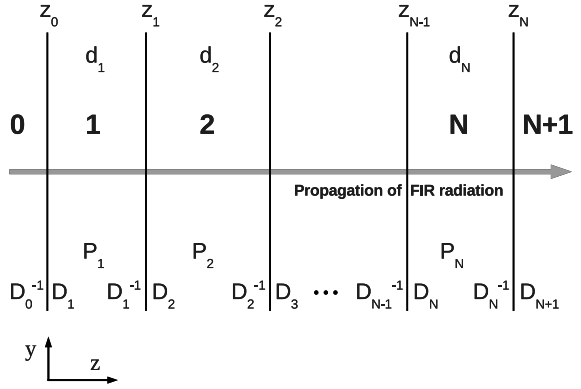

Figure .6: Schematics and orientation of a multilayered sample. Individual layers are enumerated $1, 2 \ldots N$ and surrounding environment as 0, $N+1$, respectively. The method of calculating resulting transfer matrix and orientation of the laboratory system are also indicated.

as it is indicated in Fig. .6.

In the case when m is equal to $N+1$, this equation relates amplitudes of incoming and of outcoming radiation for multilayer system with N layers. We can write

$$\begin{pmatrix} A_1(z_0^-) \\ A_2(z_0^-) \\ A_3(z_0^-) \\ A_4(z_0^-) \end{pmatrix} = \begin{pmatrix} M_{11} & M_{12} & M_{13} & M_{14} \\ M_{21} & M_{22} & M_{23} & M_{24} \\ M_{31} & M_{32} & M_{33} & M_{34} \\ M_{41} & M_{42} & M_{43} & M_{44} \end{pmatrix} \begin{pmatrix} A_1(z_N^+) \\ 0 \\ A_3(z_N^+) \\ 0 \end{pmatrix}, \tag{.10}$$

where we used the fact that incoming radiation propagates from left to right and not the other way around, therefore putting $A_2(z_N^+)$ and $A_4(z_N^+)$ equal to zero. $A_2(z_0^-)$ and $A_4(z_0^-)$ are amplitudes of light reflected from the multilayered structure with their eigenpolarisations $\mathbf{p}_2$, $\mathbf{p}_4$, respectively. Similarly, $A_1(z_N^+)$ and $A_3(z_N^+)$ are amplitudes of light transmitted through the multilayered structure with their eigenpolarisations $\mathbf{p}_2$, $\mathbf{p}_4$, respectively. These amplitudes can be related to the incoming light described by amplitudes $A_1(z_0^-)$, $A_3(z_0^-)$ via transmission coefficients:

$$t_{11}^{(0,N+1)} = \left(\frac{A_1(z_N^+)}{A_1(z_0^-)}\right)_{A_3(z_0^-)=0} = \frac{M_{33}}{M_{11}M_{33} - M_{13}M_{31}} \tag{.11}$$

$$t_{13}^{(0,N+1)} = \left(\frac{A_3(z_N^+)}{A_1(z_0^-)}\right)_{A_3(z_0^-)=0} = \frac{-M_{31}}{M_{11}M_{33} - M_{13}M_{31}} \tag{.12}$$

$$t_{31}^{(0,N+1)} = \left(\frac{A_1(z_N^+)}{A_3(z_0^-)}\right)_{A_1(z_0^-)=0} = \frac{-M_{13}}{M_{11}M_{33} - M_{13}M_{31}} \tag{.13}$$

$$t_{33}^{(0,N+1)} = \left(\frac{A_3(z_N^+)}{A_3(z_0^-)}\right)_{A_1(z_0^-)=0} = \frac{M_{11}}{M_{11}M_{33} - M_{13}M_{31}} \tag{.14}$$

Using the defined transmission coefficient, we can simplify the algebra:

$$\begin{pmatrix} A_1(z_N^+) \\ A_3(z_N^+) \end{pmatrix} = \begin{pmatrix} t_{11} & t_{31} \\ t_{13} & t_{33} \end{pmatrix} \begin{pmatrix} A_1(z_0^-) \\ A_3(z_0^-) \end{pmatrix}. \tag{.15}$$

In the case of isotropic multilayered structure, t_{13} and t_{31} are zero so the matrix in eq. (.15) is diagonal.

Transmittance is given as

$$\mathcal{T} = \frac{n_N}{n_0}(|A_1(z_N^+)|^2 + |A_3(z_N^+)|^2) \tag{.16}$$

assuming isotropic non-dissipative surroundings.

Analogically, the whole procedure can be applied for reflection.

In our case, the dynamical matrices of helium gas ($\tilde{n}_x = \tilde{n}_y = 1$) and superconducting NbN layer have the same structure:

$$D = \begin{pmatrix} 1 & 1 & 0 & 0 \\ \tilde{n}_x & -\tilde{n}_x & 0 & 0 \\ 0 & 0 & 1 & 1 \\ 0 & 0 & -\tilde{n}_y & \tilde{n}_y \end{pmatrix}, \tag{.17}$$

while the dynamical matrix, D_{sap}, for sapphire is more complicated:

$$\begin{pmatrix} \cos(\alpha) & \cos(\alpha) & \sin(\alpha) & \sin(\alpha) \\ \tilde{n}_o\cos(\alpha) & -\tilde{n}_o\cos(\alpha) & \tilde{n}_e(\varphi)\sin(\alpha) & -\tilde{n}_e(\varphi)\sin(\alpha) \\ \sin(\alpha) & \sin(\alpha) & -\cos(\alpha) & -\cos(\alpha) \\ -\tilde{n}_o\sin(\alpha) & \tilde{n}_o\sin(\alpha) & \tilde{n}_e(\varphi)\cos(\alpha) & -\tilde{n}_e(\varphi)\cos(\alpha) \end{pmatrix} \tag{.18}$$

Here $\tilde{n}_o$ is the ordinary refractive index, $\tilde{n}_e(\varphi)$ is the extraordinary refractive index and $\alpha = 45°$ is the angle between the direction of eigenpolarisation of the normal beam and x-axis of the laboratory frame. The propagation matrix has the same form as expression (.7) for every system. In table .2 we specify the corresponding values of k_σ (positive sign corresponds to k_1, k_3, negative sign to k_2, k_4).

Table .2: Values of wavevectors

Layer	$k_{1,2}$	$k_{3,4}$
NbN	$\pm 2\pi n_x/\lambda$	$\pm 2\pi n_y/\lambda$
sapphire	$\pm 2\pi n_o/\lambda$	$\pm 2\pi n_e/\lambda$
helium gas	$\pm 2\pi/\lambda$	$\pm 2\pi/\lambda$

As one can see from explicit expressions for dynamical and propagation matrices, in the case of isotropic

systems both matrices will become block-diagonal and coupling between modes disappears. It is thus possible to investigate each polarisation independently and corresponding formulae are greatly simplified. In nonzero magnetic field the dynamical matrix of NbN film, eq. (.17), is still block diagonal, thanks to suitably chosen laboratory system, so x- and y-axes correspond to the direction of eigenpolarisations of ordinary and extraordinary beams.

By different suitable choice of laboratory system one can make the dynamical matrix of the R-cut sapphire, eq. (.18), block diagonal, too. However, there is no laboratory system in which these two dynamical matrices would be block diagonal at the same time.

Mansuripur [29] found a recursive 2x2 matrix formalism which gives results in agreement with Yeh formalism. We have used this formalism to check that results obtained by the numerical recipe described above are indeed correct.

References

[1] X. Xi, J. Hwang, C. Martin, D. B. Tanner, G. L. Carr, Far-Infrared Conductivity Measurements of Pair Breaking in Superconducting $Nb_{0.5}Ti_{0.5}N$ Thin Films Induced by an External Magnetic Field, Phys. Rev. Lett. 105 (2010) 257006.

[2] R. Tesař, J. Koláček, Z. Šimša, M. Šindler, L. Skrbek, K. Ilin, M. Siegel, Terahertz transmission of NbN superconductor thin film, Physica C 470 (2010) 932-934.

[3] M. Šindler, R. Tesař, J. Koláček, L. Skrbek, Z. Šimša, Far-infrared transmission of a superconducting NbN film, Phys. Rev. B 81 (2010) 184529.

[4] R. Tesař, M. Šindler, K. Il'in, J. Koláček, M. Siegel, L. Skrbek, Terahertz thermal spectroscopy of a NbN superconductor, Phys. Rev. B 84 (2011) 132506.

[5] G. D. Holah, S. Perkowitz, Far infrared laser thermal spectroscopy of superconductors, Int. Journal of Infrared and Millimeter Waves 2 (1981) 581-586.

[6] W. Zimmermann, E.H. Brandt, M. Bauer, E. Seider, L. Genzel, Optical conductivity of BCS superconductors with arbitrary purity, Physica C 183 (1991) 99-104.

[7] P. Yeh, Electromagnetic propagation in birefrigent layered media, J. Opt. Soc. Am. 69 (1979) 742-756.

[8] P. Yeh, Optics of anisotropic layered media: A new 4×4 matrix algebra, Surface Science 96 (1980) 41-53.

[9] D. C. Mattis, J. Bardeen, Theory of the Anomalous Skin Effect in Normal and Superconducting Metals, Phys. Rev. 111 (1958) 412-417.

[10] M. Tinkham, Introduction to Superconductivity, Dover Publications, New York, 2004.

[11] Y. Ikebe, R. Shimano, M. Ikeda, T. Fukumura, M. Kawasaki, Vortex dynamics in a NbN film studied by terahertz spectroscopy, Phys. Rev. B 79 (2009) 174525.

[12] A. Semenov,B. Günther, U. Böttger, H.-W. Hübers,H. Bartolf, A. Engel, A. Schilling, K. Ilin, M. Siegel,R. Schneider, D. Gerthsen, N. A. Gippius, Optical and transport properties of ultrathin NbN films and nanostructures, Phys. Rev. B 80 (2009) 054510.

[13] S. D. Brorson, R. Buhleier, I. E. Trofimov, J. O. White, Ch. Ludwig, F. F. Balakirev, H.-U. Habermeier, J. Kuhl, Electrodynamics of high-temperature superconductors investigated with coherent terahertz pulse spectroscopy, J. Opt. Soc. Am. B 13 (1996) 1979-1993.

[14] Yun-Shik Lee, Principles of Terahertz Science and Technology, Springer, New York, 2009.

[15] J.R. Clem, Simple model for the vortex vore in a type II superconductor, Journal of Low Temperature Physics 18 (1975) 427-434.

[16] G. L. Carr, S. Perkowitz, D. B. Tanner, Far infrared properties of inhomogeneous material, Infrared and millimeter waves, Vol. 13, pp. 171-263, Orlando, FL, Academic Press, Inc. (1985).

[17] H. J. Lee, J. H. Jung, K. W. Kim, M. W. Kim, T. W. Noh, Y. J. Wang, W. N. Kang, Eun-Mi Choi, Hyeong-Jin Kim, Complicated nature of the gap in MgB_2: Magnetic-field-dependent optical studies, Phys. Rev. B 65 (2002) 224519.

[18] S. Skalski, O. Betbeder-Matibet, P. R.Weiss, Properties of Superconducting Alloys Containing Paramagnetic Impurities, Phys. Rev. 136 (1964) A1500-A1518.

[19] M. Tachiki, T. Koyama, S. Takahashi, Electromagnetic phenomena related to a low-frequency plasma in cuprate superconductors Phys. Rev. B 50 (1994) 70657084.

[20] H. T. S. Lihn, S. Wu, H. D. Drew, S. Kaplan, Q. Li, D. B. Fenner, Measurement of the Far-Infrared Magnetoconductivity Tensor of Superconducting $YBa_2Cu_3O_{7-\delta}$ Thin Films, Phys. Rev. Lett. 76 (1996) 3810-3813.

[21] L. Kang, B. B. Jin, X. Y. Liu, X. Q. Ji J. Chen, Z. M. Ji, W. W. Xu, P. H. Wu, S. B. Mi, A. Pimenov, Y. J. Wu, B. G. Wang, Suppression of superconductivity in epitaxial NbN ultrathin films, J. of Appl. Physics 109 (2011) 033908.

[22] E. D. Palik, Handbook of Optical Constants of Solids, Academic Press, New York, 1985.

[23] M. Born, E. Wolf, Principles of Optics, Pergamon, Oxford, 1975.

[24] B. Gorshunov, A. Volkov, I. Spektor, A. Prokhorov, A. Mukhin, M. Dressel, S. Uchida, A. Loidl, Terahertz BWO-Spectroscopy, International Journal of Infrared and Millimeter Waves 26 (2005) 1217-1240.

[25] M. W. Coffey, J. R. Clem, Unified theory of effects of vortex pinning and flux creep upon the rf surface impedance of type-II superconductors, Phys. Rev. Lett. 67 (1991) 386-389.

[26] Pei-Jen Lin, P. Lipavský, Time-dependent Ginzburg-Landau theory with floating nucleation kernel: Far-infrared conductivity in the Abrikosov vortex lattice state of a type-II superconductor, Phys. Rev. B 80 (2009) 212506.

[27] H. Shibata, S. Kimura, S. Kashiwaya, S. Ueno,M. Koyanagi, T. Masao, N. Terada, E. Kawate, Y. Tanaka, Far-Infrared Reflectance and Transmittance Studies of YBa2Cu3O7-x Single-Crystal Thin Films, Jap. J. of Appl. Phys. 40 (2001) 3163-3170.

[28] A. A. Volkov, Y. G. G, Goncharov. V. Kozlov, S. P. Lebedev, A. M. Prokhorov, Dielectric measurements in the submillimeter wavelength region, Infrared Phys. 25 (1985) 369-373.

[29] M. Mansuripur, Analysis of multilayer thin-film structures containing magneto-optic and anisotropic media at oblique incidence using 2×2 matrices, J. App. Phys. 67 (1990) 6466-6475.